From microphysics to galactic scales: probing galaxy formation with magnetic fields, cosmic rays, radiation and dust



Francisco Rodríguez Montero

Wolfson College

University of Oxford

A thesis submitted for the degree of

Doctor of Philosophy

Trinity 2024

DECLARATION

I declare that no part of this thesis has been accepted, or is currently being submitted, for any degree or diploma or certificate or any other qualification in this University or elsewhere. Except where otherwise stated, the work in this thesis is entirely my own, and has been carried out under the supervision of Professor Julien Devriendt and Professor Adrianne Slyz.

My work has been supported by the Wolfson Harrison UK Research Council Physics Scholarship, generously funded by Dr Simon Harrison. This work used the DiRAC Data Intensive service (DIaL2 and DIaL3) at the University of Leicester, managed by the University of Leicester Research Computing Service on behalf of the STFC DiRAC HPC Facility (www.dirac.ac.uk). The DiRAC service at Leicester was funded by BEIS, UKRI and STFC capital funding and STFC operations grants. This work used as well the DiRAC Memory Intensive service (Cosma8 and Cosma7) at Durham University. The DiRAC service at Durham was funded by BEIS, UKRI and STFC capital funding, Durham University and STFC operations grants. DiRAC is part of the UKRI Digital Research Infrastructure. This project has received funding from the European Research Council (ERC) under the European Union's Horizon 2020 research and innovation programme (grant agreement No 693024).

The chapters of this thesis are based on either already published works, or projects due to be submitted. Chapter 3 is based on Rodríguez Montero et al. (2024). The initial conditions were provided by Julien Devriendt, the simulations were performed by me, as well as its analysis. Chapter 4 contains the results presented in Rodríguez Montero et al. (2024b), which will be submitted to Monthly Notices of the Royal Astronomical Society. The model presented in Chapter 5 is built on the theoretical work I developed for Katz et al. (2022b) in collaboration with Harley Katz, and in Dubois et al. (2024) in collaboration with Yohan Dubois. Its contents will be published in Rodríguez Montero et al. (2024c) in Monthly Notices of the Royal Astronomical Society. Chapter 6 is based on results presented in Dubois et al. (2024) by Yohan Dubois, for which I contributed to the theoretical and numerical development, as well as to the analysis of the simulations.

Francisco Rodríguez Montero — October 9, 2024

Acknowledgements

I want to express my deepest gratitude to Adrianne Slyz and Julien Devriendt, my supervisors. Thank you for your unwavering support and care, from the first day of this DPhil in the midst of the pandemic, to these tumultuous final months of thesis writing. It has been incredibly fun to travel through the minutiae of science and academia along with you. I am honoured to call you my friends. An immense thanks goes to Sergio Martin-Alvarez, who was oblivious to how much he would have to see of me when he supervised me in Cambridge more than 4 years ago. It goes without saying that I would not have taken this path if it was not for you. Thank you for being my friend and collaborator, even in my most anxious moments.

I am also indebted to my collaborators Joakim Rosdahl, Harley Katz, Martin Rey and Harry Desmond, whose expertise and dedication have enriched my research. A special *merci* goes to my friend Yohan Dubois, who has hosted me (probably too many times) at the IAP and his office, always greeting me warmly with a smile. I am incredibly fortunate to work with you on the countless topics we find fascinating.

To all my friends in Oxford. To Lilian and Mei, who made me feel at home. To the BIPACers, that made my long days in the department fun, but the after-work drinks even better. To the cultural, intellectual and social centre of Oxford, the OIPP and its founders: Mads, Alex, Jaime, Casey and Eric. You were essential in shaping my time in Oxford, being a source of complete madness, joy and inspiration. I will always be in debt for your kindness and warmth. *To the sesh and beyond.*

My life has been a journey between two countries and two homes. I am profoundly grateful for the love from my friends back in Spain: Juan, Lucia, Blanca, Maria, Yolanda, Almu y Amaro. I want to acknowledge and thank them for their enduring friendship and for standing by me despite the distance. Heartfelt gratitude to my friends Manu and Pablo. Their presence in my life has been a cherished anchor through every transition.

And last but certainly not least, to *mi familia*, not just because of everything they have done for me (even as I embarked on this adventure so far away from them), but because you taught me the beauty in the chaos and the strength in family.

Esto es para vosotros.

Abstract

Modelling galaxy formation in a cosmological context is one of the most complex and multi-disciplinary endeavours in theoretical physics. In our current paradigm, galaxies are formed in the potential wells of dark matter halos, with small perturbations collapsing earlier than larger ones. Cosmological simulations are capable of predicting the formation of galaxies in this theoretical context, but require feedback – the injection of energy from stars and super-massive black holes – to slow down, or prevent altogether, the stellar mass growth of galaxies. However, this approach notoriously fails to predict the properties of the population of extremely star-forming galaxies in the early Universe unveiled by current state-of-the-art observations.

In this thesis, we argue that the difficulty in forecasting the properties of these galactic systems stems from models being *calibrated* to observations rather than *derived* from fundamental principles. We propose a holistic approach to galaxy formation, examining how small-scale microphysical processes combine to shape emergent properties like feedback and mass regulation. Through high-resolution simulations of a Milky Way-like galaxy, we find that cosmic rays, beyond merely boosting feedback efficiency, inhibit gas collapse, reduce star formation, and enhance outflows by weakening the gravitational potential and disrupting inflows. This leads to the formation of a *meta-stable* CR-supported corona, providing a reservoir of gas that fuels later galaxy growth.

With the goal of predicting current and future observations with state-of-the-art observational facilities, we have implemented a novel thermo-chemical evolution model of dust, including polycyclic aromatic hydrocarbons within the RAMSES cosmological hydrodynamical code, called Dusty-PRISM. For the first time, we are able to self-consistently predict the seeding, growth and destruction of multiple grain sizes and chemical species within fully multi-phase radiation-hydrodynamics simulations of galaxy formation. We explore the physical processes giving rise to observed extinction curves in the Local Group. Our model successfully reproduces the observed dust-to-metal and dust-to-gas ratios across metallicities, revealing key differences in grain accretion efficiency that explain extinction curve diversity. We also generate mock attenuation curves that highlight the impact of radiative transfer and demonstrate how dust evolution insights can distinguish between different star formation sub-grid models.

Contents

1 Introduction **1**

1.1 Astronomy with supercomputers – the recipe to build our own Universes 1

1.1.1 ΛCDM as a canvas for galaxy formation across cosmic time . . 2

1.1.2 The ingredients for cosmological simulations 6

1.2 On extreme galaxy formation 10

1.2.1 A peek into early galaxy formation with ALMA and JWST . . 12

1.2.2 The roles of chemistry and non-thermal physical components . 14

1.3 The case for a holistic approach to theoretical galaxy formation . . . 16

1.3.1 Emergence as the fundamental nature of galaxies 17

1.3.2 Aims and structure of this thesis 18

2 Galaxy formation with magnetic fields, cosmic rays, radiation and chemistry **20**

2.1 The RAMSES code 20

2.1.1 Cosmic ray magneto-hydrodynamics 21

2.1.2 Radiation hydrodynamics with non-equilibrium metal thermo-chemistry 26

2.1.3 Star formation 29

2.1.4 Type II supernova feedback 32

2.2 The NUT suite of cosmological simulations 33

3 The impact of cosmic rays on the interstellar medium and galactic outflows of Milky Way analogues **37**

3.1 Motivation 37

3.2 The global impact of cosmic rays on the evolution of NUT 41

3.3 How cosmic rays alter the pressure balance of the ISM and star formation efficiency 47

3.4 Cosmic rays reshape how supernovae interact with the galactic region 52

3.4.1 Distribution of supernova sites and feedback effectiveness . . . 52

3.4.2 Influence of cosmic rays on outflow rates 55

3.4.3 Dynamics of multi-phase outflows 60

3.4.4 Cosmic ray-driven re-acceleration of outflows in the CGM . . . 63

3.5 Conclusions 69

4 Cosmic ray-dominated halos in Milky Way analogues **71**

4.1 A step further – The circum-galactic medium of NUT across cosmic time 71

4.2 Falling but not free - the influence of cosmic rays on accretion 77

4.2.1 Inflow properties at the boundary of the galactic region 77

4.2.2 Gas inflow from super-halo scales to the galactic region 80

4.2.3 Gas support in the circum-galactic medium 91

4.3 Gas cooling and heating in the circum-galactic medium 95

4.3.1 The meta-stable cosmic ray corona 100

4.3.2 Virial shock stability analysis 105

4.4 Conclusions 111

5 The Dusty-PRISM model **113**
5.1 Motivation and introduction . . . 113
5.2 The two-size dust model . . . 119
5.2.1 Grain seeding . . . 122
5.2.2 Gas-phase accretion . . . 124
5.2.3 Thermal sputtering . . . 129
5.2.4 Gas collisional cooling/heating . . . 132
5.2.5 Non-thermal sputtering in SN shocks . . . 137
5.2.6 Turbulent shattering of large grains . . . 139
5.2.7 Turbulent coagulation of small grains . . . 147
5.2.8 Molecular hydrogen formation on dust surfaces . . . 149
5.2.9 Dust optical properties . . . 153
5.2.10 Radiative torque disruption of large grains . . . 155
5.3 Polycyclic aromatic hydrocarbons in galaxy formation . . . 160
5.3.1 PAH optical properties . . . 161
5.3.2 PAH sputtering . . . 162
5.3.3 Photo-electric heating by PAHs . . . 170
5.3.4 PAH clustering . . . 176
5.3.5 PAH freezing . . . 179
5.3.6 PAH photo-dissociation . . . 179
5.3.7 Molecular hydrogen formation mediated by PAHs . . . 181
5.4 Conclusions . . . 185

6 The imprint of dust processes in simulated extinction and attenuation curves **188**
6.1 Motivation . . . 188
6.2 The suite of G8, G9 and G10 galaxies . . . 190
6.2.1 Initial conditions . . . 190
6.2.2 The simplified 4-bins model . . . 194
6.3 The critical metallicity for dust growth . . . 196
6.4 Bump or no bump: the dust extinction laws in the Local Group . . . 200
6.5 From extinction to attenuation with SKIRT . . . 204
6.5.1 Preparing RAMSES data for SKIRT . . . 204
6.5.2 The impact of inclination on attenuation curves . . . 207
6.5.3 Can we recover the grain size distribution? . . . 211
6.5.4 Dust growth in massive star-forming clumps . . . 215
6.6 Conclusions . . . 220

7 Conclusions **222**
7.1 Summary . . . 222
7.1.1 Cosmic rays and magnetic fields in the cosmological evolution of Milky Way-analogues . . . 222
7.1.2 Modelling radiation, dust and chemistry for the future of galaxy formation simulations . . . 224
7.2 Outlook . . . 225

References **227**

1 Introduction

Contents

1.1 Astronomy with supercomputers – the recipe to build our own Universes 1
1.2 On extreme galaxy formation 10
1.3 The case for a holistic approach to theoretical galaxy formation 16

1.1 Astronomy with supercomputers – the recipe to build our own Universes

Humankind's perspective on the heavens has profoundly evolved from prehistoric times to the present day. Whilst we have extended our reach to the most remote places of our planet, we have steadily uncovered a cosmos unimaginably large, old and mysterious. Early humans observed celestial phenomena, such as the movement of the Sun, the Moon, and the stars, in one of the first efforts to use our pattern-seeking mind for predicting the coming and going of seasons. In ancient Mesopotamia, the Babylonians developed sophisticated methods for predicting celestial events, such as eclipses. In ancient China, astronomers made meticulous observations of events like comets, supernovae, and eclipses. Similarly, in the Islamic Golden Age, scholars like Al-Battani and Al-Sufi made fundamental contributions to the measurement of the solar year and the first catalogue of stars described by a logarithmic scale in brightness (Kennedy, 1956). As time progressed, the development of observational tools and scientific methodologies drastically changed our understanding of the sky. The invention of the telescope in the early 17th century by Galileo Galilei marked a pivotal moment in the history of astronomy. This instrument allowed for detailed observations of celestial bodies, confirming the presence of moons orbiting other planets (like the observations

by Chinese astronomer Gan De suggested for Jupiter in the 4th century BCE, Cullen, 1996) or the presence of mountains on the surface of the Moon (Galilei, 1610).

A major paradigm shift occurred not much more than a century ago, with the realisation that the Milky Way is not the entirety of the Universe, but just one of the many 'island universes' scattered throughout the cosmos (Lemaître, 1927; Hubble et al., 1929). This meant that not only the sky was filled with the light from 100 billion or so Milky Way stars, but also that our 'island' did not possess any special attribute compared to the virtually infinite galaxy zoo that observations started to reveal in the mid-20th century – this marked the beginning of extra-galactic astronomy. To exacerbate the turmoil in which the scientific community was embedded, observations that the recession velocities of these galaxies are linearly related to their distances established the Universe was expanding, as suggested by Alexander Friedmann's solution to Einstein's field equations (Friedmann et al., 1922). This meant that the history of the Universe as we know it began about 13.7 billion years ago (e.g. Planck Collaboration et al., 2016, for one of the most recent observational constraints), which implies that over the lifetime of many of the galaxies we observe now, the Universe has changed considerably. This new framework was revolutionary, since it implied that not only galaxies are diverse in colours, sizes, shapes, etc. at this present epoch, but that they must have had very different properties across cosmic time, from turbulent early stages as a dense and hot primordial plasma, to the accelerated expansion epoch in which we now live (Riess et al., 1998; Perlmutter et al., 1999). This gave rise to the field of galaxy formation and evolution in a cosmological context, which we briefly review in the following sections.

1.1.1 ΛCDM as a canvas for galaxy formation across cosmic time

Under the standard paradigm for an expanding, baryon-only[1] Universe with a finite age, the Universe starts in a hot, dense state characterised by small quantum fluctuations in the energy-matter density (Hawking et al., 1982; Guth et al., 1982; Starobinsky et al., 1982; Bardeen et al., 1983). The evolution of these baryon fluctuations is then driven by a competition between (self-)gravity and pressure as argued in the Jeans et al. (1902)

[1]We note that we refer to all ordinary matter as 'baryons', while non-ordinary matter also include leptonic particles.

formalism. This predicts that density perturbations evolve depending on how large they are compared to the Jeans' scale $\lambda_{\rm J}$ (see also Section 2.1.3): baryon perturbations with $\lambda > \lambda_{\rm J}$ will be capable of growing, whereas for perturbations with $\lambda < \lambda_{\rm J}$ the restoring pressure force prevents collapse and drives the system to undergo harmonic oscillations (i.e. acoustic waves). This framework was applied to an expanding background (Gamow and Teller, 1939; Lifshitz et al., 1946; Silk, 1968) to study the linear evolution of ordinary baryonic matter and radiation perturbations. These analytic calculations showed that, when matter and radiation are fully coupled, the Jeans' mass is very large ($\sim 10^{16}$ M$_\odot$), resulting in average galaxy scale perturbations ($\sim 10^{12}$ M$_\odot$) experiencing acoustic oscillations instead of growth under gravitational collapse as seen in our Universe. Different energy/matter components experience a different evolution of their energy density as the Universe expands. The energy density of radiation decreases as $\propto a^{-4}$, where a is the scale factor, while the energy density of matter decreases as $\propto a^{-3}$. As the scale factor a increases, the radiation density thus decreases at a faster rate than matter, giving rise to a point in time at which they are equal. Continued expansion allows for the radiation-matter fluid to cool below the hydrogen ionisation temperature, resulting in electrons and protons combining together to form neutral hydrogen (at time $t_{\rm dec}$). This 'recombination', results in a sudden drop of the Thomson scattering depth and effectively decouples matter and radiation – photons can stream freely. Silk (1968) also showed that towards the end of recombination (close to $t_{\rm dec}$, see Fig. 1.1), small-scale perturbations are washed out by photon diffusion. This results in $10^{12} - 10^{14}$ M$_\odot$ perturbations being heavily reduced, in what is termed 'Silk damping'. After recombination, the Jeans' mass suddenly decreases to $\sim 10^6$ M$_\odot$, but Silk damping has already wiped out galaxy-scale perturbations at this point. Such a lack of small-scale perturbations not only results in a 'top-down' formation of galaxies, but it also means that there is simply not enough time between $t_{\rm dec}$ and now to grow the structures we see today in the Universe from the tiny fluctuations generated in the Early Universe.

There is observational evidence that the Universe is far from being composed only of radiation and ordinary baryonic matter. At the end of recombination, the thermal radiation emitted at the last surface of scattering results in what is observed as the cosmic microwave background (CMB). The CMB not only is one of the

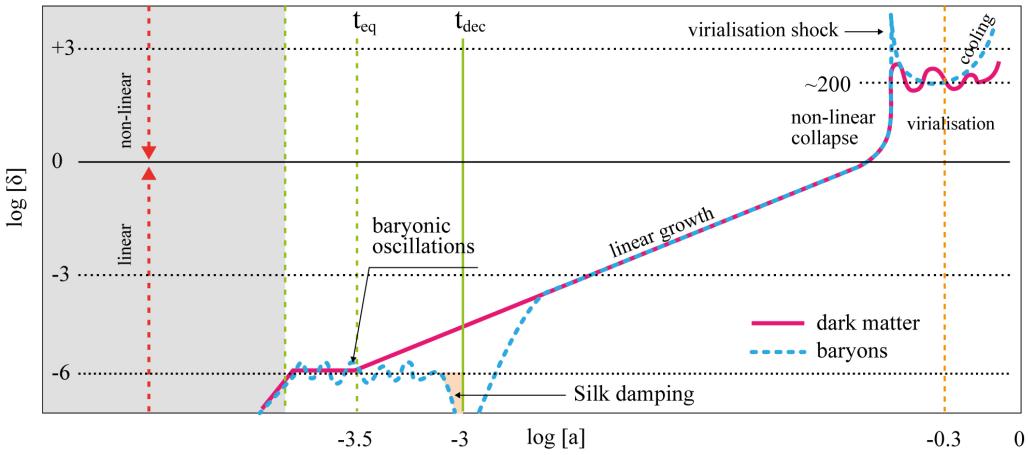


Figure 1.1: Density contrast δ of a galaxy-scale perturbation ($M \sim 10^{12}$ $M_\odot$) as it evolves from the radiation-dominated era (in the linear regime) to its final virialisation (in the non-linear regime) and the on-set of further gas cooling collapse. The solid fuchsia line shows the evolution of the cold dark matter component, while the dashed blue line represents the baryonic component. This graphically illustrates the role of collapsed dark matter structures as the potential well 'skeleton' onto which baryonic perturbations, that were prevented from growing by acoustic oscillations and Silk damping, can collapse to form the first proto-halos. We indicate the epochs of radiation-matter equality ($t_{\rm eq}$) and radiation-matter decoupling ($t_{\rm dec}$) as vertical dashed and solid lime-coloured lines, respectively.

strongest underpinnings of the hot Big Bang model, but also allows us to peek at the baryon-photon fluid properties at the end of the recombination era. By computing the temperature fluctuations from the average temperature, it is possible to obtain the power spectrum C_l representing the variance of these fluctuations at different angular scales. The aforementioned acoustic oscillations in the baryon-photon fluid are imprinted in the observed peaks and valleys in the C_l, encoding information not only about the density of baryonic matter that gave rise to higher or lower radiation temperatures, but also about the total energy-density content of the Universe. The most recent cosmological parameters inferred by Aghanim et al. (2020) suggest that only $\sim$ 15.6% of the total matter density of the Universe is composed of baryons. What is the remaining matter component? Tentative evidence for a non-baryonic (i.e. only detectable through its gravitational interaction) matter component was already proposed by Zwicky et al. (1933). The high galaxy velocity dispersion he measured in the Coma Cluster required an amount of mass $\sim$ 400 times larger than that measured from the stellar light to be explained. It took close to 40 years for the interest in this 'dark' matter component to resurface. Observations of the rotation curve of the Milky Way and nearby galaxies were extended to sufficiently high radii to show the surprising absence of the expected Keplerian fall-off which should naturally

be caused by concentrated stellar and gas distributions (Ostriker et al., 1974; Einasto et al., 1974; Roberts et al., 1973; Rubin et al., 1978; Rubin et al., 1980). The presence of an extended 'halo' of invisible matter matching the properties of a cold dark matter (CDM) particle candidate predicted by supersymmetric theories (see the review by Bertone et al., 2005) was thus inferred. Having a very large particle mass, CDM would have become non-relativistic long before recombination, preventing the erasure of small scale fluctuations. Instead, they would have been able to grow (see fuchsia line in Fig. 1.1) without being much hampered by either acoustic oscillations or Silk damping, beyond the fluctuations visible in the CMB, and ending up forming virialised structures named DM 'halos' (Lynden-Bell et al., 1967). In this scenario, CDM plays the fundamental role of a 'backbone' of potential wells which speeds up baryonic matter collapse after recombination to form the galaxies that we see today. The first CDM N-body simulations (Davis et al., 1985) predicted galaxy clustering in agreement with observations, provided that the luminous matter of galaxies is a biased tracer of the total matter density distribution (Kaiser et al., 1984). The idea of bias was developed further by Bardeen et al. (1986) and extended Press-Schechter theory (Mo and White, 1996) to determine that this bias mainly depends on the size of the perturbation (or equivalently, the mass of the DM halo). This also meant that bias evolves with redshift, becoming naturally larger at earlier epochs, as the first galaxies to form would have been hosted in the most massive halos (Fry et al., 1996; Tegmark and Peebles, 1998). We will return to this very interesting point of the galaxy-halo connection (Wechsler and Tinker, 2018) in Section 1.2.

It became apparent in the early 1990s that, although CDM was capable of predicting the formation of gravitationally bound systems with the size of galaxies, galaxy surveys were starting to point at a Universe where galaxy clustering was lower than predicted by the CDM model (Maddox et al., 1990; Efstathiou et al., 1990). This gave rise to modifications of the 'vanilla' CDM model, that included contribution from DM with different thermal properties (i.e. different velocities after decoupling from other matter and radiation fields, like the case of massive neutrinos) or an open geometry. Out of this plethora of parameter modifications, a 'concordance' model was built, based on a flat Universe geometry, a CDM dominated matter content and a cosmological constant, Λ, possibly representing the vacuum energy. This marked the birth of ΛCDM, although

it was not widely accepted until observational evidence of an accelerated expansion (driven by a non-zero cosmological constant) was provided by SNIa light curves (Riess et al. 1998; Perlmutter et al. 1999) and the confirmation of a spatially flat Universe by measurements of the small-scale anisotropy in the CMB (De Bernardis et al., 2000). The source of this late time acceleration and the need for a cosmological-constant-like term in Einstein field equations is referred to as 'dark energy'. Together with DM, they represent the two current major energy-mass components of our Universe, and yet their nature remains a mystery.

1.1.2 The ingredients for cosmological simulations

With ΛCDM predicting the formation of collapsed DM structures, we now contemplate the assembly of galaxies out of the gas accreted into these DM halos. This is the so-called 'two-stage' model of galaxy formation proposed by White et al. (1978), which, based on the Press-Schechter formalism, is capable of predicting the luminosity function (i.e. number of objects per unit volume and unit luminosity) of galaxies. Already in this early work, it became clear that the luminous matter in galaxies cannot account for the entirety of the ordinary matter contribution, and that a good fraction of it remains in intergalactic space. This result agreed with the earlier idealised spherical collapse simulations of Larson et al. (1974a), Larson et al. (1974b), Larson et al. (1975), and Larson et al. (1976), which showed that energy injection by massive stars could be enough to gravitationally unbind a significant fraction of the ordinary matter in small galaxies, drastically reducing their mass and numbers. However, it failed to emphasise that even with such a source of energy injection at the low-mass end of the luminosity function, the number of small galaxies predicted by the CDM model was still too large. Furthermore, it was unclear why galaxies with masses above 10^{12} $M_\odot$ were also much rarer in the local Universe than predicted.

To further understand these questions, we need to introduce the role of radiative cooling in galaxy growth. The concept of a 'virialised' halo can be understood as the balance between expansion and collapse, and is reached when the halo average kinetic energy becomes equal to half its average potential energy (as set by the virial theorem). A useful approximation, borne out by N-body cosmological simulations, is that halo virialises once its overdensity reaches $\Delta_{\rm vir} \sim 200$ times the critical density

of the Universe, defined as $\rho_{\rm crit} = 3H^2(a)/(8\pi G)$, where H is the Hubble parameter ($H \equiv \dot{a}/a$) and G is the gravitational constant. By analogy between velocity dispersion and temperature, the virial velocity $V_{\rm vir}$ of a spherical structure of average density $\Delta_{\rm vir}\rho_{\rm crit}$ and virial radius $R_{\rm vir}$ can be expressed as:

$$T_{\rm vir} = \frac{\mu m_{\rm H}}{5k_{\rm B}} V_{\rm vir}^2, \tag{1.1}$$

where $T_{\rm vir}$ is the virial temperature, μ is the average mass per particle in the gas in units of the hydrogen mass $m_{\rm H}$, and $k_{\rm B}$ is the Boltzmann constant. In the original discussions on collapse and cooling (Silk, 1977; Rees and Ostriker, 1977; Binney et al., 1977), gas falling into a DM halo is shock-heated to approximately $T_{\rm vir}$ ('hot-mode' accretion), setting it in hydrostatic equilibrium in the halo potential well (Birnboim and Dekel, 2003), and effectively slowing down its accretion onto the central galaxy. Gas can also fall ballistically in the halo, effectively reaching the inner regions in the form of cold and dense gas filaments ('cold mode' accretion, Kereš et al., 2005a). Whatever the accretion mode, the final problem is how the energy of the gas (either in the form of thermal or kinetic) is lost as this latter ultimately collapses, settles into a centrifugally supported disc, and forms stars (White et al., 1978). This can be achieved by internal atomic processes that allow the transfer of energy from the gas to radiation, which, if the system is optically thin, propagates away and effectively reduces this latter's support against gravity. Efstathiou et al. (1983) argued that gas cooling, combined with the two-stage model of White et al. (1978) could better explain the formation of disk galaxies than the monolithic collapse invoked in earlier models (Eggen et al., 1962; Gott et al., 1976).

With this, we have the 'blueprint' for the current paradigm of galaxy formation (Somerville and Davé, 2015):

- **Cosmological Initial Conditions**: Extracting the cosmological parameters from the information contained in the CMB angular power spectrum, use the solutions of Einstein's field equations to determine both the expansion of the Universe and the (linear) growth of large scale structure (LSS) all the way to the present day.

- **DM Halo**: Follow the small scale perturbations as they become non-linear, collapse and merge to form larger systems in a bottom-up hierarchical manner. These gravitationally bound halos are embedded in a network of 2D structures (walls), which intersect forming 1D filaments constituting the backbone in which gas collapse takes place.
- **Accretion and Cooling**: Track the accretion of gas from cosmological scales right to the centre of DM halo potential wells, as it experiences shock heating, and winds up either supported by thermal pressure (hydrostatic equilibrium) or the centrifugal force after it radiatively cools (disc) and further fragments and condenses into stars.
- **Feedback**: Inject the energy released by massive stars to prevent the full conversion of ordinary matter into stars over a free-fall time.

Originally introduced by White et al. (1991), semi-analytic models of galaxy formation based on this blue print and grafted onto halo merging histories calibrated on numerical N-body cosmological simulations, burst onto the scene (Kauffmann et al., 1993; Dalcanton et al., 1996; Mo et al., 1998; Somerville and Primack, 1998). Pushing further the frontier of theoretical and numerical models, progress in high-performance computing in the mid-1990s allowed for the emergence of the first 3D hydrodynamical simulations of galaxy formation (Katz et al. 1991; Katz 1992).

A key aspect that all semi-analytic and numerical studies of cosmological galaxy formation to date agree on is the need for various forms of baryonic feedback to create galaxy populations in agreement with observations. However, we remind the reader of a fundamental issue which arises from this realisation: while the original modelling of galaxy formation within ΛCDM was constructed with a logical set of steps that related cosmological scales to the formation of the first bound structures (recall the evolution portrayed in Fig. 1.1), the final piece of the puzzle in the construction of a 'concordance' model for galaxy formation relies on physical processes emanating from the evolution of individual stars (or black holes). This 'inverse cascade' propagates from interstellar medium (ISM) scales, all the way to the distribution of ordinary matter on scales of galaxy clusters and the inter-galactic medium (IGM). This means that the physical processes ultimately involved to achieve a complete modelling of galaxy formation

cover more than 13 orders of magnitude in spatial scale. Furthermore, we need to connect a physical model which can be fully constrained with just 6 parameters (the ΛCDM model) on cosmological scales, to the great complexity of all the astrophysical processes taking place within galaxies, and involving many uncertain parameters from plasma physics, thermodynamics, electrodynamics, molecular chemistry, atomic, nuclear and high-energy physics. For this reason, large scale cosmological simulations have resorted to an 'effective' theory perspective, with the aim of constraining the parameters of the 'concordance' galaxy formation model by comparing to cosmological-averaged studies of galaxy populations. In other words, due to the intrinsic resolution limitations of cosmological simulations, this complex interplay of physical processes on small scales are parameterised as *sub-resolution* models (a set of simplified partial differential equations). These latter range from sub-grid models describing star formation and the injection of stellar feedback energy and mass, to the growth of super-massive black holes (SMBH) and their feedback, or the interaction of gas, elements and molecules with radiation (see the extensive reviews by e.g. Somerville and Davé, 2015; Naab and Ostriker, 2017).

Using such an approach, cosmological simulations with different numerical techniques have made spectacular progress in the latest decade (we refer to the recent review by Vogelsberger et al., 2020a). They are capable of reproducing many properties of galaxy populations, such as sizes, abundances, star formation rates, gas fractions, gas-phase metallicities[2], but also the fractions of star-forming to quiescent galaxies, or the correlation between galaxy mass and SMBH mass (e.g. Davé et al., 2013; Hirschmann et al., 2014; Schaye et al., 2015; Sijacki et al., 2015; Dubois et al., 2016; Davé et al., 2019; Nelson et al., 2019). The wide success of cosmological galaxy formation simulations marks a milestone in astrophysics, highlighting the field's remarkable progress. This accomplishment not only underscores the predictive power of human reasoning but also demonstrates how far our understanding of the Universe has advanced, from analytic theoretical models to sophisticated computational tools that mirror the cosmos with stunning accuracy.

[2]Metallicity Z is defined as the ratio of gas mass in elements heavier than helium over the total gas mass.

1.2 On extreme galaxy formation

Building a deeper picture of the galaxy formation process requires forensic studies of the present galaxy population, considering stellar ages, metal and gas contents, morphologies, etc., as well as observations of the initial growth of baryonic structures at high redshift, before the global trends in the current galaxy population were even in place. Observations of present day elliptical galaxies (see review by Dekel and Birnboim, 2006) support the idea that a large fraction of their stellar mass was formed at $z \geq 2$, which places the formation of spheroids as key in the understanding of the evolution of galaxy formation across cosmic time. However, it has been known since the launch of the InfraRed Astronomical Satellite (IRAS) and the Cosmic Background Explorer (COBE) that a substantial fraction of the star formation taking place at these early epochs is enshrouded in dust (Hauser et al., 1998).

Of particular interest in the high-redshift infrared (IR) population are the bright sub-millimetre galaxies (SMGs) discovered in the 200 μm to 1 mm range by the SCUBA camera on the James Clerk Maxwell Telescope (JCMT) (Holland et al., 1999). SMGs have now been identified with a population of particularly dusty, high (rest-frame) IR luminosity galaxies ($L_{\rm IR} > 10^{12} L_{\odot}$), typically found at high redshift ($1 \leq z \leq 4$) (Smail et al., 1997; Smail et al., 1999). Under the assumption that their IR continuum luminosity is a result of dust absorbing UV light and re-emitting at longer wavelengths, these observations imply large dust masses and extreme star-formation rates (up to 10^3 $\mathrm{M}_{\odot}$ yr^{-1}) (e.g. Sun et al., 2024), with signatures of an already evolved stellar population only $\lesssim 400$ Myr after the Big Bang (e.g. Capak et al., 2011; Walter et al., 2012; Strandet et al., 2016; Marrone et al., 2018; Casey et al., 2019). They appear to be significant contributors to both the cosmic star formation rate density ($\sim 20\%$) and stellar mass density ($\sim 30 - 50\%$) between $z = 2$ and 4 (Michałowski et al., 2010). With such high star formation rates, SMGs can increase their already high stellar mass in short periods of time. This extreme evolution, along with the high metallicities found, challenges the hierarchical modelling of galaxy growth (Marrone et al., 2018) and raises questions about their dust enrichment (Hughes et al., 1997; Omont et al., 2001; Mancini et al., 2015). Indeed, SMGs may be an important phase for the most massive galaxies of the Universe, the seeds from which the local luminous spheroids and elliptical galaxies will be formed (Chapman et al., 2005;

Toft et al., 2014; Simpson et al., 2014). This connection is further supported by the similarity in the peak of the redshift distribution between SMGs and SMBH accretion-powered quasi-stellar objects (QSOs) (Swinbank et al., 2006; Hickox et al., 2012; Simpson et al., 2012). The original ultra-luminous IR galaxies (ULIRG) and QSO evolutionary connection suggested by Sanders et al. (1988) would further support this association, making the study of the most extreme star-forming galaxies at high redshift the study of the first SMBHs' growth.

It is not a surprise that this extreme galaxy population has been the subject of many studies based on the semi-analytic models and cosmological hydrodynamics simulations approach of galaxy formation. Granato et al. (2000) found that their modelling under-predicted the number counts of these galaxies by a factor $\sim 20-30$, similar to other semi-analytic models (Fontanot et al., 2007; Somerville et al., 2012). It was not until Devriendt and Guiderdoni (2000) modified the stellar IMF for starbursts by making it top-heavy that these were able to reproduce the SMG number counts and redshift distributions. Nevertheless, such IMF variations are still fiercely debated (Hopkins et al., 2013b; Krumholz, 2014) and it is unclear whether they are necessary, rather than just sufficient, given the many free parameters employed in SAMs (although there are increasing hints for a deviation of a local IMF in high redshift galaxies, e.g. Zhang et al., 2018; Romano et al., 2019). Large cosmological simulations have also experienced difficulties in predicting the properties of highly star-forming galaxies in the Early Universe. Hayward et al. (2021) showed that, while the older *Illustris* model is in poorer agreement with local constraints compared to the newer *IllustrisTNG* iteration, it featured a larger population of highly star-forming systems at high redshift, in better agreement with observations. In fact, this has become a common trend of current state-of-the-art cosmological simulations, where an improved agreement of the present-day simulated galaxy population usually comes with an under-prediction of the amount of star-formation at earlier stages of galaxy formation (e.g. Davé et al., 2010; Shimizu et al., 2012; McAlpine et al., 2019; Lovell et al., 2021; Finkelstein et al., 2023). This discrepancy stems from several assumptions in these galaxy evolution sub-grid models (about star formation and feedback, ISM properties, dust and metal enrichment), establishing the population of star-forming galaxies at high redshift as a powerful way to discriminate between these various models.

1.2.1 A peek into early galaxy formation with ALMA and JWST

The Atacama Large Millimeter/submillimeter Array (ALMA) has significantly advanced our understanding of star-forming galaxies at high redshift thanks to its high sensitivity and spatial resolution. The IR-derived intense periods of star formation appear to be fuelling large galactic winds and outflows, with redshift offset velocities between nebular emission lines and UV absorption lines of $\sim 1,000 - 3,000$ km s^{-1} (Harrison et al., 2012; Danielson et al., 2017). Additionally, SMGs appear to have a brighter and bluer stellar emission (Da Cunha et al., 2015), which suggests that SMGs may be more extended than ULIRGs and/or that there exists some offset between the dust and star spatial distributions, a highly difficult de-correlation to observe in galaxy simulations without on-the-fly dust modelling (e.g. Cochrane et al., 2019; Pallottini et al., 2022). In fact, one of the general findings of FIR-bright objects is the difference in compactness between the FIR continuum and the cool gas traced by CO emission (Chen et al., 2017; Tadaki et al., 2017; Rivera et al., 2018; Álvarez-Márquez et al., 2023), naively implying a varying dust-to-gas ratio across individual galaxies. Gravitationally-lensed objects have allowed ALMA to observe some massive SMGs at high redshift with unprecedented resolution. This has allowed for a deeper look into the spatial variations within these objects, suggesting a non-uniform distribution of dust in clumps of size $\sim$ 200 pc (Dye et al., 2015; Rybak et al., 2015a; Rybak et al., 2015b) with a similar offset from the near-IR emission seen in lower resolution observations (Hodge et al., 2012; Hodge et al., 2015). These large scale 'clumps' have long been theorised as features not only in merging/interacting systems (Ivison et al., 2013; Noguchi, 1999), but also in the turbulent disc structures of high redshift galaxies (Bournaud et al., 2013), supporting the idea that high star formation rates could also be sustained by efficient continuous cold gas accretion from the cosmic web (Ocvirk et al., 2008; Dekel et al., 2009a). These high resolution observations have also allowed a glimpse into galactic dynamics at high redshift: most studies find signatures of rotationally supported discs (Bouché et al., 2015; Davies et al., 2011; di Teodoro and Fraternali, 2015), which does not however completely dismiss the merger/interaction-induced starburst scenario that has long been theorised to drive highly star-forming galaxies. Dye et al. (2015) and Swinbank et al. (2015) measure a

low Toomre stability parameter ($Q \sim 0.3$) in these galaxies, suggestive of an unstable disk, with an external hydrostatic pressure for the ISM approximately 10^4 times higher than typical in the Milky Way (Swinbank et al., 2015). This is in agreement with other observational evidence of an overall denser ISM (than the star-forming sequence in the local Universe) permeated with strong UV fields (Bothwell et al., 2017), although it remains to be seen as to what extent cold molecular lines observed with ALMA trace the gas mass at these redshifts (see e.g. Palla et al., 2024, for a discussion).

The James Webb Space Telescope (JWST) has surpassed the expectations of the galaxy formation community for its ability to probe the high redshift Universe. Soon after the first observations of the SMACS 0723 lensing cluster, drop-out methods have already detected a large population of galaxies out of reach of the Hubble Space Telescope (HST) in the mid-IR wavebands (Yan et al., 2022). Further progress in the photometric and spectroscopic observations of this high redshift population have confirmed that a higher proportion of the star-forming galaxies are in a extreme emission line (EEL) state (from 23% at $z \sim 2$ to 61% at $z \sim 5$, Boyett et al., 2024), albeit with up to an order of magnitude in scatter, suggesting a large diversity of ISM physical conditions (Cameron et al., 2023) for intense starbursts at high redshift (contributing $\lesssim 70\%$ of star-forming galaxies at $6 \leq z < 12$, Dressler et al., 2024). One of the systems that has become the focus of numerous JWST studies is the GN-z11 galaxy (Bunker et al., 2023), presenting tentative signatures of a harder radiation field characteristic of the first stars (Population III, or Pop III) exciting the HeIIλ1640 line (Maiolino et al., 2024a). The contribution of a SMBH accreting at $\sim 5\times$ the maximum luminosity rate[3] has also been argued as an alternative/additional source of high ionisation states in the observations of GN-z11 (Maiolino et al., 2024b). In fact, this is becoming a more common conclusion of many observations with JWST (e.g. Tacchella et al., 2023; Juodžbalis et al., 2023; Juodžbalis et al., 2024), suggesting that close to 20% of galaxies harbour an active galactic nuclei (AGN) regardless of redshift (determined at $2 \lesssim z \lesssim 10$ Scholtz et al., 2023), with some of them sufficiently obscured by dust that their mid-IR spectra is dominated by the heating from the AGN (Yang et al., 2023). These observations confirm the difficulties in

[3]The Eddington luminosity, or Eddington limit, is the maximum luminosity that a body can attain before the outward radiation pressure overcomes the inward pull of gravity in a spherically symmetric environment.

predicting SMBH masses at these early times, as it remains a challenging modelling task to correctly predict simultaneously the stellar mass growth (Qin et al., 2023) and the SMBH growth (Schneider et al., 2023).

1.2.2 The roles of chemistry and non-thermal physical components

The observations previously described point at the study of the ISM properties to study the joint signatures of intense galaxy and SMBH growth. While CO is commonly used to detect cold gas in high redshift objects, the relatively low energy required to collisionally excite it, makes it less reliable as a tracer of the dense cold gas which will truly collapse to form stars. A less 'conventional' line emission, hydrogen cyanide (HCN), has been found to correlate with SFR across a large range in HCN luminosity (Gao and Solomon, 2004; Wu et al., 2005; Zhang et al., 2014). Excitation analysis of HNC, HCN, HCO+, and CN has shown that emission originates in a warm (40-90 K), dense, and optically thick medium (Spilker et al., 2014; Oteo et al., 2017), with volume-filling photo-dissociation regions (PDRs). Also, these authors find the ratio of line luminosity of the HCN 1-0 transition to the CO 1-0 transition to be significantly higher than for local highly star-forming galaxies (Oteo et al., 2017), suggesting that a higher fraction of the molecular gas in high redshift massive galaxies is in the form of dense gas. H_2O (water) is a significant dense gas tracer, believed to be one of the most abundant molecules in molecular clouds (Tielens et al., 1991), with high excitation lines (radiatively excited by the local infrared radiation field) as bright as the CO emission lines. Therefore, H_2O lines are a powerful diagnostic of the radiation field in dense cold gas regions, hinting at a dense, warm and optically thick medium as well (Van Der Werf et al., 2011; Omont et al., 2011; Omont et al., 2013; Vlahakis et al., 2015; Yang et al., 2016; Yang et al., 2019) as the source of emission. For example, SMGs appear to show a clear scaling of the IR luminosity with H_2O luminosity (Omont et al., 2013; Yang et al., 2016), making them very strong emitters in water vapour with no counterpart at low redshift. This evidence supports the idea that extremely star-forming systems may be dominated by radiation pressure in the high density clumps where star formation is taking place (Van Der Werf et al., 2011). Furthermore, there also exists evidence of a particularly carbon-rich ISM in some

of these high redshift observations (Arellano-Córdova et al., 2022; D'Eugenio et al., 2023; Jones et al., 2023), indicative of Pop III enrichment that could have a significant impact on the growth of carbonaceous grains (Witstok et al., 2023).

As they are shaped by very energetic processes, extreme star-forming galaxies are also expected to be places where strong magnetic fields and large amounts of cosmic rays (CRs) are produced. Understanding the relation between high star formation and high magnetic/CR energy is key to understanding the far-infrared/radio correlation (FIRRC) (van der Kruit, 1971; van der Kruit, 1973; de Jong et al., 1985; Helou et al., 1985; Condon, 1992; Yun et al., 2001; Bell et al., 2003; Magnelli et al., 2015). In the 'calorimeter' model proposed by Völk et al. (1989) and Lisenfeld et al. (1996), galaxies are completely opaque to the UV emission from massive stars which is re-radiated by dust in the far-infrared band. These same massive stars ($M \sim 8 - 40 M_{\odot}$, Condon, 1992; Heger et al., 2003) will end their lives as core-collapse supernovae (SNe), one of the major sources of CRs (Bell, 1978b; Bell, 1978a). The resulting CRs will travel through the galaxy guided by magnetic fields and, while they gyrate around the field lines, they will emit radio synchrotron radiation. If the diffusivity of CRs is sufficiently small and they experience large synchrotron losses, only a small fraction will escape the galaxy, giving rise to the aforementioned FIRRC. The tight FIRRC has been extensively used as a probe of highly obscured star formation (Haarsma et al., 1999; Smolcic, 2009; Karim et al., 2011; Novak et al., 2017), but its application at high redshift requires a better understanding of its evolution across cosmic time. Furthermore, as was pointed out by Thompson et al. (2006), the aforementioned calorimeter model assumes that synchrotron losses dominate the energy loss processes of CR processes, while in starbursts systems inverse Compton, Bremsstrahlung and ionisation losses can easily dominate. This means that the synchrotron flux would not be directly measuring the magnetic field strength but the rate at which energy is supplied to CR electrons (i.e. SNe), and hence directly relating the star formation rate to the synchrotron emission. The subdominant contribution of synchrotron emission to the energy loss of CR electrons has been further confirmed by isolated galaxy simulations (e.g. Werhahn et al., 2021) and semi-analytic models for CR transport and losses (e.g. Roth et al., 2024). From an observational standpoint, studies have both shown that $q_{\rm IR}$ (logarithmic ratio of the FIR and radio luminosity) does not change

with cosmic time (Ivison et al., 2010b; Sargent et al., 2010; Duncan et al., 2020; Algera et al., 2020) and the contradictory result of a slight decrease in $q_{\rm IR}$ with increasing redshift (Ivison et al., 2010a; Thomson et al., 2014; Magnelli et al., 2015; Delhaize et al., 2017; Rivera et al., 2018; Ocran et al., 2020). Note that this is contrary to the theoretically expected trend of an increase with redshift (Murphy, 2009), mostly from synchrotron e^- inverse Compton scattering off CMB photons which pollutes the FIRRC. This argues in favour of strong magnetic fields ($B \gtrsim 0.2$ mG) and the production of secondary CR electrons in the extreme environments of these systems (Lacki et al., 2010; Lacki and Thompson, 2010; Thomas and Pfrommer, 2019; Algera et al., 2020; Roth et al., 2024). The discrepancy of $q_{\rm IR}$ between SMGs and normal star forming galaxies may be related to SMG size estimates depending on whether one deduces them from FIR dust emission or radio continuum (Simpson et al., 2015; Miettinen et al., 2015; Miettinen et al., 2017). Simpson et al. (2015) argue that this disparity may be related to a higher CR diffusion creating an extended synchrotron halo, which disagrees with evidence for starburst galaxies given the rapid cooling times (Dahlem et al., 1995; Lacki et al., 2010). The production of secondary CR electrons in the extended disk of SMGs or the formation of interacting bridges (Litke et al., 2019) bright in synchrotron emission (Miettinen et al., 2017) have also be invoked as ways to overcome this disagreement. Line emission diagnostics may shed more light on the issue, e.g. the formation of H_2O and H_2O^+ (Yang et al., 2016; Indriolo et al., 2018), H_2 line emission (Gaches et al., 2022), and high [OIII]λ4363/[OIII]λ5007 (Katz et al., 2022a) can be used to constrain the ionisation rate of CRs and how it varies across the disk and in the extended halo (see also Yokoyama and Ohira, 2023, for the heating generated by streaming CRs).

1.3 The case for a holistic approach to theoretical galaxy formation

We have reviewed recent observations by ALMA and JWST of the surprising aspects of early galaxy evolution and the properties of extremely star-forming systems. These findings indicate that the current theoretical paradigm of galaxy formation has significant gaps, particularly in predicting the early stages of development, the intense growth of massive galaxies and SMBHs, and the properties of outliers which

significantly deviate from the average galaxy. Such issues typically constitute the telltale sign of a model crossing the boundaries of the parameter space in which it was qualitatively[4] calibrated.

1.3.1 Emergence as the fundamental nature of galaxies

As we discussed in Section 1.1.2, the injection of energy from stellar processes and SMBH growth are fundamental components of the current paradigm of galaxy formation (Hopkins et al., 2012), as they limit the efficiency of gas-to-star conversion and drive the interaction of ordinary matter located at the centre of the potential well of the halo with the larger scales of the circum-galactic medium (CGM) and the IGM (in what is called the 'baryon cycle'). But the concept of 'feedback' is not a fundamental physical concept – individual stars and SMBHs are not 'aware' of the excessive global gas consumption in the galaxy. Instead, feedback is the result of many individual components in the galactic environment, interacting under a set of rules which results in a very clear global property. This idea of 'More is different' was originally proposed by Andersen (1972) under the concept of 'emergence'.

Emergence is a fundamental concept in complex systems and can be observed across various scientific disciplines, from solid-state physics to sociology. It refers to the phenomenon where larger entities, patterns, and properties arise through the interactions among smaller or simpler entities that themselves do not exhibit such properties. Emergent properties are not predictable from the properties of the individual components alone; rather they arise from the collective behaviour and interactions within the system (Gu et al., 2009). Note that the concept of emergence in complex systems is not equivalent to chaos theory. In fact, chaos is the epistemological opposite to emergence, as the former is the result of many simple interaction that results in a highly-dimensional exploration of the dynamical phase-space of the system, while the latter is how a large number of extremely complicated and dynamics set of relationships (e.g. stellar evolution, plasma physics, turbulence, radiative cooling,

[4]We stress that such a calibration process is practically always performed in a biased and qualitative manner. For example, in an extensive literature search of feedback parameter choices in cosmological simulations we were only capable of finding a single model (the FLAMINGO simulation) that performed a Bayesian analysis to determine the most likely set of parameters given the observational data (Schaye et al., 2023). See also Forbes et al. (2019) and Elliott et al. (2021) for machine learning approaches to this problem in semi-analytic models of galaxy formation.

mixing, etc.) can generate some simple behavioural patterns (e.g. feedback). This also implies that chaotic systems do not rely on their evolutionary history, whereas complex systems do. Many real complex systems are, in practice, robust (Gell-Mann, 1995), but they possess the potential for radical change, like we observe in the transition from a star-forming to a quiescent galaxy.

The evolution of galaxies and their properties are prime examples of these concepts. At the core of galaxy formation lies the interplay of a large variety of physical processes (one could even argue that, in this sense, galaxy formation is a branch of applied physics), but current models have opted for an ever increasing reductionist approach, with new proxies for physical processes being introduced in order to improve the agreement with observations. This effort of capturing a 'theory of everything' for galaxy formation relies on the assumption that the combination of all these physical processes can be encapsulated by a set of simple rules (e.g. the amount of gas expelled from a galaxy depends on the current redshift and mass of the galaxy). However, as we have argued here, these large scale processes which we attempt to summarise as effective models *cannot* be captured as a sum of their components. A clear signature of this effect is the increase over the years in the complexity of the calibrating laws used in cosmological simulations (e.g. Pillepich et al., 2018; Davé et al., 2019; Schaye et al., 2023), to try to capture the diversity of galaxy properties while at the same time retaining an acceptable match to the properties of the average population. As mentioned in Vogelsberger et al. (2020a), a pitfall of using progressively more convoluted sub-resolution models that reproduce the observational data is that it amounts in itself to finding a correct and physically plausible effective model of galaxy formation.

1.3.2 Aims and structure of this thesis

In this thesis, we advocate for an approach to galaxy formation that carefully examines the interconnected nature of the physical processes affecting it. The work presented here aims to lay out a theoretical framework for examining microphysical processes relevant to galaxy evolution and how they translate into emergent global properties, through direct comparison with observational probes. The fundamental driver of this effort is the idea that the core goal of theoretical models and simulations is not to

fit the observed data, but rather to provide insights into the fundamental physics driving galaxy formation and evolution across cosmic time.

The remainder of this thesis is organised as follows:

Chapter 2 — the numerical methods and tools with which we develop our exploration of magnetic fields, cosmic rays, radiation and dust are introduced.

Chapter 3 — the influence of magnetic fields and cosmic rays on the evolution of a Milky-Way analogue is explored, by determining their influence in the launching of outflows and the thermodynamical properties of the interstellar medium across cosmic time.

Chapter 4 — building on the previous results, the impact of cosmic rays on the scale of the galactic halo, and how they affect the properties of cosmological gas accretion is quantified.

Chapter 5 — a novel thermo-chemistry model (Dusty-PRISM) capable of capturing the non-equilibrium evolution of dust and molecules in galactic environments, fully coupled to the local gas properties and an accurate modelling of radiative transfer on-the-fly, is introduced.

Chapter 6 — isolated galaxy simulations, exploring the role of different dust processes in setting the shape of extinction curves in the Local Group are carried out to test our new dust model. We also showcase the power of coupling our self-consistent dust modelling with mock observation tools to constrain star formation models.

Chapter 7 — progress brought by this effort to understand non-thermal components and dust chemistry is summarised, and we explore the exciting science questions and developments that we will be able to pursue in the near future.

2

Galaxy formation with magnetic fields, cosmic rays, radiation and chemistry

Contents

2.1 The RAMSES code 20
2.2 The NUT suite of cosmological simulations 33

2.1 The RAMSES code

The numerical work presented in this thesis is primarily obtained with the code RAMSES (Teyssier, 2002). RAMSES solves the evolution of three components (DM, stars and gas) on a Cartesian grid. Gas is represented as fluid cells, and the fluid quantities are updated by computing fluxes at cell interfaces. DM and stars are treated as collisionless particles, coupled to the gas via the Poisson equation solved using a Particle Mesh (PM) scheme. With this approach, the equations are solved on a mesh (naturally provided by the gas grid) and interpolated back to the individual particle positions. The particle contributions to the density field is determined by a Cloud-In-Cell (CIC) interpolation scheme (Hockney and Eastwood, 2021). The grid structure is built using an adaptive mesh refinement (AMR) technique, in which a parent cell at level l is subdivided to form 2^n, where n is the number of spatial dimensions, new cells (an *oct*) at level $l+1$ if it fulfils a user defined refinement condition. A common refinement used in galaxy-scale simulations (like the ones presented in this thesis) is to use a quasi-Lagrangian refinement, in which cells are refined to higher level $l+1$ if the current mass in that cell (including the deposition by the CIC of stellar and DM particles) exceeds a given mass threshold. Also, of particular importance for the dense ISM in which star formation is (preferentially) taking place, the cell sizes are compared to a multiple of the local thermal Jeans

length (see Section 2.1.3). Both the coarsest $l_{\rm min}$ and finest $l_{\rm max}$ levels are set by the user, effectively determining the spatial range of the simulation, and the width of a cell at level l is given by $\Delta x_l = L_{\rm box}/2^l$, where $L_{\rm box}$ is the physical width of the simulation domain. The time integration of the system is performed by discretising time in finite timesteps Δt_l at each level l, whose values are determined on each level by applying a Courant-Friedrich-Lewy (CFL) condition:

$$\frac{u_{\rm max}\Delta t_l}{\Delta x_l} \leq C, \tag{2.1}$$

where C is called the Courant factor, a real constant which takes values between 0 and 1, and $u_{\rm max}$ is the maximum local velocity (either the gas bulk flow, (magneto)-sonic wave speed, or particle velocity). This condition prevents information from travelling more than one cell width Δx_l over a timestep Δt_l and ensures the numerical stability of the code.

Unless stated otherwise, all simulations solve the (magneto)-hydrodynamical equations using a Godunov scheme with the Harten-Lax-van Lear-Dicontinuity Riemann solver from Miyoshi and Kusano (2005). The Godunov solver is extended to second order accuracy using the unsplit Monotone Upstream-centred Scheme for Conservation Law Limiter (MUSCL; Teyssier et al., 2006) in conjunction with the MinMod slope limiter to preserve the total variation diminishing property of the scheme.

2.1.1 Cosmic ray magneto-hydrodynamics

Cosmic rays (CRs), due to their charged nature, travel along magnetic fields lines. Therefore, any self-consistent modelling of CR transport in galaxies demands a magnetic field to be simultaneously evolved. The equations of magneto-hydrodynamics (MHD) describe the dynamical evolution of an electrically conductive fluid (i.e. a plasma) in the presence of magnetic fields. The time evolution of the magnetic field $\vec{B}$ is given by the induction equation (in rational units) in the presence of Ohmic resistivity:

$$\frac{\partial \vec{B}}{\partial t} = \vec{\nabla} \times (\vec{u} \times \vec{B}) + \eta \nabla^2 \vec{B}, \tag{2.2}$$

where $\vec{u}$ is the fluid velocity, and η_Ω is the Ohmic resistivity. Furthermore, the magnetic field needs to follow the solenoidal constraint ($\vec{\nabla} \cdot \vec{B} = 0$) to prevent the presence of monopoles imposed by the non-existence of a magnetic charge and current in

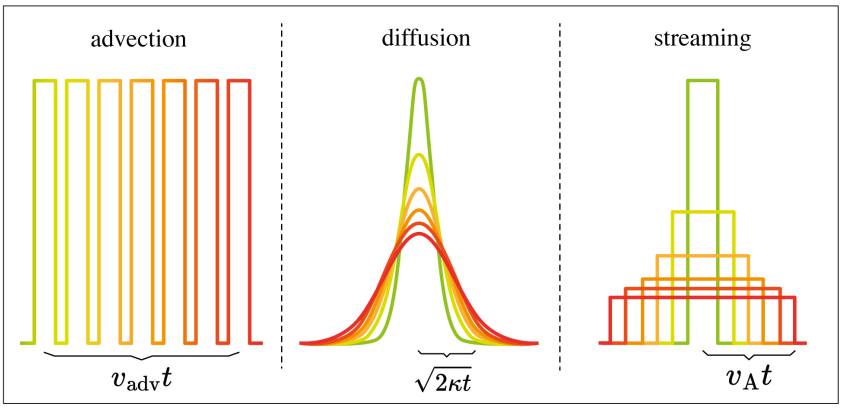


Figure 2.1: Diagram representing the three main modes of CR transport considered in this work: gas advection (left panel), which transports the CR energy density in space, anisotropic diffusion (middle panel), which reduces CR energy density in a canonical diffusion manner, and streaming (right panel), which stretches the CR energy density while preserving CR energy density gradients. Temporal evolution is shown from green to red.

Maxwell's equations. Ohmic resistivity plays an equivalent role in the MHD equations as viscosity for the velocity field, controlling how much the fluid is decoupled from magnetic field lines (or equivalently, a non-zero η_Ω implies a violation of the frozen-in flux theorem Alfvén, 1943). The non-ideal component of Ohmic resistivity have been implemented in MHD codes (e.g. Masson et al., 2012; Hopkins, 2017; Zier et al., 2023), but they only become important at very high gas densities ($\gtrsim 10^7$ cm^{-3}) and very weakly ionised astrophysical plasmas. We therefore restrict our modelling of MHD to regimes for which explicit magnetic diffusivity is negligible ($\eta_\Omega \to 0$).

Instead of defining the magnetic field as cell-centred quantities like the rest of hydrodynamical variables, magnetic fields are defined as averages on each of the cell faces (i.e. six quantities per cell in 3D). This implementation of magnetic fields in RAMSES allows for the implementation of the so-called constrained transport (CT) method (Teyssier et al., 2006; Fromang et al., 2006) which ensures that the solenoidal condition is fulfilled to numerical machine precision, thus preventing spurious numerical growth of magnetic monopoles (see Tóth et al., 2000; Mocz et al., 2016, for a comparison of CT with other MHD methods). Modelling CRs as individual protons and electrons transported in the MHD fluid is prohibitively (computationally) expensive at galactic or inter-galactic scales. Fortunately, when considering the averaged CR spectrum observed on Earth (extending to the low energy regime thanks to *Voyager* data, Stone et al., 2019; Lenok, 2021), the maximum contribution to the CR energy density is coming from protons in the ∼GeV regime. For particles with such momentum, the

gyro-radius is of the order of $\sim 10^{-6}$ pc for $\sim \mu$G magnetic fields, which means that a fluid approach can be implemented for the transport of these particles in $\gtrsim$ pc scale galaxy simulations (e.g. Strong et al., 2007; Trotta et al., 2011). These CRs are frequently scattered by small scale magnetic field disturbances, confining them to closely follow magnetic field lines. Using CR properties integrated over the full spectrum in energy/momentum – the *grey* approximation and taking CR kinetic energy moments (i.e. multiplying by the CR energy and integrating over momentum space) of the Fokker-Planck CR transport equation (Skilling, 1971; Skilling, 1975) in the form derived by McKenzie et al. (1982), one obtains:

$$\frac{\partial e_{\rm CR}}{\partial t} + \vec{\nabla} \cdot (e_{\rm CR}\vec{u} + (e_{\rm CR} + P_{\rm CR})\vec{u}_{\rm st}) = -P_{\rm CR}\vec{\nabla} \cdot \vec{u} - \vec{\nabla} \cdot \vec{F}_{\rm CR,d}, \tag{2.3}$$

where $e_{\rm CR}$ is the CR energy density, related to the CR pressure as $P_{\rm CR} = (\gamma_{\rm CR} - 1)e_{\rm CR}$, with $\gamma_{\rm CR} = 4/3$ being the adiabatic constant for the relativistic CR fluid, and $\vec{F}_{\rm CR,d}$ is the CR diffusion flux. The streaming velocity is given by:

$$\vec{u}_{\rm st} = -\vec{u}_{\rm A}{\rm sign}(\vec{b} \cdot \vec{\nabla} e_{\rm CR}), \tag{2.4}$$

where $\vec{u}_{\rm A} = \vec{B}/\sqrt{4\pi\rho}$ is the Alfvén velocity[1] and $\vec{b} = \vec{B}/|\vec{B}|$ the magnetic unit vector. Eq. 2.3 is surprisingly simple, showing that the CR energy density is advected with the total CR velocity $\vec{u} + \vec{u}_{\rm st} + \vec{u}_{\rm diff}$ (see also Fig. 2.1), with the diffusion velocity expressed as:

$$\vec{u}_{\rm diff} = D_{xx}\vec{b}\left(\frac{\vec{b} \cdot \vec{\nabla} e_{\rm CR}}{e_{\rm CR}}\right), \tag{2.5}$$

where D_{xx} is the anisotropic spatial diffusion coefficient with dimensions of area per unit time. This means that CRs can gain (lose) energy by adiabatic compression if $\vec{\nabla}(\vec{u} + \vec{u}_{\rm st})$ is negative (positive). Because the magnetic field lines are frozen in the fluid for ideal MHD, the CRs are advected with the magnetic field lines as they are themselves advected with the plasma flow velocity $\vec{u}$. On the other hand, streaming originates from taking into account the cyclotron resonance instability (Kulsrud and Pearce, 1969), which is initiated when a population of CRs travel with a bulk velocity

[1]Note that we compute Alfvén velocity using the total gas density, when the physically correct expression makes use of the ion density. In our CRMHD simulations we do not make use of radiative transfer to compute the local ionisation fraction, which could potentially affect the local CR transport in very cold, dense gas. We leave this caveat for future work.

close to or exceeding the local Alfvén velocity. At this point, gyroresonant Alfvén waves generated by the CRs themselves increase the scattering of CRs, limiting the velocity at which they can descend down gradients in $e_{\rm CR}$ caused by spatial anisotropies (e.g. Wiener et al., 2017). These self-generated waves are subject to damping mechanisms (ion-neutral damping, non-linear Landau damping or turbulent cascade of the waves to smaller scales, see e.g. Kulsrud and Pearce, 1969; Yan and Lazarian, 2002; Farmer and Goldreich, 2003; Lazarian and Beresnyak, 2006; Wiener et al., 2013). Equilibrium for this energy transfer is reached when the CR bulk velocity is isotropised in the frame moving with the Alfvén waves, effectively forcing the bulk velocity to be at the local Alfvén velocity. This is termed the *self-confinement* regime of CR transport. In practice, wave damping means a transfer of energy from CRs to the thermal plasma via scattering of self-excited Alfvén waves. The gas heating due to this process is expressed as:

$$\Gamma_{\rm st} = -{\rm sign}(\vec{b}\cdot\vec{\nabla}e_{\rm CR})\vec{u}_{\rm A}\cdot\vec{\nabla}P_{\rm CR}. \tag{2.6}$$

If the damping of waves is reduced, CRs are then allowed to stream faster than $\vec{u}_{\rm A}$. As a preliminary step towards a deeper understanding of CR feedback in a cosmological context, we assume that CR streaming velocities cannot reach super-Alfvénic velocities, and leave the implementation of self-consistent CR diffusion coupling (like the one presented in Farber et al., 2018; Xu and Lazarian, 2022; Armillotta et al., 2022; Thomas et al., 2023) for future work.

The typical value of $D_{xx} \simeq 3\times10^{28}(R_{\rm CR}/1{\rm GV})^{0.34}{\rm cm}^2\ {\rm s}^{-1}$ depends on the particle rigidity $R_{\rm CR}$ (Jóhannesson et al., 2019), which for 1 GeV proton has a value of $R_{\rm CR} = 1$ GV. Previous efforts to constrain κ in CR simulations by comparing to Fermi LAT γ-ray observations (e.g. FIRE-2, AREPO and RAMSES, Chan et al., 2019; Werhahn et al., 2021; Nuñez-Castiñeyra et al., 2022, respectively) have resulted in large discrepancies in the inferred diffusion coefficient favoured by observations. Nuñez-Castiñeyra et al. (2022) argue that, although differences in the assumed CR spectrum or γ-ray emissivity per atom can reduce the discrepancy by factors of up to 2.5, these are not sufficient to bring the different simulations in agreement. They suggest that discrepancies in the thermal state of the gas and magnetic field properties, when evolved with different MHD codes, more likely source these differences. The

exploration of how different CR transport mechanisms and diffusion coefficients affect the γ-ray luminosity is the scope of an upcoming paper (Rodríguez Montero et al., *in prep*). We adopt here a value of $D_{xx} \equiv \kappa = 3 \times 10^{28} \mathrm{cm}^2\,\mathrm{s}^{-1}$, which in RAMSES isolated galaxy simulations provides the best agreement with the γ-ray luminosity of observed nearby galaxies (Dashyan and Dubois, 2020; Farcy et al., 2022; Nuñez-Castiñeyra et al., 2022), and leave the analysis of a higher $\kappa = 3 \times 10^{29} \mathrm{cm}^2\,\mathrm{s}^{-1}$ (favoured by the FIRE-2 simulations Chan et al., 2019; Hopkins et al., 2021b) to future work.

Solving Eq. 2.3 numerically is challenging. Using traditional upwind time-evolution algorithms (e.g. similar to the treatment of hydrodynamics equation in RAMSES) with a CFL time step limiter results in spurious numerical instabilities near minima and maxima, due to the unrealistic flux caused by the discontinuity in the streaming velocity (Eq. 2.4). This yields a modified condition for stability $\Delta t \propto \Delta x^3$, where Δx is the grid resolution. Sharma et al. (2010) proposed a regularisation based on a smooth approximation to the streaming velocity as $\tanh u_{\rm st}/\epsilon$, where ϵ is a small parameter which acts as an additional diffusive term to the CR transport. In this work, we use the implementation from Dubois and Commerçon (2016) and Dubois et al. (2019) where the streaming velocity is re-written as:

$$\vec{u}_{\rm st} \equiv -\frac{\vec{b}\cdot\vec{\nabla}e_{\rm CR}}{|\vec{b}\cdot\vec{\nabla}e_{\rm CR}|}\vec{u}_{\rm A}, \tag{2.7}$$

such that the term $\vec{\nabla}\cdot((e_{\rm CR}+P_{\rm CR})\vec{u}_{\rm st})$ in Eq. 2.3 can be re-cast as a diffusion-like term (Uhlig et al., 2012):

$$\begin{aligned}\vec{\nabla}\cdot F_{\rm CR,s} &= \vec{\nabla}\cdot\left(-\frac{(e_{\rm CR}+P_{\rm CR})|\vec{B}|}{\sqrt{4\pi\rho}}\vec{b}\frac{\vec{b}\cdot\vec{\nabla}e_{\rm CR}}{|\vec{b}\cdot\vec{\nabla}e_{\rm CR}|}\right)\\ &= -\vec{\nabla}\cdot(D_{\rm st}\vec{b}(\vec{b}\cdot\vec{\nabla}e_{\rm CR})),\end{aligned} \tag{2.8}$$

where we have collapsed the resulting equation to define a streaming-diffusion coefficient $D_{\rm st}$. This can be combined with the original diffusion flux to create a *full* CR streaming-diffusion flux:

$$\vec{\nabla}\cdot F_{\rm CR,ds} = -\vec{\nabla}\cdot(D\vec{b}(\vec{b}\cdot\vec{\nabla}e_{\rm CR})), \tag{2.9}$$

where $D = D_{xx} + D_{\rm st}$. With such an approach, we can then define a full set of CR-MHD equations coupling the evolution of the thermal and CR fluids in the

presence of gravity:

$$\frac{\partial \rho}{\partial t} + \vec{\nabla} \cdot (\rho \vec{u}) = 0, \tag{2.10}$$

$$\frac{\partial \rho \vec{u}}{\partial t} + \vec{\nabla} \cdot \left(\rho \vec{u} \vec{u} + P_{\rm tot} - \frac{\vec{B}\vec{B}}{4\pi} \right) = \rho \vec{g}, \tag{2.11}$$

$$\begin{aligned} &\frac{\partial e}{\partial t} + \vec{\nabla} \cdot \left((e + P_{\rm tot}) \vec{u} - \frac{\vec{B}(\vec{B} \cdot \vec{u})}{4\pi} \right) \\ &= \rho \vec{u} \cdot \vec{g} - \vec{\nabla} \cdot \vec{F}_{\rm CR,ds} - P_{\rm CR} \vec{\nabla} \cdot \vec{u} + \mathcal{L}_{\rm rad}, \end{aligned} \tag{2.12}$$

$$\frac{\partial \vec{B}}{\partial t} - \vec{\nabla} \times (\vec{u} \times \vec{B}) = 0, \tag{2.13}$$

$$\begin{aligned} &\frac{\partial e_{\rm CR}}{\partial t} + \vec{\nabla} \cdot (e_{\rm CR} \vec{u}) \\ &= -P_{\rm CR} \vec{\nabla} \cdot \vec{u} - \vec{\nabla} \cdot \vec{F}_{\rm CR,ds} - \Gamma_{\rm st} + \mathcal{L}_{\rm rad,CR,} \end{aligned} \tag{2.14}$$

where ρ is the gas mass density, $\vec{g}$ the gravitational field, $e = 0.5\rho|\vec{u}|^2 + e_{\rm th} + e_{\rm CR} + |\vec{B}|^2/(8\pi)$ is the total energy density, $e_{\rm th}$ is the thermal energy density, $P_{\rm tot} = P_{\rm th} + P_{\rm CR} + P_{\rm mag}$ is the sum of the thermal $P_{\rm th} = (\gamma - 1)e_{\rm th}$, CR and magnetic $P_{\rm mag} = |\vec{B}|^2/(8\pi)$ pressures, with an adiabatic index $\gamma = 5/3$ for the ideal gas. Practically, one can view the terms on the right side of Equations (2.12) and (2.14) as source/sink terms, with $P_{\rm CR}\vec{\nabla} \cdot \vec{u}$ the CR pressure work, $\vec{F}_{\rm CR,d}$ the anisotropic diffusion flux (κ is the diffusion coefficient, assumed constant), $\mathcal{L}_{\rm rad} = \mathcal{L}_{\rm rad,th} + \mathcal{L}_{\rm rad,CR\to th}$ the total radiative losses which includes thermal and CR radiative losses, respectively[2]. The CR loss term encompasses both energy losses due to hadronic and Coulomb interactions (see e.g., Ensslin, 2004; Guo and Oh, 2008)

$$\mathcal{L}_{\rm CR} = -7.51 \times 10^{-16} (n_{\rm e}/{\rm cm}^{-3})(e_{\rm CR}/{\rm erg\ cm}^{-3})\ {\rm erg\ s}^{-1}, \tag{2.15}$$

transferred to the thermal component at a rate

$$\Gamma_{\rm CR\to th} = 2.63 \times 10^{-16} (n_{\rm e}/{\rm cm}^{-3})(e_{\rm CR}/{\rm erg\ cm}^{-3})\ {\rm erg\ s}^{-1}. \tag{2.16}$$

2.1.2 Radiation hydrodynamics with non-equilibrium metal thermo-chemistry

As we have emphasised in Chapter 1, radiation plays an essential role in our micro-physics approach to galaxy formation. Not only it is the fundamental means by

[2]Tabulated radiative loses are detailed for the NUT suite in Section 2.2.

which we compare galaxies to observations, but it also plays an important role in shaping the thermal properties of the ISM gas, drives early stellar feedback and is responsible for the reionisation of the Universe at the end of the Dark Ages. Studying emission and absorption lines from elements heavier than helium in the spectrum of galaxies consitutes the richest source of information that can be extracted from observations. Unfortunately, modelling emission line diagnostics in a self-consistent way within galaxy simulations is a non-trivial task, since both the spatial distribution and ionisation state of metals, molecules and dust are critical when performing a comparison between theoretical models and direct observables. In state-of-the-art simulations, it is common to assume collisional ionisation equilibrium (CIE) for metal cooling (Gnat and Sternberg, 2007). However, metal line cooling is highly dependent on the shape and strength of the local radiation field, which means that another commonly used approach of assuming a uniform UV background fails to capture spatial and temporal variations of heating and cooling terms in the gas equation of state. Furthermore, the assumption of chemical and ionisation equilibrium may break in ISM conditions in which dynamical, ionising, and cooling time-scales are very short compared to chemical processes (e.g. Richings et al., 2014; Richings et al., 2022), resulting in large variations in predicted line emission luminosities.

RAMSES-RTZ

Therefore, progressing our understanding of galaxy observations across cosmic time relies on an accurate and self-consistent modelling of radiation transfer from the ISM all the way through to the IGM. With this goal in mind, we make use of RAMSES-RT (Rosdahl et al., 2013; Rosdahl and Teyssier, 2015), the radiation hydrodynamics (RHD) version of RAMSES. This on-the-fly RT uses the M1 closure relation (Levermore et al., 1984) to eliminate the angular degrees of freedom from the RT equations (Mihalas and Mihalas, 1984), allowing the code to scale very well with the number of sources. This has made RAMSES-RT an RHD code capable of working from cloud-scale simulations (e.g. Geen et al., 2015; Geen et al., 2017), to cosmological galaxy zoom simulations (e.g. Trebitsch et al., 2018; Martin-Alvarez et al., 2022), all the way to large cosmological simulations (e.g. Rosdahl et al., 2018; Katz et al., 2021). Furthermore, we make use of the variable-speed-of-light approximation (Katz et al.,

2017), which allows for an important reduction in computational time when solving the RHD equations while also correctly capturing the evolution of ionisation fronts in low density gas. This permits to relax the CFL condition and works well as long as the value of the reduced speed of light remains faster than the fastest ionisation front propagating in the simulation (Rosdahl et al., 2013).

RAMSES-RT is capable of computing the ionisation fractions of HI, HeI and HeII, allowing for non-equilibrium radiative cooling/heating of a gas with primordial composition. In order to extend this approach to non-pristine gas, we make use of RAMSES-RTZ (Katz, 2022), an extension to RAMSES-RT that tracks the non-equilibrium ionisation states of metals. This time evolution of ionisation states is dependent on a number of physical processes including: radiative recombination, di-electronic recombination, collisional ionisation, photo-ionisation, Auger ionisation, and charge exchange. These reactions are determined by coefficients compiled from a variety of sources, closely resembling the values used in the photo-ionisation code CLOUDY (v17.02) (Ferland et al., 2017). Solving this chemical network requires the integration of temperature, ionising photon number densities, and species ionisation states simultaneously and implicitly. However, this quickly becomes an extremely expensive task, as reaction coefficients are highly temperature and density dependent, forcing solvers to cycle for many sub-steps to reach the solution. To overcome this problem, RAMSES-RTZ follows a similar approach as for the non-equilibrium H and He chemistry in RAMSES-RT (Rosdahl et al., 2013): 1) it updates the temperature, photon number densities, H, H_2, and He abundances first, and then 2) it cycles over ionisation states and updates them semi-implicitly using forward-in-time values for the e^-, H, H_2 and He abundances. This method is still partially implicit (see the discussion in e.g. Anninos et al., 1997; Rosdahl et al., 2013), since it relies on already computed values (e^-, H, H_2 and He) and at the same time on the un-updated values of the ionisation states. In order to make this semi-implicit procedure more robust, it imposes a 10% rule: if a given thermo-chemistry step results in the variation of one of the quantities exceeding 10% of its original value, the thermo-chemistry step is re-started with a smaller sub-step value. In practice however, the RT Courant condition limits the hydrodynamics time-step to well below the average chemistry timescale, and sub-cycling the chemistry is rarely necessary.

PRISM

The thermo-chemistry of the ISM is a highly non-linear system in which a rich plethora of physical and chemical processes affect the thermal state of gas and the properties of observational probes (for a review on the topic, see e.g. Draine, 2010). These processes are well studied for the ISM of the Milky Way (e.g. Wolfire et al., 1995; Wolfire et al., 2002), and theoretical models have led to significant progress in our understanding of the ISM in lower metallicity environments at high redshift (e.g. Omukai et al., 2005; Bialy and Sternberg, 2019; Kim et al., 2022). Following our choice of the on-the-fly RT version of RAMSES, we build on our modelling of ISM non-equilibrium thermo-chemistry (see Chapter 5) using the platform provided by the PRISM ISM model (Katz et al., 2022b). Thermo-chemistry processes in PRISM include:

- Molecular hydrogen formation and destruction following the primordial gaseous route via H^- as introduced in Katz et al. (2017).
- CO formation and destruction following the model presented in Nelson et al. (1997) and Glover and Clark (2011). This also accounts for rotational and vibrational cooling of CO, following Koyama and Inutsuka (2000).
- Low-energy ($\sim$MeV) CR heating following Goldsmith and Langer (1978) as updated in Bialy and Sternberg (2019).
- Heating from H_2 pumping following Baczynski et al. (2015), which combines the UV pumping rate of H_2 from Draine and Bertoldi (1996) with the energy released per UV pumping event from Burton et al. (1990).
- H_2 cooling following the form presented in Hollenbach and McKee (1979). At very low metallicites, this form of cooling is the dominant process that allows gas to reach temperatures $\lesssim 10^4$ K.

Other cooling/heating mechanisms (e.g. primordial H cooling and metal line cooling) follow RAMSES-RT (Rosdahl et al., 2013) and RAMSES-RTZ (Katz, 2022).

2.1.3 Star formation

In our galactic scale simulations, we do not reach the sub-pc resolutions appropriate for sink particles to predict the formation and growth of individual proto-stars in

molecular clouds (see Bleuler and Teyssier, 2014, for the implementation in RAMSES). Therefore, we use sub-grid models to account for the physical processes determining the efficiency of star formation.

Star formation was originally implemented in RAMSES by Rasera and Teyssier (2006) using a Schimdt law (Schmidt, 1959):

$$\dot{\rho}_* = \frac{\epsilon_{\rm SF}\rho}{t_{\rm ff}}, \tag{2.17}$$

where $\dot{\rho}_*$ is the stellar mass formation rate, ρ is the gas density, and $\epsilon_{\rm SF}$ is the star-formation efficiency per free fall time $t_{\rm ff} = \sqrt{\frac{3\pi}{32G\rho}}$. When the gas density in a particular cell exceeds a given threshold density $\rho_{\rm SF,thres}$ (see the specific values for the different simulations performed for this work in Section 2.2 and 6.2.1), the cell is considered as potentially star-forming and star particles are spawned stochastically from the local gas mass according to a Poisson distribution, with each particle being given an initial mass which is an integer multiple of a minimum stellar mass set by the resolution of the simulation. Therefore, Eq. 2.17 only holds in a statistical average sense.

Contrary to the most common practice in the field, the efficiency of star formation $\epsilon_{\rm SF}$ is not assumed to be constant throughout the simulation domain, but rather is computed locally based on the thermo-dynamical properties of the gas. This modelling is based on two main concepts: 1) the dominance of self-gravity over all forms of thermal and non-thermal support of the gas, and 2) the dependence of star formation efficiency on local gas properties. This is known as the magneto-thermo-turbulent (MTT) star formation model and provides a physically-motivated approach to the problem of implementing sub-grid star formation in galactic environments. Originally introduced in its thermo-turbulent form in Kimm et al. (2017) and Rosdahl et al. (2018), we use a modified version of the one of Martin-Alvarez et al. (2020) which includes magnetic pressure. This model considers that turbulent, thermal, magnetic and CR pressure can support gas against gravitational collapse, therefore limiting star formation to gravitationally unstable cells. The modified turbulent Jeans length accounting for all these components is computed at the highest level of refinement as: (Rasera and Teyssier, 2006):

$$\lambda_{\rm MTT} = \frac{\pi\sigma^2 + \sqrt{36\pi c_{\rm s,eff}^2 G\Delta x^2\rho + \pi^2\sigma^4}}{6G\rho\Delta x}, \tag{2.18}$$

where G is the gravitational constant, σ is the local gas velocity dispersion and $c_{\rm s,eff}$ is an effective sound speed taking into account thermal, magnetic and CR pressure:

$$c_{\rm s,eff} = \sqrt{\frac{P_{\rm th} + P_{\rm mag} + P_{\rm CR}}{\rho}}. \tag{2.19}$$

If $\lambda_{\rm MTT} < \Delta x$ the gas cell is physically expected to continue collapsing. When this happens, we allow star formation to take place below the maximum resolution allowed by the AMR grid, converting some of the gas into star particles and thus increasing the Jeans length.

The efficiency of such a conversion, $\epsilon_{\rm SF}$ is computed using the mult-freefall model (Krumholz and McKee, 2005; Padoan and Nordlund, 2011; Federrath and Klessen, 2012):

$$\epsilon_{\rm SF} = \frac{\epsilon_{\rm ecc}}{2\phi_t} \exp\left(\frac{3}{8}\sigma_s^2\right) \left[2 - {\rm erfc}\left(\frac{\sigma_s^2 - s_{\rm crit}}{\sqrt{2\sigma_s^2}}\right)\right], \tag{2.20}$$

where $\epsilon_{\rm ecc}$ is the maximum gas fraction that can be accreted by stars before protostellar feedback blows away the cloud, set to 0.5. In this model, the unresolved density distribution follows a log-normal distribution with a standard deviation of

$$\sigma_s = \ln\left(1 + b^2\mathcal{M}^2\right), \tag{2.21}$$

where b accounts for the nature of turbulence (ratio between solenoidal and compressive modes), and $\mathcal{M} = \sigma/c_{\rm s,eff}$ is the turbulent Mach number. We fix $b = 0.4$, corresponding to an approximate 3:1 mixture of solenoidal to compressive modes. The critical density above which collapse takes place is given by (Hennebelle and Chabrier, 2011):

$$s_{\rm crit} = \ln\left(0.067\theta^{-2}\alpha_{\rm vir}\mathcal{M}^2 f(\beta)\right), \tag{2.22}$$

where $f(\beta)$ captures the influence of magnetic fields (Padoan and Nordlund, 2011):

$$f(\beta) = \frac{(1 + 0.925\beta^{-3/2})^{2/3}}{(1 + \beta^{-1})^2}, \tag{2.23}$$

with $\beta = P_{\rm th}/P_{\rm mag}$. The parameter $\theta = 0.33$ is a proportionality constant relating cloud size and gas volume affected by turbulence shocks (Padoan and Nordlund, 2011). Finally, the virial parameter reads:

$$\alpha_{\rm vir} = \frac{5(\sigma^2 + c_{\rm s,eff}^2)}{\pi\rho G\Delta x^2}. \tag{2.24}$$

In all these equations, we have made use of the local gas velocity dispersion σ as a proxy for the injection of turbulent velocity from the unresolved turbulent velocity cascade. In practice, σ is calculated on a cell by cell basis by removing the local bulk (mass-weighted mean) velocity and estimating the divergence of the velocity field, such that $\sigma^2 = \mathrm{sum}(\nabla \otimes u\mathrm{d}x)^2$.

2.1.4 Type II supernova feedback

Massive stars undergo processes throughout their lifetime which deposit energy and momentum in their vicinity. Their cataclysmic explosions as supernovae (SNe) are central to galaxy formation and evolution, where SNe are often invoked as a key feedback mechanism, particularly dominant at the low-mass end of the galaxy mass function (see e.g. Naab and Ostriker 2017; Vogelsberger et al. 2020a). In order to regulate star-formation, SNe need to drive galactic winds that eject gas from galaxies. However, as we have discussed in Chapter 1, different simulations have showcased the inefficiency of SN feedback to halt star formation, as the exclusive injection of thermal energy is prone to *over-cooling* (Katz, 1992; Marri and White, 2002), resulting in too weak galactic outflows to overcome the run-away formation of stars on a free-fall time (Hopkins et al., 2012).

This has lead to the development of alternative models with the aim to better capture SN impact on the ISM (see e.g. Rosdahl et al. 2018; Smith et al. 2018 for a comparison of methods). Solutions to the aforementioned over-cooling include disabling radiative cooling of the affected gas for a limited amount of time after the explosion (e.g. Stinson et al., 2006; Teyssier et al., 2013), employing a stochastic energy deposition (e.g. Dalla Vecchia and Schaye, 2012), or applying gas 'kicks' from analytic momentum-driven winds (Murray et al., 2005; Kimm et al., 2015). The use of hydrodynamically decoupled wind particles is also required in many large volume cosmological simulations to reproduce realistic outflows (Springel and Hernquist, 2003; Oppenheimer et al., 2009; Vogelsberger et al., 2013; Pillepich et al., 2018). Ideally, one would want to circumvent the issue of over-cooling without artificially removing radiative cooling (which is in itself a physical process affecting supernova remnants, SNRs), but rather by correctly injecting the appropriate form of energy or momentum depending on local gas properties. We accomplish this by using the

mechanical feedback prescription introduced by Kimm and Cen (2014), in which either thermal energy or momentum are injected depending on which of the Sedov-Taylor phase or the snowplough phase of the SN explosion is locally resolved (Blondin et al., 1998; Thornton et al., 1998).

2.2 The NUT suite of cosmological simulations

The new suite of simulations presented in this work uses the same initial conditions as the NUT galaxy zoom suite Powell et al. (2011) and Geen et al. (2013) generated at $z = 499$ with cosmological parameters consistent with WMAP5 results (matter density $\Omega_{\rm m} = 0.258$, dark energy density $\Omega_\Lambda = 0.742$, baryon density $\Omega_{\rm b} = 0.045$, amplitude of the linear power spectrum at the 8 Mpc scale $\sigma_8 = 0.8$ and Hubble constant $H_0 = 72\,{\rm km\,s^{-1}\,Mpc^{-1}}$ Dunkley et al., 2009). The computational box has a length of 9 comoving Mpc h^{-1} on a side, within which is embedded a spherical region of approximately 2.7 comoving Mpc h^{-1} in diameter where the high resolution calculation is performed. Inside this zoomed-in region a $M_{\rm vir}(z=0) \simeq 5 \times 10^{11} M_\odot$ Dark Matter (DM) halo hosts a Milky Way-like galaxy (from this moment on simply identified as the NUT galaxy). The DM particle resolution is $m_{\rm DM} = 5.5 \times 10^4 M_\odot$. To probe the multi-phase structure of the ISM, we allow refinement within this region to be triggered according to a quasi-Lagrangian method, i.e. cells with a total mass (i.e. gas, stars and dark matter) 8 times larger than $m_{\rm DM}\Omega_{\rm b}/\Omega_{\rm m}$ are subdivided into 8 smaller cells of equal size, down to a minimum cell size $\Delta x_{\rm min} \simeq 23$ pc approximately constant in proper units (an extra level of refinement is triggered for expansion factors of $a_{\rm exp} = 0.1, 0.2, 0.4, 0.8$).

In these NUT suite simulations we do not use the non-equilibrium thermo-chemistry implemented in RAMSES-RT and RAMSES-RTZ. Instead, we include metal-dependent radiative cooling with interpolated cooling curves from CLOUDY (Ferland et al., 1998), down to $\sim 10^4$ K. Below this temperature, gas is allowed to cool further via metal fine structure atomic transitions (Rosen and Bregman, 1995) (to a minimum of 15 K). We employ a uniform UV background that is turned on at a redshift of $z = 9$ (Haardt and Madau, 1996), with gas denser than $n_{\rm H} = 0.01$ cm^{-3} considered to be self-shielded from UV radiation with an exponential dependence on $n_{\rm H}$. Furthermore, despite the high resolution of our simulation, we lack the cooling modelling capabilities to resolve

primordial (Population III) SN explosions in mini-halos (e.g. Whalen et al., 2008; Wise et al., 2012) that would potentially raise the initial gas metallicity to $\sim 10^{-3}\,Z_{\odot}$ and hence increase cooling at high redshift. To circumvent this issue, we initialise the simulation using a uniform metallicity floor of $10^{-3}\,Z_{\odot}$ for the gas.

The formation of star particles from the gas only takes place in cells at the highest level of refinement when the gas is found to be gravitationally unstable, and the gas density $n_{\rm H} \geq 10$ cm^{-3}. This follows the MTT model described in 2.1.3, using a minimum stellar particle mass of 4.5×10^3 M$_{\odot}$. For the purpose of this work, instead of performing a calibration process to determine artificial 'boosting' factors to the canonical type II SN energy of 10^{51} erg that may allow, e.g., the recovery of a stellar-to-halo-mass (SMHM) relation in agreement with local observations (Rosdahl et al., 2018), we simply model SN feedback using the 'mechanical' approach of Kimm and Cen (2014) described in Section 2.1.4 with a canonical energy of 10^{51} erg. In order to determine when a stellar particle should experience a SN feedback event, we follow the *multiple explosions* method by Kimm et al. (2015), in which we use the real delay of SNe given by the population synthesis code STARBURST99 (Leitherer et al., 1999), with SNe taking place as early as 3 Myr and as late as 50 Myr. These SN events inject mass, momentum and energy into the host and a maximum number of 48 neighbouring cells, with an efficiency of $\varepsilon_{\rm SN} = 10^{51}$ erg$/(10 M_{\odot})$ and a fraction of 0.2 of the SN mass returned to the SN host cell. Additionally, a fraction 0.075 of this total mass is input as metals, which are followed using a passive scalar advected with the gas flow. We further assume a Kroupa IMF (Kroupa, 2001) for the individual stars which make up our stellar particles. The simulation including these physical components and solving the hydrodynamics equations is denoted *HD*.

The ideal MHD induction equation prohibits the formation of magnetic fields in the absence of an initial non-zero $\vec{B}$ field. Several mechanisms have been presented over the last decades as candidates to generate galactic magnetic fields of the order of $10^{-7} - 10^{-5}$ G (e.g. Mulcahy et al., 2014; Beck, 2016). These can be classified by their cosmological (e.g., electroweak or quantum chromo-dynamics phase transitions Vachaspati, 1991; Olesen, 1993) or astrophysical (plasma seeding processes like Biermann battery Biermann, 1950; Pudritz et al., 1989) nature (see Durrer and Neronov, 2013; Vachaspati, 2021, for recent reviews on the matter). Whether magnetic

fields in galaxies are primordial in nature or rapidly amplified by astrophysical or dynamo processes (Pakmor and Springel, 2013; Rieder and Teyssier, 2017; Vazza et al., 2017; Martin-Alvarez et al., 2018; Martin-Alvarez et al., 2021), the theoretical expectation is that they reach $\sim 10^{-6}$ G strengths no later than a few hundred Myr after galaxy formation (Martin-Alvarez et al., 2022) begins. We thus permeate the simulation box with an uniform magnetic field along the z axis[3]. In order to mimic a rapid amplification, we initialise the primordial magnetic field strength to $B_0 = 3 \times 10^{-12}$ G. This simple magnetic field initialisation directly provides the expected strengths of $1 - 10$ μG in the NUT galaxy shortly after its formation (Martin-Alvarez et al., 2021). The simulation solving the ideal magneto-hydrodynamics equations is denoted *MHD*.

In order to properly capture CR evolution, we activate the CR solver when the first stars are formed, shortly prior to their first injection into the simulation. This is because SNe are the exclusive source of CRs in our simulations. We assume that each SN event injects a fixed fraction of its total energy as CR energy into the gas cell hosting the SN particle. We choose this fraction to be $\chi_{\rm CR} = 0.1$, which leads to a total CR injected energy per SN event of 10^{50} erg. This value is in fair agreement with the estimated acceleration efficiency of CRs by non-relativistic shocks (e.g. Morlino and Caprioli, 2012; Caprioli and Spitkovsky, 2014). In order to keep the energy injection for type II SN fixed to its canonical value, the energy available for thermal energy and momentum injection by the mechanical feedback prescription is reduced accordingly. The simulation that includes the injection of CRs and they transport is called *CRMHD*. All HD, MHD and MHD use otherwise the same initial conditions.

Simulation snapshots are analysed using OZYMANDIAS[4] a new cosmological simulation analysis package which includes a smooth interfacing of halo and galaxy selection codes, in-depth analysis algorithms and the ability to generate simulated mock observations. It is developed with an easy-access philosophy in mind, combining PYTHON for accessing the data catalogues and Fortran 90, OPENMP parallelised routines to access the raw RAMSES data. It reads in a cosmological simulation snapshot and outputs a galaxy and halo catalogue in the HDF5 format, which enables the study

[3] In this work we do not explore the effect of different orientations, as this does not significantly alter the evolution of the NUT galaxy (Martin-Alvarez et al., 2020), but the magnetisation of the large scale environment changes.

[4] https://github.com/Currodri/ozymandias

of many physical properties in the simulation without the need to read back again the original binary files. Additionally, these files are usually less than 0.3% the size of the original outputs, making simple analysis and comparison between simulations much less memory and computationally expensive. OZYMANDIAS has been written to work with two different halo and galaxy finders (although the I/O for halo catalogues is fully compatible with other halo finders, providing the data structure information): the HALOMAKER code of Tweed et al. (2009), a 3D density-threshold structure finder extended to use the shrinking spheres centering method (Power et al., 2003); and the VELOCIraptor code (Elahi et al., 2019; Cañas et al., 2019) in its enhanced version by Rhee et al. (2022), a robust, scale-free, phase-space structure-finder. Once halos and galaxies are identified, a hierarchical structure is built, linking galaxies with their host halos and satellite galaxies with central galaxies. In order to allow for an easy tracking of each galaxy/halo across cosmic time, particle lists for each identified object are compared between consecutive snapshots, yielding an easy access to their progenitors at any previous snapshot. We use this package to identify the main galaxy, and refer to the *galactic region* as the sphere with radius $0.2R_{\rm vir,DM}$, $R_{\rm vir,DM}$ being the host DM halo virial radius. Quantities such as the galaxy stellar mass M_* and gas mass $M_{\rm gas}$ are measured within this spherical volume at every snapshot.

3

The impact of cosmic rays on the interstellar medium and galactic outflows of Milky Way analogues

Contents

3.1 Motivation 37
3.2 The global impact of cosmic rays on the evolution of NUT 41
3.3 How cosmic rays alter the pressure balance of the ISM and star formation efficiency 47
3.4 Cosmic rays reshape how supernovae interact with the galactic region 52
3.5 Conclusions 69

3.1 Motivation

Consider a special case of the general wind equation (e.g. Quataert et al., 2021) for which the gas is assumed to flow parallel to the magnetic field lines (thus it does not experience magnetic stress) and to the vertical z direction:

$$(v^2 - c_{\rm eff}^2)\frac{d\ln v}{d\ln z} = c_{\rm eff}^2\frac{d\ln A}{d\ln z} + zg_z, \tag{3.1}$$

where v is the is the gas velocity, A is the cross-sectional area of the magnetic flux tube along which the gas flows, g_z is the gravitational acceleration in the z direction, and $c_{\rm eff}$ is the effective sound speed of the gas. Originally proposed in the analytic study by Breitschwerdt et al. (1991), the physical motivation for such an approximation is that SNe and galactic chimneys tend to open up magnetic field lines in the vertical direction and, as the gas is accelerated outwards and expands adiabatically, the cross-sectional area of the flux tubes increases to maintain pressure equilibrium with its surrounding medium. The expansion of A is then dictated

by Gauss' law $\mathrm{B}A = \text{const.}$ where $\mathrm{B} = \mathbf{B}(0, 0, \mathrm{B}(z))$, and we ignore thermal/CR sources/sinks along the flux tube. This equation illustrates a fundamental problem with thermally-driven winds: for adiabatic expansion of an ideal mono-atomic gas ($\gamma_{\rm gas} = 5/3$) the equation of state follows $P \propto \rho^{\gamma_{\rm gas}}$, which means that the sound speed decreases with the expansion of the wind as $c_{\rm eff} \propto \rho^{2/3}$. Consequently, if the circular velocity is practically flat, i.e. $g_z \sim -V_{\rm circ}^2/r$ (e.g. NFW profile), the first term in the right hand side of Eq. 3.1 decreases faster than the gravitational acceleration term. This prevents the outflowing gas from reaching the singularity (critical point) of the wind equation and from accelerating past the sound speed[1]. Besides the specific assumptions used in the Breitschwerdt et al. (1991) model (see Mao and Ostriker, 2018, for a more general approach based on flow streamlines aligned with the gradient of the effective gravitational potential), Eq. 3.1 clearly states the difficulties faced by thermal gas pressure in efficiently driving gas mass out of the gravitational potential of a galaxy. We have discussed the pitfalls faced by numerical implementations of thermal SN feedback in Section 2.1.4, and how cosmological simulations rely on controlling wind mass-loadings ($\eta_{\rm m} \equiv \dot{M}_{\rm outflow}/\,\mathrm{SFR}$) with sub-grid wind models (e.g. Pillepich et al., 2018; Davé et al., 2019) or by artificially boosting the SN rate to aid in raising the $c_{\rm eff}$ at injection (e.g. Rosdahl et al., 2018). The scaling of the outflow mass-loading factor with circular velocity can vary depending on the specific feedback model used (e.g. Somerville and Davé, 2015), but momentum-driven winds with $\eta_{\rm m} \propto V_{\rm circ}^{-1}$ and energy-driven winds with $\eta_{\rm m} \propto V_{\rm circ}^{-2}$ bracket the usual range of scalings predicted. Observations point at trends within these theoretical bounds (e.g. Veilleux et al., 2005; Heckman et al., 2015; McQuinn, 2016; Chisholm et al., 2017), but with consistently lower normalisation and shallower slope than what is measured in current cosmological galaxy formation simulations (Vogelsberger et al., 2013; Mitchell et al., 2020; Nelson et al., 2019; Davé et al., 2019) and high-resolution zoom-in simulations (Muratov et al., 2015; Christensen et al., 2016; Tollet et al., 2019; Pandya et al., 2021). This mismatch between the required stellar feedback efficiency in cosmological simulations and the observed $\eta_{\rm m}$ remains a topic of active debate in the ISM and galaxy formation community. It points out that a fully comprehensive model of stellar feedback can no

[1]See Recchia et al. (2017) for a similar argument based on the similarities of this problem with the De Laval nozzle equation. This also follows the solution topology of the solar plasma wind by Parker, 1962.

longer be limited to the dynamical properties of isolated radial gas flows, but rather that we need to simultaneously understand its role within the galactic multi-phase ISM and in combination with a CGM influenced by cosmological accretion flows. The work on CR feedback contained within this thesis is fundamentally driven by this careful consideration, which we expose in the following pages.

They key factor to understand about CR transport in wind launching is that it regulates the magnitude of the outward-pointing gas acceleration, either by shaping the CR pressure gradient and/or by allowing the CR momentum to be deposited in a gas phase that is more easily accelerated. As argued in Hopkins et al. (2021a), when the total gas pressure $P_{\rm total} \sim P_{\rm CR}$, there is a critical density $\rho_{\rm crit}(r)$ above which the outward CR pressure gradient force exceeds the gravitational force, hence rendering lower density phases more easily ejected by CR pressure gradients. While CR injection by SN shocks will preferentially take place within the galactic midplane, over-pressurising it, the actual impact of CRs on the gas acceleration is given by the pressure gradient rather than its magnitude. In cold, dense gas, CR hadronic and Coulomb losses are larger (Guo and Oh, 2008), hence reducing the possibilities of building up a sufficiently large $\vec{\nabla} P_{\rm CR}$. However, if we depart from the advection-dominated regime ($v_{\rm gas} \gg v_{\rm diff} \gg v_{\rm st}$), CR diffusion and streaming may allow for a displacement between CR pressure and gas density, and large CR pressure gradients can break the hydrostatic balance and allow the gas to be accelerated outwards (Salem et al., 2014; Girichidis et al., 2016; Simpson et al., 2016). Once gas begins to move radially out, extended CR pressure gradients can continue accelerating the gas. A generic feature of these CR-driven outflows is that outflow speed increases with distance, a feature that has been confirmed by both one-dimensional models (Dorfi and Breitschwerdt, 2012; Quataert et al., 2021) and stratified tall-box simulations (Girichidis et al., 2018; Armillotta et al., 2024). The additional non-thermal component further alters the pressure and dynamical balance of the ISM and the gravitationally stratified gas, even when the gas is not outflowing. Both magnetic fields and CRs are essentially weightless components of the galactic gas, meaning that, in a stratified atmosphere, disturbances can become unstable due to effective buoyancy (i.e. the Parker instability; Parker, 1969). The classical treatment by Parker (1969) assumed a fixed CR pressure along the magnetic field lines, with CRs as a fluid with $\gamma_{\rm CR} = 0$.

In this framework, CRs only affected the stratification via their pressure gradient, increasing the scale height of the gas and thus destabilising it further. Conversely, when approximating the CR fluid as relativistic ($\gamma_{\rm CR} = 4/3$), the gas becomes less compressible, hence stabilising the system (Zweibel et al., 1975; Boettcher et al., 2016; Uhlig et al., 2012; Ruszkowski et al., 2017; Heintz and Zweibel, 2018), maintaining the disk atmosphere puffed up. By allowing for diffusion and streaming transport, CRs are more decoupled from the gas, reducing the support by CR pressure gradients, resulting in a destabilising effect (Ryu et al., 2003; Kuwabara and Ko, 2006; Rodrigues et al., 2016; Heintz and Zweibel, 2018), with the growth rate of the Parker modes increasing with the diffusion constant κ (see Section 2.1.1). If κ is large (small), filaments may form perpendicular (parallel) to the local magnetic field (Kuwabara and Ko, 2006; Kuwabara and Ko, 2020), as larger (smaller) diffusion is capable to stabilise (destabilise) the gas against the Jeans instability.

The works here enumerated are strong incentives to study the role of CR feedback not just in their driving of more efficient outflows, but also within the multi-phase ISM where ultimately stars are formed. It remains uncertain whether or not the predictions from these models will be met in a realistic, cosmological zoom-in simulation, as their applicability is limited by the fact that they neglect driving of supersonic turbulence by SNe and super-bubbles in the ISM, and by accretion flows from the cosmic web in the CGM. It does not come as a surprise that the underlying complexity of all of these physical processes, within the already non-linear and intricate physical system that is a galaxy, has hampered our comprehension of CR feedback. While isolated galaxy simulations find CRs modelled with a constant diffusion coefficient κ are able to affect the star formation of galaxies over a range of masses (Booth et al., 2013; Ruszkowski et al., 2017; Dashyan and Dubois, 2020; Farcy et al., 2022; Nuñez-Castiñeyra et al., 2022), their inclusion in cosmological simulations shows (e.g. Jubelgas et al., 2008; Buck et al., 2020; Martin-Alvarez et al., 2022) that their effect on the final stellar mass of a galaxy is usually small, preferentially affecting the most massive galaxies at low redshift (e.g. Hopkins et al., 2020).

In our NUT simulations, CRs are injected by each SN event. Therefore, the source of CRs in our simulations are also intimately linked to the regions of star formation within the ISM of NUT. Exploring the effects of CRs in the cosmological evolution

of galaxies requires a clear understanding of how CRs couple with other physical components influencing the thermodynamical state of the ISM and outflows. Given the feedback role of CRs, this means disentangling the intricate synergy of gas phases, magnetic fields, pressure support, turbulence and gravity.

3.2 The global impact of cosmic rays on the evolution of NUT

In Fig. 3.1 we show density-weighted projections of NUT at $z = 1.5$ for the three simulations (HD, MHD and CRMHD) composing the vanilla suite, comparing face-on views (line-of-sight parallel to the angular momentum vector of all baryons assigned to the galaxy by the halo finder) and edge-on views. On the rightmost column we have included mock JWST RGB images obtained with SKIRT. At $z = 1.5$, the NUT galaxy has formed a thin gas disk in all simulations, that has large-scale spiral features with high density clumps and low density inter-arm regions. In the HD and MHD simulations (top and middle rows) the galaxy has the general properties of a disk galaxy within a virialised halo: a cold ($T < 10^4$ K) thin disk with close to solar metallicity $Z_\odot$ is embedded within a low density, hot ($T > 10^6$ K) CGM. The edge-on views aid in identifying long filaments of cold, dense and low metallicity gas inflowing into the galaxy. In the CRMHD simulation (bottom rows), while the dense and cold region of the disk can still be clearly seen in the projections, there are significant differences with respect to the no-CR simulations. Firstly, the gas disk shows much more filamentary substructure, and in comparison to the HD and MHD simulations the maximum value of density in the clumps is substantially reduced, as well as the volume occupied by low density, hot gas in the inter-arm regions. Secondly, the high density centre of the galaxy in HD and MHD extends to $\sim 1 - 2$ kpc, while in CRMHD it is 3 times smaller. However, the most striking difference to the HD and MHD simulations is the thermodynamical state of the CGM: the CRMHD run has no clear inflow filaments, and it is instead dominated by homogeneous and denser gas at $T \sim 10^5$ K. Against this lower temperature 'background', recent hot outflows can clearly be distinguished in the edge-on view, although the lower average metallicity of the disk gas compared to HD and MHD makes the metal enrichment of outflows less prominent. Instead, the CGM of NUT is now uniformly enriched to ~ 0.1 $Z_\odot$. Furthermore, the mock

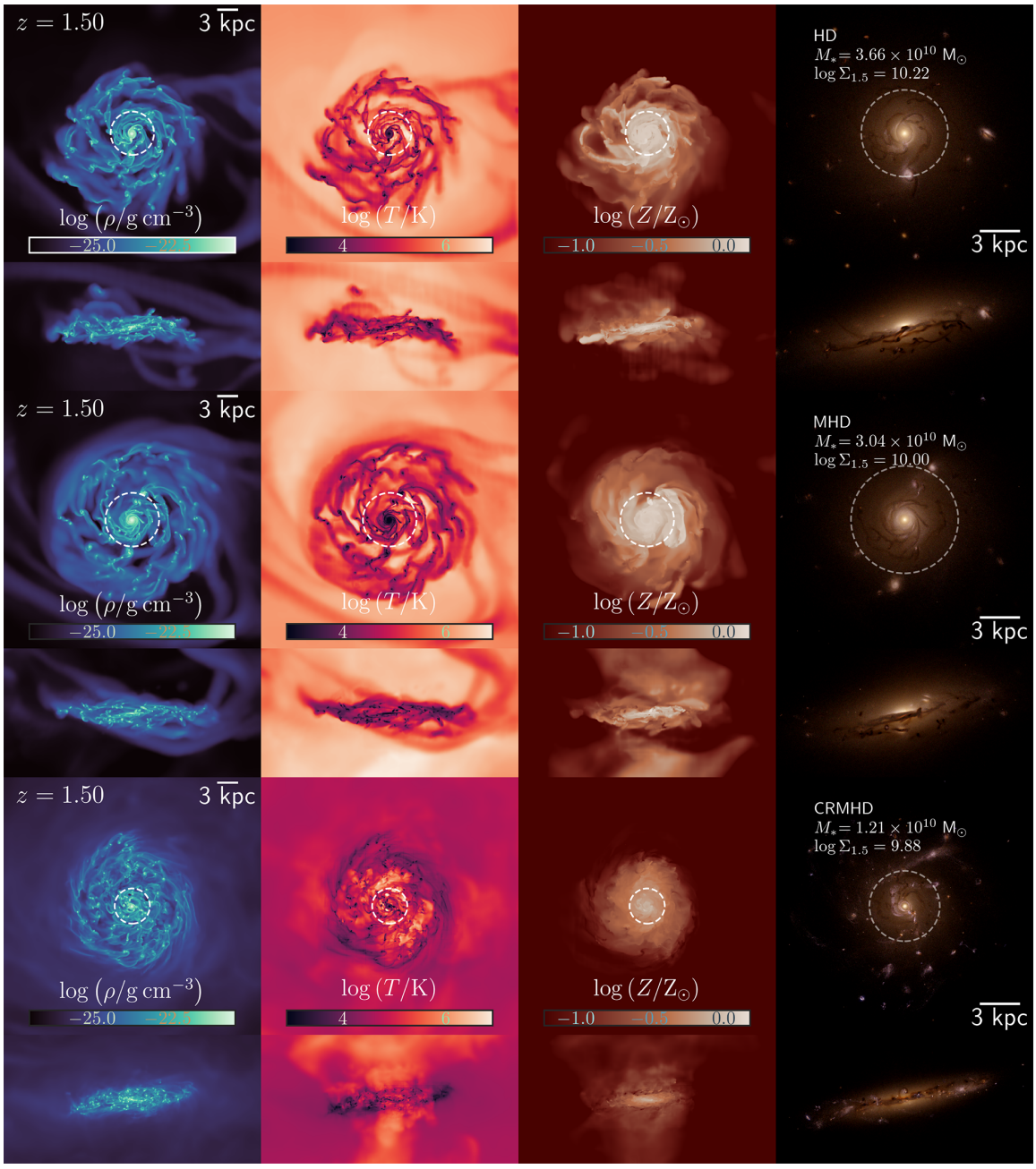


Figure 3.1: Projections of the NUT galaxy for the three models of the vanilla suite: HD (top 2 rows), MHD (middle 2 rows), and CRMHD (bottom 2 rows), generated at $z = 1.5$. We include density-weighted projections of gas density (first column), gas temperature (second column), and gas metallicity (third column), 20 kpc on a side. The last column includes RGB synthetic SKIRT observations in the JWST F200W, F150W and F090W filters, respectively, for a zoom region of 10 kpc on a side. Face-on and edge-on views are shown for all models. Dashed white circles indicate the half-light radius r_{50} obtained by fitting the RGB images with a 2D Sérsic profile. For each simulation the stellar mass within $0.2\,R_{\mathrm{vir,DM}}$ and galaxy compactness $\log \Sigma_{1.5}$ (Barro et al., 2013), is listed, with a larger value indicating a more compact stellar emission.

JWST images of the HD and MHD simulations show NUT as a disk galaxy dominated by a massive bulge and an old stellar population, with dark, dense filaments seen as dust lanes in the edge-on views. Also, massive stellar clumps formed by large-scale disk instabilities persist due to inefficient feedback (e.g. Inoue et al., 2016; Bournaud et al., 2013). In comparison, the CRMHD simulation shows a dramatic bulge reduction, with the central luminosity of the galaxy reduced by 0.5 dex. Additionally, instead of having massive clumps within its disk, small star forming regions are seen all across the disk, with the luminosity of young stellar population more extended. To better quantify this important difference, we have measured the compactness of the stellar emission of NUT using the total luminosity in the JWST filters. By fitting a 2D Sérsic profile, we obtain half-light radii r_{50} (shown as white dashed circles) for the three face-on observations, which allow us to compute the compactness as defined in Barro et al. (2013) and used for SDSS galaxies (Baldry et al., 2020):

$$\log \Sigma_{1.5} = \log \left(\frac{M_*}{\mathrm{M}_\odot} \right) - 1.5 \log \left(\frac{r_{50}}{\mathrm{kpc}} \right) , \tag{3.2}$$

with a larger value of $\log \Sigma_{1.5}$ corresponding to a more compact galaxy. The HD simulation has the highest level of compactness, with the MHD simulation being slightly less compact but very similar as their total M_* and r_{50} are comparable. When considering the CRMHD simulation, a significantly reduced r_{50} and a stellar mass three times smaller than in the HD simulation results in the least compact of our galaxies.

We begin by briefly revisiting the evolution of the HD and MHD runs, as these have already been explored for the same initial conditions in previous works (Powell et al., 2011; Kimm et al., 2015; Martin-Alvarez et al., 2018). The stellar (left panel) and gas (right panel) masses inside the galactic region are shown for the HD model with blue lines in Fig. 3.2. The stellar mass growth follows the common trend for a MW-like halo (e.g. Kim and Ostriker, 2015; Martin-Alvarez et al., 2018): 1) *accretion phase*: significant gas accretion at high redshifts allows for a fast growth of stellar mass, reaching $10^{10}\mathrm{M}_\odot$ at $\sim 1.5\,\mathrm{Gyr}$ after the start of the simulation; 2) *feedback phase*: feedback from SNe and the formation of a virial shock after $z \sim 4$ slows down star formation, leading to self-regulation with $M_* \sim 4 \times 10^{10}\mathrm{M}_\odot$ at $z = 1.5$, in agreement with the equivalent *MFBm* model in Kimm et al. (2015). The evolution of M_{gas} is also in agreement with the findings from Kimm et al. (2015), exhibiting

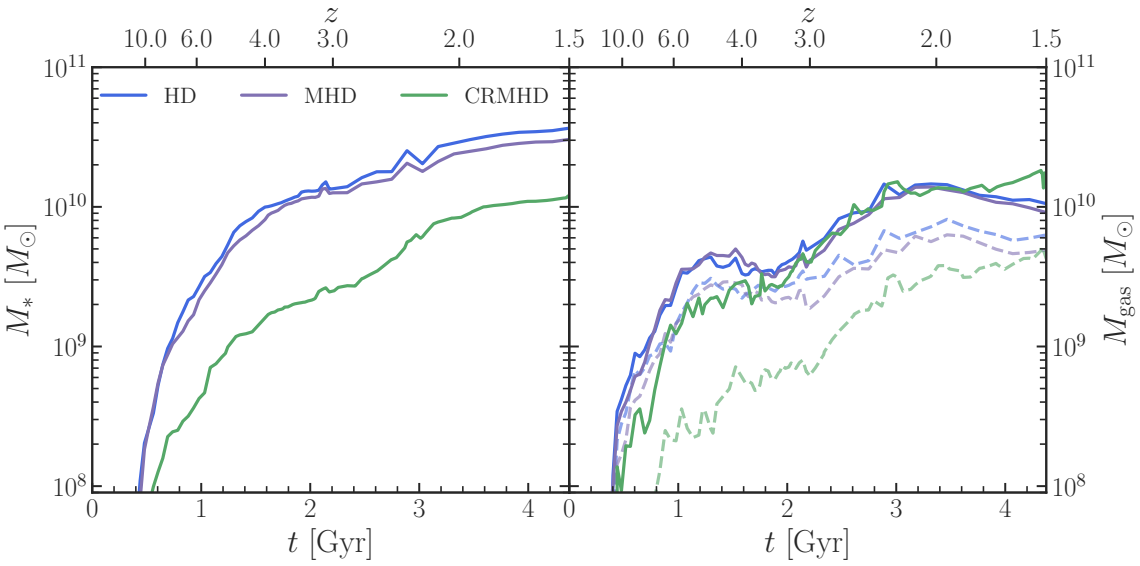


Figure 3.2: Evolution of the stellar (left panel) and gas (right panel) masses contained within the galactic region (i.e. $0.2\,R_{\rm vir,DM}$) of the NUT galaxy in the HD (blue line), MHD (purple line) and CRMHD (green line) simulations. The right panel distinguishes the total gas mass (solid line) from the cold gas mass (dashed line), as defined by the constant entropy limit of the cold phase of the ISM by Gent (2012). In all runs stellar mass grows rapidly up to $z \sim 4$, which marks the end of the accretion dominated phase, but the simulation with CRs has a stellar mass 1 dex lower than the HD and MHD runs. During this rapid growth period, the total gas mass of the CRMHD run is lower than in the other two simulations, but the largest difference is seen in the cold gas mass, which is reduced by ~ 1 dex at $z \gtrsim 4$. Below $z \sim 3$, the CRMHD run experiences a fast growth in cold gas mass, which translates into a faster growth of stellar mass at lower redshifts, causing the gas mass at $z = 1.5$ to be similar to that in the HD and MHD runs, whilst the stellar mass remains 4 times lower.

a rapid growth until $z \sim 5$. Subsequently, the fast depletion timescale reduces the gas mass inside the galactic region until $z \sim 3$. A new inflow of gas mass takes place from $z = 3$ to $z = 2$, coinciding with the last major merger that the NUT galaxy experiences (Martin-Alvarez et al., 2018, e.g.). Fig. 3.2 includes the MHD run with a primordial magnetic field of 3×10^{-12} G but no cosmic rays. This illustrates that the moderate primordial magnetisation employed here does not significantly affect the global properties of the galaxy (Su et al., 2017; Pillepich et al., 2018; Hopkins et al., 2020; Martin-Alvarez et al., 2018).

However, the addition of CRs gives rise to a radical difference in the star formation history (SFH) of the NUT galaxy: the steepness of the stellar mass growth is reduced during the accretion phase, resulting in $M_* \simeq 2 \times 10^9 \mathrm{M}_\odot$, ~ 1 order of magnitude lower with respect to the HD and MHD models at $z \sim 4$. During this period of high-redshift gas accretion, the CRMHD run only exhibits a $\sim \times 2 - 4$ deficit in $M_{\rm gas}$ inside the galactic region. Therefore the decrease in M_* cannot be solely attributed

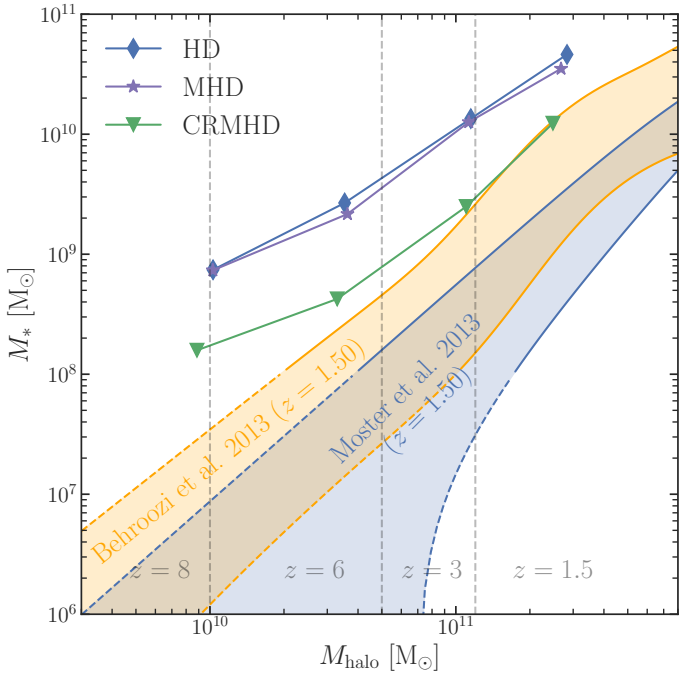


Figure 3.3: Stellar mass to halo mass function of the NUT galaxy for our fiducial models: HD (blue), MHD (purple) and CRMHD (green) shown in 4 redshift ranges ($z \sim 8, 6, 3$ and 1.5 – separated by dashed vertical lines), representative of their evolution. We have superimposed, as a visual guide, the results from abundance matching of Moster et al. (2013) (blue-shaded region) and Behroozi et al. (2013) (orange-shaded region), evaluated at $z = 1.5$. Coloured dashed orange and blue lines indicate the stellar masses at which observational mass functions are subject to incompleteness. The HD and MHD runs are able to transform the majority of their baryonic content into stars, while the CRMHD run from early on ($z \sim 8$) sits ~ 1 dex below, approaching the prediction by Behroozi et al. (2013) at $z \sim 1.5$.

to the depletion of $M_{\rm gas}$ from the galactic region. We also include on the right panel the cold gas mass (dashed lines) as defined by the constant entropy limit[2] of Gent (2012), showing that for the CRMHD simulation the cold gas mass decreases by ~ 1 dex compared to HD and MHD at $z \gtrsim 4$. This points at the depletion of the cold gas mass in the ISM as the major cause of the lower stellar mass growth at these cosmic times. Following this period of strong star formation suppression, the CRMHD run undergoes a similar period of gas accretion beginning at $z \sim 3$ as the rest of the runs, which eventually translates into a new phase of steep M_* growth. This growth of stellar mass is higher in relative terms for the CRMHD run than for the HD and MHD runs, reducing the gap between stellar masses to a factor of ~ 4, while the cold gas mass becomes similar in the three runs.

To provide further context for the evolution of the NUT stellar masses, Fig. 3.3

[2]The cold phase specific entropy limit is given by $s \leq 4.4 \times 10^8$ erg K^{-1} g^1, e.g. corresponding to a density of 7.8×10^{-23} g cm-3 at 300 K.

shows the stellar mass (M_*) to halo mass ($M_{\rm halo}$) relation for the HD (blue diamonds), MHD (purple stars) and CRMHD (green triangles) runs at four different redshift ranges from $z = 1.5$ to $z = 8$. We define the halo mass as the full gas and DM mass enclosed within $R_{\rm vir,DM}$ plus the stellar mass of the galaxy. These redshift ranges are separated by vertical dashed lines with their central redshift values indicated at the bottom of the panel. Results from the abundance matching models by Behroozi et al. (2013) (orange shaded region) and Moster et al. (2013) (blue shaded region) at $z = 1.5$ are included for reference. The HD and MHD runs show very similar behaviour across the redshift range presented, with only a small stellar mass suppression by magnetic fields. Both feature large baryonic conversion efficiencies, close to the upper limit of total conversion of gas into stars for a given halo, given by $f_{\rm b}M_{\rm halo}$, where $f_{\rm b}$ is the universal baryon fraction defined as $\Omega_{\rm b}/\Omega_{\rm m}$, the ratio of the cosmological baryon and matter density parameters. This result is consistent with the well established understanding of non-calibrated, canonical SN feedback: it fails to reproduce the results of abundance matching models, leading to a too massive stellar mass for a given dark matter halo mass. The HD run begins with $\sim 32\%$ baryon conversion efficiency, which grows to $\sim 56\%$ by $z = 2$, while the MHD run reaches a slightly lower efficiency of $\sim 47\%$. The CRMHD run shows a consistent decrease of the baryonic conversion efficiency across all redshifts, with a maximum value of $\sim 14\%$ at $z = 2$ and a minimum of 5% at $z = 6$. This significant decrease in stellar mass for a given DM halo in the CRMHD model results in a much better match to the semi-empirical constraints of Behroozi et al. (2013) by $z = 1.5$. Despite the decrease of almost an order of magnitude in M_* for the CRMHD run compared to the HD and MHD runs, the CRMHD model does not follow the 'natural' extrapolation of the abundance matching models to lower halo masses. It is important to point out that reliable constraints on the number density of galaxies hosted by small halos with masses of $10^{10}{\rm M}_\odot$ or lower between $z = 6$ and $z = 8$ are scarce, increasing the uncertainty of abundance matching models at high redshift. Additionally, the observational stellar mass functions used in these works are subject to observational incompleteness below $10^{7}{\rm M}_\odot$ (shown with the dashed orange and blue lines). We expect observations by JWST and Rubin-LSST will be able to remedy the situation in a near future.

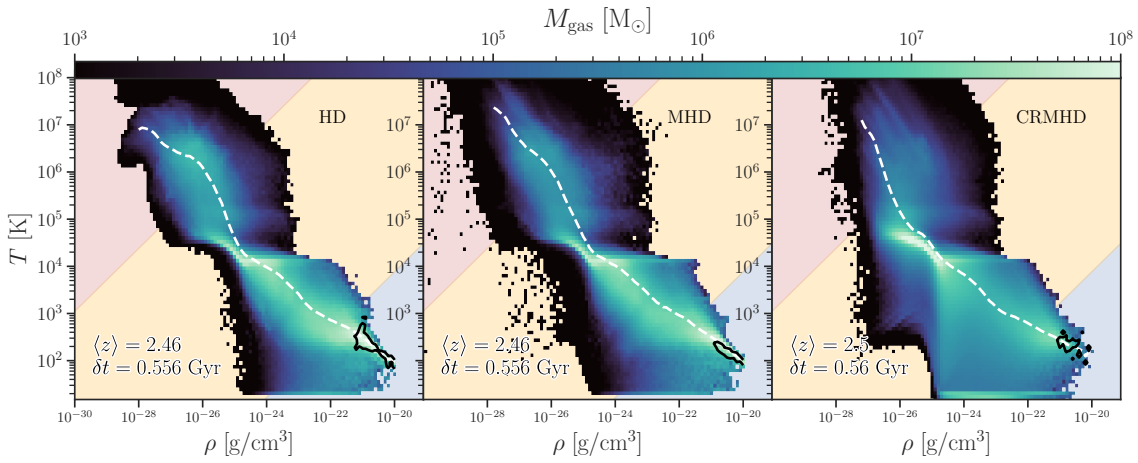


Figure 3.4: Stacked gas temperature-density phase diagrams of the NUT galaxy (within $0.2\,R_{\rm vir,DM}$) in HD (left panel), MHD (middle panel) and CRMHD (right panel) at $z \sim 2.5$. Colour maps indicate the total gas mass in each bin, with lower masses shown in dark blue and higher masses in bright aquamarine. We include a dashed white line corresponding to the median of the 2D profile. Gas phases are separated by lines of constant specific entropy given by Gent, 2012, into hot (top left, red), warm (central, orange), and cold (bottom right, blue). Black contours enclose regions where $\sim 80\%$ of the gas with $\epsilon_{\rm SF}^{\rm MTT} \geq 1\%$ lie.

3.3 How cosmic rays alter the pressure balance of the ISM and star formation efficiency

As shown in Section 3.2, the CRMHD simulation contains a factor of $\sim 2-3$ lower amount of gas in the galactic region of NUT (compared to HD and MHD) between $z = 8$ and $z = 4$. This epoch also is where we find the largest discrepancy in M_* between the CRMHD and HD/MHD runs. However, the 10 times smaller stellar mass measured at these redshifts cannot be solely attributed to the lower gas content in the galaxy which is much more moderate, and we need to consider whether the star formation efficiency of the gas is reduced compared with the HD and MHD runs. To explore the physical conditions of the ISM gas in NUT, Fig. 3.4 shows temperature-density phase diagrams for the three runs used in this study. Phase diagrams based on a single simulation snapshot can be hard to interpret as they are subject to the stochasticity driven by processes such as feedback events and mergers. To avoid this issue, the phase diagrams in Fig. 3.4 are averaged over multiple snapshots within the dynamical time of the galaxy at $z \sim 2.5$, weighted by their distance in time to $z \sim 2.5$. We estimate the dynamical time of the galaxy $\tau_{\rm dyn}$ as the time required for a test particle to complete one full orbit at $R_{\rm vir,DM}$ with circular velocity $v_{\rm circ}(r) = \sqrt{\frac{GM(<r)}{r}}$, where $M(<r) = M_{\rm baryons} + M_{\rm DM}$ is the combined baryon and DM mass within that

sphere. Additionally, to ensure the comparison between runs occurs over the same time span, we use the largest $\tau_{\rm dyn}$ of the three runs compared, which for $z \sim 2.5$ corresponds to the CRMHD simulation and has a value of $\delta t = 0.556$ Gyr. Therefore, our measurements have a central redshift $\langle z \rangle$ and a physical time range δt.

For the HD run, the left panel of Fig. 3.4 shows that the low density gas (10^{-26} g cm^{-3} to 10^{-24} g cm^{-3}) in the galactic region is dominated by gas with temperature $T \sim 10^4$ K (where hydrogen recombination and resonance lines of atomic hydrogen dominate the cooling of gas) and above, a typical signature of SNe shock-heating. Gas accumulates in the $T \sim 10^4$ K region due to thermal instability (Field et al., 1969; Wolfire et al., 1995). When this gas is perturbed by processes such as shock compression, it collapses into cold dense clumps that populate the tip of the phase diagram in the bottom right corner. In agreement with the results found by Martin-Alvarez et al. (2018) and Martin-Alvarez et al. (2020) for NUT, the addition of magnetic fields helps sustain a somewhat larger fraction of gas in hotter phases, as well as allows for gas cells to reach lower densities whilst retaining their temperature. This is reflected in the size of the 'dark' regions of the phase diagram with densities below $10^{-24}\,\mathrm{g\,cm^{-3}}$, which are larger in the MHD run as opposed to the HD run, due to the extra magnetic pressure support. To further aid this analysis, we have separated the temperature-density diagrams into three phases according to specific entropy s: cold and dense (blue region), warm (orange region) and hot and diffuse (red region). This separation is inspired by the work of Gent (2012). Similar amounts of gas are found in the hot and warm regions of the HD and MHD runs, with the MHD run having a slightly higher gas mass in the warm phase (from 49% in HD to 55% in MHD). The hot phase only contributes 3% to the total gas mass in both HD and MHD.

However, the gas phase diagram for the CRMHD run (right panel of Fig. 3.4) shows marked differences compared with the non-CR models: (a) at densities $\rho < 10^{-24}\,\mathrm{g\,cm^{-3}}$, gas is no longer confined to temperatures above 10^4 K when $\rho < 10^{-24}\,\mathrm{g\,cm^{-3}}$, which opens a new region in phase space for low density cold gas, although limited by the self-shielding threshold (vertical feature at $10^{-26}\,\mathrm{g\,cm^{-3}}$); (b) the bottom right of the warm region (i.e. $T < 10^4$ K with $10^{-24} < \rho < 10^{-22}\,\mathrm{g\,cm^{-3}}$) has a larger scatter around the median (dashed white line) of the 2D histogram; and (c) the cool dense region below the diagonal blue line which separates the cold and

warm phases contains less gas mass than the HD and MHD runs. In fact, when computing the total masses in the three phases, the cold phase mass in the CRMHD run is reduced by a factor of two compared to the HD model as this gas now resides in the warm medium (as indicated by the less intense white hue visible in this region on the right panel of Fig. 3.4). Notably, it is in these dense regions of the phase diagram that we expect gas to undergo a more efficient star formation. Overlaid black contours enclose the regions in temperature-density space that contain 80% of the star-forming gas with efficiency (as given by the MTT model) above 1%. It is readily discernible that the gradual incorporation of additional sources of support (such as magnetic and/or CR pressures) results in a reduction of the area encompassed by these contours[3]. While the HD and MHD star-forming gas contributes to 3% and 2% of the gas in the galactic region, for CRMHD is limited to 0.06%. This considerable reduction of star-forming gas mass explains, at least partially, the causal link with the measured decrease of stellar mass in this simulation as inferred from Fig. 3.2. Note that we have not yet quantified the turbulent or magnetic support of the gas, and how these affect the efficiency of star formation. Indeed, in combination with the thermal pressure, the additional CR pressure is able to support gas against further collapse, and the build up of a pressure gradient allows for the warm gas reservoir above the disk to be kept there for longer (e.g. Dashyan and Dubois, 2020; Chan et al., 2022; Farcy et al., 2022; Armillotta et al., 2022). This depletion of cold gas, now transferred to the warm phase in the presence of CRs is in good agreement with other works (e.g. Dubois et al., 2019; Nuñez-Castiñeyra et al., 2022). By considering the medians of the 2D phase diagrams, two main features are readily visible: (i) the larger contribution to the mass budget by gas between 10^{-24} g cm^{-3} to 10^{-22} g cm^{-3} in the CRMHD run creates a more pronounced concave inflection point towards lower T at $\rho \sim 10^{-23}$ g cm^{-3}; (ii) gas mass accumulates more tightly around the thermal instability shoulder at densities below 10^{-24} g cm^{-3}, driving the median line closer to this feature of the phase diagram as the relative amount of gas above $T \geq 10^5$ K is greatly reduced, particularly at higher densities.

[3]Likewise, the additional support provided by CR pressure allows gas to more frequently reach the pressure floor of the solver at 15 K, explaining the presence of the bright horizontal line in the phase diagram of the CRMHD simulation.

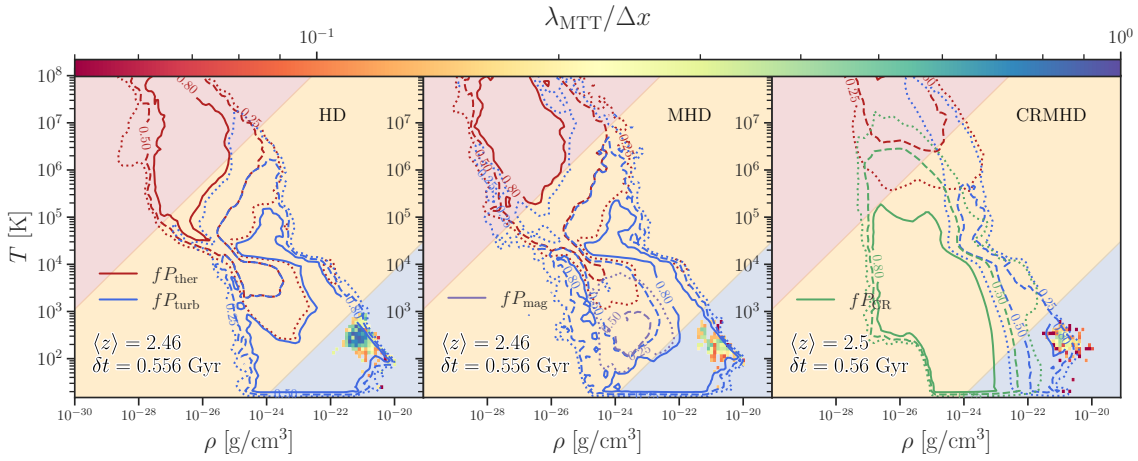


Figure 3.5: Stacked gas temperature-density phase diagrams of the NUT galaxy (within $0.2\,R_{\rm vir,DM}$) in HD (left panel), MHD (middle panel) and CRMHD (right panel) at $z \sim 2.5$. Colour maps indicate the mass-weighted average of the ratio between the MTT Jeans length and the cell size, only considering the cells that are actively star-forming (i.e. satisfy the condition $\lambda_{\rm MTT}/\Delta x < 1$). Overlaid contours indicate regions of the phase space for which a given pressure P_X contributes 80% (solid lines), 50% (dashed lines), and 25% (dotted lines) to the total pressure in the cell $P_{\rm tot}$. Depending on the physics included in the simulation, contours are shown for the turbulent pressure fraction $fP_{\rm turb}$ (blue), the thermal pressure fraction $fP_{\rm ther}$ (red), the magnetic pressure fraction $fP_{\rm mag}$, and the CR pressure fraction $fP_{\rm CR}$ (green). Star formation is limited to the highest densities in all simulations, where turbulent pressure dominates the pressure budget with at least 80%.

In order to further comprehend the structures observed in the temperature-density space of Fig. 3.4, in Fig. 3.5 we go deeper into the understanding of gas support and star formation. We remind the reader that our NUT simulations include a magneto-thermo-turbulent (MTT) model of star formation, in which an effective Jeans scale is computed taking into account (when present) thermal, turbulent, magnetic and CR pressures (see Eq. 2.18). If the local Jeans length is smaller than the cell size Δx at the highest level of refinement, star formation will take place in the cell during the current fine step. In Fig. 3.2 we saw that the gas mass between HD, MHD and CRMHD at $z \sim 2.5$ is practically the same, but the cold gas mass for CRMHD remained a factor of $\sim 2-3$ below HD and MHD. Fig. 3.5 shows that star formation (i.e. in cells for which at least $\lambda_{\rm MTT}/\Delta x < 1$) is limited to the shaded blue region that contains the cold gas phase. Thus, a reduction in cold gas mass, as seen for CRMHD, can partially explain the inefficient conversion of gas mass into stars of this simulation (as well as the smaller black contour in Fig. 3.4 containing the gas forming stars with $\epsilon_{\rm SF}^{\rm MTT} \geq 1\%$). To better understand what prevents gas in more diffuse phases from collapsing to larger densities, we have overlaid contours that show the

regions of the temperature-density space in which a particular pressure contributes by 80% (solid lines), 50% (dashed lines), and 25% (dotted lines) to the total pressure in a given cell (computed as a mass-weighted average):

$$fP_{\rm X} = \frac{P_{\rm X}}{P_{\rm tot}} \equiv \frac{P_{\rm X}}{P_{\rm ther} + P_{\rm turb} + P_{\rm mag} + P_{\rm CR}}, \tag{3.3}$$

where the total pressure $P_{\rm tot}$ is computed as the sum of thermal ($P_{\rm ther} = \rho k_{\rm B} T/(\mu m_{\rm p})$, in red), turbulent ($P_{\rm turb} = \rho\sigma^2_{\rm sigma}$, in blue), magnetic ($P_{\rm mag} = |\mathbf{B}|^2/(8\pi)$, in purple), and CR ($P_{\rm CR} = (\gamma_{\rm CR} - 1)e_{\rm CR}$, in green) pressures. The turbulent pressure is obtained via our estimate of the local gas velocity dispersion $\sigma_{\rm turb}$ in Section 2.1.3, in the same way as would be done on-the-fly to determine the local $\lambda_{\rm MTT}$. For HD and MHD, we find a clear distinction between the regions dominated by thermal pressure (hot, low-density gas) and by turbulent pressure (cold, high-density gas). Within the band of warm gas (orange shading), both pressures have an important influence in the gas energy density, with the equipartition region easily identified with where the red and blue dashed lines lie on top each other ($fP_{\rm ther} = fP_{\rm turb} = 50\%$). For CRMHD, we find that CR pressure dominates over a large region of temperature-density space, consequently displacing the contours of thermal and turbulent pressure. Firstly, contrary to its mild presence in the MHD phase diagram, magnetic pressure does not appear to even contribute with 25% of $P_{\rm tot}$, positioning magnetic fields as a secondary component in the overall pressure support within $0.2\,R_{\rm vir,DM}$ of NUT[4]. In contrast to HD and MHD, CRMHD shows the equipartition of thermal, turbulent and CR pressures at higher temperatures (for gas in the interface between the warm and hot phases). This is indicative of the large effective support by CRs of the warm phase.

[4]We note that this result may be also subject to our choice of ~ 20 pc resolution. As shown in fig. 6 of Martin-Alvarez et al. (2022), this resolution is in the limit for achieving sufficient turbulent dynamo amplification. We also claim that the efficient acceleration of cold and warm neutral gas (with overall higher magnetic energies) in the CRMHD simulation can lead to further loss of magnetic field energy within the galactic region. We will explore the loss of magnetic field by outflows in future work, as well as the influence of CRs in the turbulent amplification in higher resolution simulations.

3.4 Cosmic rays reshape how supernovae interact with the galactic region

3.4.1 Distribution of supernova sites and feedback effectiveness

The modifications of the gas distribution across ISM phases also impact the distribution of SN explosions. In turn, these local properties affect the efficiency of SN feedback in self-regulating star formation and modifying the ISM properties. We explore this issue by recording local gas properties in the central cell where individual SN explosions occur. In Fig. 3.6 we plot the distribution of gas densities at SN locations for two redshift ranges: between $3 < z < 6$ (top panel), i.e., the period of the largest M_* difference between CRMHD and HD/MHD, and between $2 < z < 3$ (bottom panel), which samples the period of fast growth of M_* in CRMHD. We find for the HD simulation that (as in previous works Kimm et al., 2015) these PDFs are intrinsically bimodal with the two peaks at low and high densities, characterising the hot and cold phases of the ISM (see e.g. Gent, 2012). However, the high density peak dominates the overall distribution, which at higher redshifts (top panel) resembles more a log-normal distribution of the cold ISM. When SNe explode in the HD case, young star particles have not had the chance to leave the dense regions of the galaxy in which they were born. This means the 10^{51} erg from a single SN[5] will be deposited into a larger gas mass per cell, hence reducing the maximum launch velocity and making it harder for the outflowing gas to escape the gravitational potential. Including magnetic fields in the MHD simulation moves the low density peak of the distribution to lower densities ($\sim 10^{-27}$ g cm^{-3}) and produces a more bimodal distribution at higher redshifts. As already implied by the phase diagrams of MHD (see Fig. 3.4), the additional magnetic support alters the gas phase distribution inside the galaxy, allowing for SNe to take place in lower density gas. Furthermore, we also attribute this peak at lower densities to the increased clustering of star-forming regions (e.g. Hennebelle and Iffrig, 2014; Hennebelle et al., 2022), as magnetic fields reduce the

[5]At high densities the Sedov-Taylor phase will hardly be captured by our ~ 20 pc resolution, so the mechanical feedback method from Kimm et al. (2017) will mainly inject the momentum reached at the end of the snowplough phase.

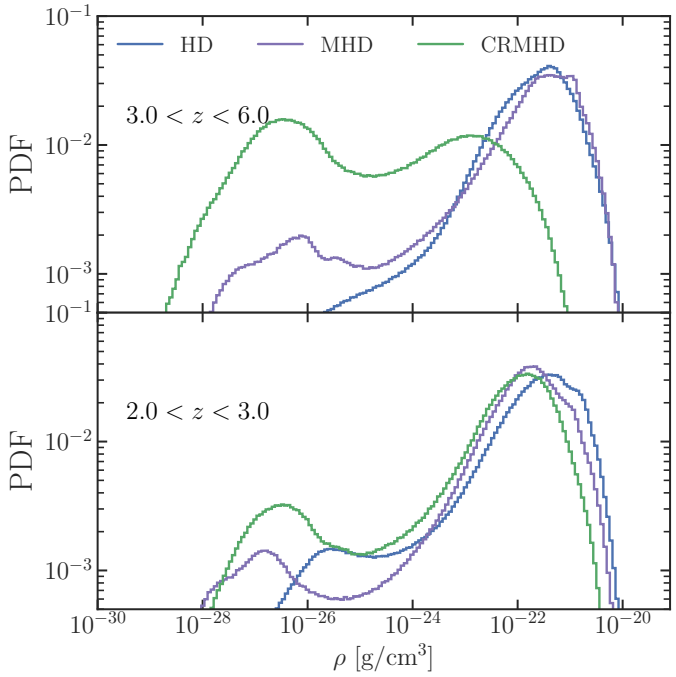


Figure 3.6: Distribution of gas densities in which SN events take place in the redshift range $z = 6.0 - 3.0$ (top panel) and $z = 3.0 - 2.0$ (bottom panel). Data corresponding to the CRMHD simulation is shown in green, the MHD simulation in purple and the HD simulation in blue. Across all redshifts, the majority of SN events in the HD and MHD simulations are found at high densities (10^{-22} g cm^{-3} to 10^{-21} g cm^{-3}), in which SNe explosions suffer from strong radiative cooling. Contrarily to HD and MHD, in the CRMHD simulation at early times (top panel) the distribution is strongly bimodal, with a peak at low densities $\sim 10^{-27}$ g cm^{-3} and a peak at $\sim 10^{-23}$ g cm^{-3}. SN events taking place at lower densities during this period are more effective in affecting the surrounding gas. This bimodality is still present in the lower redshift range (bottom panel), but the contribution of the low density peak is significantly suppressed, with the overall distribution becoming more resemblant to that measured in the HD and MHD simulations.

cold gas fragmentation, making feedback events more correlated to each other and hence promoting the formation of super-bubbles.

The presence of this bimodality in SN sites is strongly altered for the CRMHD simulation compared to no-CR runs. Although the effects seen in the MHD simulation, which arise from the support of magnetic fields, should also be in place in the CRMHD simulation, we have already seen (in Fig. 3.4) that the presence of CR pressure and heating mechanisms dominates over the effect of magnetic fields. The ISM in the CRMHD run is strongly depleted of high density cold gas (see green dashed lines in right panel of Fig. 3.2), with the high density peak of the bimodal distribution now at $\sim 10^{-23}$ g cm^{-3} in the CRMHD run instead of $\sim 10^{-21}$ g cm^{-3} in the HD and MHD runs. The regions of star formation (black contours) in Fig. 3.4 are pushed to lower densities, and the warm phase dominates the gas mass budget in the galactic

region. Therefore, it is more common for SN explosions to take place at lower densities ($\leq 10^{-22}\,\mathrm{g\,cm^{-3}}$), with a large number of SNe exploding at $\rho \sim 10^{-27}\,\mathrm{g\,cm^{-3}}$. We attribute this to star formation happening in a less concentrated manner, throughout the galactic region, with subsequent feedback events being able to sample lower density regions shaped by CR pressure and previous SN-driven bubbles. In addition, SN remnants evolve for longer and maintain higher temperatures past the canonical evolutionary sequence (e.g. Naab and Ostriker, 2017) when the effects of CR pressure are taken into account (see Rodríguez Montero et al. 2022 for a parameter space study of CR feedback effects on the evolution of individual SN using 3D MHD simulations). Furthermore, similarly to the behaviour of fully thermal SN remnants (Thornton et al., 1998), when CRs are accounted for in the evolution of SN explosions in low density environments, they can reach a larger value of deposited momentum compared to high density environments (Rodríguez Montero et al., 2022).

The bottom panel of Fig. 3.6 shows gas density PDFs for SN sites at lower redshifts (between $z = 3$ and $z = 2$). In this lower redshift range we find that the CRMHD PDF begins to resemble to the ones obtained for the HD and MHD runs, although maintaining a higher fraction of SNe at lower densities (i.e. $\sim 10^{-27}$ g cm^{-3}). We know that NUT transitions to a rotationally supported (i.e. ratio of rotational velocity to dispersion velocity larger than unity) disk at $z \sim 3.5$ (Martin-Alvarez et al., 2020). We thus attribute the change in PDF bimodality primarily to a change in the geometrical morphology of the galaxy in the CRMHD simulation. At high redshift, the galaxy exhibits an irregular, near spherical gaseous density distribution. This means that cosmic rays emitted by a supernova will have to travel a significant distance through dense, cold gas in all directions before they can escape. On the other hand, when the galactic disk becomes established at lower redshift, CR emanating from a SN going off within the thin disk will rapidly encounter diffuse gas in directions quasi-perpendicular to the disk. In other words, in a disk geometry the larger surface-to-mass ratio leads generally to CRs interacting less with the star-forming gas before they reach the edge of the galaxy.

3.4.2 Influence of cosmic rays on outflow rates

The CRMHD galaxy has both lower $M_{\rm gas}$ and M_* at high redshift than its HD and MHD counterparts. This must be, at least partially, due to outflow and inflow rate differences in these simulations. In this work, we focus on the analysis of the outflowing gas. We measure instantaneous outflow rates $\dot{M}_{\rm outflow}$ as

$$\dot{M}_{\rm outflow}(r) = \frac{1}{\delta r_{\rm shell}} \sum_i \rho_i v_{r,i} (\Delta x_i)^3 \,, \tag{3.4}$$

where we sum over all cells with positive radial velocities $v_{r,i}$ in a thin spherical shell of width $\delta r_{\rm shell}$ at a distance r from the galactic centre. We employ a shell thickness of $0.02\,R_{\rm vir,DM}$, which provides a consistent measurement across simulations and cosmic time as it naturally accounts for galaxy growth. Each cell is characterised by its gas density ρ_i, the radial velocity $v_{r,i}$ and the cell width Δx_i. Previous studies with the NUT galaxy (Tillson et al., 2015) found the contribution to the inflowing gas from satellites to be small ($\sim 1\%$) compared to that from filaments. Nevertheless, for the analysis of the outflowing gas, satellites that cross our thin shell may contain gas that could appear to be flowing radially outward in the frame of the central galaxy (either due to satellite rotation, or because a given satellite crosses the measuring shell on its way back to the outer halo regions after its apocentric passage). To avoid these subtleties, we subtract all contributions in the thin shell from passing substructures. We thus remove gas located within the tidal radius of DM sub-halos containing more than 1000 particles. The tidal radius is approximated as the Jacobi radius of a DM halo with the density profile of an isothermal sphere (see Eq. 8.107 of Binney and Tremaine, 2008).

In Fig. 3.7 we show the results of this outflow analysis when the thin spherical shell is located at a radial distance of $0.2\,R_{\rm vir,DM}$ (evolving from $\sim 1\,$kpc at $z = 10$ to $\sim 20\,$kpc at $z = 1.5$). From top to bottom, we show $\dot{M}_{\rm outflow}$ (top panel), star formation rate (SFR) averaged over 100 Myr (middle panel), and the mass loading factor $\eta = \dot{M}_{\rm outflow}/{\rm SFR}$ (bottom panel). Solid lines denote the running median calculated over 200 Myr. Note that we do not restrict our analysis to particular assumptions about the possible time delay between a star formation event in the galaxy and the consequent outflow at $0.2\,R_{\rm vir,DM}$. We distinguish three distinct epochs when comparing the HD, MHD and CRMHD simulations: (i) between $z \sim 13$ and

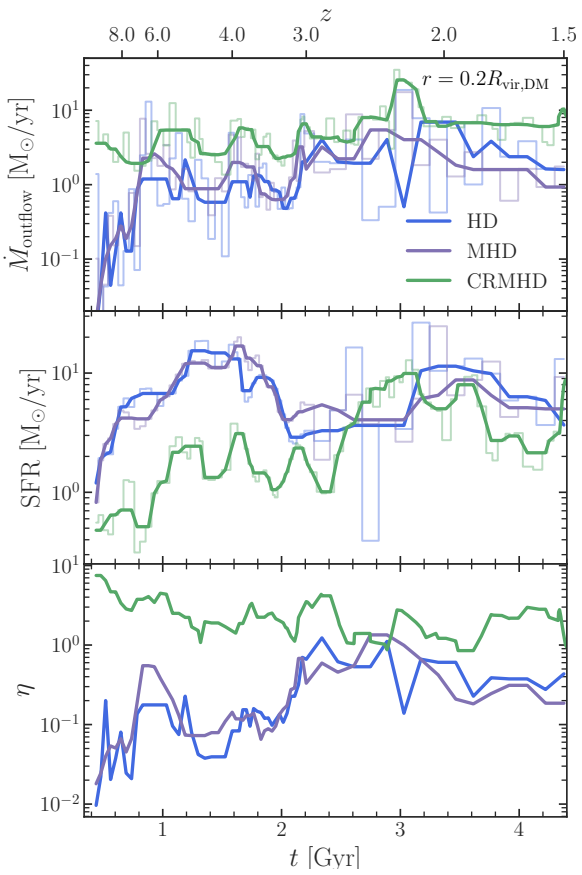


Figure 3.7: Top panel: Outflow rates measured in a thin spherical shell located at a distance $0.2\,R_{\rm vir,DM}$ from the galactic centre for the HD, MHD and CRMHD runs. The histograms show the instantaneous mass-flow rate through the shell, while the solid lines represent the running median of these measurements using a filter of size 200 Myr. **Middle panel:** Star formation rate (SFR) of the galaxy averaged over time bins of 100 Myr. **Bottom panel:** Mass-loading factor η computed using the running median of $\dot{M}_{\rm outflow}$ and SFR shown in the top panels. The simulation with CRs has large outflow rates, $\times 10 - 100$ higher than the HD and MHD simulations, and maintains them across cosmic time. Given the large suppression of star formation for $z \geq 3$, the CRMHD simulation also yields a mass-loading factor consistently exceeding unity, a value that is only reached in the HD and MHD simulations during the merger-induced starburst at $z \sim 2.3$.

$z \sim 7$ outflow rates in the CRMHD run reach $2 - 4\,{\rm M}_\odot\,{\rm yr}^{-1}$, whereas the HD and MHD runs are closer to $0.1 - 0.4\,{\rm M}_\odot\,{\rm yr}^{-1}$; (ii) between $z \sim 7$ and $z \sim 3$ outflow rates in the HD and MHD runs hover around $1\,{\rm M}_\odot\,{\rm yr}^{-1}$ (with the MHD outflows having overall larger values than their HD counterparts), corresponding to strong starburst episodes (however, given average SFRs of $10\,{\rm M}_\odot\,{\rm yr}^{-1}$, mass loading factors remain well below unity, while they consistently exceed $\eta \sim 1$ in the CRMHD run); and (iii) between $z \sim 3$ and $z \sim 1.5$, when the SFR in all three runs peaks around $10\,{\rm M}_\odot\,{\rm yr}^{-1}$ at $z \sim 2.5$ (and subsequently slowly declines to $2 - 4\,{\rm M}_\odot\,{\rm yr}^{-1}$): only the CRMHD galaxy maintains a steady outflow of $8 - 9\,{\rm M}_\odot\,{\rm yr}^{-1}$ while that in the MHD

counterpart drops to $2\,M_\odot\,yr^{-1}$ and the HD one floats around $2-4\,M_\odot\,yr^{-1}$, with the odd jump to $8\,M_\odot\,yr^{-1}$ at $z\sim2$. It is also important to note that in comparison with the HD and MHD runs, the CRMHD runs experiences a fast rise in SFR of 1 order of magnitude between the redshifts of 3 and 2.3. As mentioned before, during this period NUT experiences a merger with a large companion, causing a significant increase in the cold gas mass of the galaxy (see Fig. 3.2) and a burst in star formation. We find that a corresponding large increase in the inflow rate onto the galaxy (see Sec. 4.2.3), is fuelled by the cold, high density extraplanar gas supported by CR pressure which becomes unstable during the merger interaction. Overall, the cosmic evolution of $\dot{M}_{\rm outflow}$ appears more steady than the SFR for the CRMHD run. This shows that while SN feedback is rarely efficient in the HD and MHD runs, even when large amounts of gas are converted into stars, in the CRMHD run a significant quantity of gas is consistently ejected from the galaxy even though fewer stars are formed overall.

In Fig. 3.8 we compare the measured η at $0.2\,R_{\rm vir,DM}$ to the circular velocity of NUT in the HD, MHD and CRMHD simulations with observations of outflows in nearby dwarf, star-forming galaxies. The observations by McQuinn et al. (2019) are in the low-mass end of the CRMHD simulation (green triangles), with the majority of HD and MHD data points (blue circles and purple squares, respectively) are usually well beyond $\sim$ 100 km s^{-1}. The sample from Chisholm et al. (2017) extends to higher $v_{\rm circ}$[6], landing close to the results of the CRMHD simulations. To aid in this qualitative understanding of the trends, we have computed median values of the different simulations for three equally separated bins in circular velocity, indicated with filled symbols and with error bars showing the upper and lower quartiles of the underlying distribution. We find that the CRMHD simulation presents an overall trend that scales like $\eta\propto v_{\rm circ}^{-0.82}$, close to the prediction for a momentum driven wind, while the HD and MHD simulations show the complete opposite correlation, closer to $\propto v_{\rm circ}^{1.43}$ and $\propto v_{\rm circ}^{0.52}$, respectively. This a signature of feedback being highly inefficient in reducing the central growth of the galaxy (see e.g. Bournaud et al., 2007), although the MHD simulation shows a flatter relation signature of stronger feedback at low masses compared to HD. It is interesting to note that our results

[6]We note that the scaling with $v_{\rm circ}$ is not computed directly from the moment 1 maps, but rather by performing a calibrated Tully-Fisher relation (Reyes et al., 2011) with the SED-modelled stellar mass.

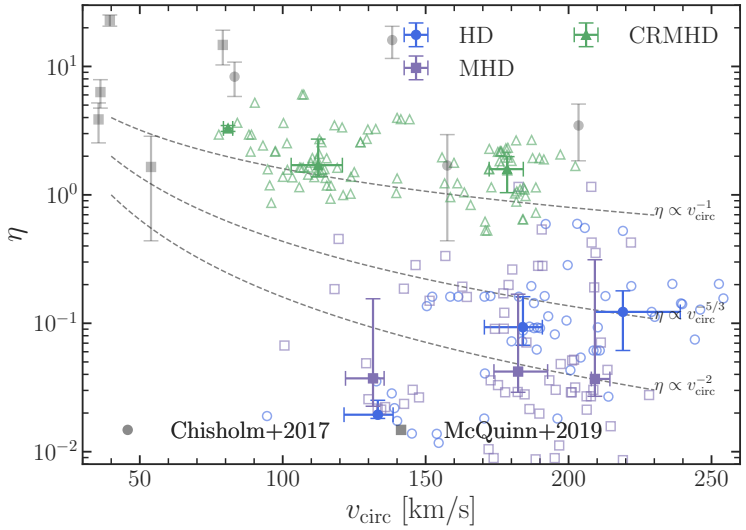


Figure 3.8: Warm-ionised mass loading factor η vs circular velocity $v_{\rm circ}(0.2R_{\rm vir,DM})$ of HD (blue circles), MHD (purple squares) and CRMHD (green triangles) in all snapshots, compared to observations of nearby Universe dwarf, star-forming galaxies (Chisholm et al., 2017; McQuinn et al., 2019). We also include median values of the simulation data points with filled markers and error bars indicating the lower and upper quartiles of the data distribution in each bin. The CRMHD simulation values land very close to the observed data, resulting in the scaling $\eta \propto v_{\rm circ}^{-0.92}$, in fair agreement with a momentum-driven wind (Somerville and Davé, 2015).

for the CRMHD simulation are close to McQuinn et al. (2019) in both the value of η and the slope ($\propto v_{\rm circ}^{-0.96}$), and with the value of η in Chisholm et al. (2017). This scaling of η is in disagreement with the analytic estimates in (Quataert et al., 2021). Our simulations show a noticeable decrease in η compared to the FIRE-1 (Muratov et al., 2015) and FIRE-2 (Pandya et al., 2021) cosmological simulations, as well as a better agreement with observations in both η and the slope of the relation with $v_{\rm circ}$ (their results are closer to energy-driven winds or even steeper at low redshifts). These results portray the excellent agreement of simulations including CRs with observations of dwarf galaxies in the local Universe.

In order to further understand the underlying differences between outflows in the non-CR runs and CRMHD, we compare their outflow velocity distributions during two distinct phases of the SFH: 1) a peak in SFR present in all simulations at $z \sim 4$; and 2) a period of similar SFRs across all runs ($\sim 8-10\,{\rm M}_\odot\,{\rm yr}^{-1}$) occurring approximately at $z \sim 2.5$. The latter is characterised by a merger with a fairly massive companion. We compute stacked outflow rate histograms following the method detailed in Sec. 3.3 for weighted stacking of PDFs, employing snapshots within a dynamical time of the median redshift. These histograms show the total $\dot{M}_{\rm outflow}$ separated into radial velocity bins

for the same thin shell used in Fig. 3.7 located at a distance $0.2\,R_{\rm vir,DM}$ from the galaxy centre. We show the HD, MHD and CRMHD simulations in blue, purple and green, respectively. The top panel of Fig. 3.9 shows that for $\langle z \rangle = 3.94$ the outflowing gas carrying the majority of the mass outside of the galaxy is found at lower radial velocities in the CRMHD run than in the HD and MHD runs. We define the quantity $\dot{M}_{\rm esc}$ as the outflow rate of gas with a speed exceeding the local escape velocity[7]. While the HD distribution is dominated by gas between $60\,{\rm km\,s^{-1}}$ and $120\,{\rm km\,s^{-1}}$, it rapidly drops at higher velocities, with just $0.01\,{\rm M_\odot\,yr^{-1}}$ exceeding the $v_{\rm esc}$ of the galaxy (indicated by the vertical dotted blue line). Note that this instantaneous escape velocity is computed at each snapshot by counting the total mass enclosed within $0.2\,R_{\rm vir,DM}$. The MHD simulation instead shows a tail that does extend to higher velocities, contributing 10 times more to the mass outflow rate above $v_{\rm esc}$ than HD. However, despite this higher efficiency in driving fast outflows, the majority of the outflowing mass between $60\,{\rm km\,s^{-1}}$ and $120\,{\rm km\,s^{-1}}$ remains the same, and the outflowing gas mass above $v_{\rm esc}$ is still 3 times lower than in the CRMHD run. This is due to the fact that $v_{\rm esc}$ is half the value for the CRMHD run than for the HD/MHD runs, because of the former's shallower potential well in the galactic region. This, in turn, is caused by the CR feedback persistently and significantly affecting the growth of the central stellar mass of NUT at higher redshifts. Therefore, the larger outflow rates in CRMHD at $z \sim 4$ can be explained by a larger fraction (almost 1 dex compared to HD and MHD) of 'low-velocity' (below 100 km s^{-1}) gas and an easier escape of fast outflows from a shallower gravitational potential. To further explore these trends, we also analyse the outflow velocity distribution at $z \sim 2.5$ (see bottom panel of Fig. 3.9). Although now the fast growth of NUT in the CRMHD simulation between $z = 3$ and $z = 2$ somewhat bridges the gap in $v_{\rm esc}$, this simulation still has 6 times as much gas outflowing above $v_{\rm esc}$ than the HD and MHD runs. This is not surprising given that during this period $\dot{M}_{\rm outflow}$ in CRMHD is more than an order of magnitude higher than HD and MHD. Furthermore, these plots also suggest that the majority of the outflowing gas at $0.2\,R_{\rm vir,DM}$ lacks the kinetic energy necessary to escape the local gravitational potential in all simulations. However, it remains an

[7]While a radial velocity higher than $v_{\rm esc}$ is, strictly speaking, not a sufficient (or even necessary) condition for gas to completely escape the gravitational potential of a halo, it nevertheless constitutes a useful proxy, and is thus commonly used both in observational and theoretical studies.

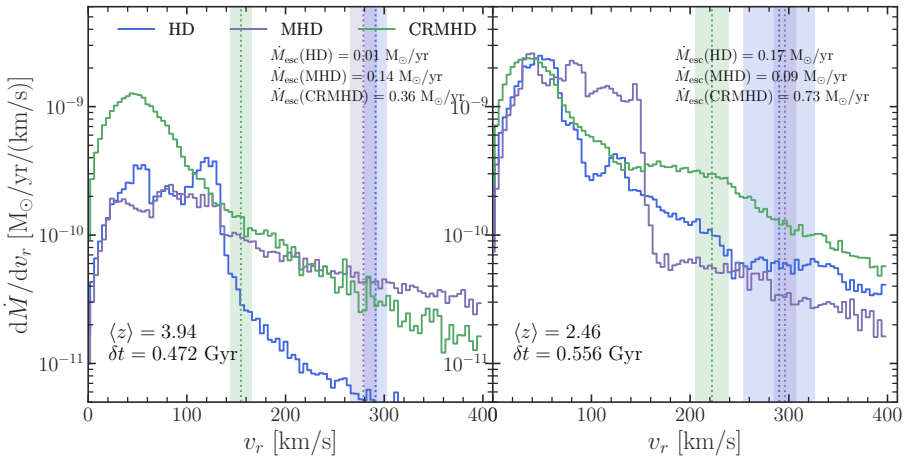


Figure 3.9: Differential mass outflow rates as a function of gas radial velocity measured in a thin shell located at $0.2\,R_{\rm vir,DM}$ from the centre of the galaxy at $\langle z \rangle = 3.94$ (top panel) and $\langle z \rangle = 2.46$ (bottom panel). We compare the HD (blue), MHD (purple), and CRMHD (green) simulations, stacking snapshots over a $t_{\rm dyn}$ period, using the method detailed in Sec. 3.3. Vertical dotted lines show the stack-weighted averages $v_{\rm esc}$ for the redshift quoted, with the corresponding standard deviations denoted by the shaded regions. Values for the total mass outflow rate above $v_{\rm esc}$ ($\dot{M}_{\rm esc}$) are included in each panel for each simulation. The peak of the outflowing gas distribution is both more prominent and displaced to lower radial velocities in the CRMHD simulation in both redshift ranges. At high redshift, the shallower gravitational potential of the CRMHD galaxy allows a much larger fraction of the high velocity tail to exceed the local $v_{\rm esc}$.

open question as to whether this gas needs to escape the halo in order to reduce the reservoir of gas available for star formation or if it is enough to prevent its re-accretion over sufficiently long timescales (see e.g. Somerville and Davé, 2015, for preventive feedback in the context of AGNs). As far as our current analysis goes, the CRMHD model systematically reaches higher mass loading factors than the no-CR runs. These outflows are mainly comprised of a slow moving wind which, without any further acceleration beyond $0.2\,R_{\rm vir,DM}$, will not be able to escape the halo and will eventually fall back onto the galaxy if left undisturbed by future feedback events.

3.4.3 Dynamics of multi-phase outflows

The higher outflow rates measured for the CRMHD simulation despite a smaller SFR are a consequence of the energy deposited by SNe being more efficient at expelling gas from the galactic disk. To provide evidence for this higher efficiency driving higher mass-loading factors in CRMHD, Fig. 3.10 shows the $\dot{M}_{\rm outflow}$ and $\dot{M}_{\rm outflow}$-weighted radial velocities of outflowing gas $v_{\rm outflow}$ in the HD (blue), MHD (purple)

and CRMHD (green) simulations, separated in the hot ($T > 10^5$ K), warm ionised (10^5 K $> T >$ 9000 K), warm neutral (9000 K $> T >$ 1000 K), and cold ($T <$ 1000 K).

HD and MHD outflows are dominated by the hot and ionised phases during the majority of the evolution of NUT. Outflowing gas in the warm neutral and cold phases in these runs are identified with abrupt, low velocity peaks in the velocity plots, which we found to be related to clumps of gas in eccentric orbits around NUT, rather than genuine outflows. Instead, in the CRMHD run, the hot phase never dominates the outflowing mass rate (see Fig. 3.11). It is the warm ionised phase which dominates ($1 - 10\,\mathrm{M_\odot\,yr^{-1}}$), with considerable contributions of the warm neutral and cold gas at $z \geq 4$. We find that multi-phase outflows (∼1:2:4:2 ratios for cold, warm neutral, warm ionised and hot phases, respectively) are only found consistently in the CRMHD simulation, and at high redshift ($z \geq 4$). The HD and MHD runs fail to ever produce such commensurable gas mass ratios across all phases.

To understand whether the outflowing gas is gravitationally bound, we compare its radial velocity with the local escape velocity at $0.2\,R_{\mathrm{vir,DM}}$ (indicated by dashed lines in the four relevant panels of Fig. 3.10). The radial velocities of the hot phase (top left panel) range from $\sim 100\,\mathrm{km\,s^{-1}}$ for $z \geq 3$ to $\sim 80\,\mathrm{km\,s^{-1}}$ at lower redshifts in the simulations without CRs. For the case of CRMHD, the velocities are consistently higher, in the range $\sim 100 - 200\,\mathrm{km\,s^{-1}}$. These outflow-weighted velocities are in agreement with observations of the warm ionised gas in local dwarf galaxies by McQuinn et al. (2019) and Marasco et al. (2023), while falling short of the $\sim 400 - 600\,\mathrm{km\,s^{-1}}$ value reported in Concas et al. (2022) for their sample of galaxies between $1.2 < z < 2.6$. However, the CRMHD simulation is the only one consistently able to reach outflow velocities above the escape velocity within the galactic region, at least until $z \sim 2.5$, after which its velocity distribution becomes more similar to the non-CR cases. This behaviour is in agreement with the histograms shown in Fig. 3.9.

Warm neutral outflows are also observed in the HD and MHD simulations during merger periods, specifically during the active merger epoch between $6 \leq z \leq 8$ and around the late merger-induced starburst at $z \sim 2.3$. In Fig. 3.11 we show the fractional contribution of each phase to the total outflow rate through the previous thin shell located at $0.2\,R_{\mathrm{vir,DM}}$. While cold outflows are found in the HD and MHD runs, they only appear as rare, low velocity peaks in the v_r panels. By examining projections

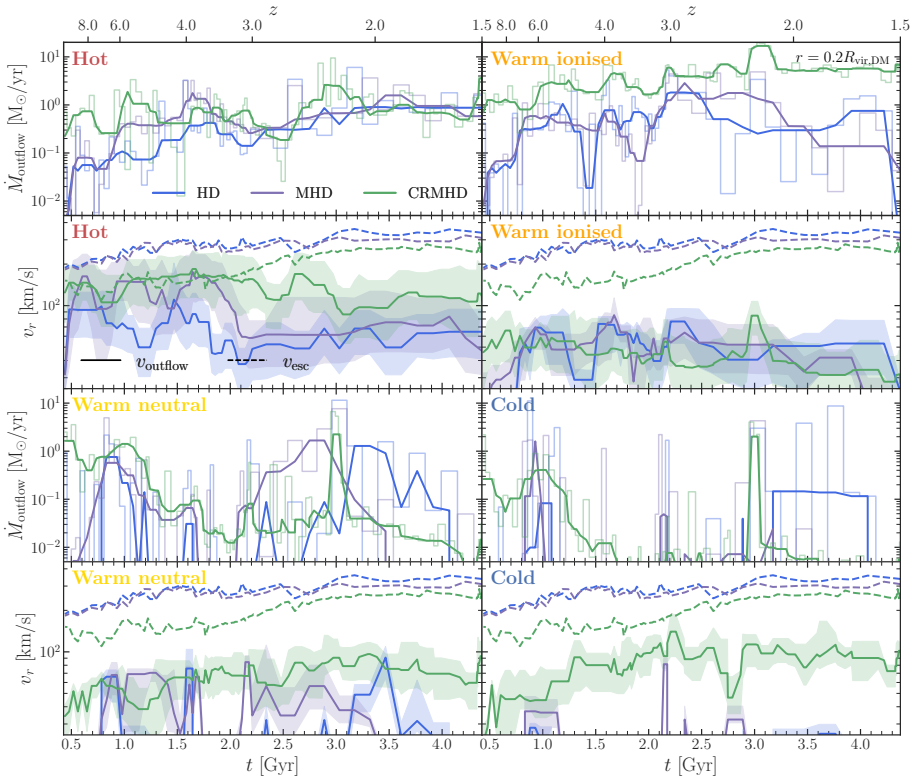


Figure 3.10: Outflow budget and kinematics of hot (top left pair), warm ionised (top right pair), warm neutral (bottom left pair) and cold (bottom right pair) gas phases for the HD (blue), MHD (purple) and CRMHD (green) runs measured at $0.2\,R_{\rm vir,DM}$. Each pair of panels shows the instantaneous outflow rate (top) and the $\dot{M}_{\rm outflow}$-weighted radial velocity of the outflowing gas (bottom). In the v_r panels, the escape velocity of each model at the shell radius is indicated by dashed lines, for ease of comparison with the median $v_{\rm outflow}$. Shaded regions represent the second and fourth quartiles of the underlying weighted distribution. Hot gas attains the largest radial velocities, with an almost constant value of $\sim 100\,{\rm km\,s^{-1}}$ for $z \geq 3$ and $\sim 70\,{\rm km\,s^{-1}}$ for $z \lesssim 3$, dominating the outflow rate in both HD and MHD simulations. The hot phase in the CRMHD run reaches the largest outflow velocities ($\sim 150 - 200\,{\rm km\,s^{-1}}$ for $z \geq 2.5$ and $\sim 100\,{\rm km\,s^{-1}}$ for $z \lesssim 2.5$), with a non-negligible fraction of the outflowing gas mass exceeding $v_{\rm esc}$ consistently up to $z \geq 2.5$. The dominant $\dot{M}_{\rm outflow}$ comes from the warm ionised phase in the CRMHD simulation, while above $z \sim 5$, warm neutral and cold phases significantly contribute to the total outflow rate.

(not shown here) of the galactic region of NUT at the redshifts corresponding to these peaks, we have found that for HD and MHD all cold outflows are linked to extended tidal features of satellites, rather than related in time to the rest of hot and warm ionised outflowing gas. In fact, CRMHD is the only run that consistently shows warm neutral and cold outflows across the majority of snapshots with non-negligible outflow velocities. These outflows are also spatially correlated with the hotter phases of the outflowing gas and are not dynamically linked to tidally stripped satellites (see Sec. 3.4.4 and Fig. 3.13 for further detail). Contrary to the hot and warm ionised phases, the outflow velocities of the warm neutral and cold gas evolve, increasing from

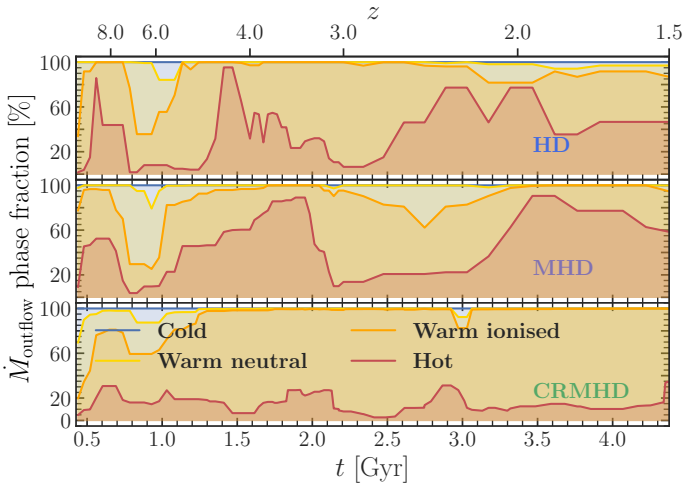


Figure 3.11: Fractional contribution of the cold (blue lines), warm neutral (yellow lines), warm ionised (orange lines), and hot (red lines) phases to the total instantaneous outflow rates, for the HD (top panel), MHD (middle panel), and CRMHD (bottom panel) runs. The HD and MHD simulations are dominated by the hot and warm ionised phases for a similar amount of time. In contrast, in the CRMHD run, the warm ionised phase dominates the outflow rates almost at all times. The only exception is at very high redshifts (i.e. the first 0.5 Gyr of evolution), when the warm neutral and cold gas constitute a non-negligible fraction of the total outflow rates. All three simulations show an important contribution of warm neutral and cold outflows around $z \sim 6$, corresponding to an intense period of mergers for NUT.

$\sim 50\,\mathrm{km\,s^{-1}}$ at high redshift to a maximum of $\sim 100\,\mathrm{km\,s^{-1}}$ at $z \sim 2.5 - 2$. Similarly to the warm ionised phase, the median v_r of these two phases sits well below $v_{\rm esc}$ (except for peaks at ~ 2.2 and $\sim 2.5\,\mathrm{Gyr}$ in the cold phase). Overall, we find that these cooler outflows struggle to reach escape velocities at $0.2\,R_{\rm vir,DM}$, even in the CRMHD simulation, despite its shallower gravitational potential.

3.4.4 Cosmic ray-driven re-acceleration of outflows in the CGM

The CRMHD simulation displays considerably higher outflow rates at $0.2\,R_{\rm vir,DM}$ than the HD and MHD runs. However, the previous analysis has shown that gas usually lacks the kinetic energy required to fully escape the gravitational potential of the galaxy. In addition, outflowing gas is further affected by the interaction with the CGM. Therefore, in this section, we investigate how such an interaction further impacts the gas dynamics at $0.2\,R_{\rm vir,DM}$. This investigation is carried out by computing the mass-flow-rate-weighted median of the radial pressure support for the outflowing gas in the thin shell at $0.2\,R_{\rm vir,DM}$. As per the hydrostatic equilibrium equation, the negative pressure gradient of the gas needs to balance the inward pull of gravity for

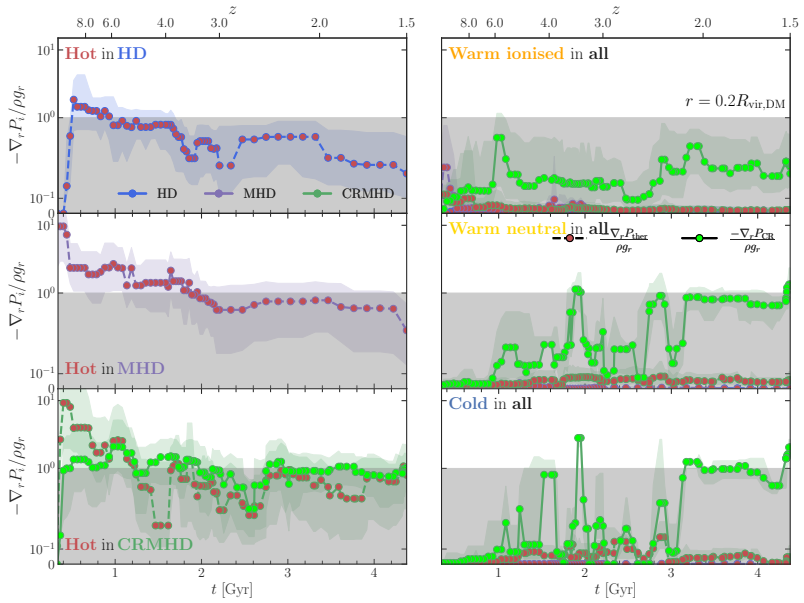


Figure 3.12: Pressure gradient support against gravity for outflowing gas separated into different temperature phases for the HD (blue), MHD (purple) and CRMHD (green) simulations. The dividing line between the shaded and unshaded region indicates marginal support. In the shaded region, gravity dominates the dynamics, while in the unshaded region, gas is accelerated outwards by the pressure gradients. Shaded, coloured bands represent the second and fourth quartiles of the underlying distribution. The left column corresponds to the hot gas, with each row corresponding to the HD (top), MHD (middle), and CRMHD (bottom) simulations, respectively. The right column combines the data for all simulations separated in warm ionised (top), warm neutral (middle) and cold (bottom) phases. Line colour and marker outline indicate the simulation to which they refer, while the marker face colour provides the decomposition in thermal (red) and CR pressure (lime) pressure gradients support. While below $z \sim 3$ the thermal pressure struggles to accelerate gas in the HD and MHD simulations, CR pressure consistently supports and accelerates the hot gas across all cosmic time. Only CR pressure supports and accelerates warm neutral and cold gas for $z \leq 5$.

a parcel of gas not to inflow. The gravitationally-dominated regime of which this equilibrium situation is a limiting case, is indicated by the grey band below a value of 1 in Fig. 3.12. For a pressured fluid x, this corresponds to $-\hat{r} \cdot \vec{\nabla} P_i = \hat{r} \cdot (\rho \vec{g})$, where $\hat{r}$ is the radial unit vector, $\vec{g}$ is the local gravitational acceleration and i is the fluid pressure component (either thermal or CR) considered. Cells with radial support below unity experience an overall deceleration whereas those with a value > 1 experience an outward acceleration. We represent the contributions from thermal pressure, $P_{\rm ther}$, as solid circle symbols coloured in red linked by dashed lines, and CR pressure, $P_{\rm CR}$, as green circles connected by solid lines.

We begin by comparing the support for the hot phase, where we separate for clarity the HD (top left), MHD (middle left) and CRMHD (bottom left) simulations. We

find that the hot and warm ionised phases show a large variance in these quantities, so we include the second and fourth quartiles of the underlying distribution as a shaded band in order to illustrate this. The three runs display a large amount of thermal pressure support against gravity for $z \geq 3$. At lower redshifts this pressure support ratio rarely exceeds unity (although it is more common for the MHD case), and has a more bursty behaviour. This change in the support of hot outflowing gas in all simulations is attributed to the growth of the virial shock at lower redshifts, as the cooling rate becomes smaller than the post-shock compression rate (Dekel and Birnboim, 2006) and cold accretion becomes less important (Powell et al., 2011). A hotter CGM means a larger thermal pressure confining gas to the galactic disk, and buoyancy forces present at high redshift becomes less important. Although, this behaviour is observed for all runs, the CRMHD run features a larger frequency of radial support peaks exceeding the force balance threshold, despite the higher density of its CGM when compared to the non-CR simulations (see Sec. 3.2). We attribute this to a colder CGM with a lower fractional contribution from thermal support due to the additional support of CR pressure. We do not include the contribution of magnetic support, as we find it to be negligible for outflows at all times for the MHD and CRMHD simulations[8]. Thermal pressure dominates the hot phase in CRMHD down to $z \sim 3$, with both CRs and thermal pressures separately capable of supporting a considerable fraction of the outflowing gas against gravity. The CR pressure support of the hot component evolves only mildly with redshift, eventually dominating for $z < 3$. This change in behaviour coincides with the drop in hot gas radial velocity after $z \sim 3$ shown for CRMHD in Fig. 3.10. While hot fast outflows in the HD and MHD simulations find it harder to travel through the CGM at lower redshifts, in the CRMHD the additional support of CRs injected by SNe to the wind bubble further accelerates them when their thermal buoyancy stalls.

We compare in the right panels of Fig. 3.12 the pressure support against gravity in the warm ionised, warm neutral and cold phases, now for the three simulations combined. As warm and cold outflows are scarce in the HD and MHD runs, we limit our analysis for these phases to the CRMHD run. This analysis confirms that the thermal pressure support (as well as the magnetic, which we do not include) in the HD

[8]Nevertheless, this should be considered also in the context of magnetic field injection by SN remnants (e.g. Martin-Alvarez et al., 2021), which we do not explore within this thesis.

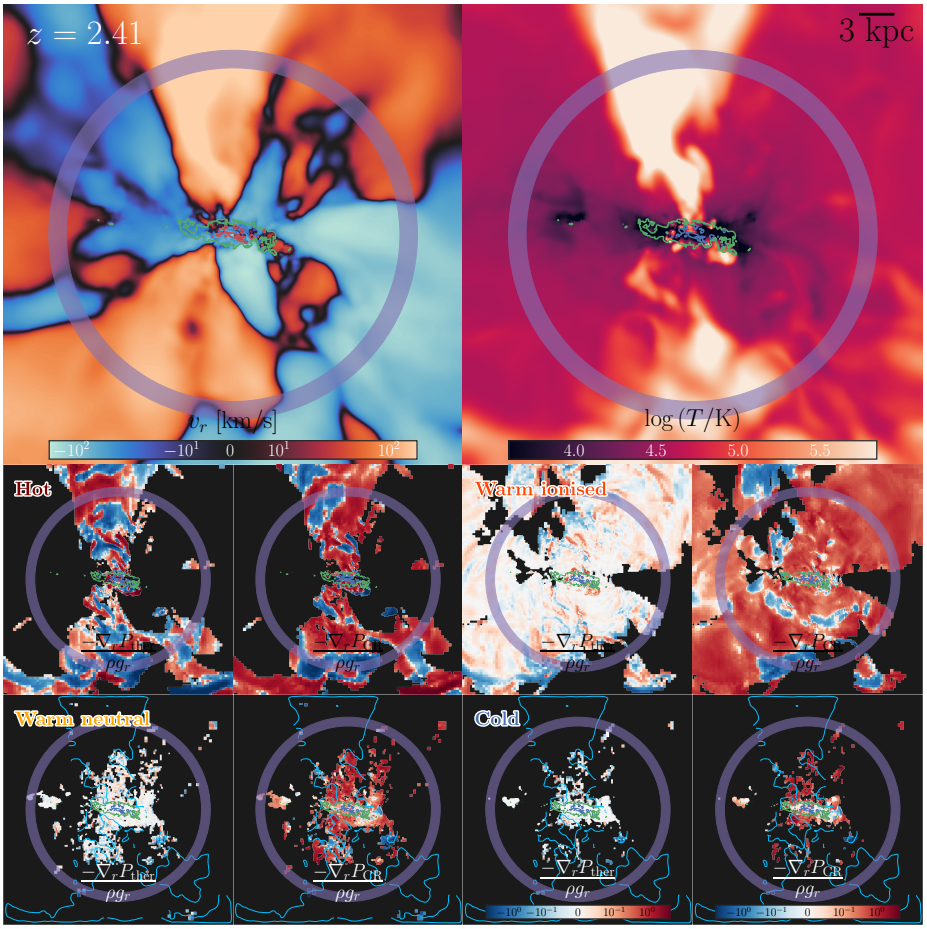


Figure 3.13: Edge-on view of NUT in the CRMHD run during a strong feedback event at $z = 2.41$. **Top panels:** $\dot{M}_{\rm outflow}$-weighted projections of a 20 kpc on a side cube centred on NUT showing the gas radial velocity (left panel) and the gas temperature (right panel). In the left panel, inflowing gas is shown in blue and outflowing gas in red. Black (green) and red (blue) contours are overlaid on the radial velocity (and temperature) projection to show gas density contours at $10^{-24}\,{\rm g\,cm^{-3}}$ and $10^{-22}\,{\rm g\,cm^{-3}}$, respectively. The purple ring shows the $0.2\,R_{\rm vir,DM}$ shell. **Bottom panels:** the same projected region now separated into four outflow gas phases (see Section 3.4.2). Each phase is plotted in two panels, corresponding to thermal and CR support of the gas against gravity, with red (outwards acceleration) or blue (inwards acceleration) colours indicating the dominant pressure gradient. From top left to bottom right, the temperature phases displayed are: hot (two top leftmost panels), warm ionised (two top rightmost panels), warm neutral (two bottom leftmost panels), and cold (two bottom rightmost panels). We include in these panels the same gas density contours (green and blue) displayed on the temperature panel (top right panel). The warm neutral and cold panels also include contour lines showing the regions dominated by the hot (blue contours) outflows. Hot outflows are clearly biconical with large gradients of both thermal and CR pressure. Both feature alternative positive and negative gradients, a tell-tale signature of consecutive outflowing waves. The warm ionised gas is the most volume filling phase, with a much more isotropic structure around NUT. Warm neutral and cold outflows present a more clumpy and filamentary structure which quickly fades off at larger radii.

and MHD runs is negligible and further supports the idea that for the runs without CRs, outflowing gas colder than 10^5 K does not experience further acceleration at $0.2\,R_{\rm vir,DM}$. Due to outflow velocities lower than $v_{\rm esc}$, outflows likely rain back down onto the galaxy as a galactic fountain. The CRMHD run features warm ionised outflows that are marginally supported against gravity, following an overall trend similar to that of the hot gas, but now with CR pressure gradients dominating over thermal pressure gradients at all times. In fact, CR pressure support dominates over thermal pressure support for the three phases in the right column of Fig. 3.12. The warm neutral and the cold components of the outflow show large accelerations due to CRs, exceeding by up to 7 times the gravitational acceleration. These phases display a large variability, also found in the analysis of $v_{\rm r}$ (see Fig. 3.10). This can be attributed to a combination of outflow 'burstiness' and a lower volume-filling of these phases. Therefore, whenever outflows entraining warm neutral and cold gas are present, they are usually subject to large CR pressure gradients that not only balance gravity but provide additional acceleration. This means that, although the outflow velocities of these two phases at these radii are not enough to escape the halo, CR pressure gradients can drastically change their dynamics as winds escape from the galaxy.

This section has described how CRs affect outflows, providing further insight on the consistently higher outflow rates that the CRMHD run exhibits when compared to the HD and MHD runs. Here we perform a more detailed analysis of a particular feedback event in the CRMHD simulation to understand how CRs are locally driving the observed differences. In Fig. 3.13 we show edge-on $\dot{M}_{\rm outflow}$-weighted projections of NUT during a feedback event at $z = 2.41$ ($t \sim 2.9\,$Gyr). This time was selected because of the presence of a corresponding peak in the outflow rate (i.e. $\sim 30\,{\rm M}_\odot\,{\rm yr}^{-1}$, see Fig. 3.7) and the CR-supported warm neutral and cold outflows. The top panels show the radial velocity (left) and gas temperature (right) maps for a region 20 kpc on a side, encompassing the $0.2\,R_{\rm vir,DM}$ thin shell (shown as a dashed purple circle). We overlay on top of the left (right) map contours for the gas density showing 10^{-24} g cm^{-3} in black (red) and at 10^{-22} g cm^{-3} in red (blue). These panels uphold the canonical understanding of wind launching in disk galaxies: at the centre lies a cold and dense disk from which high velocity, hot outflows carve bi-conical perpendicular channels through the warm ionised CGM. This particular outflow is preceded by

previous plumes of hot gas visible at larger radii. There are also regions of outflowing gas that do not have a significantly higher temperature than the surrounding CGM (see outflowing region in the top right corner of the $v_{\rm r}$ map).

In keeping with our previous analysis, we separate the outflowing gas into distinct temperature phases in the 8 lower panels. For each of the phases, we plot radial support against gravity, i.e. $-\nabla_r P_x = \rho g_r$, for thermal ($P_{\rm ther}$) and CR ($P_{\rm CR}$) pressures. To help the analysis, we keep the density contours (green and blue lines) of the temperature projection in these panels. We first examine the hot outflows (top left panels), which display in both thermal and CR pressure support maps a clear bi-conical morphology with an opening angle of $\sim 30°$. Dark red and blue colours represent high pressure acceleration anti-parallel and parallel to the gravitational acceleration, respectively. The intertwined structure of positive and negative gradients in both thermal and CR pressure is attributed to the succession of multiple outflow bubbles, ejected from the galactic disk at different times. As such, the front of a previous bubble appears as a positive gradient in the radial direction. These features are also present in the pressure support maps of the HD and MHD simulations (not shown). This reaffirms the selection of the positive support part of these outflows (see Fig. 3.12) as a method to identify galactic winds. In agreement with the peak observed at $t \sim 2.9\,$Gyr in Fig. 3.12, the thermal and CR supports are much larger than unity, both reaching similar magnitudes. Nevertheless, large positive or negative thermal and CR pressure gradients do not always spatially coincide. We surmise that such offsets could be due to CR streaming, as on $\sim$ kpc scales it can be an important driver of CR transport and displace CRs with respect to the gas, while maintaining the CR pressure gradient (see Section 2.1.1).

The warm ionised phase of the gas is the dominant volume-filling phase of the outflow, and has a more spherical, isotropic morphology. This phase does not display strong alternating features from consecutive wind bubbles, but rather a smooth pressure gradient. This pressure support extends to large radii and is dominated by CR pressure. In fact, the warm ionised, warm neutral and cold phases exhibit the same support morphology, which suggests that they are all sourced by a common underlying CR pressurised halo that surrounds the galaxy. However, based on the mild CR pressure support of the warm ionised phase in Fig. 3.12, we claim that this

phase will probably rain down as a galactic fountain given its low average radial velocity (see top right panel of Fig. 3.10). The four bottom panels examine the warm neutral (left) and cold (right) outflows. Gas in these phases is distributed in small structures that resemble cooling filaments. Blue contours are included to indicate the limits of the hot outflow cones. These colder phases appear to also be moving perpendicularly to the disk, experiencing a uniform CR pressure gradient that dominates their gravitational acceleration. This indicates that these cold regions of gas are still efficiently accelerated by the surrounding hotter phase, and hence entrained in the wind. The radial distribution of these outflowing phases reveals that they decrease in fraction of volume occupied as a function of radial distance, thus allowing to better showcase their clumpy nature. These small outflowing gas structures do traverse the $0.2\,R_{\rm vir,DM}$ shell we employ to measure outflows (indicated by a dashed purple circle) in a timescale shorter than our snapshot time resolution, naturally resulting in the fluctuating behaviour of warm neutral and cold phases present in Figs. 3.10 and 3.12.

3.5 Conclusions

In this Chapter, we have performed a detailed study of the effects of CR feedback on a Milky Way-like galaxy using a suite of new zoom-in cosmological simulations. Our hydrodynamical simulation (HD) includes a model for a resolved ISM, with a (magneto-)thermo-turbulent (MTT) star formation prescription and a 'mechanical' SN feedback implementation of canonical strength. In our magneto-hydrodynamics simulation (MHD) we additionally followed the evolution of magnetic fields as they are amplified from a primordial seed of 3×10^{-12} G. Our cosmic ray MHD simulation (CRMHD) further accounted for CRs injected by supernova (SN) explosions. Our main results can be summarised as follows.

1. Including CRs significantly reduces the resulting stellar mass of the galaxy compared to the no-CR models, yielding good agreement with abundance matching models (e.g. Behroozi et al., 2013; Moster et al., 2013) without the need to boost SN energy deposition or to use calibrated galactic winds. This reduction in stellar mass is significant as it reaches approximately an order of magnitude at high redshift ($z \gtrsim 3$) before tapering to a factor ~ 4 at $z \sim 1.5$ (Section 3.2 and Fig. 3.3).

2. CR pressure gradients support cold, low density gas against collapse, making the warm phase significantly more dominant in the ISM (Section 3.3). CR also deplete an important fraction of the mass locked in the cold, dense phase (i.e. $\rho \gtrsim 10^{-21}\,\mathrm{g\,cm^{-3}}$ and $T < 10^{3}\,\mathrm{K}$) present in non-CR simulations, and hence significantly decrease the amount of gas efficiently forming stars. In fact, galactic gas is rarely found below $10^{-27}\,\mathrm{g\,cm^{-3}}$ and the ISM has a smoother gas distribution within the disk.

3. As a consequence of the thermodynamical changes to the structure of the ISM and a CR-aided expansion of SN bubbles (e.g. Rodríguez Montero et al., 2022), the environment where SN events take place changes. In the CRMHD simulation, SN explosion sites exhibit a bi-modal distribution which both peaks at and reaches considerably lower densities than in the HD and MHD runs (see Fig. 3.6). This reduces the amount of SN energy lost due to cooling, increases the efficiency of this feedback mechanism and drives stronger outflows.

4. The mass outflow rates in the CRMHD simulation are significantly larger than those in the no-CR runs at all cosmic times, and yield a much higher mass loading factor η especially at high redshift. In contrast to the simulations without CR where the dominant phase of outflowing gas mass is hot (i.e. $T > 10^{5}\,\mathrm{K}$), CRMHD outflows are dominated by the warm ionised phase (i.e. $9000 < T < 10^{5}\,\mathrm{K}$) and can even have a significant contribution from the cold phase (see Section 3.4.2 and 3.4.3). Furthermore, hot outflows are biconical in structure whereas the colder phases embedded in the hot outflow are filamentary and clumpy. This is a direct prediction for upcoming JWST observations of multi-phase galactic outflows expected soon.

5. Outflows in the CRMHD simulation experience further acceleration due to CR pressure gradients, with a secondary contribution from the thermal pressure. Outflows in the warm and cold phases show a significant support from CRs, while their thermal pressure support remains negligible. Therefore, these outflows experience further acceleration within the CGM of our simulated galaxy (see Section 3.4.4 and Fig. 3.13).

4

Cosmic ray-dominated halos in Milky Way analogues

Contents

4.1 A step further – The circum-galactic medium of NUT across cosmic time 71
4.2 Falling but not free - the influence of cosmic rays on accretion 77
4.3 Gas cooling and heating in the circum-galactic medium 95
4.4 Conclusions 111

4.1 A step further – The circum-galactic medium of NUT across cosmic time

During the preliminary analysis of the vanilla NUT suite of simulations, edge-on projections of the simulation at $z = 1.5$ (see Fig. 3.1) hinted at substantial differences in the thermodynamical properties of the gas halo surrounding NUT. We further quantify this claim by looking at the cosmic evolution of volume-weighted average values of different quantities within the CGM. Unless otherwise specified, we define the CGM as the region within $0.2\,R_{\rm vir,DM}$ and $R_{\rm vir,DM}$ surrounding the galactic region of NUT. In the top panel of Fig. 4.1 we compare the evolution of the gas density for HD (blue line), MHD (purple line), and CRMHD (green line) with the mean baryonic density of a virialised halo (Bryan and Norman, 1998):

$$\rho_{\rm b,vir}(z) = \Delta_{\rm vir} f_{\rm b} \Omega_m(z) \frac{3H^2(z)}{8\pi G}, \tag{4.1}$$

where $\Delta_{\rm vir} \simeq 18\pi^2 + 32(\Omega_{\rm m} - 1) - 39(\Omega_{\rm m} - 1)^2$, $f_{\rm b}$ is the ordinary matter to total matter fraction, and $\Omega_{\rm m}(z)$ and $H(z)$ are the cosmological matter and Hubble parameters at redshift z. Although this approximation can effectively capture the density evolution

of individual cold filaments accreted into the galaxy (e.g. Kimm et al., 2015), our average values for the three simulations indicate that the volume-filling phase of the CGM has an overall density of $\sim 3-4\times$ lower. It is worth noting that the dispersion of these averages (given by the second and fourth quartiles spanned by the shaded region) are consistently higher at early times, reducing to ~ 0.5 dex at later times. This makes sense because dense filaments and diffuse outflows contribute more to the total volume of the CGM at earlier times, giving rise to a volume-weighted average with larger density contrasts. Compared to HD and MHD, CRMHD presents a higher ($\sim 4-5\times$) average gas density up to $z \sim 2.5$, after which the difference is clearly reduced. This period coincides with the accelerated mass growth of CRMHD observed in Section 3.2. As already suggested by the temperature projections in Fig. 3.1, the gas temperature profile for the CRMHD simulation (middle panel of Fig. 4.1) is lower than the gas temperature for the HD and MHD runs, although, in this case, the difference does not disappear at lower redshift. Within the period of accretion dominated growth ($z \leq 4$) the volume-weighted gas temperature appears to highly fluctuate for HD and CRMHD between $\sim 10^4$ K (close to the temperature of photo-ionisation equilibrium, i.e. PIE, with the UV background) to $\sim 10^5$ K (hot SN gas). These temperatures are compared to the virial temperature (Eq. 1.1, dashed lines) of a truncated isothermal sphere. Although the virial temperature is a useful quantity that we will use in the present section, realistic galaxy halos are not isothermal spheres, which means that they instead have non-constant temperature profiles. Furthermore, this derivation ignores any gas cooling, which is directly related to the gas accretion mode (Birnboim and Dekel, 2003). Given that the virial temperature depends on the specific halo studied, different dashed lines are given for each of the simulations explored in Fig. 4.1. At high redshift, large temperature variations due to large volume-filling outflows allow for all three simulations to reach $T_{\rm vir}$, with the HD and MHD simulations closely following $T_{\rm vir}$ from $z \sim 3$ onwards. After $z \sim 5$, CRMHD presents an average temperature 1 dex below HD and MHD, slowly increasing to a volume-weighted average temperature around 10^5 K. In the bottom panel of Fig. 4.1 we also include the volume-weighted average gas-phase metallicity. Compared to MHD and CRMHD, the HD simulation has the least enriched CGM. We claim this difference arises from the overall larger outflow rates of MHD and CRMHD compared to HD (see Fig. 3.10). Along the

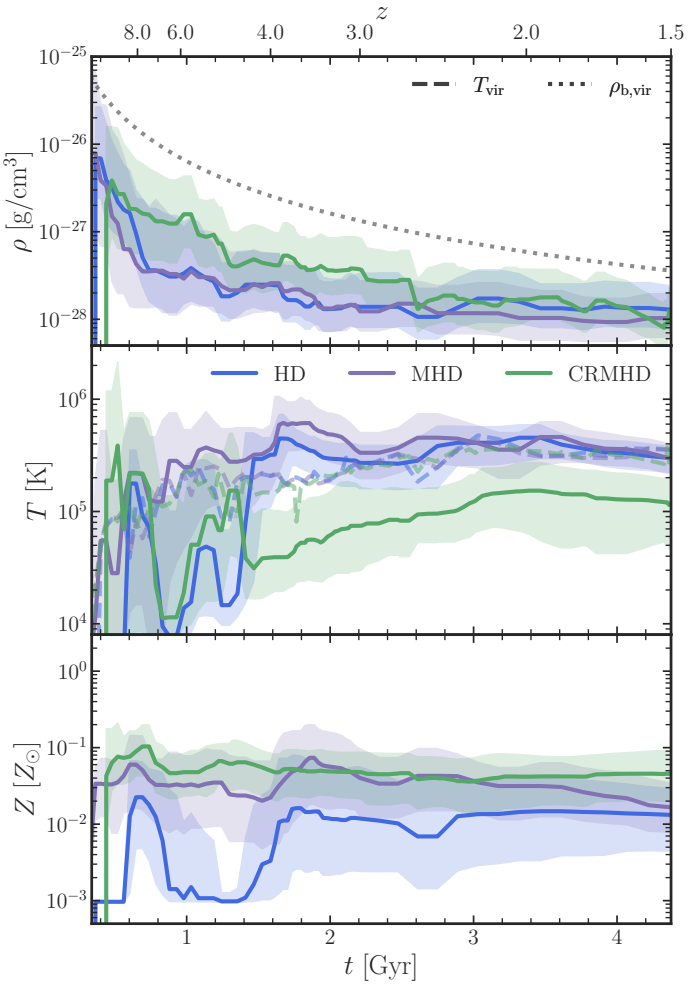


Figure 4.1: Time evolution of volume-weighted CGM ($0.2\,R_{\rm vir,DM} \leq r < R_{\rm vir,DM}$) properties in the HD (blue lines), MHD (purple lines) and CRMHD (green lines) simulations. Shaded regions indicate the second and fourth quartiles of the underlying distribution. **Top panel**: Gas density of the CGM compared to the average baryon density in the cosmology used for NUT (dotted grey curve). **Middle panel**: Gas temperature of the CGM compared to the theoretical temperature of the virial shock $T_{\rm vir}$ (dashed lines). **Bottom panel**: Gas-phase metallicity of the CGM.

same lines, the large outflow rates of CRMHD can partially explain this simulations' overall larger CGM gas metallicity compared to the other simulations. This simple analysis confirms many of our expectations based on the results of Chapter 3: CRMHD presents a denser, colder and more metal enriched CGM compared to HD and MHD. In this chapter we will explore the physical reasons behind these differences and the role that CRs play in the thermo-dynamics of halo gas and inflows.

We further probe the properties of the CGM by comparing spherical projections using the equal-area Mollweide projection. In Fig. 4.2 each cell is assigned a pixel[1] in

[1]Each cell may contribute to multiple pixels if its projected width is larger than the minimum pixel size.

the Mollweide based on their θ and ϕ using the HEALPIX algorithm (Gorski et al., 2005) implemented in OZYMANDIAS. We only consider the cells within the CGM shell (i.e. $0.2R_{\rm vir,DM} \leq r \leq R_{\rm vir,DM}$) and the final average value is volume-weighted. From top to bottom, we compare the gas density (left), gas temperature (middle) and radial flow rate (right) for HD, MHD and CRMHD. The benefits of these thick Mollweide projections is that outflows and inflows are clearly identified when comparing across the three gas quantities explored. For each simulation, the angular momentum is parallel to the central meridian, while we keep fixed the central radial vector to point along the $\hat{x}$-axis of the box. Given the common initial conditions for all three simulations, displacements of inflow filaments (seen as cold, high density inflow patches in the Mollweide) indicate different filamentary inflow patterns around NUT. NUT is primarily fed by two dense filaments and a third more diffuse filament at high redshift (Powell et al., 2011; Tillson et al., 2015). These can be visually identified as local maxima in the density Mollweide projections. As expected from the dominant large scale perturbation modes of the initial conditions, the three main filaments are positioned at very similar locations in the three simulations, with their plane on the sky closely aligned with the equator of the projections (and therefore with the galactic plane). Additionally, it is worth mentioning that the cosmological sheets in which filaments are embedded appear as lines in these projections, but become harder to see in the MHD and CRMHD simulations. In the case of the CRMHD simulation, these projections show that inflowing filaments have a lower density compared to HD and MHD, as well as a more disturbed morphology that has puffed up their radii and rendered them more diffuse. Furthermore, these inflows have now a temperature and density which resembles the volume-filling warm phase of the CGM.

In order to extend this CGM analysis further, in Fig. 4.3 we show volume-weighted median radial profiles of the CGM shell for HD, MHD and CRMHD. We compare three representative redshifts that will be the focus of study presented in this chapter: the $z = 6$ profiles show the high-redshift halo easily perturbed by volume-filling supernova feedback, $z = 3$ profiles correspond to the onset of disk formation, and the $z = 1.5$ profiles capture the secular evolution of the galaxy at low redshift. Consistent with the results of Fig. 4.1, the CGM of the CRMHD simulation is up to ~ 1 dex denser than HD and MHD at early times. Furthermore, the CRMHD shows the

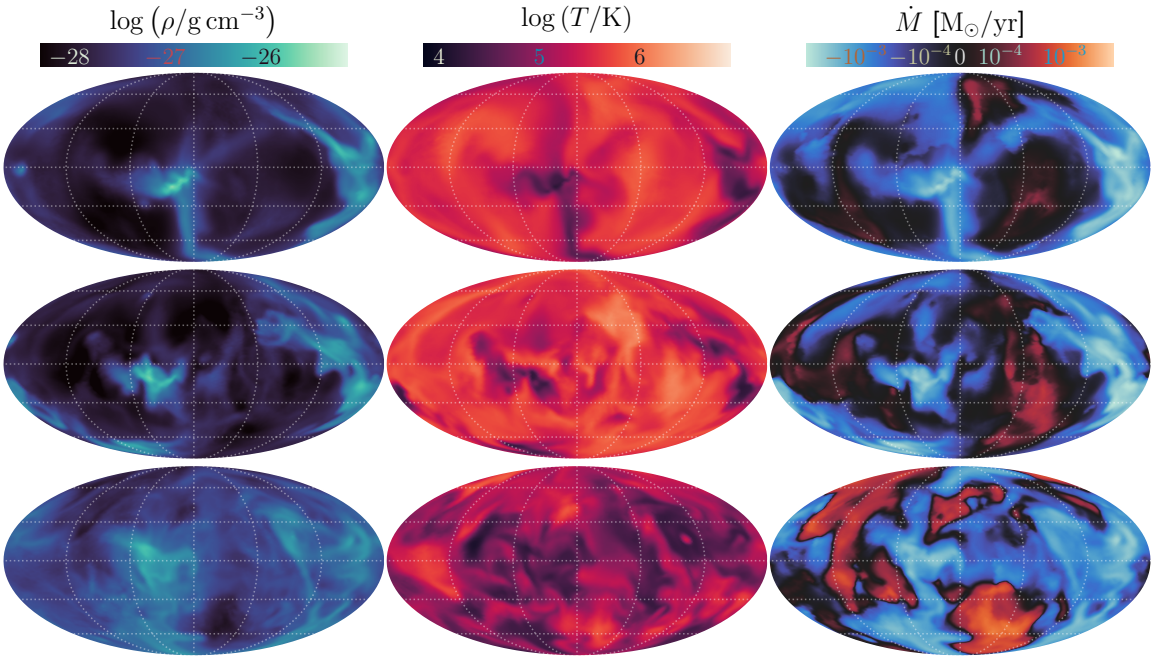


Figure 4.2: Mollweide projections of the spherical shell centred on NUT and extending from $0.2\,R_{\rm vir,DM}$ to $R_{\rm vir,DM}$, for HD (top row), MHD (middle row), and CRMHD (bottom row) at $z = 3$. From left to right, each column shows the volume-weighted averages of gas density, gas temperature, and gas radial outflow rate. The orientation of the sphere is such that the galactic plane is aligned with the equator. Compared to HD and MHD, the CGM of the CRMHD simulation is significantly more homogeneous, dominated by a diffuse, warm gas with an overall higher density and lower temperature. Inflowing filaments are easily identified in the HD and MHD projections as dense, cold, and inflowing gas close to the origin of the projection. In CRMHD these same regions appear to be more diffuse, with lower inflow rates and with densities and temperatures harder to distinguish from the volume-filling gas.

opposite temperature behaviour with radius to the HD and MHD runs, as the former increases with radius, while the temperature of the latter two runs decreases with radius. The HD and MHD simulations reach temperatures in the inner region close to $T_{\rm vir}$, while the temperature of the CGM in the CRMHD simulation reaches that of the galactic region at around $\sim 2 \times 10^4\,$K. A decreasing density and temperature profile with radius is a clear signature of gas attempting to reach thermal hydrostatic balance against gravity (e.g. Fielding et al., 2017; Esmerian et al., 2021), suggesting that if the gas within the inner regions of the CGM ($\sim 0.2 - 0.4 R_{\rm vir,DM}$) is supported against gravitational collapse, thermal pressure gradients alone may not be able to achieve it. These temperature profiles are in agreement with the properties of the CGM in the CRMHD simulations of the cosmological FIRE-2 simulations (Ji et al., 2020), although we find that the influence on the density profile remains significantly less clear in their simulations than ours.

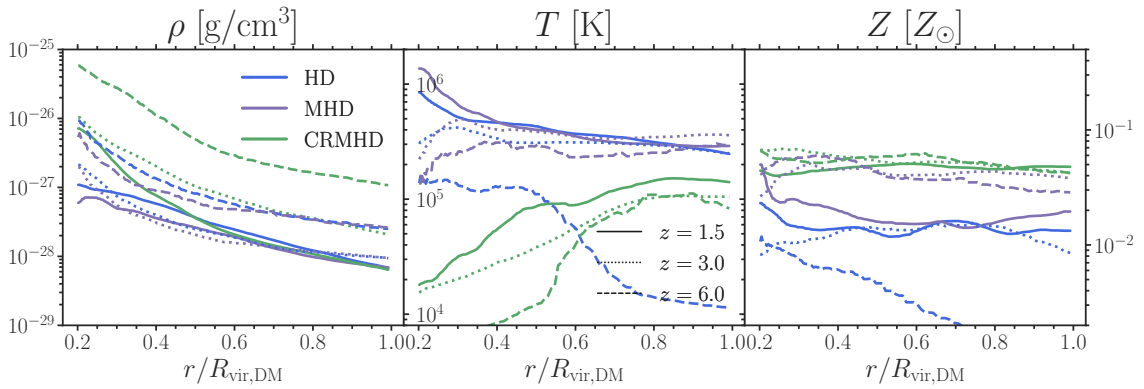


Figure 4.3: Volume-weighted median radial profiles of the CGM region for HD (blue), MHD (purple) and CRMHD (green) at three representative redshifts: $z = 6$ (dashed lines), $z = 3$ (dotted lines) and $z = 1.5$ (solid lines). At early times, volume-filling, early SN feedback easily increases the temperature and metallicity of the CGM in the three runs. With increased cosmological accretion providing pristine gas at later times, the metallicity of the HD and MHD simulations decreases, settling into a shallow radial gradient at $z = 1.5$. The CRMHD shows a much denser CGM at early times, with a temperature profile increasing with increasing radius and an almost flat metallicity profile sitting at $\sim 4\%$ solar at all cosmic times.

These profiles also reveal the extent to which the efficient, high-redshift feedback driven by CRs explored in Chapter 3 can alter the large scale properties of gas around NUT. The rightmost panel in Figure 4.3 shows the gas metallicity at the three cosmic times explored, showing decreasing metal content with radius for HD and MHD, with the MHD having a shallower slope easily explained by the larger hot gas outflow velocity between $z \sim 8$ and $z \sim 6$ compared to HD. As these profiles do not use cuts in density or radial velocity, they present the combined effect of inflows, outflows and galactic fountains. Therefore, the mixing of these processes becomes more efficient as time goes on (assuming cosmological accretion is approximately balanced by outflow rates), resulting in very shallow metallicity profiles at late times (see solid lines for $z \sim 1.5$). It is interesting to note the while HD and MHD metallicity profiles clearly evolve with cosmic time, the CRMHD simulation presents a consistently flat and high metal content across the three redshift ranges considered. This is a signature of the larger contribution of cold and warm neutral gas (generally more metal enriched, see e.g. Fig. 3.1) in the outflows of the CRMHD simulation (see Section 3.4.3), capable of enriching the halo at much larger distances from very early times. We argue that this higher metallicity and density of the gas from early on in the evolution of NUT's CGM may have a large influence on the cooling of gas, and hence on its thermal instability and the thermodynamic properties of inflows. In the following sections we

will quantitatively measure the physical processes giving rise to these global differences, exploring the influence of CRs on the galaxy-halo connection.

4.2 Falling but not free - the influence of cosmic rays on accretion

4.2.1 Inflow properties at the boundary of the galactic region

Within a cosmological context, galaxies may grow their stellar mass either by converting inflowing gas into stars or by merging with companion galaxies. NUT is the gravitationally dominant system within the zoom region that we explore, and its mass growth is dominated by cosmological gas accretion (Powell et al., 2011; Tillson et al., 2015)[2]. Therefore, quantifying the influence of magnetic fields and CRs in inflows is key to our understanding of their feedback on galaxy formation and evolution. In Figure 4.4 we begin by measuring the properties of inflowing gas ($v_r < 0$) entering $0.2\,R_{\rm vir,DM}$ for the three simulations in our suite. Similar to our analysis of outflows in Chapter 3, we measure inflow properties within a shell of $0.02R_{\rm vir,DM}$, which is an appropriate choice given our spatial and temporal resolution. The evolution of the accretion rate for HD and MHD can be summarised in 4 phases: (1) an increase to a maximum level at $z \sim 6-5$, (2) a plateau at $\sim 7-10{\rm M}_\odot/{\rm yr}$, until (3) a period of larger inflow rates (concurrently with a multiple merger), finally followed by (4) a slow decrease all the way to $z = 1.5$. The overall behaviour of the CRMHD run resembles that of HD and MHD, but with significant differences in the instantaneous $\dot{M}_{\rm inflow}$. Down to $z \sim 3.5$, CRMHD shows a consistently lower inflow rate by a factor of 2-3, while during the merger-induced increase of inflow rates at $z = 3-2.2$ the CRMHD simulation exceeds by up to a factor of 4 the plateau seen for HD and MHD, remaining above the latter for the rest of the cosmic time we study. This period of larger inflow rate in the CRMHD simulation corresponds to the accelerated growth of stellar mass found at later times in Fig. 3.2. If we examine how these differences are reflected in the $\dot{M}$-weighted median radial velocity v_r (bottom panel

[2]Although this claim has not been checked for the CRMHD simulation, we find that CR feedback affects the whole galaxy population within the simulated volume (note the difference in stellar surface mass density between simulations in Fig. 4.7a), giving rise to satellites with (on average) lower stellar mass than those in the HD simulations of Powell et al. (2011). We leave the study of CR feedback on NUT's satellites for future work.

of Fig. 4.4), the time evolution of HD and MHD shows a similar behaviour as the inflow rate curves, increasing with the free-fall velocity at $0.2\,R_{\rm vir,DM}$ until $z \sim 3$ and decreasing with redshift after the merger phase. It is interesting to note that down to $z \sim 5$, the MHD simulation presents a slightly lower inflow velocity compared to HD. Although the topic of the influence of magnetic fields on filamentary accretion remains unexplored in cosmological magneto-hydrodynamical simulations, it has been argued that magnetic braking could reduce galactic rotation (Sparke, 1982; Beck, 2016). In fact, in Martin-Alvarez et al. (2020) it was shown that, for the NUT system with primordial magnetic fields $B_0 \geq 10^{-12}$ G, the angular momentum accreted is reduced by means of a magnetic pressure dominated Lorentz force, resulting in more compact galaxies with lower spin parameter λ. CRMHD also shows the feature at $z \sim 2.5$ identified in the $\dot{M}_{\rm inflow}$ panel, but instead the weighted median v_r remains smaller at all cosmic times compared to HD and MHD. We find that while HD and MHD quickly reach the free-fall velocity of $\sim 125\,$km/s at $z \sim 10$, the CRMHD inflow is consistently slowed down, reaching a maximum of $100\,$km/s at $z \sim 7$ and falling to $\sim 75\,$km/s. We find that this drop in velocity in CRMHD at $z \sim 6$ corresponds to the inflow gas temperature (middle panel) increasing just above 10^4 K, remaining practically flat all the way to $z = 1.5$. It appears that this transition occurs later for HD ($z \sim 4$) and for MHD ($z \sim 3.5$), with the median temperature further increasing at later times reaching temperatures on the order of $T_{\rm vir}$ at $z \lesssim 2.5$. This indicates that, from the point of view of the dominant inflow flux, CRMHD is dominated by cool-warm gas across all cosmic time, while the HD and MHD simulations transition to hot gas dominating the median temperature.

To further quantify the properties of inflows at $0.2\,R_{\rm vir,DM}$, in Fig. 4.5 we present the fractional contribution of different gas phases (as defined in Section 3.4.2) for HD (top panel), MHD (middle panel), and CRMHD (bottom panel). The cold phase appears to be a largely minimal contributor to the inflow rate for all simulations and across all cosmic time, although some contribution ($\sim 5 - 10\%$) is seen in CRMHD up to $z \sim 5$, coinciding with the increase in median temperature seen in Fig 4.4. This change in the median inflow temperature appears to coincide with a rapid change in the dominant inflow phase for CRMHD. Before $z \sim 5$, inflows are dominated by the warm neutral gas (i.e. right below 10^4 K), but right after, the warm ionised phase

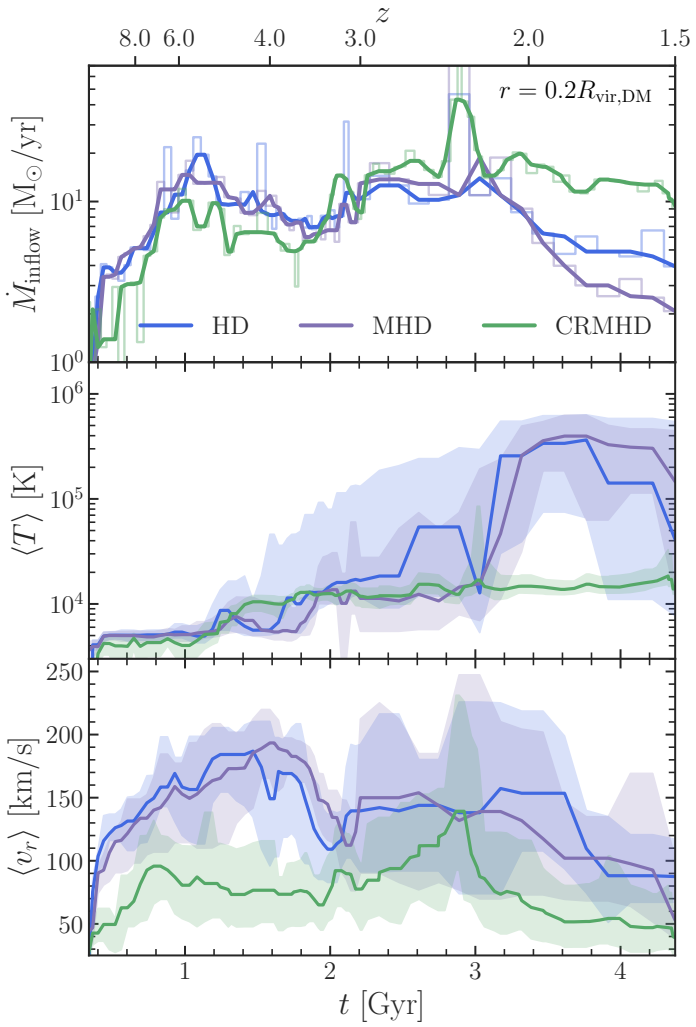


Figure 4.4: Properties of inflows reaching the galactic region ($0.2\,R_{\mathrm{vir,DM}}$) across cosmic time for HD (blue lines), MHD (purple lines), and CRMHD (green lines). Median quantities are $\dot{M}$-weighted and the shaded regions show the upper and lower quartiles of the underlying weighted distribution. **Top panel**: Gas inflow rate, showing HD and MHD following a similar evolution down to low redshift, when MHD shows a smaller inflow rate. The accretion in CRMHD shows a consistently lower rate down to $z \sim 3.5$, after which it exceeds the decreasing rate observed in the HD and MHD simulations. **Middle panel**: Median gas temperature of the inflow. With a UV background instantaneously turned on at $z = 9$ the gas is accreted close to the equilibrium temperature with the UV background, but interaction with already accreted gas (and/or outflows) after $z \sim 6$ causes the gas temperature to rise with redshift for HD and MHD, while for CRMHD it remains close to the PIE. **Bottom panel**: Median radial velocity of the inflow. Down to $z \sim 4$, the radial velocity increases with the growth of the halo mass, as inflows are falling close to the free-fall velocity. After this point, the median velocity slowly decreases from a maximum median of $\sim 150\,\mathrm{km/s}$. CRMHD presents a consistently lower infall velocity ($\sim 80\,\mathrm{km/s}$) compared to HD and MHD, until a rise close to $z \sim 2.5$ with a consequent decrease at low redshift.

quickly dominates the inflowing gas. This is not a surprising result, as what we are measuring is how the dominant gas at super-halo scales comes to equilibrium with the UV background. The fundamentally interesting result from this figure arises from comparing these phase fractions to HD and MHD. While the CRMHD run reaches a $\sim 75\%$ warm ionised composition in $\lesssim 300$ Myr, the HD and MHD runs show a more gradual increase extending over a ~ 2 Gyr period. This large difference in heating timescale could be due to cool filaments experiencing a larger heating from the UV background in the CRMHD simulation compared to HD and MHD. Fig. 4.2 showed that inflowing filaments appeared to be composed of a more diffuse (with a larger equivalent cross section) and less dense structure in the CRMHD simulation. This suggests that, in the presence of a spatially uniform UV background implemented with a $n_{\rm H}$ scaling for self-shielding, lower density filaments induced by CRs will experience an earlier influence of reionisation. Additionally, we remind that the UV ionisation rate is independent of density, while the recombination rate scales with the latter. These two effects render filaments ionised in the CRMHD earlier than in HD and MHD. We will explore how this affects star formation in dwarf systems embedded in the filaments of NUT in future work (e.g. Katz et al., 2020). Both HD and MHD show a hot phase increasing linearly with time until $z \sim 2.5$, when they both present a faster growth of the hot phase fraction, reaching $\sim 65\%$. Contrary to this behaviour, CRMHD appears to be fully dominated by the warm ionised gas at all later times. Therefore, although CRs allow for inflowing gas to be heated to the PIE temperature faster than in the HD and MHD runs, the runs without CR feedback (HD and MHD) are incapable of preventing the hot gas phase from taking over the inflow rate budget at low redshift.

4.2.2 Gas inflow from super-halo scales to the galactic region

A careful examination of the filamentary accretion onto NUT (i.e. not just via the spherical isotropic accretion) is essential to further understand the role of CRs on the halo scales. In Section 1.1.2 we introduced the concepts of 'cold mode' and 'hot mode' accretion, which are intimately related to the thermal state of inflowing gas as it reaches the inner regions of the halo: in the former radiative cooling is sufficiently fast to prevent the efficient conversion of gravitational potential energy into internal energy, while in the latter the accreting gas forms a shock at $\sim R_{\rm vir,DM}$

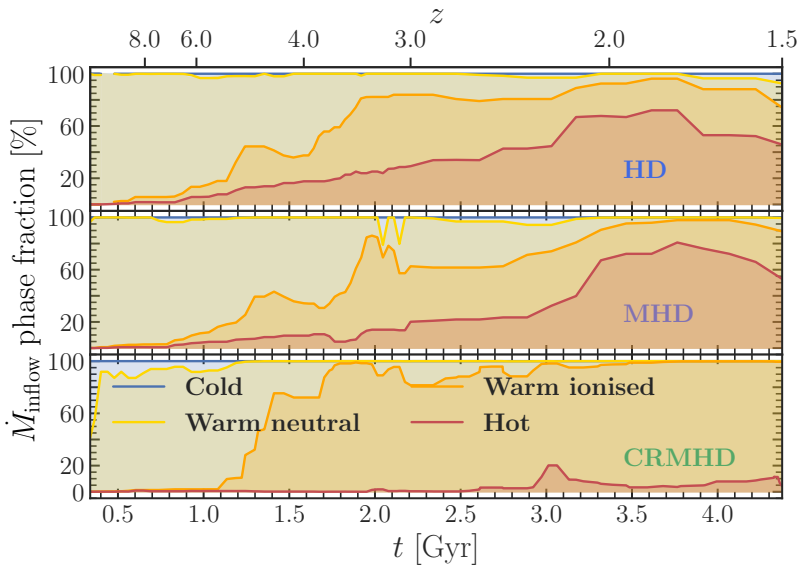


Figure 4.5: Fractional contribution of different gas phases to the inflow rate at $0.2\,R_{\rm vir,DM}$, for HD (top panel), MHD (middle panel), and CRMHD (bottom panel). Gas phases are defined in Section 3.4.2. Note the faster establishment of warm ionised gas as the dominant inflow phase at $z \sim 5$ in CRMHD, compared to the slow, but steady, increase of the hot gas fraction in HD and MHD.

(e.g. Rees and Ostriker, 1977; Silk, 1977; White et al., 1978). This simplified picture of cosmological accretion has been challenged over the last two decades by analytical and numerical experiments (e.g. Birnboim and Dekel, 2003; Kereš et al., 2005a; Dekel and Birnboim, 2006; Birnboim et al., 2007; Ocvirk et al., 2008; Danovich et al., 2012) which suggest that, at $z \gtrsim 2$, gas is accreted via thin, cold ($T \sim 10^4$ K) streams that are capable of penetrating the shocked atmosphere of the halo and directly feeding the growing galaxy (Woods et al., 2014; Stewart et al., 2017). A recurring question raised about this scenario is the physical mechanisms that could affect the stability of a cold stream flowing through the disturbed medium of a hot halo (e.g. Kelvin-Helmholtz instability, Mandelker et al., 2016; Mandelker et al., 2019a), particularly in the presence of large energy injection by stellar and AGN feedback (e.g. Rosdahl and Blaizot, 2011; Stewart et al., 2017; Ramsøy et al., 2021; Katz et al., 2020; Elias et al., 2020; Lu et al., 2024). Ramsøy et al. (2021) extracted the network of filaments in the NUT zoom region using DISPERSE (Sousbie, 2011), finding that, for a similar Type II SN feedback implementation as the one used in this work, feedback has a secondary effect on the radial properties of filaments, only accounting for a $\sim 20 - 30\%$ decrease in the central density of filaments.

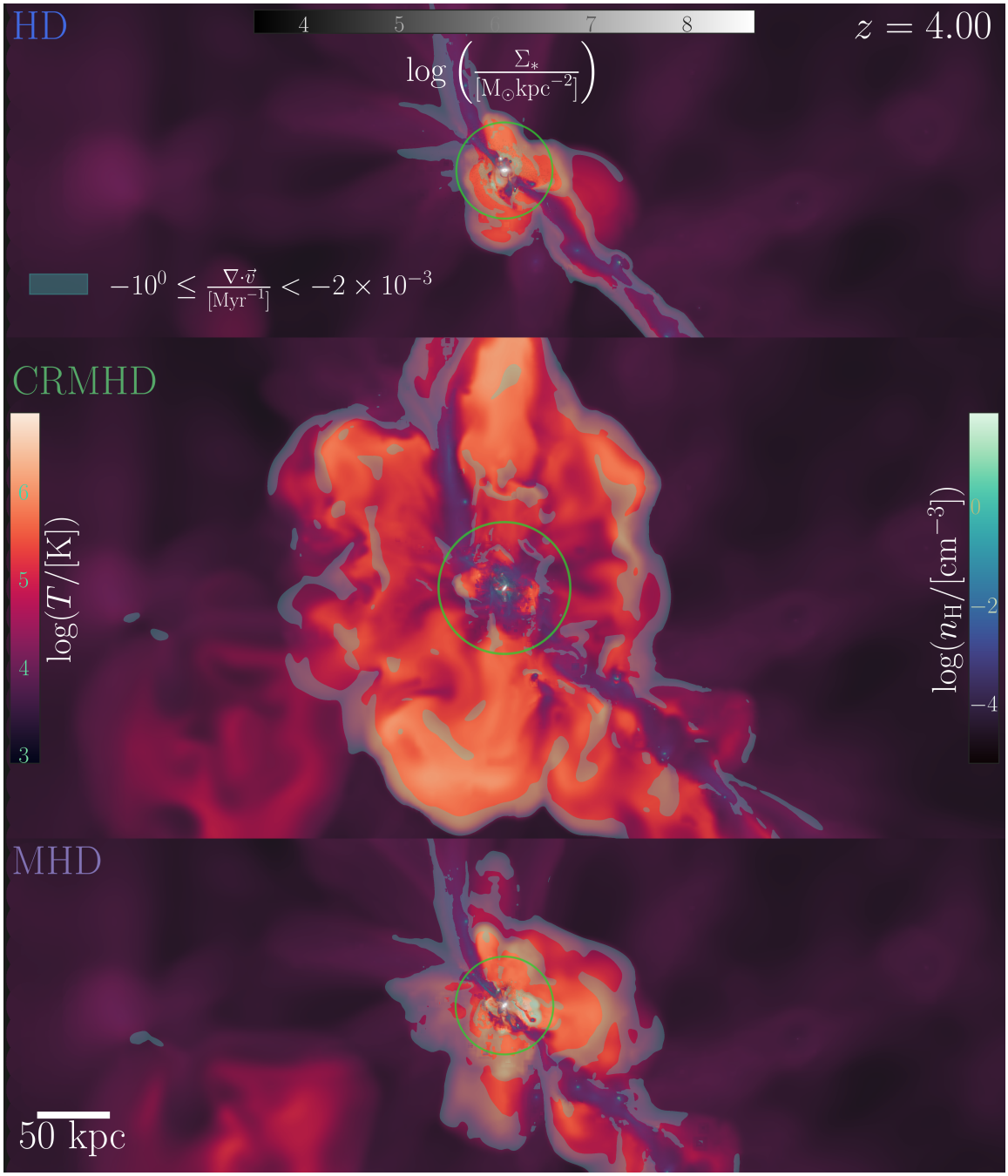
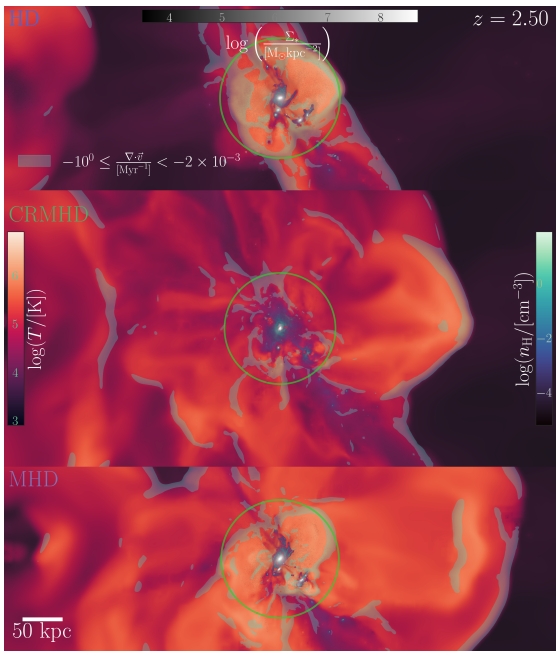
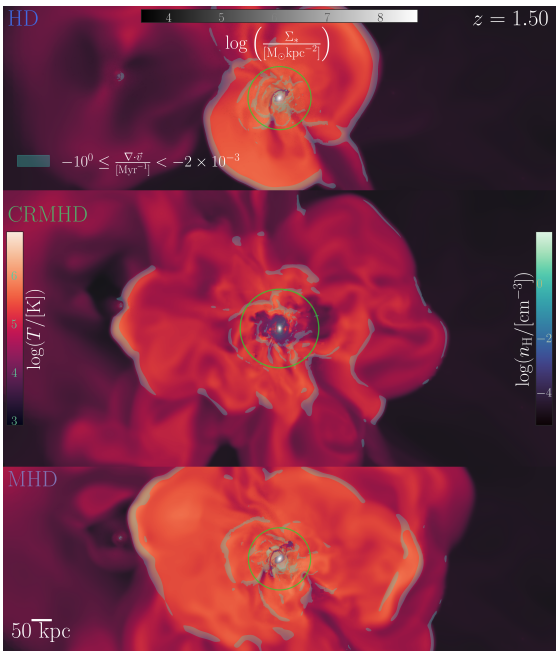


Figure 4.6: Large scale density-weighted slice of the HD (top panel), CRMHD (middle panel), and MHD (bottom panel) simulations at $z = 4$. We use a horizontal scale of 700 kpc and a depth of 34 kpc for all simulations ($\sim R_{\mathrm{vir,DM}}$ for all simulations at this redshift). The different colourmaps represent the gas temperature (red map), Hydrogen number density (blue map), and stellar surface mass density (white map). The lime coloured circles indicate the current $R_{\mathrm{vir,DM}}$, while the cyan shadings show the regions where fast inflowing gas compression is taking place (i.e. $-10 \leq \vec{\nabla} \cdot \vec{v} < 2 \times 10^{-3}$ Myr^{-1}). All projections are taken from the same direction, showing the two main filaments forming a diagonal from top-left to bottom-right. Note the presence of a compression shock at $\sim R_{\mathrm{vir,DM}}$ in HD and MHD, but its almost complete disruption in CRMHD.



(a) Same as Fig. 4.6 but at $z = 2.5$. We use a horizontal scale of 700 kpc and a depth of 70 kpc for all simulations ($\sim R_{\mathrm{vir,DM}}$ for all simulations at this redshift).



(b) Same as Fig. 4.6 but at $z = 1.5$. We use a horizontal scale of 800 kpc and a depth of 100 kpc for all simulations ($\sim R_{\mathrm{vir,DM}}$ for all simulations at this redshift).

Figure 4.7: Large-scale projection of the gas properties around the NUT galaxy.

In Fig. 4.6 we show large-scale density-weighted projections centred on NUT at $z = 4$. Similar to Ramsøy et al. (2021) and previous works (e.g. Mandelker et al., 2019b; Lu et al., 2024), the HD simulation (top panel) has two main morphological components: (1) a hot super-bubble[3] surrounding the galaxy at approximately the virial radius (green circle), and (2) thin, cold filaments, extending beyond the limits of the projection. For clarity, we have included cyan shadings that indicate regions in which gas is being quickly compressed (i.e. $-10 \leq \vec{\nabla}\cdot\vec{v} < 2\times10^{-3}$ Myr^{-1}). These shadings clearly show that gas accreting onto filaments results in compression and a rise in temperature (Ocvirk et al., 2008; Ramsøy et al., 2021), as well as showing that the boundary of the super-bubble is related to strong shock compression. We observe the same trend as Dekel et al. (2009b) in which filaments have a similar radius as the halo outside of it, but the surviving cold stream becomes much thinner as it enters the virialised halo. This is modelled with an isothermal cylinder approximation for filaments (Ostriker, 1964), in which the filament's high density core (with a radius $\sim 3-4\times$ smaller than full filament radius) survives the entrance into the hot

[3]We do not denote this as an archetypal 'virial shock' at this point and present a more cautious term to describe it later in this Chapter (see Section 4.3.2).

atmosphere of the super-bubble. The filament has a truncation radius $\sim 3-4\times$ larger than the high density core (Ramsøy et al., 2021). The MHD simulation (bottom panel) shows similar properties to HD, but with the expected signatures of a burstier feedback (see Section 3.4.2). In both simulations feedback is clearly confined to $\sim 1-2R_{\rm vir,DM}$, with the CRMHD simulation (middle panel) showing large-scale outflows pushing the quasi-spherical boundaries of the spherical accretion region (e.g. see the outflows moving towards the top and the bottom of the projection). In fact, we find that any signatures of a similar super-bubble to the one observed in HD (or partially observed in MHD) is completely eradicated from the CRMHD simulation. Filaments are still seen in similar locations, but they appear to be embedded in the hot gas from the large-scale outflows. Furthermore, instead of the filament narrowing as it enters the virialised halo, we find that the high density, cold gas is highly twisted and disturbed, to the point that it is not distinguishable from the dense gas around NUT observed in Fig. 3.1.

Fig. 4.7a and 4.7b are similar projections to Fig. 4.6 computed instead at $z = 2.5$ and $z = 1.5$, providing us with a qualitative view of the evolution of the large scale gas properties around NUT across its cosmic evolution. These projections indicate that the absence of a shock at $R_{\rm vir,DM}$ in CRMHD at $z = 4$ extends to later times. However, it also points to the difficulty of clearly identifying a shock in all simulations, as feedback events can have a large influence on its topology. We will return to these projections from a more quantitative perspective in upcoming sections.

In order to further explore the (mass) median properties of inflows, in Fig. 4.8 we include radial profiles of inflowing gas extending from $0.2\,R_{\rm vir,DM}$ to twice $R_{\rm vir,DM}$. In this case we have extended the profiles to a much larger radial distance than our definition of the CGM region, such that transition in inflow properties from super-halo scales (i.e. $r \geq R_{\rm vir,DM}$) to the CGM can be quantitatively distinguished. The density profiles (left panel) show an exponential decay of inflow density with radius, as would be expected for the compression towards hydrostatic equilibrium of a Lagrangian patch of gas as it travels from the IGM to the limit of the galactic region (e.g. Kereš et al., 2005b; Kereš et al., 2009; Dekel et al., 2009b). There is a clear evolution with redshift of the gas density on the large scales of the halo, as the average gas density of inflows is comparable to mean baryonic density of a virialised halo (Eq. 4.1). The CRMHD simulation presents significant deviations from HD and MHD as the inflows approach

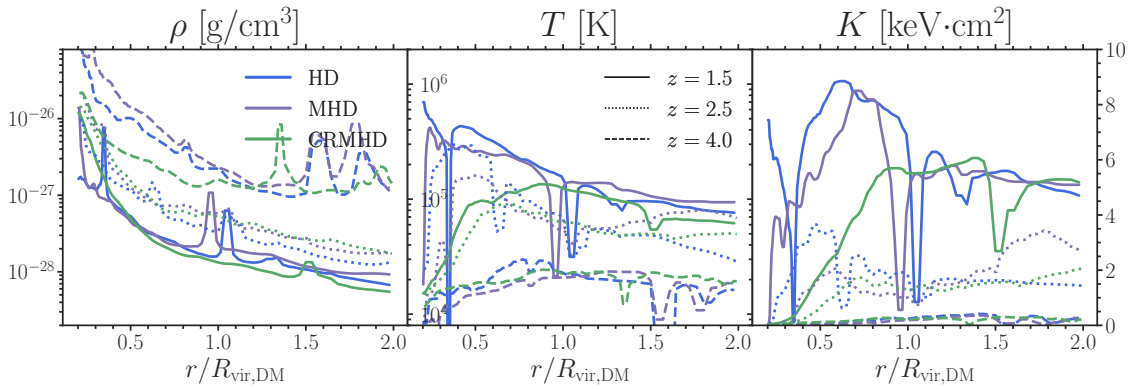


Figure 4.8: Mass-weighted median radial profiles of inflowing gas from $0.2\,R_{\rm vir,DM}$ all the way to $2R_{\rm vir,DM}$ comparing HD (blue lines), MHD (purple lines), and CRMHD (green lines) at the redshifts of $z = 4.0$ (dashed lines), $z = 2.5$ (dotted lines), and $z = 1.5$ (solid lines). From left to right, we show gas density, gas temperature, and *pseudo*-entropy K. Until the end of the simulation, inflows in the CRMHD simulation show gas density up to ~ 1 dex above HD, reaching an even steeper profile at $z = 1.5$. Combined with an average lower gas temperature and with a positive correlation with radius (compared to the decreasing profiles with radius in HD and MHD), the profiles of K in the CRMHD simulation are consistently lower than HD and MHD.

$0.2\,R_{\rm vir,DM}$, with the behaviour shifting from having a lower density at high redshift (i.e. $z = 4$) to a higher density at lower redshift (i.e. $z = 1.5$). Naively, we would expect that if this diffuse gas in PIE needs to increase its density by ~ 2 orders of magnitude along this infalling trajectory, it may have experienced a series of shocks, causing the compressional heating of the gas to high temperatures. This series of shocks could slow down the inflow (e.g. Kereš et al., 2005a) as it reaches $0.2\,R_{\rm vir,DM}$, agreeing with the slower infalling velocity observed in Fig. 4.4. However, when we focus on the radial profiles of gas temperature (middle panel of Fig. 4.8), we find that while the HD and MHD simulations do indeed present such an increase in gas temperature at later times, the CRMHD simulation departs from this behaviour at $z = 2.5$ and $z = 1.5$, showing instead a drop in temperature down to PIE temperatures.

In the right panel of Fig. 4.8 we introduce a new thermodynamical quantity: *pseudo*-entropy K. We recall that specific (i.e. per unit mass) entropy s is defined as the entropy per unit mass. Since entropy is an exact differential, the change in entropy from an initial state $s_0(T_0, V_0)$ to a final state $s_f(T_f, V_f)$ does not depend on the path taken. Using the chain rule, we have:

$$\Delta s = \int_{s_0}^{s_f} \mathrm{d}s = \int_{T_0}^{T_f} \left(\frac{\partial s}{\partial T}\right)_V \mathrm{d}T + \int_{V_0}^{V_f} \left(\frac{\partial s}{\partial V}\right)_T \mathrm{d}V, \tag{4.2}$$

where the subscripts V and T indicate partial derivatives at constant volume and temperature, respectively. Taking into account the definitions of the heat capacity at constant volume $C_V = T(\partial S/\partial T)_V$ and the Maxwell relation $(\partial S/\partial V)_T = (\partial P/\partial T)_V$, we may integrate Eq. 4.2 to obtain:

$$\Delta s = c_V \ln\left(\frac{T_f}{T_0}\right) + N k_{\rm B} \ln\left(\frac{V_f}{V_0}\right) = \tag{4.3}$$

$$= c_V \left[\ln\left(\frac{T_f}{T_0}\right) - (\gamma_{\rm gas} - 1)\ln\left(\frac{\rho_f}{\rho_0}\right)\right], \tag{4.4}$$

where we have made use of the definition of the adiabatic index $\gamma_{\rm gas} = c_P/c_V$, the definition of heat capacity at constant pressure $C_V = T(\partial S/\partial T)_P$ and the definition of enthalpy $H = U + PV$. In Chapter 3 we have used this definition of specific entropy change to separate cold, warm and hot phases within the galactic region of NUT. To avoid determining an *ad hoc* value of the reference state s_0 as in Gent (2012), we instead use *pseudo*-entropy as is commonly done in studies of cluster gas entropy (e.g. Sijacki et al., 2007; Sharma et al., 2009; Babyk et al., 2018). Ignoring the exact value of s_0, we can re-write Eq. 4.3 as:

$$\frac{s}{c_v} = \ln\left(\frac{T}{\rho^{\gamma_{\rm gas}-1}}\right) + {\rm c}^{\rm st}. \tag{4.5}$$

$$\exp\left(s/c_v - {\rm c}^{\rm st}\right) = \frac{k_{\rm B}T}{(m_{\rm p}\mu_e)^{2/3} n_e^{2/3}} = \frac{K}{(m_{\rm p}\mu_e)^{2/3}}, \tag{4.6}$$

where we have used the definition of *pseudo*-entropy $K = k_{\rm B}T/n_e^{2/3}$, and the mean molecular weight per electron $\mu_e \simeq 1.136$ for a fully ionised gas of primordial composition. One of the fundamental predictions of semi-analytic models of galaxy formation is the formation of an accretion shock in a steady-state spherical flow within a galactic halo when the inflow velocity exceeds the local sound speed (see the seminal work by Birnboim and Dekel, 2003). This is traditionally referred to as the transition from 'cold-mode' to 'hot-mode' accretion (see the review by Somerville and Davé, 2015), which is expected around the critical halo scale of $\sim 6 \times 10^{11}$ M$_\odot$. One would expect that, as the halo mass of NUT only approaches $\sim 5 \times 10^{11}$ M$_\odot$ at $z \sim 0$, NUT accretes in the 'cold-mode' across the cosmic evolution explored in this work. However, in the presence of realistic feedback and a UV background, cosmological simulations have shown that a virial accretion shocks can form at halo masses below the critical mass (Fielding et al., 2017; Stern et al., 2020; Stern et al., 2021), which

raises the interesting question of whether NUT will form a virial shock, and if the presence of CR pressure will influence its evolution (Ji et al., 2021). Similar to other shock waves, the virial shock can be physically understood as a non-linearly steepened wave that has reached a stable balance between steepening and energy dissipation, and thus irreversibility. Since a mass shell that reaches the shock is abruptly compressed and slowed down, its bulk kinetic energy is rapidly and irreversibly converted into random kinetic energy (i.e. temperature) in the downstream flow, which equivalently implies an increase in entropy across the shock. The right panel of Fig. 4.8 also suggests that the gas accretion history of the halo can be followed by the amplitude of the K profiles, given that gas accreted at later times will be at a lower cosmic density and experience a higher jump in temperature ($T_{\rm vir} \propto M_{\rm vir}^{2/3}$, see Eq. 1.1). However, these profiles do not conform with the canonical identification of virial shocks that is used for low redshift galaxies (e.g. Aung et al., 2021; Ji et al., 2021), since a jump in *pseudo*-entropy is not observed around $r = R_{\rm vir,DM}$. We argue that spherically averaged profiles are a poor method to identify accretion shocks in realistic cosmological simulations and at high redshift (as is our case), given the non-sphericity of the shocks observed in Fig. 4.7a (particularly for MHD). Despite this fact, it is interesting to further examine these K profiles.

The HD and MHD profiles show a different behaviour, depending on the redshift range explored. At high redshift (e.g. $z = 4$) the entropy profiles are largely dominated by shock heating from SN feedback in the inner region of the halo (as would the expected from trapped outflows), and by the low entropy primordial gas. At lower redshift (i.e. $z = 1.5$), a linearly increasing K profile is established all the way to super-halo scales, but changes slope around the virial radius. Furthermore, note that the trends of the CRMHD run are fundamentally different to HD and MHD across the redshift ranges explored. The CRMHD simulation has increasing entropy profiles from very early on, suggesting that in its case high entropy outflows are capable of escaping the inner halo and reaching the super-halo scales. It is interesting to note that the profile to which CRMHD converges at $z = 1.5$ shows a plateau for gas outside of $R_{\rm vir,DM}$. This implies that inflowing gas from the IGM follows an isentropic thermodynamic path until it reaches $R_{\rm vir,DM}$ and the shock compression makes the

gas thermally unstable and cooling becomes faster (we will carefully examine the role of different timescales in the thermodynamic properties of inflows in Section 4.3).

So far, the thermodynamical properties of inflowing gas in the CRMHD simulation appear to show a fundamentally different flow dynamics compared to HD and MHD. In Fig. 4.9 we compare two dimensional mass histograms of the gas radial velocity with radius from high to low redshift, representative of the low and high inflow periods (see Fig. 4.4) of the CRMHD simulation. As inflowing mass is dominated by filaments, these are easily identified in these mass histograms as bright curves extending from super-halo scales all the way to the inner regions of the CGM. Their upward curvature is the signature of gravitational acceleration. In the absence of any deceleration process, these curves would be expected to follow a free-fall velocity path (e.g. Rosdahl and Blaizot, 2011) until they ballistically shock with the gas disk within $0.2\,R_{\rm vir,DM}$ (Agertz et al., 2011). The HD and MHD show gas infalling without interruption until $0.2\,R_{\rm vir,DM}$, supporting the claim previously extracted from Fig. 4.4 that streaming inflows in these simulations freely travel from the IGM to the galactic region. Careful examination of these filaments suggests that their mass probability (i.e. ratio of gas mass at a given radius r and radial velocity v_r over the total gas mass $M(v_r, r)/M_{\rm tot}$) suffers noticeable decreases at $\sim 0.5R_{\rm vir,DM}$ at $z = 4$ and closer to $R_{\rm vir,DM}$ at $z = 1.5$. This may be a signature of a virial shock establishing at lower redshifts and settling at $\sim R_{\rm vir,DM}$, although this decrease in mass probability is also present at $z \sim 6$ (see bottom row). We argue that this disruption of filament mass flow in the inner CGM may be both due to the thermal support of a virial shock as well as the thermal and ram pressure support of outflowing gas due to the strong feedback period at $z \sim 6$ seen in Fig. 3.7. If we now focus on the CRMHD simulation (rightmost panels), we find that, contrary to the well defined inflowing filaments in HD and MHD, the CRMHD simulation appears to show large disruption at much earlier times, with the gas now populating a broad range of velocities well below the expected free-fall velocity path. This confirms our previous suspicions that filaments are dramatically slowed down close to the halo of NUT in the CRMHD simulation, rendering cold filaments at high redshift incapable of reaching the galactic region with the free-fall velocity (see also middle panel in Fig. 4.6 for a qualitative confirmation of this effect). Furthermore, we find that this drastic slow

down of inflows is accumulating slowly moving gas between $0.2\,R_{\rm vir,DM}$ and $0.5R_{\rm vir,DM}$, matching the cool, diffuse gas reservoir around NUT at these cosmic times (see middle panel of Fig. 4.7a). We also bring attention to a larger maximum radial velocity in the CRMHD simulation at this redshift (comparable to HD and MHD), suggesting that the physical process/es causing the slow down of inflows at high redshift plays a less substantial role at lower redshift. This agrees with the time evolution of the instantaneous inflow rates for CRMHD in Fig. 4.4.

The large differences observed in gas temperature and gas velocity in the CGM and on super-halo scales also raise the question of the sonic properties of inflows in the three simulations of the vanilla suite. In Fig. 4.9 we have included volume-weighted median profiles of the gas sound speed c_s and the local gas turbulent velocity dispersion $\sigma_{\rm turb}$ as defined in Section 2.1.3. In this case, we opt for obtaining volume weighted profiles instead of mass weighted to show the sonic properties of mass-dominating inflows with respect to their surrounding halo environment. At both redshifts, the sound speed profiles of HD and MHD increase towards the galactic centre, as would be expected from the increasing gas temperature profile seen in Fig. 4.8. These profiles show that for the majority of the inflowing gas mass (dominated by the streaming inflows) the gas is supersonic when it reaches the galaxy (e.g. Powell et al., 2011). No significant trend is observed for the different simulations, besides a consistently larger $\sigma_{\rm turb}$ close to $0.2\,R_{\rm vir,DM}$ in MHD and CRMHD, which could easily be accounted for by the more effective feedback in these models. Our estimate of the velocity dispersion points to subsonic turbulence on these scales of the galaxy and at these redshifts. In the case of the CRMHD, $P_{\rm CR}$ has a dominant contribution in the inner regions of the halo, making necessary the comparison instead with the effective sound speed of the thermal-CR mixed fluid (e.g. Pfrommer et al., 2017; Dubois et al., 2019):

$$c_{\rm s,eff} = \sqrt{\frac{\gamma_{\rm gas} P_{\rm th} + \gamma_{\rm CR} P_{\rm CR}}{\rho}}. \tag{4.7}$$

The $c_{\rm s,eff}$ is plotted in the rightmost column of Fig. 4.9 (lime dashed lines), supporting the dominant role of CR-like adiabatic properties on the inner regions of the CGM, becoming more prevalent on the large scales of the halo at higher redshift. This means that the effective sound speed within $\sim 0.5R_{\rm vir,DM}$ is kept at $\sim$ 60 km/s to 80 km/s, making the dominant inflowing material at $0.2\,R_{\rm vir,DM}$ subsonic (recall

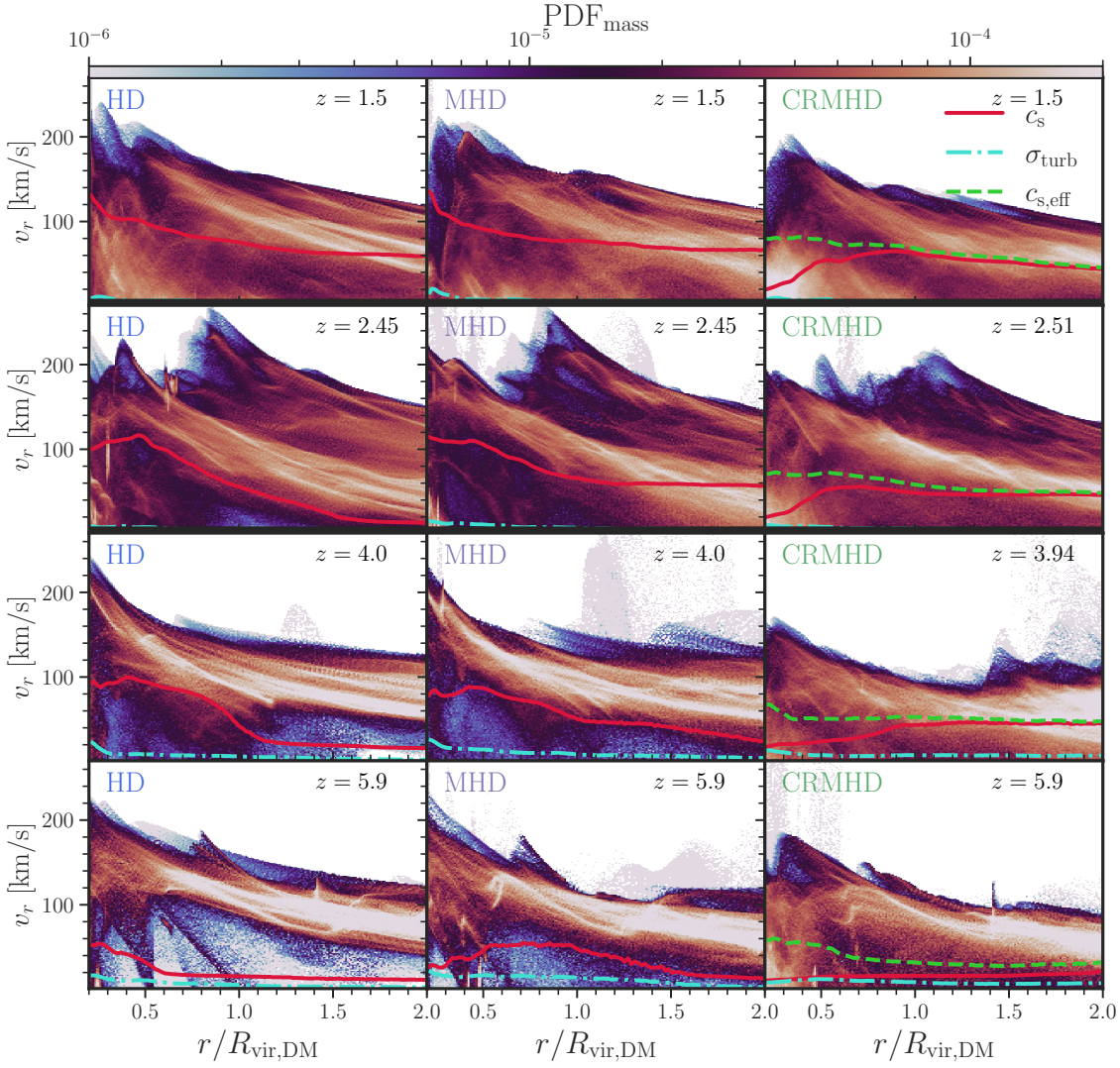


Figure 4.9: Mass weighted phase space diagram for gas within $0.2\,R_{\rm vir,DM}$ to $2R_{\rm vir,DM}$ at different redshifts for HD, MHD and CRMHD. Overplotted lines show the volume-weighted median sound speed (crimson lines), turbulent velocity dispersion (turquoise lines) as defined in Section 2.1.3, and, only for CRMHD, the effective sound speed (lime lines). Streaming filaments correspond to thick, high mass probability curves extending from high radii to $0.2\,R_{\rm vir,DM}$, increasing their speed as they are gravitationally accelerated. HD and MHD show filaments that are capable of reaching the galactic region in a free-fall, while the CRMHD simulation shows filaments becoming disturbed outside of $R_{\rm vir,DM}$, not capable of reaching the free fall velocity and instead populating a region of low v_r. This gas accumulates at later times ($z \sim 2$), contributing to the enhanced inflow rates in the CRMHD simulation during this period. Turbulence is subsonic in the CGM and beyond ($\sigma_{\rm turb} \sim 0.1 c_{\rm s}$), and filaments are supersonic in HD and MHD, while the increased $c_{\rm s,eff}$ in CRMHD in the inner halo makes slow inflowing gas subsonic.

the bottom panel of Fig. 4.4). We claim that this results in the disappearance of a strong shock of inflowing gas as it enters the $0.2\,R_{\rm vir,DM}$ and joins the rotating gas disk. It is interesting to note that, from the point of view of thermal sound speed $c_{\rm s}$, the turbulence in the CRMHD halo appears to have a larger contribution, becoming transonic close to $0.2\,R_{\rm vir,DM}$.

4.2.3 Gas support in the circum-galactic medium

So far, the quantitative analysis of NUT's CGM and the properties of inflowing gas has unveiled a dramatically different narrative for the galaxy-halo connection at high redshift in the presence of CR feedback. The overreaching influence of CR pressure across super-halo scales appears to slow gas infall towards the galactic region, while at the same time rendering cosmological streaming filaments more volume filling and cooler across all cosmic times. In previous works (e.g. Hopkins et al., 2021a; Ji et al., 2021), these changes to the CGM and to inflow properties have been explained by invoking CRs: similar to their role in outflows, the presence of large scale CR pressure gradients support gas against gravitational acceleration. However, similar to what was needed to justify this physical argument in the case of outflows, a quantitative exploration of CR support in the CGM needs to be done in a realistic cosmological simulation and across cosmic time. With this aim, we present in Fig. 4.10 radial histograms of the gas mass supported by different physical processes for the HD (left column), MHD (middle column), and CRMHD (right column) across 4 different redshifts. Similar to the analysis presented in Section 3.4.4, we explore different forms of pressure gradient support against gravitational acceleration on a purely local, per-cell basis. We have also included dynamical support $v_t^2/r \geq \nabla_r \phi$, where v_t is given by the tangential component of the gas velocity with respect to the centre of NUT (dashed black lines). We allow for rotational velocities larger than local circular velocity, as this gas, unless perturbed, will be displaced to larger radii orbits (i.e. with a larger specific angular momentum h) and hence will not fall towards the centre of the gravitational potential. Interestingly, a large fraction of gas within the CGM appears to have sufficiently large centripetal acceleration to maintain a circular orbit or to move to larger radii. For HD and MHD, rotational support appears to dominate the support of inner gas across the majority of redshifts explored here. The radius at

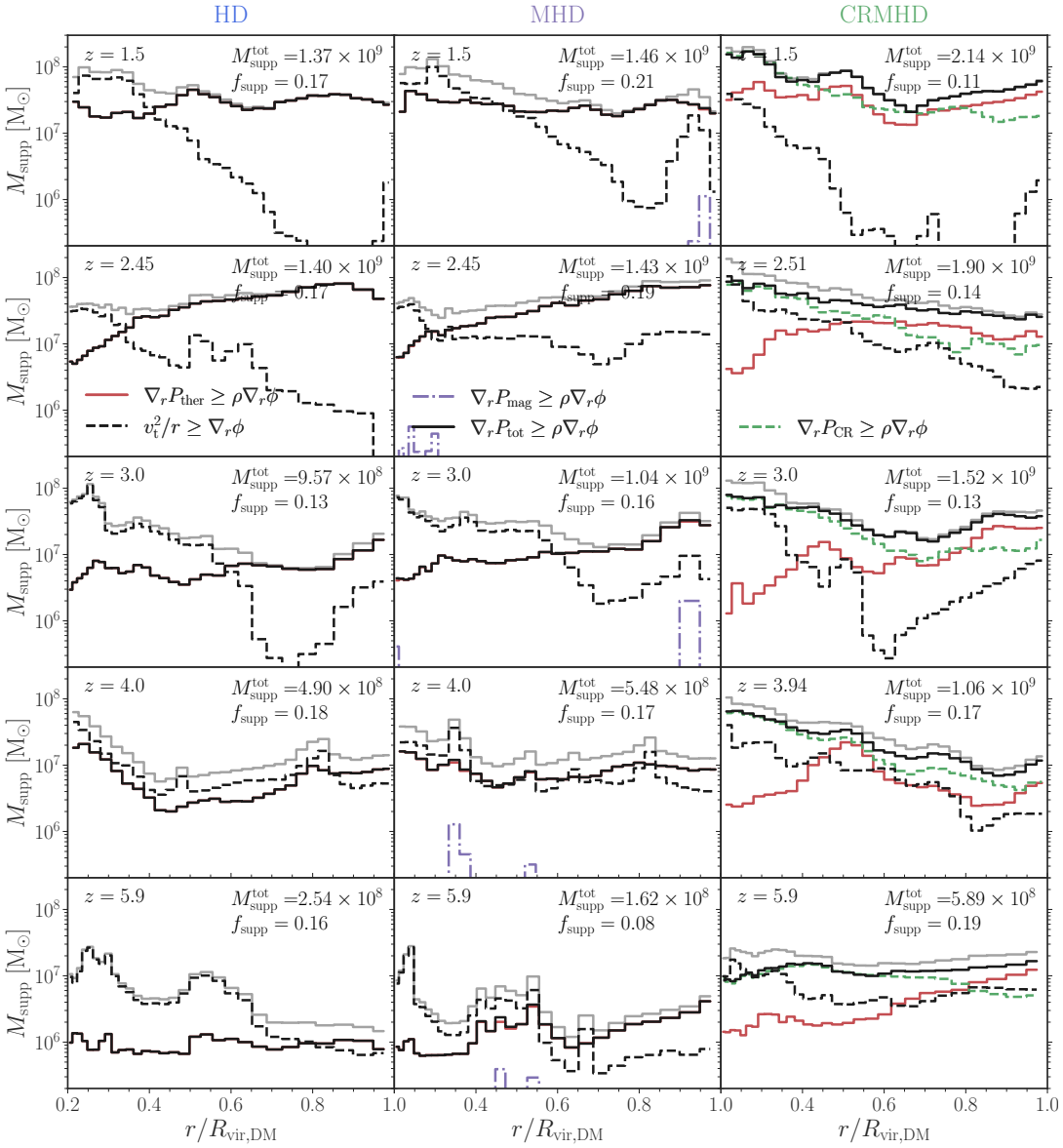


Figure 4.10: Radial histograms of the supported gas mass in the CGM for HD (left), MHD (middle) and CRMHD (right) at $z \sim 6$, 4, 3, 2.5 and 1.5. Different line styles represent gas fully supported by either thermal pressure (red solid lines), magnetic pressure (purple dot-dashed lines), CR pressure (green dashed lines), and rotation (black dashed lines). Additionally, the gas supported by the total pressure $P_{\rm tot}$ is given by the black solid line, and the grey line is the total supported gas (by any means) at a particular radial bin. In the upper right corner of each simulation and redshift panel, we also include the integrated supported gas mass $M_{\rm supp}^{\rm tot}$ and the fraction that this represents for the total gas mass within $0.2\,R_{\rm vir,DM}$ and $R_{\rm vir,DM}$ (i.e. $f_{\rm supp}$). Rotation (i.e. $v_t^2/r \geq \nabla_r \phi$) is an important contribution to support in the inner regions of the CGM, becoming less important at later times for all simulations, but primarily for CRMHD. Note the CR pressure gradient dominates the support in the inner region of the CGM at all redshifts, but becomes less important at larger radii at lower redshifts, resulting in a lower $f_{\rm supp}$.

which support switches from pressure gradient support to rotational support evolves with cosmic time, being close to $0.6 - 0.8 R_{\rm vir,DM}$ at $z \sim 6$, and becoming closer to $0.3 - 0.4 R_{\rm vir,DM}$ at $z = 1.5$. This convergence towards rotationally supported gas occurs within $\sim R_{\rm vir,DM}/3$, a region identified in previous work (Danovich et al., 2015; Cadiou et al., 2022) as the spin realignment region, where gravitational torques from the disk modify the angular momentum of the inflowing filament, effectively slowing it down. In contrast, rotationally supported gas becomes less important with cosmic time in the CRMHD simulation. Thermal pressure gradients in HD and MHD contribute to the gas support close to $0.2\,R_{\rm vir,DM}$ at high redshift and at large radii at low redshift. This radial segregation results in interesting features in the overall gas mass support in the CGM: when rotation support dominates, gas quickly flows from $R_{\rm vir,DM}$ to the inner CGM, resulting in a mass profile decreasing with radius. Furthermore when pressure support dominates, gas is efficiently maintained in a hot halo at large radii, while in the higher density inner CGM cooling is more efficient and becomes more thermally unstable, hence giving rise to either flat or increasing profiles with radius (see grey lines in Fig. 4.10). If we now consider the case of the CRMHD simulation, so far we have evidence of slower inflows and a cooler inner CGM, suggesting that the mass support profile shape will be mainly driven by the ability of CR pressure gradients to support gas, which dominates in the inner regions of the CGM. However, we also find that the volume in which CRs can support gas in the CGM increases with redshift. To further quantify this trend, we include in each simulation and redshift panel of Fig. 4.10 the total gas mass that is supported in the CGM $M^{\rm tot}_{\rm supp}$ and what fraction $f_{\rm supp}$ of the total CGM mass that mass corresponds to. All simulations show gas mass supported against gravity increasing with cosmic time, as would be expected for uninterrupted cosmological accretion. When we compare the relative masses between the different simulations, we find that $M^{\rm tot}_{\rm supp}$ is within $\sim 10 - 20\%$ at all redshifts between HD and MHD, while the CRMHD supports up to 4 times more gas mass at high redshift. This gap in supported gas shrinks after $z = 3$. In fact, we find that $f_{\rm supp}$ for CRMHD is smaller after this point, resulting in a consistently lower fraction than HD and MHD. This period correlates with the larger inflow rates for the CRMHD simulation found in Fig. 4.4.

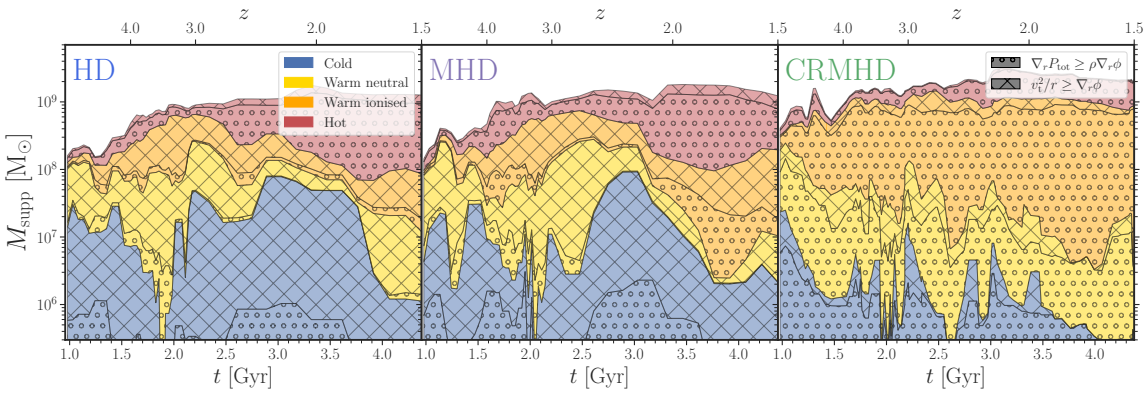


Figure 4.11: Evolution of the supported gas mass $M_{\rm supp}$ in the CGM (i.e. $0.2R_{\rm vir,DM} \leq r \leq R_{\rm vir,DM}$) for the HD, MHD and CRMHD simulations. We have separated the contribution from different phases (cold, warm neutral, warm ionised and hot) to the gas mass budget, as well as whether the support against gravity is given by pressure gradients (circles hash) or by centrifugal forces (tilted grid hash). Centrifugal forces dominates the support of all gas phases in HD and MHD until $z \sim 3$. Pressure gradients drive the support of gas in the CGM of the CRMHD simulation, with warm ionised gas dominating from very early times. Rotational support is small, but becomes non-existent after the merger at $z \sim 2.5$.

To support our conclusions, we have computed the integrated gas mass $M_{\rm supp}$ supported by pressure gradients and centrifugal forces across cosmic time within $0.2R_{\rm vir,DM} \leq r \leq R_{\rm vir,DM}$ in Fig. 4.11. These are stacked area curves, with the area under a curve colour indicating the contribution to the total $M_{\rm supp}$ at a given time t. Curves with the same colour but different hash indicated pressure gradient support (circles hash) and rotational support (tilted grid hash). From the results for HD and MHD (left and middle panels) we can confirm that the majority of the gas in the CGM is supported by rotation, as the large inflow velocities of these simulations (bottom panel in Fig. 4.4) result in gas that needs to loose angular momentum to be finally accreted to the inner $0.2\,R_{\rm vir,DM}$. Furthermore, the increasing contribution of pressure-supported hot gas after $z \sim 3$ in both simulations agrees with the virialisation of the CGM at these later times, supporting the claim that virialisation is concurrent with the formation of a rotationally supported disk (e.g. Stern et al., 2021). We find that the contribution of cold clumps (recall the cold clumps seen in Fig. 4.6) do not exceed $0.5 - 1\%$ of the total $M_{\rm supp}$ in the CGM, but is noticeably larger than this same phase supported mass in the CGM of the CRMHD simulation (see right panel). However, we note that the majority of this cold gas is supported in the CGM by pressure gradients (similar to the result for outflows in Section 3.4.4), while in HD and MHD rotationally supported cold gas dominates. This argues for different origins of the cold gas in the CGM: in the case of HD and MHD, cold gas is preferentially

primordial clumps that have been accreted at high infall velocity, while in CRMHD cold outflows populate the CGM with enriched cold gas. The CRMHD simulation shows a dominance of warm ionised gas already at $z \sim 6$, with an increasing role at lower redshift. As predicted in Fig. 4.10, the gas supported by rotation is reduced significantly after the merger at $z \sim 2.5$, as can be seen by its negligible contribution for $z \leq 2$. Instead the sole support mechanism left is pressure gradients, with the gas phase becoming dominated by the warm ionised gas.

4.3 Gas cooling and heating in the circum-galactic medium

At the interface between primordial gas accreting from the cosmic web and metal enriched outflows, cooling is a fundamental process driving the evolution of the CGM (see Faucher et al., 2023, for recent reviews). Not only have we extensively quantified the thermodynamical properties of the CGM gas and shown it to be dramatically different when CR feedback is included, but we also found strong evidence of a much more metal enriched halo (Fig. 4.3, right panel). Furthermore, inflowing gas appears to retain its large, shock-heated thermal energy as it reaches $0.2\,R_{\rm vir,DM}$ in the HD and MHD simulations, while it is capable of cooling down to (or maintaining) the PIE temperature in the CRMHD run. Therefore, the missing piece for a full description of the influence of CR feedback on the CGM and inflows are the cooling and heating mechanisms.

Different thermodynamic processes give rise to different temperature-density scalings in the halo gas. Therefore, we begin by exploring the phase diagrams for the gas out to super-halo scales (i.e. from $0.2\,R_{\rm vir,DM}$ to $2R_{\rm vir,DM}$) in temperature-density space in Fig. 4.12. For reference, we compare the gas properties on these larger scales at low redshift ($z = 1.5$) and at high redshift ($z = 4$) for HD (left column), MHD (middle column) and CRMHD (right column). For each bin in (ρ, T), the cumulative gas mass is divided by the total gas mass within the integrated region. We remind the reader that, as has been done consistently throughout this Chapter, the volume corresponding to intervening substructures (either satellites or companions in the outskirts of the halo) have been ignored. The probability density clearly extends over a large range of temperatures and densities in all simulations and redshifts, a signature

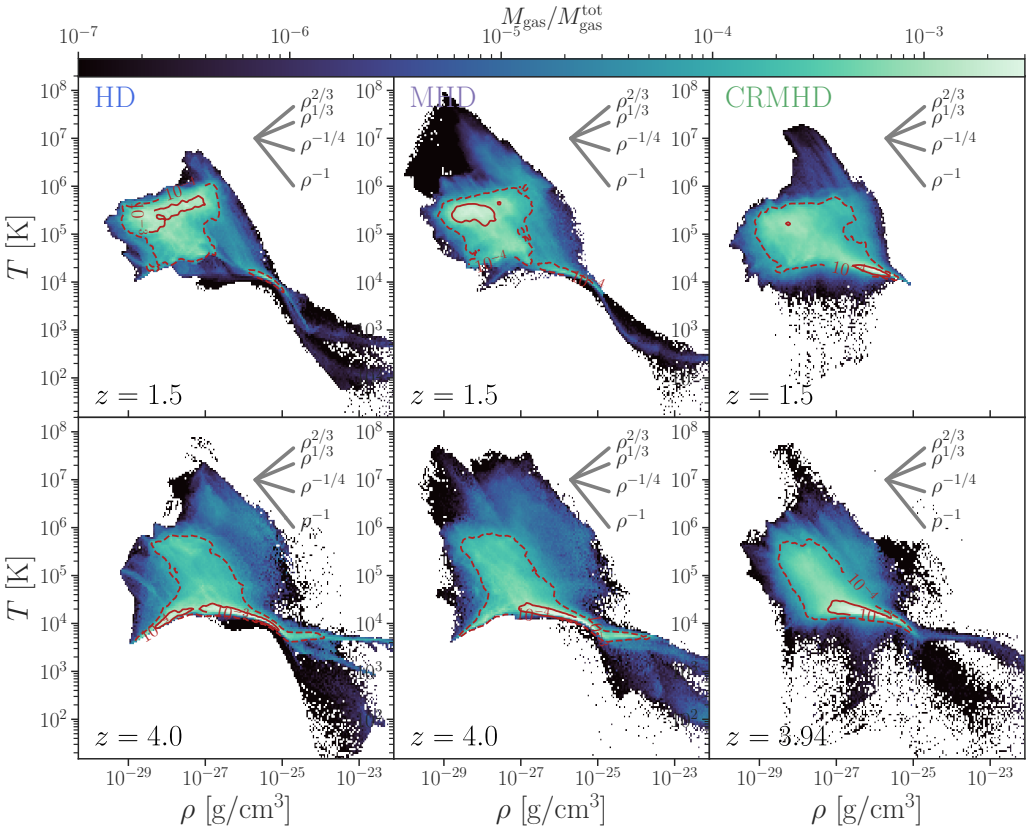


Figure 4.12: Mass-weighted phase diagram of the HD (left), MHD (middle) and CRMHD (right) simulations at $z = 1.5$ and at $z \sim 4$ for the volume spanning from $0.2\,R_{\rm vir,DM}$ to $2R_{\rm vir,DM}$. The colormap is constructed such that high gas mass fraction corresponds to bright turquoise, while low probability is dark blue. Red contour lines indicate regions for which $M_{\rm gas}$ is above 10^{-3} (solid lines) and 10^{-4} (dashed lines) of $M_{\rm gas}^{\rm tot}$. Trend lines in each panel aid in identifying regions of adiabatic processes ($T \propto \rho^{2/3}$ or $T \propto \rho^{1/3}$, depending on γ), equilibrium with the UV background ($T \propto \rho^{-1/4}$) and isobaric ($T \propto \rho^{-1}$). Gas above $\sim 10^{-25}$ g cm^{-3} is highly suppressed in the CRMHD simulation, while also presenting a much broader hot/warm gas distribution preferentially in equilibrium with the UV background.

of the multiphase CGM that observations suggest to be present in the local Universe (for a review, see e.g. Tumlinson et al., 2017). At $z = 4$, gas is preferentially clustered around the equilibrium temperature curve (see also Fig. 4.14). Gas at temperatures above this $T_{\rm eq}$ experiences an effective cooling, driving it towards a minimum in $|\Gamma - \Lambda|$, while for lower temperatures effective heating raises the temperature. An undisturbed cooling flow can be identified with this high probability gas curve, starting at 10^{-29} g cm^{-3} and below 10^4 K, increasing its temperature towards the PIE (i.e. $\sim 1.5 \times 10^4$ K along $T_{\rm eq}$ until the cooling instability takes place at $\sim 10^{-25}$ g cm^{-3} and the gas drops to the cold phase[4]. The high temperature cloud above $T_{\rm eq}$ at low gas densities can be

[4]This depends on the gas metallicity and the efficiency of photo-electric heating (e.g. Bialy and Sternberg, 2019; Katz et al., 2022b).

identified as the shock-heated gas, whether by SN feedback or by an accretion shock in the streaming filament. This shock-dominated heating can easily be recognised as diagonal lines of adiabatic expansion, i.e. $T \propto \rho^{-1}$. In the CRMHD simulation these overall trends are also visible at $z = 4$, although it can easily be appreciated that the adiabatic shocked gas ridge sits at a lower gas temperature in the same density range as HD and MHD, while also having a less defined equilibrium cooling curve at low densities and significantly less gas mass at densities above $\sim 10^{-25}$ g cm^{-3} (red contours indicate regions for which the cumulative gas at (ρ, T) is 10^{-3} or 10^{-4} of the total gas mass with solid lines and dashed lines, respectively). We find that these differences become more accentuated at low redshift (see top row of Fig. 4.12), to the point that the CRMHD simulation does not show neither an extended ridge along the cooling equilibrium temperature nor gas above $\sim 10^{-25}$ g cm^{-3}. The structure of the hot gas cloud has also changed at this lower redshift in the HD and MHD simulations. Besides the isobaric regions caused by SN shock heating, we find that both simulations have driven a high mass fraction to this region for which the temperature has a positive correlation with the gas density. In the classical picture of cosmological gas accretion and the formation of a virial shock (e.g. Birnboim and Dekel, 2003; Dekel and Birnboim, 2006), gas flows along isentropic lines in temperature-density space (i.e. $T \propto \rho^{2/3}$) in order to establish a global hydrostatic balance. We find that these ridges have a shallower slope, closer to the isentropic lines of a fluid with $\gamma \sim 4/3$ (i.e. we have instead a scaling like $T \propto \rho^{1/3}$). The assumption of isentropicity appears not to hold even at $z = 1.5$ in a realistic zoom-in cosmological simulation like NUT as cooling remains sufficiently efficient at this halo mass compared to compressional heating, so that the effective adiabatic index $\gamma_{\rm eff} < 5/3$. Similar to the results of Ji et al., 2020 (see their figure 7), gas traces a large range of temperatures at a fixed density, instead maintaining the trend given for diffuse gas in PIE with the UV-background (i.e. $T \propto \rho^{-1/4}$ Stern et al., 2018).

These phase diagrams further indicate a very distinct difference between no-CR and CR simulations: when CRs are included, gas is overall more diffuse and colder, but incapable of cooling below the equilibrium temperature resulting from PIE with the UV background. In order to further examine the effect of this difference on the relevance of UV heating and its spatial location, in Fig. 4.13 we present

mass-weighted projections of the gas cooling time $t_{\rm cool}$ on a thick slice centred on NUT with a width equivalent to $4R_{\rm vir,DM}$ and a thickness of $R_{\rm vir,DM}$ at each redshift and for each simulation. We compute the cooling time for each cell in the volume by taking into account the cooling and heating determined by the RAMSES tables (recall Section 2.2), and the heating from CRs:

$$t_{\rm cool} = \frac{2k_{\rm B}\rho T}{m_{\rm p}\mu(n_{\rm H}^2\Lambda_{\rm net} - \Gamma_{\rm CR} - \Gamma_{\rm st})}, \tag{4.8}$$

where $\Lambda_{\rm net} = \Lambda - \Gamma$ is the net cooling rate per unit volume (i.e. units of [erg/(s cm^3)]), $\Gamma_{\rm CR}$ is the heating rate due to Coulomb and Hadronic collisions of GeV CRs, and $\Gamma_{\rm st}$ is the heating rate from the damping of self-excited Alfvén waves by streaming CRs[5]. These last two terms are only considered for the CRMHD simulation. In the case of a negative sum of cooling and heating terms in the denominator of Eq. 4.8, the gas is effectively heated. We then set the current cooling time to be infinitely large. This is for example the case of gas below the equilibrium temperature and at densities lower than the self-shielding density of $n_{\rm H} = 10^{-2}$ cm^{-3}. We can see how this is the case for the majority of the super-halo gas at high redshift (e.g. $z \sim 6$ in Fig. 4.13, dark-blue colours), and that only gas in small patches has been heated above this $T_{\rm eq}$. The stronger feedback in MHD and CRMHD can easily be identified as it carves larger regions of collisionally heated gas (compared to HD). As feedback becomes more continuous and far-reaching at $z \sim 4$, heated gas which is also metal-enriched becomes more volume filling in the halo, allowing for the overall cooling time to significantly decrease below ~ 100 Myr. In the HD and MHD projections one can appreciate how the two larger filaments feeding NUT (on a diagonal going from bottom right to top left, as in e.g. Fig. 4.6) reach the $R_{\rm vir,DM}$ region (purple circles) with a large cooling time and cross-section, becoming collimated and acquiring short cooling times as they finally travel to the centre of the potential. At even later times ($z = 2.5$ and 1.5), both simulations result in gas heated on all scales, reducing the average cooling times, although this latter still remains similar to the Hubble time (~ 10 Gyr). Only gas approximately located within $R_{\rm vir,DM}$ has cooling times below ~ 1 Gyr, although the geometry of these regions is not completely spherical (see also e.g. Fig. 4.7a) and instead short cooling time structures map onto the co-rotating inflowing filaments.

[5]See Section 2.1.1 for details on CR cooling and heating terms in the CRMHD equations.

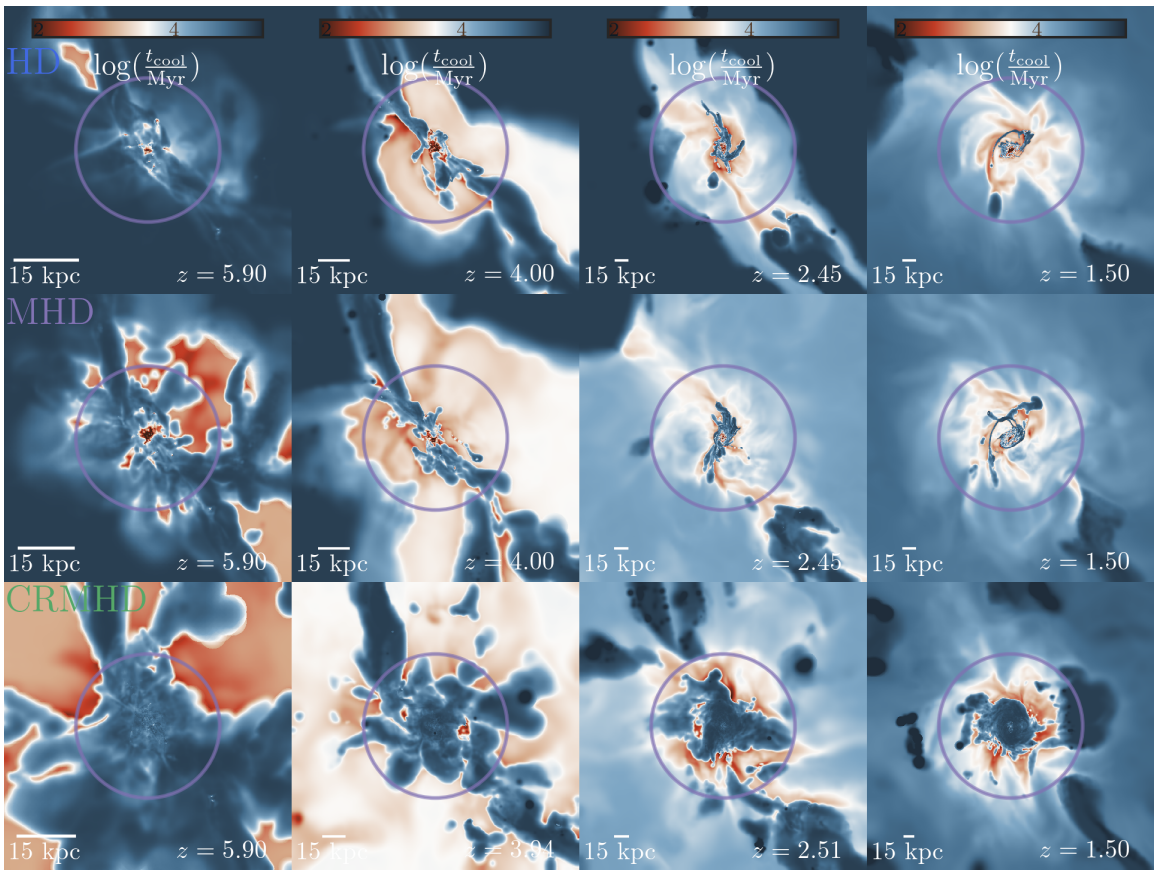


Figure 4.13: Thick slice ($4R_{\rm vir,DM}$ width and $R_{\rm vir,DM}$ thickness) of the mass-weighted $t_{\rm cool}$ in the HD (top row), MHD (middle row) and CRMHD (bottom row) at four different redshifts. The purple circle indicates the current $R_{\rm vir,DM}$ sphere. The majority of the large scale diffuse gas in the HD and MHD simulation has long cooling times (dark blue) at low redshift, with only the thin collimated end of filaments capable of reaching the galaxy with short cooling times (dark red). The CRMHD simulation instead creates a large region ($\sim 0.3 - 0.5 R_{\rm vir,DM}$) in which heating dominates.

The mass-weighted $t_{\rm cool}$ projections of the CRMHD simulation present large differences from those for the HD and MHD runs from early on. The extreme feedback in CRMHD at early times that gave rise to mass loading factors $\eta \gtrsim 10$ in Section 3.4.2 is a heating source capable of making the gas thermally unstable on the halo scales. However, as the CR pressure gradient can also support a larger fraction of gas in the CGM, there exists a large amount of cool gas at sufficiently low densities making UV heating efficient. Similar to the HD and MHD simulations, at lower redshifts, the metal enrichment of the halo yields an overall lower cooling time, which nevertheless remains ~ 10 Gyr due to the low density of the gas. However, the increased gas density in the CRMHD simulation for $r \lesssim R_{\rm vir,DM}$ (compared to HD and MHD) results in a faster decrease in the cooling time right before reaching the UV-heating region. This corresponds to the gas that has been largely disrupted from the high velocity inflows

and compressed without increasing its temperature much (see Fig. 4.9 and Fig. 4.8). In other words, due to efficient cooling and the larger contribution of CR pressure, gas is transported along approximately isothermal paths in temperature-density space, at some point having a temperature lower than $T_{\rm eq}$ for a given density (e.g. consider straight lines in Fig. 4.14 crossing the dashed orange line). This results in a sharp increase in $t_{\rm cool}$ at lower radii, giving rise to a region of $\sim 0.3 - 0.5 R_{\rm vir,DM}$ which is dominated by gas with cooling times larger than the Hubble time. This is the cool, diffuse gas with low v_r that we have been characterising in this Chapter.

4.3.1 The meta-stable cosmic ray corona

In order to provide a more quantitative understanding of the trends inferred from the $t_{\rm cool}$ projections, we have computed equivalent mass-weighted cooling times for each (ρ, T) in the phase diagrams of Fig. 4.14. To aid the eye in distinguishing the regions of dominant gas mass in the temperature-density plane, we also include the same contours as in Fig. 4.12 (red dashed and solid lines). We have computed the equilibrium temperature $T_{\rm eq}$ for each snapshot and simulation as minima in the temperature-density plane of $|\Gamma - \Lambda|$, and plotted it as a dashed orange line. Since this curve is dependent on the gas metallicity, $T_{\rm eq}$ is obtained for the mass-weighted median $Z_{\rm gas}$ for each panel. Furthermore, the density at which self-shielding takes effect is indicated by a vertical purple dotted line. Across all cosmic times, the HD and MHD simulations show a a tight adherence to the limits in phase space set by the cooling function, with the gas above $T_{\rm eq}$ regardless of density. For CRMHD, we see instead an evolution towards an adiabatic-like ridge for the dominant gas mass within the $0.2\,R_{\rm vir,DM}$ to $2R_{\rm vir,DM}$ volume around NUT ($T \propto \rho^{1/3}$, see Fig. 4.14). It is interesting to note, in the HD and MHD phase-diagrams, that at higher redshift gas is sometimes found along a parallel continuation of $T_{\rm eq}$ for $\rho \gtrsim 10^{-25}$ g cm^{-3}, also displaying larger cooling times (notice the shallow whiter ridge) with the temperature of the gas decreasing at these densities. We argue that this is clearly primordial gas from cold streaming inflows, for which the cooling instability triggered at $\sim 10^{-25}$ g cm^{-3} is not present to the same extent given their much lower metallicity ($Z = 10^{-3} Z_{\odot}$). Similar to our conclusions in Section 3.3, the CRMHD simulation populates other regions of the gas-phase space. We find that the gas below $T_{\rm eq}$ in CRMHD is fully dominated by

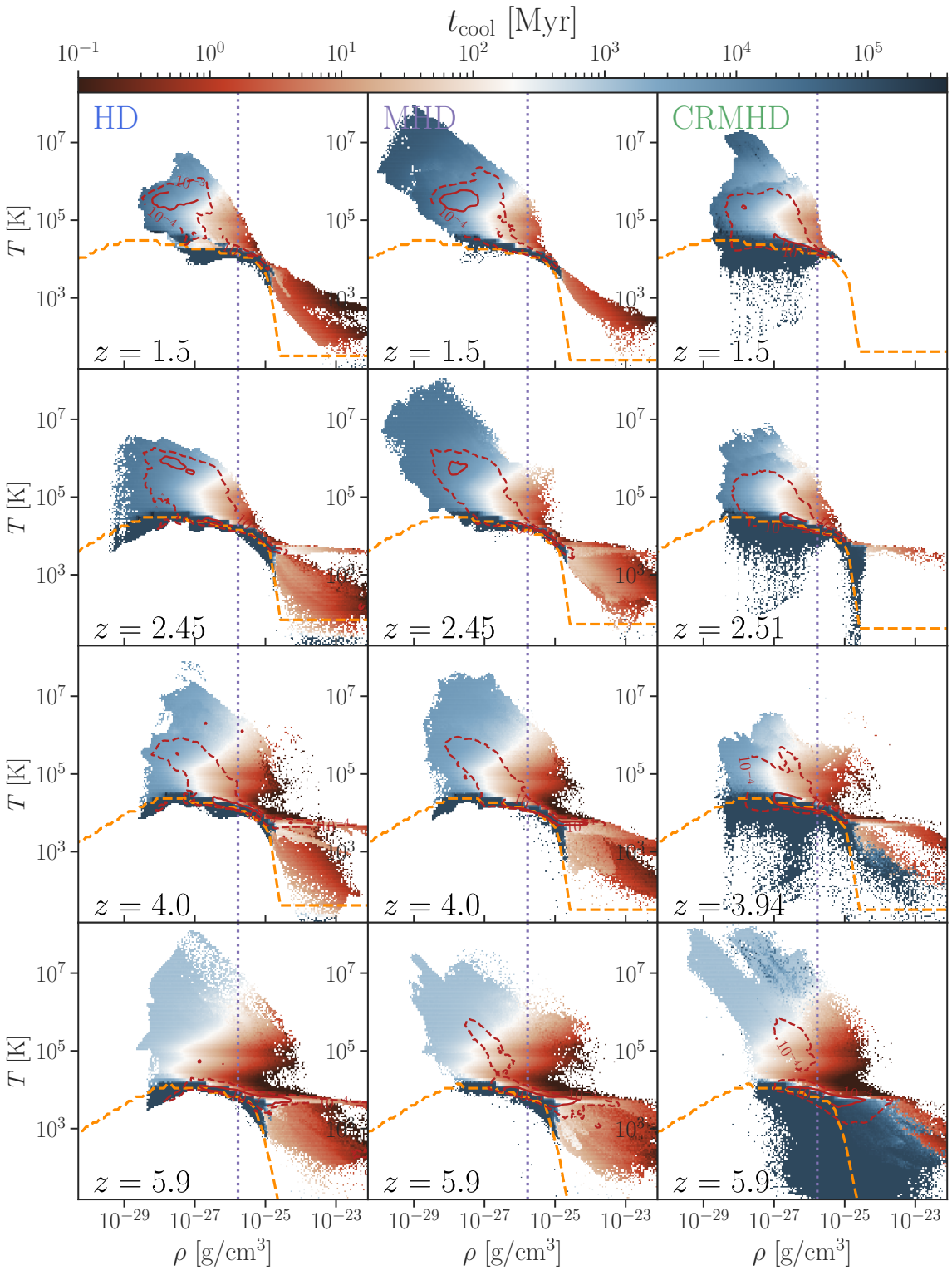


Figure 4.14: Mass-weighted $t_{\rm cool}$ phase-diagrams for the gas from $0.2\,R_{\rm vir,DM}$ to $2R_{\rm vir,DM}$ for the HD (left column), MHD (middle column), and CRMHD (right column). Red contours correspond to the mass distribution in Fig. 4.12, while the orange dashed line represents the mass-weighted median cooling equilibrium temperature, and the dotted purple line represents the self-shielding threshold at $n_{\rm H} = 10^{-2}$ cm^{-3}.

heating. In fact, we find that a large fraction of the cold, dense gas at densities well above the self-shielding threshold ($\rho \geq 10^{-25}$ g cm^{-3}) still experiences long cooling times. We claim that in this dark blue *rhomboidal* region of the temperature-density space, the combination of a slow cooling rate close to the equilibrium temperature and sufficiently large CR heating rates give rise to a CR-induced thermal stability. Contrary to the traditionally coined thermal instability (TI) in the CGM , this maintains a long cooling time for the gas. At lower redshifts this physical process contributes to the depletion of gas at densities above 10^{-25} g cm^{-3}. In this regime of high density gas in the CGM, it is also interesting to consider the role of CR diffusion in order to understand the dynamical role of CRs on the dissipation of this gas phase. Consider the turbulent timescale ($t_{\rm turb} \equiv \frac{L}{\sigma}$) as the time taken by a turbulent fluctuation to travel across a gas blob of scale L. In the same blob, we can define the CR diffusion timescale $t_{\rm diff} = \frac{L^2}{\kappa}$, with κ the CR diffusion constant (Section 2.1.1). One can estimate a critical diffusion coefficient (Commerçon et al., 2019) for which CR diffusion is not fast enough to prevent energy fluctuations caused by turbulence. This causes CRs to become trapped, leading to strong CR dynamical effects (like we found in the ISM, see Section 3.3). This is given by the condition $\kappa_{\rm crit} < L\sigma$. If one considers the typical scales of ~ 5 kpc for the cold clumps formed in the inflowing filaments of the HD simulation (top panel of Fig. 4.6), and the observed $\sigma \sim 10 - 20$ km/s for the inner CGM in Fig. 4.9 that results in a critical diffusion of $\kappa_{\rm crit} \sim 1.5 \times 10^{28}$ cm^2/s, very close to our value of $\kappa = 3 \times 10^{28}$ cm^2/s. Therefore, it can be argued that CR diffusion may play an important role in dispersing cold clumps[6] in inflowing gas, together with the CR heating mechanisms here described.

At these later times, gas mass at halo scale predominantly obeys the $T \propto \rho^{-1/4}$ relation, with an important contribution from the adiabat with $T \propto \rho^{1/3}$ (see Fig. 4.12), but, different from the HD and MHD runs, we also find gas below $T_{\rm eq}$. This gas appears to evolve following isochores (vertical lines in the phase diagram) and quickly re-heats back to $T_{\rm eq}$ by the UV-background. We identify the gas in this state as the high $t_{\rm cool}$ halo around NUT observed in Fig. 4.13. Together with the results of Section 4.2.3, this means that in the CRMHD there is a fundamentally different CGM region that

[6]We remind the reader than in this density regime our computation of Alfvén velocity should be based on the local gas ionisation state. We will re-examine this claim in future works with self-consistent CR transport.

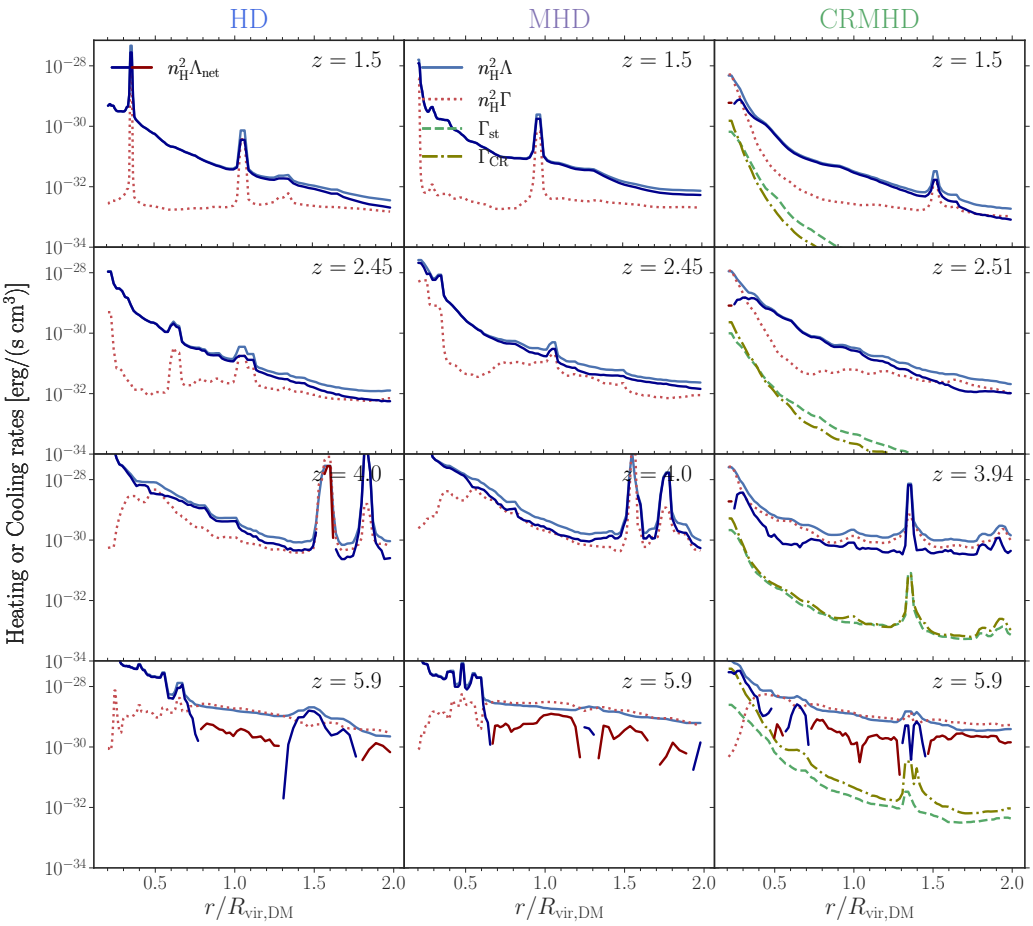


Figure 4.15: Mass-weighted radial profiles of cooling and heating terms for the inflowing gas within $0.2\,R_{\rm vir,DM}$ and $2R_{\rm vir,DM}$ for the HD (left column), MHD (middle column), and CRMHD (right column) at the four different redshifts explored in this Section. We separate the different components that contribute to the final $t_{\rm cool}$: cooling Λ, heating Γ, CR collisional heating $\Gamma_{\rm CR}$, and CR streaming Alfvén heating $\Gamma_{\rm st}$. We also include the final net cooling $\Lambda_{\rm net}$ as a solid line, being either blue or red depending on whether the gas reaches net cooling or heating. The lower temperature for the same gas density caused by CR support in the halo allows it to be more easily heated by the UV background and CR processes.

was not previously observed in the HD and MHD simulations: CR pressure gradients are supporting a large gas mass within $0.2\,R_{\rm vir,DM}$ and $\sim 0.3-0.5R_{\rm vir,DM}$ which is cool, diffuse and at densities below the self-shielding threshold, hence continuously isochorically cooling and being re-heated by the UV background. We call this region the meta-stable CR corona of the CGM.

In Fig. 4.15 we show mass-weighted radial profiles of inflowing gas on super-halo scales, i.e. dominated by the dense filaments. We separate the contributions to the cooling time in Eq. 4.8, namely the cooling Λ and heating Γ rates, the streaming heating $\Gamma_{\rm st}$ and the collisional (Coulomb and Hadronic) CR heating $\Gamma_{\rm CR}$. Furthermore,

in order to clearly identify the regions which have a dominant cooling (heating) rate, we also include solid blue (red) lines for the net cooling $\Lambda_{\rm net}$. Spikes in these profiles are related to gas clumps within inflowing filaments that due to small or nonexistent star formation have been disregarded by our structure finder at early cosmic times (i.e. see the large dark clumps in the $z = 1.5$ projections in Fig. 4.13). HD and MHD simulations show net cooling gas in the inner regions at high redshift ($z = 6$ and $z = 4$), with UV heating becoming an important driver of effective heating in the outskirts. This becomes inefficient at lower redshifts ($z = 2.5$ and $z = 1.5$), with the inflowing gas always experiencing effective radiative cooling from $2R_{\rm vir,DM}$ to the boundary. The profile develops a steep radial dependence (e.g. Ji et al., 2021), resulting in only the very inner region of the CGM having sufficiently large cooling rates to allow the cooling of gas within a Hubble time. Given that CRs dominate within the inner regions of the halo, it is no surprise that profiles of $\Gamma_{\rm st}$ and $\Gamma_{\rm CR}$ present a steep gradient with radius. Despite their consequent lower magnitude (by up to 2 dex at large radii), these heating sources can play a significant role in the thermodynamical evolution of the halo gas. For example, in CRMHD at $z \sim 6$ there is a high mass gas clump embedded within the filament (see the clump in the lower right filament of Fig. 4.13 at $r \sim 1.5R_{\rm vir,DM}$) which due to the overall larger density is capable of becoming self-shielded in HD and MHD and effectively cool. A larger density also implies a larger CR heating, which we can identify as a large spike in these heating terms in the $z \sim 5.90$ profiles of the CRMHD simulation at $r \sim 1.3R_{\rm vir,DM}$, giving rise to a resulting heating instead of cooling. This is also observed in the spikes at $z = 4$. Therefore, we claim that early CR feedback may have a non-negligible effect on the onset of star formation in low mass halos (Munshi et al., 2013; Oñorbe et al., 2015; Wheeler et al., 2018; Wright et al., 2019; Agertz et al., 2021; Gutcke et al., 2022; Rey et al., 2023). For the lower redshifts explored here, we find that indeed cooling becomes efficient in the CRMHD run as the density drops sufficiently for CR heating to become inefficient and the gas temperature increases for cooling to be efficient ($T \geq 10^4$). In agreement with the results of Fig. 4.13 and 4.14, net heating rises in the very inner region of the CGM. As the structure of the meta-stable CR corona deviates from a pure spherical geometry, these spherical profiles are a poor way to quantify their spatial extent. Nevertheless, we are capable of assessing

that at later times CR heating works differently across the different radii: at the very large densities of the corona, collisional cooling dominates, while in the inner regions where radiative cooling and heating are balanced, CR streaming and collisional heating drive the net heating of the gas. Nonetheless, we note that the absolute magnitude of these CR heatings are well below the values of the canonical heating and cooling rates, and their main importance lies in heating gas at this equilibrium of heating and cooling (Ji et al., 2021). CR heating mechanisms are capable of exceeding the gas heating rate magnitude in the very high density gas of the inner CGM at $z \sim 6$ (see also bottom row of Fig. 4.14). Therefore, without CR heating, gas would be maintained at this meta-stable equilibrium (unless disturbed by compression or expansion), but the presence of the additional CR heating drives this gas away from the equilibrium without a restoring cooling mechanism available.

4.3.2 Virial shock stability analysis

We write a generalised adiabatic index $\tilde{\gamma}_{\rm eff}$ as:

$$\tilde{\gamma}_{\rm eff} = \frac{{\rm d}\log P_{\rm tot}/{\rm d}t}{{\rm d}\log \rho/{\rm d}t}, \tag{4.9}$$

where we are taking total derivatives with respect to time t for the gas density ρ and the gas total pressure $P_{\rm tot} = P_{\rm th} + P_{\rm CR} + P_{\rm mag}$. Given the overall secondary role of magnetic pressure in the halo gas of NUT at the redshifts of interest for this Chapter, we neglect the contribution of the magnetic pressure to the computation of an effective adiabatic index in the halo. We recall that the thermal and CR pressures are related to the specific thermal and CR energies as:

$$P_{\rm th} = (\gamma_{\rm gas} - 1)\rho\epsilon_{\rm th} \tag{4.10}$$

$$P_{\rm CR} = (\gamma_{\rm CR} - 1)\rho\epsilon_{\rm CR}, \tag{4.11}$$

where $\gamma_{\rm gas}$ and $\gamma_{\rm CR}$ refer to the thermal and relativistic adiabatic indices, respectively. Under conservation of energy, the time derivative of the specific thermal energy is given by the work done on the gas minus the specific cooling rate:

$$\dot{\epsilon}_{\rm th} = -P_{\rm th}\dot{V} - q_{\rm th}, \tag{4.12}$$

such that:

$$\dot{P}_{\rm th} = (\gamma_{\rm gas} - 1)\left[\dot{\rho}\epsilon_{\rm th} + \frac{P_{\rm th}\dot{\rho}}{\rho} - q_{\rm th}\rho\right] = (\gamma_{\rm gas} - 1)[\gamma_{\rm gas}\epsilon_{\rm th}\dot{\rho} - q_{\rm th}\rho] \tag{4.13}$$

where we have defined the specific cooling rate $q_{\rm th}$, and $V = \rho^{-1}$ is the specific volume. We can follow an equivalent derivation for the time derivative of the CR pressure, resulting in:

$$\dot{P}_{\rm CR} = (\gamma_{\rm CR} - 1)\left[\dot{\rho}\epsilon_{\rm CR} + \frac{P_{\rm CR}\dot{\rho}}{\rho} - q_{\rm CR}\rho\right] = (\gamma_{\rm CR} - 1)[\gamma_{\rm CR}\epsilon_{\rm CR}\dot{\rho} - q_{\rm CR}\rho] \tag{4.14}$$

where $q_{\rm CR}$ includes the losses by Coulomb and Hadronic collisions, and the energy loss via CR streaming self-excited Alfvén waves. Inserting the expressions for $\dot{P}_{\rm th}$ and $\dot{P}_{\rm CR}$ into Eq. 4.9 results in:

$$\tilde{\gamma}_{\rm eff} = \frac{\gamma_{\rm gas}P_{\rm th} + \gamma_{\rm CR}P_{\rm CR}}{P_{\rm tot}} + \frac{1}{P_{\rm tot}(\vec{\nabla}\cdot\vec{u})}\left[\frac{q_{\rm th}}{\epsilon_{\rm th}}P_{\rm th} + \frac{q_{\rm CR}}{\epsilon_{\rm CR}}P_{\rm CR}\right], \tag{4.15}$$

where we have used the fact that $\dot{\rho}/\rho = -\vec{\nabla}\cdot\vec{u}$. The first term in Eq. 4.15 is the classical adiabatic constant $\gamma_{\rm eff}$ for a mixed gas of thermal and non-thermal components (e.g. Pfrommer et al., 2017; Dubois et al., 2019). The second terms take into account the influence of cooling/heating processes on the effective gas compressibility. We define the CR cooling timescale:

$$t_{\rm cool,CR} = \frac{e_{\rm CR}}{\mathcal{L}_{\rm CR} + \mathcal{L}_{\rm st}}, \tag{4.16}$$

where $e_{\rm CR} = \rho\epsilon_{\rm CR}$, $\mathcal{L}_{\rm CR}$ and $\mathcal{L}_{\rm st}$ are the CR Hadronic/Coulomb heating and the streaming heating, respectively (see Section 2.1.1). This allows us to write Eq. 4.15 as:

$$\tilde{\gamma}_{\rm eff} = \gamma_{\rm eff} + \frac{1}{P_{\rm tot}(\vec{\nabla}\cdot\vec{u})}\left[\frac{P_{\rm th}}{t_{\rm cool}} + \frac{P_{\rm CR}}{t_{\rm cool,CR}}\right], \tag{4.17}$$

where $t_{\rm cool}$ is gas cooling time defined in Eq. 4.8. From the cooling/heating values obtained for Fig. 4.15 we have computed mass-weighted radial profiles of $\tilde{\gamma}_{\rm eff}$ for the inflowing gas in super-halo scales, shown in the top row of Fig. 4.16 for a series of redshifts (different line colours). In the idealised case of gas isotropically accreting towards a central mass, Birnboim and Dekel (2003) have obtained a criterion for the formation of a stable shock on $\tilde{\gamma}_{\rm eff}$:

$$\tilde{\gamma}_{\rm eff} > \frac{2\gamma_{\rm gas}}{\gamma_{\rm gas} + \frac{2}{3}} \equiv \tilde{\gamma}_{\rm crit}, \tag{4.18}$$

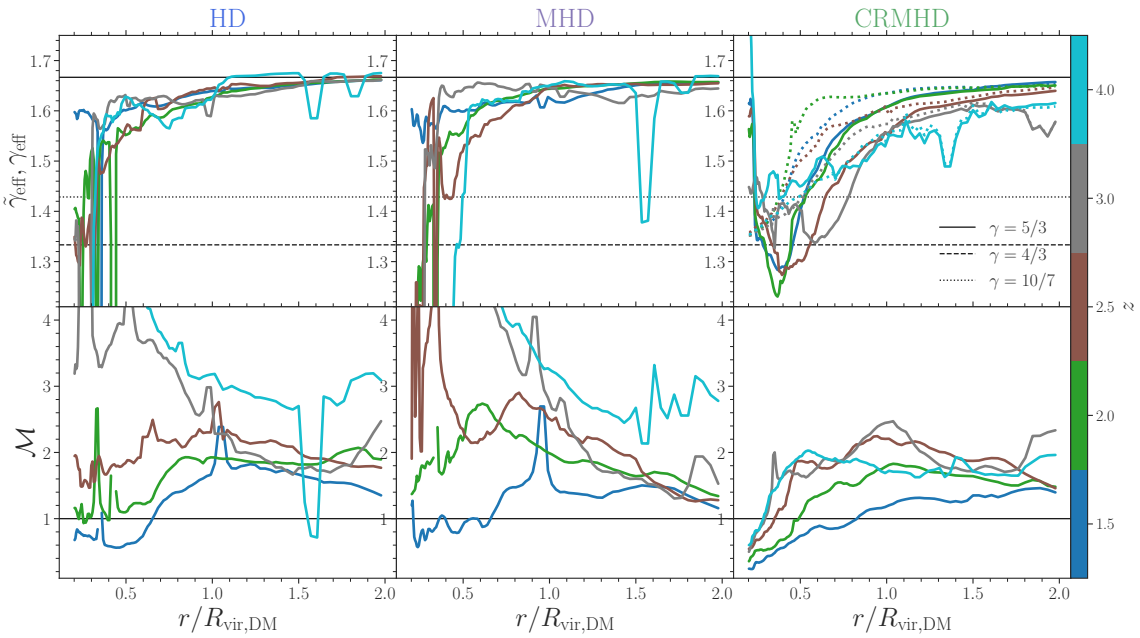


Figure 4.16: Mass-weighted radial profiles of the inflowing gas $\tilde{\gamma}_{\rm eff}$ (top row) and local Mach number $\mathcal{M}$ (bottom row) at the cosmic times explored in this Chapter for the HD, MHD and CRMHD simulations. Different line colours correspond to different redshifts. Horizontal lines indicate the adiabatic index values of relevance for our stability criterion. Dashed lines in the CRMHD panel are for the traditional $\gamma_{\rm eff}$ for a CR+thermal gas mixture. HD and MHD have $\tilde{\gamma}_{\rm eff} > 10/7$ at all relevant radii, resulting in the formation of an accretion shock at $\sim R_{\rm vir,DM}$, although it is not always there due to the influence of large scale outflows. Higher metal enrichment and the presence of CR pressure makes the profile significantly steeper with radius, but still with $\tilde{\gamma}_{\rm eff} > 10/7$. Despite its compliance with the Birnboim and Dekel (2003) criteria for shock stability, the Mach number does not show a peak around $R_{\rm vir,DM}$ and instead is mildly supersonic and quickly slowed down below $R_{\rm vir,DM}$.

which for a monatomic ideal gas is equivalent to $\tilde{\gamma}_{\rm crit} = 10/7$. This derivation assumes that $q_{\rm th} \propto \rho$. We can follow a similar derivation by also assuming that $q_{\rm CR} \propto \rho$, which is equivalent to assuming that strong CR cooling takes place in high density gas, which gives the same expression as Eq. 4.18 but with $\gamma_{\rm gas} \rightarrow \gamma_{\rm eff}$. This means that, for the CRMHD simulation, the $\tilde{\gamma}_{\rm crit}$ depends on the ratio of CR pressure to thermal pressure. As the CR pressure increases above the thermal pressure $\gamma_{\rm eff} \rightarrow 4/3$, which means that $\tilde{\gamma}_{\rm CR} \rightarrow 4/3$. In Fig. 4.16 we also show the profiles for $\gamma_{\rm eff}$ as dotted lines, exhibiting a large drop in the inner regions of the halo, where CR pressure plays a critical dynamical role.

We have included the critical γ as a dotted horizontal line in the top row of Fig. 4.16. HD and MHD simulations show a mild departure from $\gamma = 5/3$ (solid black line), only accentuated within $R_{\rm vir,DM}$. This indicates that cooling has little effect on the effective compressibility of the inflowing gas in the outskirts of the halo,

as these mass-weighted averages are preferentially looking at gas with primordial composition. This is supported by the fact that MHD (and also CRMHD), with feedback reaching larger scales, shows lower values of $\tilde{\gamma}_{\rm eff}$ at $2R_{\rm vir,DM}$. The influence of cooling causes $\tilde{\gamma}_{\rm eff}$ to become less steep with radius at lower redshifts, showing that metallicity (which plateaus at $Z \sim 10^{-2} Z_{\odot}$ at low redshifts) has a minor influence on the shock instability, and instead the access to primordial cooling routes dominates the variability of $\tilde{\gamma}_{\rm eff}$ with gas density (as assumed in Birnboim and Dekel, 2003). Overall, these curves indicate that a shock formed due to fast inflowing gas on the super-halo scales should be able to form based on the Birnboim and Dekel (2003) criteria. We examine the presence of a shock by computing the Mach number $\mathcal{M}$ for the inflowing gas based on the effective sound speed which uses $\tilde{\gamma}_{\rm eff}$ (note the difference with the effective CR+thermal mixture sound speed used in Section 4.2.2):

$$\mathcal{M} = v_r \sqrt{\frac{\rho}{\tilde{\gamma}_{\rm eff} P_{\rm tot}}}. \tag{4.19}$$

The results for $\mathcal{M}$ are shown in the bottom row of Fig. 4.16, presenting inflowing gas that is consistently supersonic at large radii at all redshifts. Interestingly, we find that the HD simulation presents a large jump in $\mathcal{M}$ close to $R_{\rm vir,DM}$ from $z = 3$ onwards, in agreement with the signatures of gas virialisation in Section 4.2.1. Similarly, in MHD the profiles for $z = 3$ and $z = 1.5$ show jumps in $\mathcal{M}$, while for $z = 2.5$ and $z = 2.0$ this sharp jump is less noticeable. We recall the projections of the large scale gas flows around NUT in Fig. 4.7a and 4.7b, which show that bursty, strong feedback can easily pierce through accretion shocks, rendering them highly disturbed. This analysis is again witness to the transitory nature of virial shocks in realistic cosmological simulations at high redshift.

The presence of a significantly more enriched halo (see Fig. 4.3) with a large contribution from CR pressure results in a modified $\tilde{\gamma}_{\rm eff}$ which drastically decreases in the inner halo, approaching 4/3. However, similar to the HD and MHD simulations, the criteria of 10/7 is still fulfilled beyond $\gtrsim 0.5 R_{\rm vir,DM}$. As expected from the analysis of the meta-stable CR corona in Section 4.3.1, $\tilde{\gamma}_{\rm eff}$ abruptly rises below $\sim 0.3 R_{\rm vir,DM}$. When we inspect the shape of the $\mathcal{M}$ profiles in the bottom row of Fig. 4.16 we find that, although the gas has similar $\mathcal{M}$ at $\sim 2R_{\rm vir,DM}$ as the HD and MHD simulations, its evolution as it goes to lower r is significantly shallower.

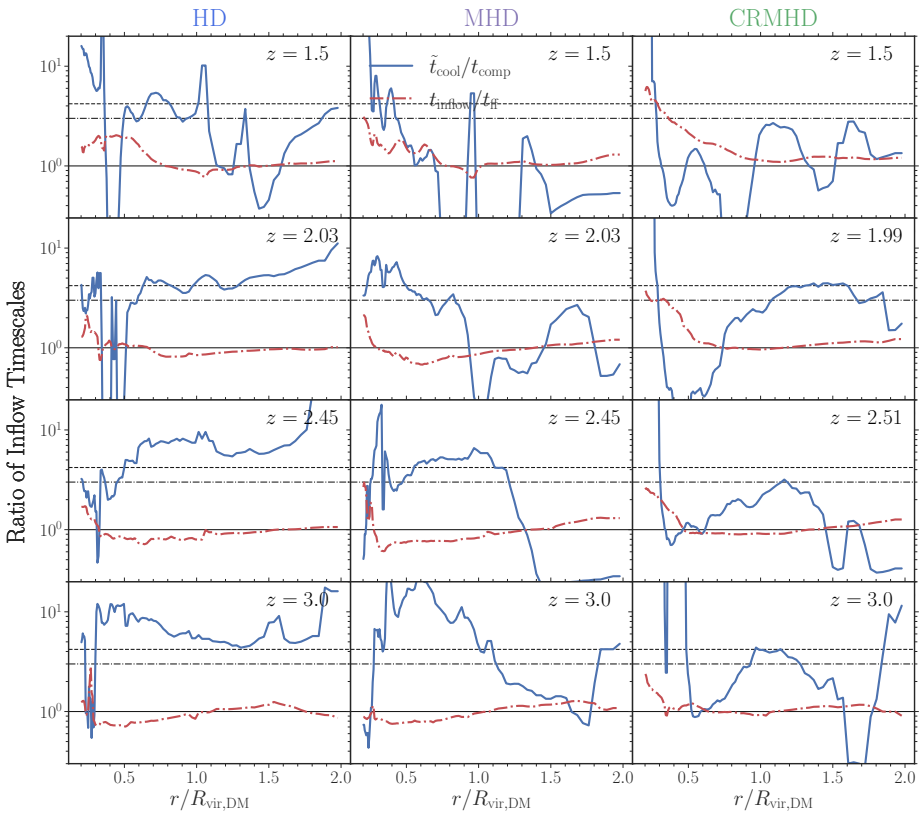


Figure 4.17: Mass-weighted radial profiles of relevant timescales to inflowing gas in the halo, compared across different redshifts for the HD (left column), MHD (middle column), and CRMHD (right column) simulations. The shortest timescales are usually the free-fall time $t_{\rm ff}$ and the inflow time $t_{\rm inflow}$. Compressional timescales $t_{\rm comp}$ are usually larger than the cooling timescales in the CRMHD simulation, while the opposite is true in the HD and MHD simulations. Only withing the very inner region $t_{\rm cool}$ rises over $t_{\rm comp}$ in CRMHD.

Instead, the gas flow achieves a maximum value of $\mathcal{M}_{\rm max} \sim 2 - 2.5$ at $R_{\rm vir,DM}$ in the high redshift snapshots, becoming just transonic at lower redshifts. Even with the large decrease in $\tilde{\gamma}_{\rm eff}$ at $r \leq 0.5 R_{\rm vir,DM}$ which would make it easier for inflowing gas to become supersonic, our results confirm our claim that the formation of the meta-stable CR corona is intimately related to the slowing down of inflowing gas in the CRMHD simulation. This is a clear result of gas becoming more compressible in the CGM of the CRMHD simulation (i.e. shock-heating from sudden conversion of kinetic to thermal energy is highly suppressed).

The previous results appear to suggest that the idealised virial shock stability criteria from Birnboim and Dekel (2003) is not a sufficient condition for the CRMHD simulation. An alternative perspective on this condition was given in Dekel and Birnboim (2006), which we write in our CR+thermal gas mixture as:

$$\tilde{t}_{\rm cool} > \beta(\gamma_{\rm eff})^{-1} t_{\rm comp}, \tag{4.20}$$

where the compression time is defined as $t_{\rm comp} = -(\vec{\nabla} \cdot \vec{u})^{-1}$ and the coefficient $\beta(\gamma_{\rm eff})$ is $\beta(5/3) = 21/5$ and $\beta(4/3) = 3$. We have also defined a cooling timescale for the whole CR+thermal mixture:

$$\tilde{t}_{\rm cool} = \frac{P_{\rm tot}}{(\gamma_{\rm eff} - 1)(n_{\rm H}^2 \lambda_n et - \Gamma_{\rm CR} + \Lambda_{\rm CR})}, \tag{4.21}$$

which effectively captures the net energy loss of the CR+thermal gas mixture. We show the ratio of this cooling timescale to the compression time as blue lines in Fig. 4.17 for the inflowing gas in HD, MHD and CRMHD. We also include horizontal lines showing the location of $\beta(5/3) = 21/5$ (dashed line) and $\beta(4/3) = 3$ (dot dashed line). In agreement with the results explored in Fig. 4.16, this ratio exceeds 21/5 for the HD and MHD simulations at $R_{\rm vir,DM}$. In the MHD simulation (middle column), the effect of higher metal enrichment on the enhanced cooling can easily be seen at early times compared to HD. Despite this, all these representative redshifts after $z = 3$ show a clear transition in the $t_{\rm cool}/t_{\rm comp}$ at $r \sim R_{\rm vir,DM}$. In comparison, the CRMHD simulation never exceeds the 21/5 condition, just grazing it at $r \sim R_{\rm vir,DM}$, which is in agreement with some regions of the spherical surface at $R_{\rm vir,DM}$ fulfilling these conditions while others not (see e.g. Fig. 4.7a). These curves also show that in the inner regions of the halo $r \leq 0.5 R_{\rm vir,DM}$, where $\tilde{\gamma}_{\rm eff} = 4/3$ (corresponding to $\beta(4/3) = 3$ (dot dashed line)), the inflows in CRMHD do not fulfil the condition for an accretion shock in the CR pressure dominated gas, except when the meta-stable CR corona is reached and the cooling time steeply increases. Therefore, we find that the comparison of effective cooling time $\tilde{t}_{\rm cool}$ to the local compression time $t_{\rm comp}$ is a more adequate strategy to determine the stability of an accretion shock in CR halos with realistic cooling/heating with CRs.

In Fig. 4.17 we have also included the ratio of the local inflow time:

$$t_{\rm inflow} = \frac{r}{v_r}, \tag{4.22}$$

to the local free-fall time:

$$t_{\rm ff} = \sqrt{\frac{2r}{\hat{r} \cdot \vec{\nabla}\Phi}}. \tag{4.23}$$

This quantity (shown as red dot dashed lines) allows us to peer further into the dynamical properties of this inflowing gas. The change in $\tilde{t}_{\rm cool}/t_{\rm comp}$ with decreasing

radius can be understood as indicating that gas approaches free-falling velocities as it falls into the halo (shown by the red curve approaching a ratio of unity). At around $r \sim R_{\rm vir,DM}$, the gas shows different behaviours depending on the redshift and the simulation. The HD and MHD simulations show gas crossing the unity boundary (solid black line) at this point, and to continue falling at high speeds, signature of the ballistic cold flow seen in Fig. 4.9. For $z \leq 2$ we instead find the gas reaching a minimum at $r \sim R_{\rm vir,DM}$ and then increasing in its $t_{\rm inflow}/t_{\rm ff}$, a signature of the build up of thermal pressure after the accretion shock. Interestingly, the CRMHD simulation shows this behaviour already at $z \sim 3$, sourced by the quickly developed CR-dominated halo gas. This means that inflowing gas in CRMHD rarely reaches the free-fall velocity, and instead slows down smoothly, becoming more significant at lower redshifts (in agreement with Fig. 4.9).

4.4 Conclusions

In this Chapter, we have extended our understanding of CR feedback in galaxies embedded in a cosmological context by exploring their influence in the halo gas properties and the accretion by streaming filaments. Our main conclusions can be summarised as follows:

1. In the presence of CRs, the circum-galactic medium (CGM) deviates from the CGM properties of the HD and MHD simulations already at $z \sim 6$, rendering it denser, colder and more metal enriched. Inflow rates measured at $0.2\,R_{\rm vir,DM}$ are dramatically slower and less dense than in the HD and MHD simulations, and the CGM temperature does not increase to the virial temperature of the halo as it does in HD and MHD.

2. Clear cold inflows are seen in the HD and MHD simulations, capable of piercing through the super-bubble around the galaxy, while in the CRMHD simulation strong feedback disrupts filaments well beyond the virial region. This causes the inflowing material to be at lower density when approaching the inner halo, but remaining at the temperature set by equilibrium with the UV background.

3. While cold inflows survive up until $z \sim 2.5$ in HD and MHD (reaching $0.2\,R_{\rm vir,DM}$ ballistically), the CRMHD dense filaments are largely disturbed for $z \lesssim 6$. This slow-down of the streaming inflows creates a reservoir of low velocity gas between 0.3 and $0.5 R_{\rm vir,DM}$.

4. Studying radial profiles of the gas dynamics, a centrifugally supported region develops around the halo of the HD and MHD simulations at early times, transitioning to a pressure supported halo for $z \lesssim 3$. In contrast, the CRMHD simulation instead supports a large reservoir of warm neutral and warm ionised gas by CR pressure gradients. The minimal support from rotation is completely lost after a major merger takes place at $z \sim 2.5$, resulting in the observed increase in inflow rate and the rapid growth of stellar mass beyond this point.

5. We find that the reservoir of warm ionised gas outside of $0.2\,R_{\rm vir,DM}$ is CR supported gas which cools below the cooling/heating equilibrium temperature and is then heated by the UV background. We term this region the meta-stable CR corona.

6. Based on our findings, we present an updated analysis of the virial shock stability condition for gas dominated by CR pressure. We find that a virial shock is strongly disturbed by CR feedback, slower inflows and a softer equation of state, resulting in no clear virial shock in the cosmic time explored by our simulations (i.e. down to $z \sim 1.5$).

5

The Dusty-PRISM model

Contents

5.1 Motivation and introduction 113
5.2 The two-size dust model 119
5.3 Polycyclic aromatic hydrocarbons in galaxy formation . 160
5.4 Conclusions 185

5.1 Motivation and introduction

Given the large dust obscuration of highly star forming galaxies, their properties and ISM conditions across cosmic time have been accessed through the information imprinted in dust emission, fine-structure lines, and by molecule energy transitions, originating deep within the multiphase ISM. However, the interpretation of these observations suffers from many uncertainties in the modelling of the dense ISM and its dust content. Firstly, dust properties are usually assumed to closely follow some combination of Milky Way and SMC extinction curves. Such assumptions are unrealistic, as different time scales of metal production, intense radiation densities, or high SN rates and ISM turbulence drive large variations in dust-to-metal (DTM) ratios, dust composition and dust grain sizes. Secondly, as much of the thermo-chemistry taking place in different environments, ranging from the diffuse CGM to the dense ISM, is driven by the interaction of radiation, CRs and gas-phase atoms with dust grains, spatial and temporal variations in these quantities can lead to large departures from equilibrium states or dust models calibrated in the local Universe (see e.g. Galliano et al., 2018, for a recent review). And thirdly, modern, state-of-the-art cosmological simulations that have been used to test galaxy population models in the Early Universe (e.g. Vogelsberger et al., 2020b; Hayward et al., 2021; Lovell et al., 2021) lack the spatial resolution and modelling capabilities to predict the dense gas phases where intense

star formation, dust growth, and molecular chemistry occurs. Hence, both analytical models and large-scale simulations lack the predictive power needed to interpret observations of dust formation and evolution in a realistic ISM across cosmic time.

Beyond its influence on galactic SEDs and observables, dust plays a fundamental role in the thermo-chemistry of the ISM. Dust acts as a catalyst for molecular reactions in the dense gas, playing a fundamental role in the formation of H_2 (see the review by Wakelam et al., 2017) and in driving the rich molecular and pre-organic chemistry within dense clouds (e.g. Tielens and Alexander, 2021). In the small grain regime, polycyclic aromatic hydrocarbons (PAHs) are considered to be the extension of the classical grain distribution into the molecular regime, argued to give rise to pervasive mid-IR emission lines and to act as a tracer of star formation in the local and distant Universe (Peeters et al., 2004). Thanks to the unprecedented spatial resolution of JWST, observations are beginning to quantify the large variation in PAHs' spectral features and their dependence on the local gas phase, metallicity and radiation field (Egorov et al., 2022; Chastenet et al., 2022). This in turn implies that the influence of these molecules on the thermal state of the gas via photo-electric heating (e.g. Bakes et al., 1994; Weingartner and Draine, 2001c), or by the formation of H_2 and other molecules varies with a galaxy's thermodynamic phases, a common assumption of chemical models of the ISM (Ferland et al., 1998; Grassi et al., 2014; Bialy and Sternberg, 2019; Kim et al., 2022; Katz et al., 2022b).

To thoroughly understand the evolution of dust and molecules within the ISM of galaxies across cosmic time, and to discern their impact on galactic properties and the interpretation of observables, it is crucial to develop theoretical models. These models must be rooted in fundamental principles that interlink atomic, molecular, and chemical physics with the processes driving the evolution of galaxies and their multiphase ISM. A crucial outcome of these models is self-consistent, observable predictions. The self-consistency is paramount to more accurately model the complex interplay of these processes, leading to more reliable interpretations of observational data and a deeper insight into galactic evolution. With this goal in mind, we present in this chapter the state-of-the-art Dusty-PRISM model, the first chemical model for the formation and evolution of dust and PAHs fully coupled to the non-equilibrium thermo-chemistry of the ISM and on-the-fly radiation hydrodynamics. This model

builds on the success of the multi-grain, multi-species dust model that we have implemented in RAMSES (Dubois et al., 2024), capable of predicting the influence of different dust processes on the extinction curves of galaxies. At the heart of the Dusty-PRISM-model lie the following goals:

1. Coupling the non-equilibrium evolution of atomic species (e.g. H and He), metals (e.g. C, N, O, Fe, Ne, Mg, Si, S, etc.), and molecules (e.g. H_2 and CO) with the growth, destruction and evolution of dust, in order to directly predict the contribution of each dust component, molecule and gas phase atom to the abundance of metals in the ISM and the CGM.

2. Using direct observables of the ISM to constrain the physical properties of dust and PAHs and the processes that fundamentally affect their presence and influence in galaxies.

3. Directly modelling the interaction of dust grains with the on-the-fly radiation transfer of RAMSES-RTZ, in order to self-consistently predict dust obscuration, dust equilibrium emission, radiation pressure, photo-electric emission, charge exchange, and H_2 and CO formation.

4. Understanding the formation and evolution of dust across cosmic time, from the highly star-forming galaxies in the early Universe, to the irregular dwarf galaxies in the local Universe.

5. Determining the origin of PAHs and their physical properties across the galaxy population, disentangling the influence of stellar and AGN feedback on their evolution.

Dusty-PRISM is a unique code, as it is the first capable of seamlessly coupling the evolution of different dust species with radiation and chemistry, in environments ranging from dense, cold clouds to hot outflows, allowing a full understanding of dust evolution within a cosmological and galactic context. In this Chapter, we introduce the model, summarising it by the overview presented in Fig. 5.1. For a given cell in RAMSES-RTZ, Dusty-PRISM evolves a large system of coupled differential equations,

governing the transfer of dust mass between different grain bins and between the dust and the gas phase. For carbonaceous grains and PAHs this mass transfer is given by:

$$\begin{aligned}\dot{M}_{\mathrm{S,C}} &= \sum_k \dot{M}_{\mathrm{S,C}}^{\mathrm{acc,\,k}} + \dot{M}_{\mathrm{S,C}}^{\mathrm{eje}} + \dot{M}_{\mathrm{S,C}}^{\mathrm{sha}} + \dot{M}_{\mathrm{S,C}}^{\mathrm{RATD}} \\ &\quad + \dot{M}_{\mathrm{S,C}}^{\mathrm{free}} - \dot{M}_{\mathrm{S,C}}^{\mathrm{coa}} - \dot{M}_{\mathrm{S,C}}^{\mathrm{spu}} - \dot{M}_{\mathrm{S,C}}^{\mathrm{SN}}, \qquad (5.1)\\ \dot{M}_{\mathrm{L,C}} &= \sum_k \dot{M}_{\mathrm{L,C}}^{\mathrm{acc,\,k}} + \dot{M}_{\mathrm{L,C}}^{\mathrm{eje}} + \dot{M}_{\mathrm{L,C}}^{\mathrm{free}} + \dot{M}_{\mathrm{S,C}}^{\mathrm{coa}} - \dot{M}_{\mathrm{L,C}}^{\mathrm{RATD}} \\ &\quad - \dot{M}_{\mathrm{L,C}}^{\mathrm{sha}} - \dot{M}_{\mathrm{L,C}}^{\mathrm{spu}} - \dot{M}_{\mathrm{L,C}}^{\mathrm{SN}}, \qquad (5.2)\\ \dot{M}_{\mathrm{S,PAH}} &= \dot{M}_{\mathrm{S,PAH}}^{\mathrm{eje}} + \dot{M}_{\mathrm{S,PAH}}^{\mathrm{sha}} + \dot{M}_{\mathrm{S,PAH}}^{\mathrm{RATD}} + \dot{M}_{\mathrm{L,PAH}}^{\mathrm{evap}} - \dot{M}_{\mathrm{S,PAH}}^{\mathrm{SN}} \\ &\quad - \dot{M}_{\mathrm{S,PAH}}^{\mathrm{free}} - \dot{M}_{\mathrm{S,PAH}}^{\mathrm{coal}} - \dot{M}_{\mathrm{S,PAH}}^{\mathrm{UV}} - \dot{M}_{\mathrm{S,PAH}}^{\mathrm{spu}}, \qquad (5.3)\\ \dot{M}_{\mathrm{L,PAH}} &= \dot{M}_{\mathrm{L,PAH}}^{\mathrm{eje}} + \dot{M}_{\mathrm{L,PAH}}^{\mathrm{sha}} + \dot{M}_{\mathrm{L,PAH}}^{\mathrm{RATD}} + \dot{M}_{\mathrm{S,PAH}}^{\mathrm{coal}} - \dot{M}_{\mathrm{L,PAH}}^{\mathrm{free}} \\ &\quad - \dot{M}_{\mathrm{L,PAH}}^{\mathrm{evap}} - \dot{M}_{\mathrm{L,PAH}}^{\mathrm{spu}} - \dot{M}_{\mathrm{L,PAH}}^{\mathrm{SN}}, \qquad (5.4)\\ \dot{M}_{\mathrm{gas,C}} &= -\sum_k (\dot{M}_{\mathrm{S,C}}^{\mathrm{acc,\,k}} + \dot{M}_{\mathrm{L,C}}^{\mathrm{acc,\,k}}) + \dot{M}_{\mathrm{S,C}}^{\mathrm{spu}} + \dot{M}_{\mathrm{L,C}}^{\mathrm{spu}} + \dot{M}_{\mathrm{S,PAH}}^{\mathrm{spu}} \\ &\quad + \dot{M}_{\mathrm{L,PAH}}^{\mathrm{spu}} + \dot{M}_{\mathrm{S,PAH}}^{\mathrm{UV}} + \dot{M}_{\mathrm{gas,C}}^{\mathrm{sha}}, \qquad (5.5)\end{aligned}$$

and silicate grains by:

$$\begin{aligned}\dot{M}_{\mathrm{S,Sil}} &= \sum_X \sum_k \dot{M}_{\mathrm{S,Sil}}^{\mathrm{acc,\,X,k}} + \dot{M}_{\mathrm{S,Sil}}^{\mathrm{eje}} + \dot{M}_{\mathrm{S,Sil}}^{\mathrm{sha}} + \dot{M}_{\mathrm{S,Sil}}^{\mathrm{RATD}} \\ &\quad - \dot{M}_{\mathrm{S,Sil}}^{\mathrm{coa}} - \dot{M}_{\mathrm{S,Sil}}^{\mathrm{spu}} - \dot{M}_{\mathrm{S,Sil}}^{\mathrm{SN}}, \qquad (5.6)\\ \dot{M}_{\mathrm{L,Sil}} &= \sum_X \sum_k \dot{M}_{\mathrm{L,Sil}}^{\mathrm{acc,\,X,k}} + \dot{M}_{\mathrm{L,Sil}}^{\mathrm{eje}} + \dot{M}_{\mathrm{S,Sil}}^{\mathrm{coa}} - \dot{M}_{\mathrm{L,Sil}}^{\mathrm{RATD}} \\ &\quad - \dot{M}_{\mathrm{L,Sil}}^{\mathrm{sha}} - \dot{M}_{\mathrm{L,Sil}}^{\mathrm{spu}} - \dot{M}_{\mathrm{L,Sil}}^{\mathrm{SN}}, \qquad (5.7)\\ \dot{M}_{\mathrm{gas,\,X}} &= -\sum_k (\dot{M}_{\mathrm{S,Sil}}^{\mathrm{acc,\,X,k}} + \dot{M}_{\mathrm{L,Sil}}^{\mathrm{acc,\,X,k}}) + \dot{M}_{\mathrm{S,Sil}}^{\mathrm{spu\,X}} + \dot{M}_{\mathrm{L,Sil}}^{\mathrm{spu\,X}} + \dot{M}_{\mathrm{gas,Sil}}^{\mathrm{sha\,X}}, \qquad (5.8)\end{aligned}$$

where the subscripts S denotes small grain bins, C carbonaceous grains, PAH PAH molecules, and Sil silicate grains. The sum over ions for a given element X is computed over index k. The super-scripts indicate abbreviations for the different dust (and PAH) processes contributing to the evolution of a particular dust bin, with acc referring to accretion (Section 5.2.2), eje to stellar ejecta (Section 5.2.1), sha to turbulent shattering (Section 5.2.6), coa to turbulent coagulation (Section 5.2.7), RATD to destruction by radiative torques (Section 5.2.10), spu to thermal sputtering (Section 5.2.3 and 5.3.2), free for freezing of PAHs onto carbonaceous grains (Section 5.3.5), coal for the coalescence of small PAHs to form large PAH clusters (Section 5.3.4) and its inverse

process due to evaporation as evap, and SN for the non-thermal sputtering in SN shocks (Section 5.3.2).

For each cooling step in the simulation, we solve this system of equations using a Runge-Kutta 4th order solver (Iserles, 2008). We apply the 10 per cent rule as it is done in the thermo-chemistry step of RAMSES-RT (Rosdahl et al., 2013): for each cell, the chemistry is solved quasi-implicitly taking the full RT step, and if the variation in a dust quantity exceeds 10% of its original value, the step is repeated with a smaller timestep than the RT, effectively performing a sub-cycle. In Dusty-PRISM we neglect the differential dynamical motion of dust with respect to gas, therefore, the dust content of each bin and its chemical composition can be treated as passive variables that are transported along with the flow of gas in the exact same way as metals are transported in the gas phase. This is justified because of the relatively short stopping time associated to Epstein aero-dynamical drag in dense gas $t_{\rm st} \simeq 0.5\, a_{0.1} (n_{\rm H}/1\,{\rm cm}^{-3})^{-1} (c_{\rm s}/10\,{\rm km\,s}^{-1})^{-1}\,{\rm Myr}$ (where $a_{0.1}$ is the grain radius in units of 0.1 μm, $n_{\rm H}$ is the H number density, and $c_{\rm s}$ is the gas sound speed) compared to dynamical time $t_{\rm dyn} \simeq 10\,(L/100\,{\rm pc})(\sigma_{\rm gr}/10\,{\rm km\,s}^{-1})^{-1}\,{\rm Myr}$, where $\sigma_{\rm gr}$ is the grain velocity dispersion and L the turbulence injection scale. The constraint on the stopping time gives a diffusion length scale of $L \simeq 5\, a_{0.1} (n_{\rm H}/1\,{\rm cm}^{-3})^{-1} (\sigma_{\rm gr}/c_{\rm s})\,{\rm pc}$, which is in general below the resolution scale of this work (see also the discussion in Commerçon et al., 2023).

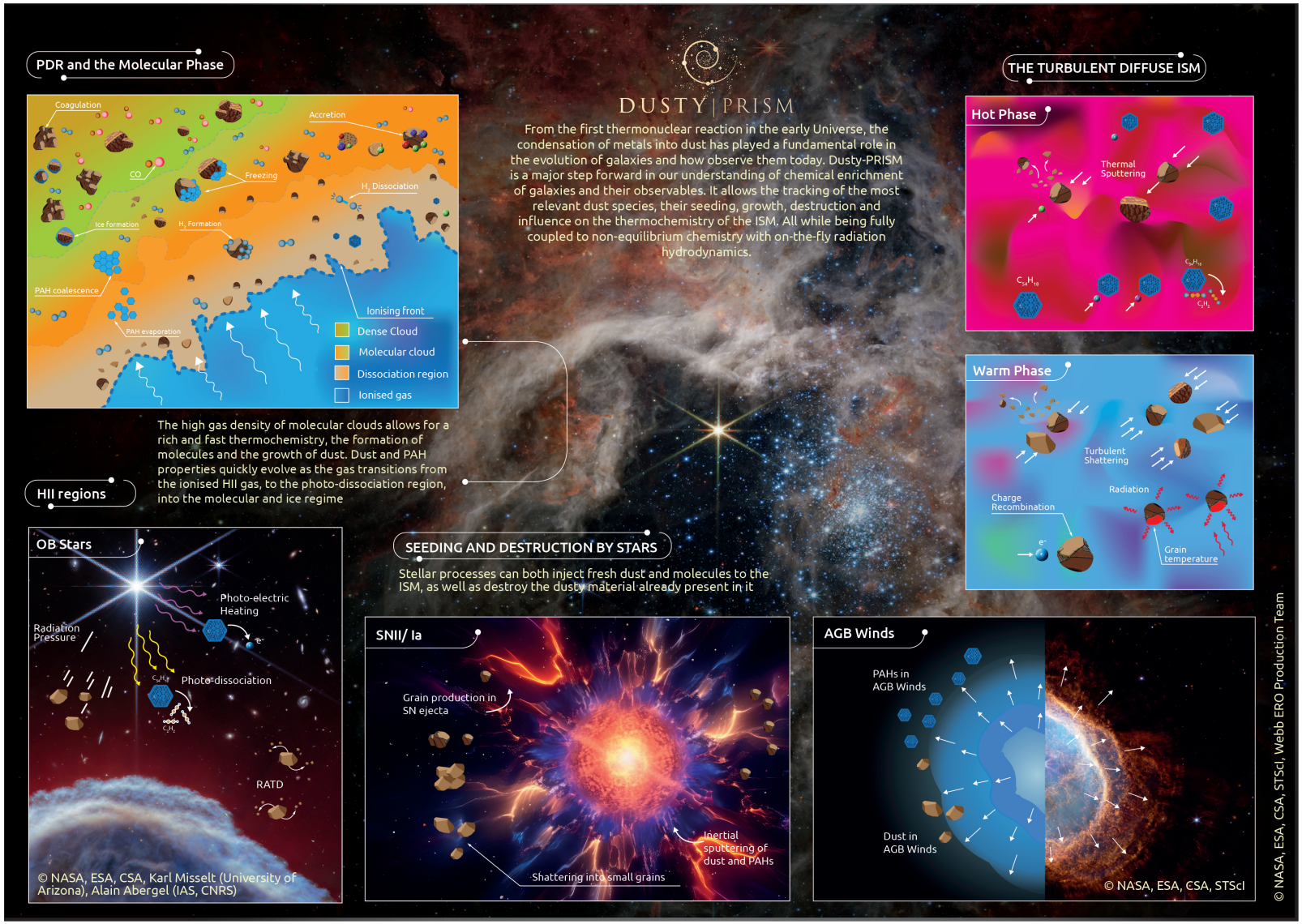


Figure 5.1: Overview diagram of the Dusty-PRISM model.

5.2 The two-size dust model

The dust size distribution is the result of the complex interplay between dust formation and destruction processes. As the interstellar extinction curve spans a large range of wavelengths, it is reasonable to expect that for each wavelength λ there is a grain radius a for which $2\pi a/\lambda \sim 1$, meaning that the extinction properties are maximal. The grain-size distribution (GSD) derived from this premise extends over many orders of magnitude and is usually explained by two fundamental processes: collisional fragmentation and turbulent grain growth. If one considers an initial distribution dominated by large dust grains (maybe seeded by AGB winds or SNe Type II ejecta, but see Section 5.2.1 for further details) large relative velocities of grains can easily result in strong collisions that break apart these grains into fragments of smaller sizes. This process of shattering was originally coined by Hellyer (1970) in the context of asteroid collisions, and later introduced within the framework of interstellar dust grains by Dorschner et al. (1982). We point the interested reader to the simplified derivation in chapter 5.5.2 of Krügel and Endrik (2008), but the fundamental result is the prediction for a power-law grain distribution such that the number density n of grains of radius a scale according to $n(a) \propto a^{-3.5}$, in agreement with the canonical Mathis-Rumpl-Nordsieck (MRN) distribution (Mathis et al., 1977). While the collisional fragmentation model to evolve an initial large dust grain distribution to a power law distribution is based on the conservation of dust mass in high velocity collisions hence ignoring evaporation, (see also Section 5.2.6), turbulent grain growth explains the growth of dust mass after it is injected into the ISM.

There is well established observational evidence for supersonic ISM turbulence, which according to theory and simulations gives rise to a log-normal[1] distribution of gas densities (see reviews by Low and Klessen, 2004; Elmegreen and Scalo, 2004; McKee and Ostriker, 2007; Hennebelle and Falgarone, 2012). In Section 5.2.2 we carefully examine how the growth of dust grains by gas-phase accretion of metals depends on gas density. Given the large variance of the gas density field caused by compressible turbulence, dust accretion takes place on different timescales throughout a turbulent ISM. In the context of the most prevalent GSD, the assumption that

[1]There is strong evidence that the density PDF deviates from log-normal at high Mach numbers (e.g. Federrath and Klessen, 2012; Hopkins, 2013; Federrath and Banerjee, 2015; Hennebelle et al., 2024).

gas and dust grains are highly coupled then means that dust grain size correlates with gas density distribution. Even if the initial dust grain size distribution follows a power law, the memory of the initial conditions will be quickly erased by the underlying gas density field (Mattsson et al., 2020).

These two scenarios explain the origin of two widely used GSDs: power-laws and log-normals (e.g. Compiègne et al., 2010; Jones et al., 2017; Zubko et al., 2004; Hensley and Draine, 2021). However these models make different assumptions about grain type and GSD spatial variation. Nevertheless, both models agree (to some extent) on the following aspects (Krügel and Endrik, 2008):

- The sizes of very small carbonaceous grains (VSGs) need to peak in the range between 3Å $\leq a \leq$ 30Å, so that they can be stochastically heated to the high temperature necessary to explain the mid-IR features (see Section 5.3).
- Small (but larger than VSGs) grains in the range from $\sim$ 5 nm to $\sim$ 30 nm contribute to the mid-IR continuum. Whether or not silicate grains are also found at these sizes determines whether there are 9.7 and 18 μm emission features due to O-Si-O bending.
- The sizes of large grains need to peak at $\sim$ 0.1 μm and have a sharp cut-off at larger a. This constraint arises from the FIR emission curve observed in the local Universe, as larger grains would shift the peak of the modified blackbody emission.

Therefore, if one ignores the source of aromatic features attributed to VSGs for now, the GSD can be roughly described by a population of small grains with $a \leq 30$ nm and a population of large grains with $a > 30$ nm. This is considered to be the minimal two-size approximation for the evolution of the GSD in the ISM (Hirashita, 2015), and capture of the main features of the full GSD (Asano et al., 2013). Similar to the introduction of this two-size approximation in previous galaxy formation simulations (Aoyama et al., 2017; Gjergo et al., 2018; Granato et al., 2021), we model small and large grains with central bin sizes of $a_{\rm S} = 5$ nm and $a_{\rm L} = 0.1$ μm, respectively. We assume that the underlying GSD is a modified log-normal:

$$n(a)\mathrm{d}a = \frac{C}{a^4} \exp\left(\frac{[\log(a/a_0)]^2}{2\sigma^2}\right) \mathrm{d}a, \tag{5.9}$$

where the grain number density $n(a)$ has been defined as the number of grains per unit volume with radius in the range $a \to a + \mathrm{d}a$. This log-normal is centred at a_0, which takes the value of a_S and a_L for the small and large grain bins respectively, and with standard deviation given by σ. The normalisation constant C is obtained for each cell and each grain type j:

$$C_j = \frac{m_j n_{\mathrm{d},j}}{\int_{a_{\mathrm{min},j}}^{a_{\mathrm{max},j}} \frac{4}{3}\pi \frac{s_j}{a} \exp\left(\frac{[\log(a/a_0)]^2}{2\sigma^2}\right) \mathrm{d}a}, \tag{5.10}$$

which arises from relating the local dust density to the integral of the underlying distribution. In the process, we have used the definitions of the mass of a single dust grain $m_j = 4/3\pi s_j a^3$, the dust number density $n_{\mathrm{d},j}$ and the grain material density s_j. In addition to dividing the dust grain population into large and small size bins, we separate the dust composition into amorphous carbonaceous grains and silicate grains with a fixed stoichiometry for a given simulation.

We briefly review our choice of silicate properties. Silicate compounds are built around the silica tetrahedra $\mathrm{SiO_4^{4-}}$. Due to their overall negative charge, they pair by ionic bonds with interstellar cations, which due to cosmic abundance are limited to $\mathrm{Mg^{2+}}$ and $\mathrm{Fe^{2+}}$ (e.g. Asplund et al., 2009). Olivine and pyroxene are usually considered the relevant silicate compositions for astrophysical dust grains. Olivine crystals are characterised by a orthorhombic network of silica tetrahedrae joined by dications, while in pyroxene the crystalline structure can be either orthorhombic or monoclinic. The general composition of olivine is $\mathrm{Mg_{2x}Fe_{2-2x}SiO_4}$, and of pyroxene is $\mathrm{Mg_xFe_{1-x}SiO_3}$, with x ranging from 0 to 1 depending on the Mg-Fe inclusion ratio. As Mg and Fe can replace each other on the crystalline lattice, both olivine and pyroxene can be considered as a solid solution of magnesium and iron. Most of the silicates observed in the Galactic diffuse ISM show the characteristic broad mid-IR resonances at 9.7 μm(Si-O stretching) and 18 μm(O-Si-O bending) of amorphous silicates. The degree of crystallinity, defined as the mass ratio of crystalline silicate to the total silicate mass, has been found to be $\sim 1\%$ in the diffuse ISM (Kemper et al., 2004; Kemper et al., 2005), while observations of the silicate absorption/emission features near asymptotic giant branch (AGB) stars indicate a non-negligible fraction of crystalline silicates (Sylvester et al., 1999; Kemper et al., 2001; Suh, 2002; Jones et al., 2012; Marini et al., 2023). We assume that silicate amorphisation processes

(e.g. CRs and high velocity ions, see Bringa et al., 2007; Jäger et al., 2003) are sufficiently fast to maintain a negligible contribution of crystalline silicates to the galactic dusts' physical and optical properties.

Since we fix the silicate composition in any given Dusty-PRISM simulation, our choice will influence the exact depletion of refractory elements from the gas phase. Given the modelling difficulty involved, we leave the exploration of different silicate compositions for future work and instead assume a composition of olivine with equal amounts of Mg and Fe inclusions ($MgFeSiO_4$) as commonly done to represent the interstellar silicate absorption profiles (Draine et al., 1984; Li and Draine, 2001; Kemper et al., 2004; Chiar and Tielens, 2005), although we note that there is tentative evidence of Mg-rich silicates in starburst systems (Min et al., 2007).

This minimal model (two grain size bins, and two chemical species, i.e. carbonaceous and silicate grains) is capable of capturing the major features of the Galactic GSD, while having a minimum memory impact and simplifying the number of inter-grain reaction rates.

5.2.1 Grain seeding

The amount of silicates $m_{\rm key}$, traced by its key element (here Si), released by a single star is given by the mass of the least abundant element entering its composition:

$$m_{\rm key} = \min_{\ell={\rm Mg,Fe,Si,O}} \left(\frac{M_\ell}{A_\ell N_\ell} \right) , \tag{5.11}$$

with M_ℓ the total mass of the ℓ-th element released by the star, A_ℓ its atomic weight and N_ℓ the number of ℓ-th element atoms entering the composition of the silicate. The key element condensates within the ejecta into dust of mass $D^k_{{\rm ej,sil},\ell}$ with a given efficiency $\delta_{\rm Sil}$ according to the formula:

$$D^k_{{\rm ej,sil},\ell} = \delta^k_{\rm Sil} m_{\rm key} A_\ell N_\ell \tag{5.12}$$

which guarantees a constant mass ratio with values $A_\ell N_\ell / \sum(A_\ell N_\ell) = 0.14, 0.33, 0.16,$ 0.37 for ℓ = Mg, Fe, Si, and O respectively for the case of $x = 1$ olivine[2]. The superscript k denotes the origin of the stellar mass release with k = AGB, SNII or SNIa. The condensation efficiency for SNII following Dwek (1998) is equal to

[2] $A_\ell N_\ell / \sum(A_\ell N_\ell) = 0.11, 0.24, 0.24, 0.41$ for ℓ = Mg, Fe, Si, and O respectively for the case of $x = 1$ pyroxene.

$\delta_{\rm Sil}^{\rm SNII} = 0.8$[3]. For AGB stars, the condensation efficiency depends on the ratio of C/O: if C/O ≥ 1 all the oxygen is associated to carbon in CO molecules, and, hence, silicates do not condensate anymore due to the unavailability of O, while with C/O < 1 oxygen is still available to condense into silicates. We adopt $\delta_{\rm Sil}^{\rm AGB,C/O<1} = 0.8$ and $\delta_{\rm Sil}^{\rm AGB,C/O\geq1} = 0$ as in Dwek (1998). For the same reasons, accretion of elements onto silicates from the ISM will be limited by the least abundant of the elements in the ISM entering the composition of the grain, replacing the total mass M_ℓ released by the star by the gas mass of the given element ℓ in the cell.

Similarly to silicates, the amount of carbonaceous dust and its condensation efficiency $\delta_{\rm C}^k$, vary with the nature of the stellar ejecta. We assume $\delta_{\rm C}^{\rm SNII} = 0.5$ and $\delta_{\rm C}^{\rm SNIa} = 0.5$, while for AGB stars this efficiency depends on the ratio of C/O in the ejecta. If the ratio C/O < 1, then all the C elements form CO molecules that are then not available for dust $\delta_{\rm C}^{\rm AGB,C/O<1} = 0$, while for C/O ≥ 1 the efficiency is 1 with a mass released into C dust:

$$D_{\rm ej,C}^{\rm AGB} = \delta_{\rm C}^{\rm AGB,C/O\geq1} \left(M_{\rm C}^{\rm AGB} - \frac{A_{\rm C}}{A_{\rm O}} M_{\rm O}^{\rm AGB} \right) . \tag{5.13}$$

The dust produced in stellar ejecta is divided into a population of small and large grains, i.e. $\dot{D}_{{\rm ej},i,{\rm S}}^k = f_{{\rm ej},i,{\rm S}} \dot{D}_{{\rm ej},i}$ and $\dot{D}_{{\rm ej},i,{\rm L}}^k = (1 - f_{{\rm ej},i,{\rm S}}) \dot{D}_{{\rm ej},i}$, where $f_{{\rm ej},i,{\rm S}}$ is the fraction of small grains released for a given chemical type i (carbonaceous or silicate grains). For sake of simplicity, we assume that all the dust released in the ejecta condenses into the large grain population[4] only, thus, $f_{{\rm ej},i,{\rm S}} = 0$ (see Appendix B in Dubois et al. 2024 for the predictions of extinction curves with different values of $f_{{\rm ej},i,{\rm S}}$). These efficiencies can easily be used with the metal yields of any stellar model. We use the stellar yield models of RAMSES-RTZ (Katz et al., in prep.). Finally, it is important to note that the predicted and observed dust condensation efficiencies are very uncertain and can vary by up to an order of magnitude (see Schneider and Maiolino, 2024).

[3]Note that, contrary to Dwek (1998), we do not consider dust formation in SN Ia, as models suggest that formation efficiency is drastically reduced in SN Ia(e.g. Nozawa et al., 2011), and observations have yet to find newly formed dust around them (Gomez et al., 2012).

[4]There is tentative evidence for the formation of PAHs in AGB winds (Allamandola et al., 1989), and multiple theoretical chemical mechanisms have been proposed to explain their abundance (Frenklach, n.d.; Cherchneff et al., 1992; Cau, 2002): we will explore this mechanism as a source of PAHs in the future.

5.2.2 Gas-phase accretion

The primary mode of dust mass growth in the ISM is by accretion of refractory elements from the gas phase. As in Dubois et al. (2024), we model accretion of metals onto grains by a modified version of the collisional argument laid out in Dwek (1998). The accretion rate onto dust is given by:

$$\dot{\rho}_{\mathrm{acc},\,j} = \left(1 - \frac{\rho_{d,j}}{\rho_{\mathrm{Z},\,j}}\right) \frac{\rho_{d,j}}{\tau_{\mathrm{acc},\,j}}, \tag{5.14}$$

where the index j runs over each dust bin (small, large) and chemical species (silicate, carbonaceous), $\rho_{d,j}$ is the density of dust in bin j, and $\rho_{\mathrm{Z},\,j}$ is the density of metals (combining gas and dust in bin j). The accretion timescale is written as:

$$(\tau_{\mathrm{acc},\,j})^{-1} = \alpha \frac{\pi \overline{a}_j^2}{f_X m_{\mathrm{gr},j}} \rho_X v_X, \tag{5.15}$$

where $m_{\mathrm{gr},\,j}$ is the mass of a single grain of type j, α is the sticking coefficient, and $\pi\overline{a}_j^2$ is the effective grain cross-section, which considers the effect of Coulomb focusing (Weingartner and Draine, 1999) with the factor F_C as $\pi\overline{a}_j^2 \equiv F_C \pi a_j^2$. The quantities ρ_X, v_X and f_X denote the gas-phase mass density, gas thermal velocity and fractional contribution of the *limiting* element X to the grain j composition. The concept of *limiting* element requires some care. In our current implementation for dust composition in Dusty-PRISM, the stoichiometry of a given dust species is kept fixed across the simulation. This does not complicate the treatment of accretion for amorphous carbonaceous grains, as for these $X = C$. However, when determining the accretion rate of the different elements that compose a silicate grain, we ensure that the increase in dust mass corresponds to a decrease in metal mass in order to keep the stoichiometry of a given grain fixed. This means that at a given time, the abundance of a particular element X contributing to the silicate composition may be lower and/or the element X may experience a lower interaction rate with the grain, hence *limiting* the final growth of mass by accretion. More specifically, we make use of the following 'frequentist argument': given that the mean Maxwellian thermal velocity is given by $v_X = (8k_{\mathrm{B}}T/(\pi m_X))^{1/2}$, we compute the *limiting* element parameters for the accretion time-scale using:

$$\frac{\rho_X v_X}{f_X} = \left(\frac{8k_{\mathrm{B}}T}{\pi}\right)^{1/2} \min\left[\frac{\rho_l}{f_l m_l^{1/2}}\right]_{l=\mathrm{Mg,Fe,Si,O}}, \tag{5.16}$$

where l runs over the gas elements that contribute to the silicate composition and m_l is the atomic mass of element l.

The effective grain cross-section includes the contribution from electrostatic interaction between ionised gas and dust grains and requires knowing a dust grain's charge acquired through many ISM processes. Collisions of dust grains with electrons are very frequent in the ionised medium, leading to negatively charged grains (Draine and Sutin, 1987; Draine, 2011), while in high radiation environments, energetic photons can cause the photo-emission of electrons, giving dust grains a positive charge (Bakes et al., 1994; Weingartner and Draine, 2001b). Additionally, in high density plasmas several processes, such as ion collisions, secondary electron production and field emission (Kimura et al., 1998), can further influence the total grain charge. This combination of processes results in a large numerical network which would add a significant computational cost to Dusty-PRISM, so we use the fitting results provided by Ibanez-Mejia et al. (2019) instead to compute grain charge. These read, for the charge centroid $\langle Z \rangle$ and the charge distribution width σ_Z:

$$\langle Z \rangle = k \left[1 - \exp\left(-\frac{G_0 \sqrt{T}}{n_e h_Z} \right) \right] \left(\frac{G_0 \sqrt{T}}{n_e} \right)^{\alpha} + b, \tag{5.17}$$

$$\sigma_Z = \begin{cases} c^+ \left[1 - \exp\left(-\frac{\langle Z \rangle}{\eta^+} \right) \right] + d, & \text{if } \langle Z \rangle > 0, \\ c^- \left[1 - \exp\left(-\frac{|\langle Z \rangle|}{\eta^-} \right) \right] + d, & \text{if } \langle Z \rangle \leq 0, \end{cases} \tag{5.18}$$

with G_0 the strength of the local radiation field, n_e the electron density (both obtained locally from the simulation) and the values of the fitting parameters $\alpha, k, b, h_Z, c^+, \eta^+, d, c^-$ and η^- are given in in tables 1 and 2 of Ibanez-Mejia et al. (2019). We model the local dust charge distribution $f(Z_{\mathrm{g},i})$ for each grain as a Gaussian with charge centroid $\langle Z \rangle$ and width σ_Z, which allows us to obtain on-the-fly the Coulomb focusing factor F_{C} (Weingartner and Draine, 1999):

$$F_{\mathrm{C}}(a, T, Z_k) = \sum_i f(Z_{\mathrm{g},i}) B(Z_{\mathrm{g},i}, Z_k, a, T), \tag{5.19}$$

where the sum goes over each charge state (small grain, large grain, silicate, carbonaceous) present in the distribution of the grain charge Z_{g}, Z_k is the charge of the ion and where (Draine and Sutin, 1987):

$$B(Z_{\mathrm{g},i}, Z_k, a, T) = \begin{cases} \exp\left(-\frac{Z_{\mathrm{g},i} Z_k e^2}{k_{\mathrm{B}} T a} \right), & \text{if } Z_{\mathrm{g},i} Z_k > 0, \\ \left(1 - \frac{Z_{\mathrm{g},i} Z_k e^2}{k_{\mathrm{B}} T a} \right), & \text{if } Z_{\mathrm{g},i} Z_k < 0, \\ 1 + \left(\frac{\pi Z_k^2 e^2}{2 k_{\mathrm{B}} T a} \right), & \text{if } Z_{\mathrm{g},i} = 0. \end{cases} \tag{5.20}$$

In Fig. 5.2 we show the value of $F_{\rm C}$ for ISM phases traditionally considered in dust charging models (see Table 1 in Weingartner and Draine, 1999). We fix the charge of the ion to be $Z_k = 1$ (e.g. CII), such that we can compare with the values of the Coulomb correction factor presented in Figure 1 of Weingartner and Draine (1999) (black lines, separated for silicate and graphite grains). The Ibanez-Mejia et al. (2019) fitting functions only extend to 0.1 μm, so we have extrapolated them by linearly interpolating in log-log space (low opacity coloured curves). Similarly to Weingartner and Draine (1999), we find that the Coulomb correction factor spans a large range of values for different ISM conditions and grain sizes, causing a significant variation in the accretion timescale that has been overlooked in dust evolution models. Our computed curves show qualitatively similar trends to Weingartner and Draine (1999), although with very important differences for both larger grains and silicate grains. An important prediction of their model is that large (~ 0.1 μm) carbonaceous grains show $F_{\rm C}$ dropping to $\sim 4 \times 10^{-12}$, effectively halting the accretion of carbon in this phase, and allowing the gas-phase carbon to be available for CO formation. However, we find that the prediction from Ibanez-Mejia et al. (2019) instead shows $F_{\rm C}$ for carbonaceous grains to scale similarly to $F_{\rm C}$ for the silicate grains. The reason for this difference is shown in Figure 6 of Ibanez-Mejia et al. (2019): the modelling in Weingartner and Draine (1999) assumes a linear scaling of $\langle Z \rangle$ with the charging parameter $G_0\sqrt{T}/n_e$ for the fitting to the results of Weingartner and Draine (2001c), but this is a very poor approximation to the true behaviour of the dust charge distribution, resulting in an underestimation of grain charging in such environments. The rest of the phases roughly agree with Weingartner and Draine (1999) for the carbonaceoustext grains. In the WNM and WIM, silicate grains show consistently lower ($\sim \times 1/4$) Coulomb enhancements than the values obtained in Weingartner and Draine (1999) and those that we assumed in Dubois et al. (2024).

Efficient accretion occurs in the dense, cold phases of the ISM, which are barely reproduced by current cosmological galaxy simulations. In Dubois et al. (2024) we found that simulations with different maximum spatial resolution (from $\Delta x = 72$ pc to 9 pc resolution) led to a significant increase (up to a factor of 2) in the final DTM. This lack of numerical convergence for the DTM can be attributed to the lack of very cold and dense gas where accretion of metals from the gas phase is expected

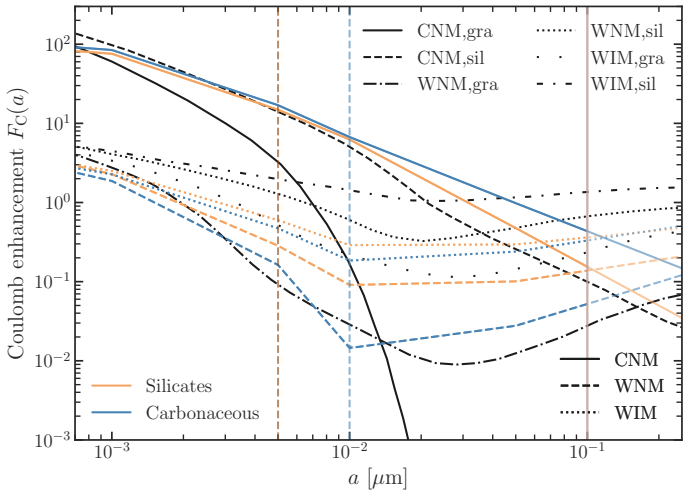


Figure 5.2: Coulomb enhancement factor F_C as function of grain size for different ISM phases assuming a colliding ion with charge $Z_k = 1$. Black lines correspond to the results of Weingartner and Draine (1999) for graphite and silicate, while blue and sandy brown colours correspond to our computed F_C for carbonaceous and silicate grains using the fitting functions (Equations 5.17 and 5.18) presented in Ibanez-Mejia et al. (2019). Vertical lines indicate the centroids of our dust size bins in our fiducial model (see Section 5.3), with sandy brown colours for the silicates and blue for the carbonaceous, with the line style indicating the bin size (large in solid, small with a dashed line).

to be more efficient (see Equation 5.15). To alleviate this problem, in Dubois et al. (2024), we employ a sub-grid model for the gas density similar to the one used in the MTT star formation model (see Section 2.1.3). Sub-grid accretion is locally estimated by assuming that a cell's gas density is actually the mean gas density $\overline{n}$ of a log-normal PDF of gas densities shaped by turbulence:

$$p(s) = \frac{1}{\sqrt{2\pi}\sigma_s} \exp\left(-\frac{(s-s_0)^2}{2\sigma_s^2}\right), \tag{5.21}$$

where $s = \log(n/\overline{n})$, $s_0 = -\sigma_s^2/2$ and $\sigma_s = \log(1 + b^2\mathcal{M}^2)$, with b the compression ratio (we take $b = 0.4$ for a mixture of compressible and solenoidal turbulence which is the same value used in the MTT model for star formation efficiency) and $\mathcal{M}$ the turbulent Mach number. The effective accretion timescale $t_{\rm acc,eff}$ is obtained by integrating the mass accretion rate over the log-normal PDF for a given set of mean density, temperature and metallicity $(\bar{n}, \bar{T}, \bar{Z})$, hence:

$$\frac{t_{\rm acc}(\bar{n}, \bar{T}, \bar{Z})}{t_{\rm acc,eff}} = \int_{-\infty}^{s_{\rm max}} \frac{t_{\rm acc}(\bar{n}, \bar{T}, \bar{Z})}{t_{\rm acc}(n, T, Z)} \frac{n}{\bar{n}} p(s) ds\,, \tag{5.22}$$

up to a maximum density $s_{\rm max} = \log(n_{\rm max}/\bar{n})$, where the maximum density is $n_{\rm max} = 10^4\,{\rm H\,cm^{-3}}$, i.e. the density where grains start to be significantly coated with a water ice mantle ($n \geq 10^3\,{\rm H\,cm^{-3}}$ Cuppen and Herbst, 2007; Hollenbach et al., 2008; Lamberts

et al., 2014; Elyajouri et al., 2024) which suppresses the accretion of refractory material onto the grain surface. This unresolved density distribution should also give rise to an unresolved temperature and gas metal density distribution. However, there is no simple correspondence between these three random fields. Instead, we assume that the average metal fraction and temperature are those given by the local value of these quantities (i.e. $T = \overline{T}$ and $n_X/n_{\rm H} = \overline{n}_X/\overline{n}_{\rm H}$). This leads to:

$$\begin{aligned} \frac{t_{\rm acc}(\bar{n},\bar{T},\bar{Z})}{t_{\rm acc,eff}} &= \int_{-\infty}^{s_{\rm max}} \exp(2s)p(s)ds \\ &= \frac{e^{\sigma_s^2}}{2}{\rm Erfc}\left(\frac{3\sigma_s^2/2 - s_{\rm max}}{\sqrt{2}\sigma_s}\right), \end{aligned} \tag{5.23}$$

where Erfc is the complementary error function.

Many different expressions have been suggested in the literature for the sticking coefficient $\alpha(T)$ (see the discussion in Zhukovska et al., 2016), but much of our knowledge of the sticking probability of gas phase atoms onto grain surfaces is based on the physical-chemistry modelling and experiments that have studied the sticking of H atoms to form molecular hydrogen either by the Langmuir-Hinshelwood or the Eley-Rideal mechanisms (see e.g. Chaabouni et al., 2012; Le Bourlot et al., 2012; Bron et al., 2014, but also Section 5.2.8). It remains unclear how heavier atoms (that are also found in different ionisation states in the ISM) stick to surface grains, which has resulted in one-zone models simplifying the problem by assuming $\alpha = 1$ (e.g. Asano et al., 2013; McKinnon et al., 2016; Vogelsberger et al., 2019; Li et al., 2019; Lewis et al., 2023; Choban et al., 2022; Hu et al., 2023, either at all T or only for a range of low temperatures $\lesssim 300$ K). Zhukovska et al. (2016) have shown that using a fixed value of $\alpha = 1$ tends to over predict the depletion of gas-phase metals in the Galactic ISM, and instead argues that a lower value of $\alpha = 0.3$ is more appropriate to match current constraints of metal depletion (e.g. Jenkins, 2009). We identify the choice of $\alpha(T)$ as a significant source of uncertainty in our model (as it has been for previous implementations of dust evolution in one-zone models and hydrodynamical simulations Hirashita and Kuo, 2011; Grassi et al., 2014; Zhukovska et al., 2016; Aoyama et al., 2017; Gjergo et al., 2018) and leave the sticking coefficient as a free parameter. Sticking coefficients values we explored are detailed in appendix D of Dubois et al. (2024).

	s [g cm^{-3}]	U_0 [eV]	K	$\langle Z_j \rangle$	$\langle m_j^{\rm atom} \rangle$ [a.m.u.]	$\langle N_{\rm val} \rangle$	$Q_{\rm d}^*$ [dyn cm g^{-1}]
Carbon	2.2	4.0	0.61	6	12.011	4	8.9×10^9
Silicate	3.3	5.7	0.10	12	24.605	5	4.3×10^{10}

Table 5.1: Dust material properties.

5.2.3 Thermal sputtering

Dust particles in high temperature coronal gas are subject to the destructive effect of collisions with fast moving ions. If the kinetic energy of the collision is sufficiently large, the energy of a dust atom may be able to overcome the dust grain binding energy. This process of sputtering is capable of removing a large fraction of the dust grain mass in high temperature gas and is hence of high importance for the hot phase DTM. We follow a derivation similar to the one outlined in Kirchschlager et al. (2019), which is similar to the original approach in Tielens et al. (1994) but considers the finite size a of the target dust grain and the effect of grain charge in the interaction energy. The thermal sputtering rate is a function of the velocity of the incident gas particles (ions, atoms or molecules) which is determined by the gas temperature (e.g. Barlow et al., 1978; Draine and Salpeter, 1979):

$$\frac{{\rm d}a}{{\rm d}t} = \frac{\langle m_j^{\rm atom} \rangle}{2 s_j} \Sigma_k n_k \langle Y_k v \rangle, \tag{5.24}$$

where $\langle m_j^{\rm atom} \rangle$ is the average atomic mass of the dust grain, s_j is the material density of the dust grain, and $\langle Y_k v \rangle$ is the sputtering yield of gas species k defined as the mean number of emitted atoms per incident particle averaged over the Maxwellian distribution $f_{\rm M}$:

$$\langle Y_k v \rangle = \int_0^\infty Y_k(E) v f_{\rm M}(v) {\rm d}v, \tag{5.25}$$

where $E = m_k v^2/2 + Z_k e Q_{\rm j}/a_{\rm j}$ is the energy of the incident gas particle, Z_k is the charge of the ion, e is the elementary charge, and $Q_{\rm j}$ and $a_{\rm j}$ are the charge and radius of the dust grain j involved in the collision. The sputtering yields due to particle k impacting at normal incidence with energy E is given by Equation 11 of Nozawa et al. (2006):

$$Y_k(E) = 4.2 \times 10^{14} \frac{S_k(E)}{U_0} \frac{\alpha_k(\mu_k)}{K \mu_k + 1} \left[1 - \left(\frac{E_{\rm sp}}{E} \right)^{\frac{2}{3}} \right] \left(1 - \frac{E_{\rm sp}}{E} \right)^2, \tag{5.26}$$

where U_0 is the surface binding energy in units of eV, $\mu_k = \langle m_j^{\rm atom} \rangle / m_k$ is the ratio of the average atomic mass number of the dust grain and the impinging ion, α_k is

a function of μ_k and is discussed further below, and K is a free parameter which is used to calibrate this analytic function for $Y_k(E)$ to experimental data (Tielens et al., 1994). Incident gas particles can cause sputtering of dust grains if their energies are equal or above the threshold energy $E_{\rm sp}$ given by (Bohdansky et al., 1980; Andersen and Bay, 1981):

$$E_{\rm sp} = \begin{cases} \frac{U_0}{4\langle m_j^{\rm atom}\rangle m_k} \frac{(\langle m_j^{\rm atom}\rangle + m_k)^4}{(\langle m_j^{\rm atom}\rangle - m_k)^2}, & \text{if } \frac{m_k}{\langle m_j^{\rm atom}\rangle} \leq 0.3, \\ 8U_0 \left(\frac{m_k}{\langle m_j^{\rm atom}\rangle}\right)^{1/3}, & \text{if } \frac{m_k}{\langle m_j^{\rm atom}\rangle} > 0.3. \end{cases} \tag{5.27}$$

In Eq. 5.26 we also introduced the nuclear stopping cross-section $S_k(E)$ in units of ergs cm^2 given by (Sigmund, 1981):

$$S_k(E) = 4\pi a_{\rm sc} Z_k \langle Z_{\rm j}\rangle e^2 \frac{m_k}{m_k + \langle m_j^{\rm atom}\rangle} \iota_k(\epsilon_k), \tag{5.28}$$

where Z_k and $\langle Z_j\rangle$ are the atomic number for the ion and the grain average atomic number. The screening length for the interaction potential between the nuclei is given by:

$$a_{\rm sc} = 0.885 a_0 (Z_k^{2/3} + \langle Z_j\rangle^{2/3})^{-1/2}, \tag{5.29}$$

with the Bohr radius $a_0 = 0.529$ Å. The function $\iota_k(\epsilon_k)$ encapsulates the details of the screened Coulomb interaction and can be approximated by (Matsunami et al., 1984):

$$\iota_k(\epsilon_k) = \frac{3.441\sqrt{\epsilon_k}\ln(\epsilon_k + 2.718)}{1 + 6.35\sqrt{\epsilon_k} + \epsilon_k(-1.708 + 6.882\sqrt{\epsilon_k}}, \tag{5.30}$$

with the reduced energy defined as:

$$\epsilon_k = \frac{\langle m_j^{\rm atom}\rangle}{m_k + \langle m_j^{\rm atom}\rangle} \frac{a_{\rm sc}}{Z_k\langle Z_j\rangle e^2} E. \tag{5.31}$$

The α_k function encapsulates how the energy is distributed in the material upon collision of the incident particle (see Sigmund, 1969, for further details). We use the updated version of the Bohdansky (1984) approximation obtained by Nozawa et al. (2006) based on sputtering data:

$$\alpha_k = \begin{cases} 0.2, & \text{if } \mu_k \leq 0.5, \\ 0.1\mu_k^{-1} + 0.25(\mu_k - 0.5)^2, & \text{if } 0.5 < \mu_k \leq 1, \\ 0.3(\mu_k - 0.6)^{2/3}, & \text{otherwise.} \end{cases} \tag{5.32}$$

We refer to Table 5.1 for the relevant material parameters required for the expressions presented in this Section. The experimental yields that were used to calibrate the

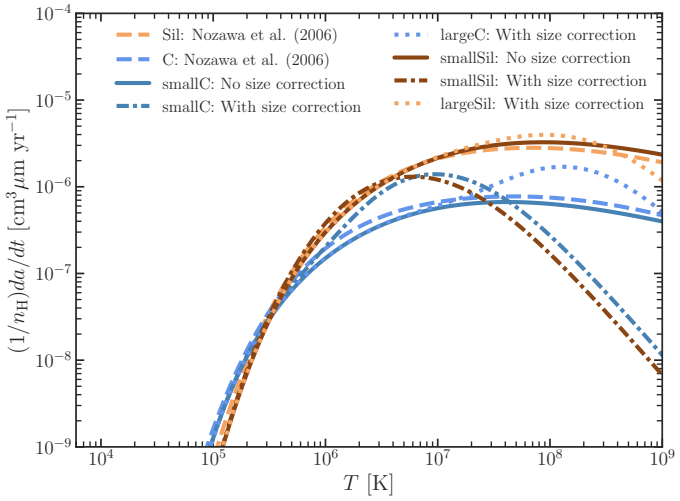


Figure 5.3: Erosion rate (i.e. $(\mathrm{d}a/\mathrm{d}t)/n_{\rm H}$) by thermal sputtering given by Equation 5.24 for each dust species. These have been computed for a gas composition of $Z = 10^{-4} Z_\odot$. We compare the results of Nozawa et al. (2006) to our updated model that considers the finite size of the grain for the effective energy deposited by ions. This results in small grains becoming less affected by sputtering beyond $\sim 10^7$ K.

analytic expression for $Y_k(E)$, and to hence derive the value of K, were measured for a semi-infinite target, rather than finite size dust grains, (e.g. Tielens et al., 1994). The semi-infinite target approximation may break down for small grains and for sufficiently high gas temperatures. First proposed by Jurac et al. (1998), a size-dependent sputtering yield arises from the consideration that if the grain size is close to the stopping length (or penetration depth, i.e. $r_{\rm pd}$), then the energy deposition per unit mass of the grain will be maximal. We apply the results of the size-dependent sputtering yield model by Bocchio et al. (2012) and Bocchio et al. (2014) who obtain multi-Gaussian fittings to the correction function $f(x)$ between the sputtering yield of a semi-infinite target Y_∞ and the sputtering yield Y_a of a grain of finite radius a, $Y_a = f(x) Y_\infty$. We have further modified $f(x)$ to prevent unstable behaviour in the $x \ll 1$ regime:

$$f(x) = \begin{cases} 1 + p_1 \exp\left[-\frac{(\ln(x/p_2))^2}{2p_3^2}\right] - p_4 \exp[-(p_5 x - p_6)^2], & \text{if } x \geq 1, \\ q_1 \exp\left[-\frac{(\ln(x/q_2))^2}{2q_3^2}\right], & \text{otherwise,} \end{cases} \tag{5.33}$$

where the fitting parameters are given in Table 5.2 and $x = a/(0.7 r_{\rm pd})$. The 0.7 factor comes from the fact that the ion usually loses the majority of its energy after it has travelled $\sim 0.7 r_{\rm pd}$ through the grain material (e.g. Serra Díaz-Cano et al., 2008). The penetration depth and the effective value of Y_a are the result of very complex theoretical work using codes like the Stopping and Range of Ions in Matter (SRIM;

	p_1	p_2	p_3	p_4	p_5	p_6	q_1	q_2	q_3
Carbon	4.9	0.55	0.77	4.7	3.0	1.2	4.51	0.92	0.4
Silicate	1.5	1.2	0.57	1.1	0.52	0.37	1.48	1.31	0.59

Table 5.2: Parameters for the size-dependent correction of thermal sputtering yields.

Ziegler and Biersack, 1985). For Dusty-PRISM we instead estimate the value of $r_{\rm pd}$ via the integration of the total stopping power considering nuclear and electronic interactions derived in Section 5.2.4. As an example, we present in Fig. 5.3 the erosion rate $({\rm d}a/{\rm d}t)/n_{\rm H}$ for the different dust species considering the finite size correction detailed above. In order to compare to the rates obtained by Nozawa et al. (2006), we have computed these for a gas with $10^{-4}Z_{\odot}$. Our vanilla rates (solid brown and blue lines) closely follow the shape and absolute values obtained by Nozawa et al. (2006) (dashed orange and blue lines), confirming the higher sputtering yield predicted for silicate grains compared to carbonaceous. When the finite size correction is applied (dotted lines), our large and small grain rates deviate from each other at temperatures above $\sim 10^6$ K, resulting in rates that clearly peak at different temperatures. The most remarkable result of these updated erosion rates is their decrease by $\gtrsim 2$ dex and $\gtrsim 1$ dex for small and large grains above 5×10^7 K. This could have a significant effect on the sputtering timescale of dust grains in SN and shock heated X-ray gas within galaxy clusters (Vogelsberger et al., 2019).

5.2.4 Gas collisional cooling/heating

So far, we have not explicitly detailed the direct collisional transfer of energy between dust grains and gas atoms. In Section 5.2.3 we have explored how the high velocity collisions that take place at high temperature cause a sputtering of atoms from dust grains. This fragmentation reaction takes place via the transfer of thermal energy of the gas to the internal energy of the grain, which effectively means an additional source of cooling for gas enriched with dust. Collisional heating may be an important source of dust heating in high density shocks, which could explain the infrared-to-X-ray (IRX) relation observed for SNRs in the Galaxy and the LMC (e.g. Graham et al., 1987; Seok et al., 2015). Furthermore, in highly obscured dense regions, collisional heating may drive the equilibrium temperature of dust grains, as well as play an important role in gas cooling (Hollenbach and McKee, 1989; Glover and Jappsen, 2007; Dopcke et al., 2011). Dust-gas collisional cooling has been implemented in various

ISM chemistry models (e.g. Wolfire et al., 2003; Grassi et al., 2014; Krumholz, 2014; Bialy and Sternberg, 2019; Kim et al., 2022; Katz et al., 2022b) and hydrodynamical simulations with explicit dust modelling (Vogelsberger et al., 2019; Granato et al., 2021; Dubois et al., 2024). Models of dust cooling are primarily based on the seminal work by Hollenbach and McKee (1979) and Dwek and Werner (1981), and indeed the high-temperature dust-electron collisional cooling in our vanilla dust model (Dubois et al., 2024) is based on a fitting function provided in appendix A of Dwek and Werner (1981). However, we would like to stress that these models have been applied, within the ISM and galaxy formation community, with little scrutiny as to the extent of their applicability. We briefly review these aspects and propose a more appropriate modelling of dust-grain collisional cooling.

The collisional model by Hollenbach and McKee (1979) is based on the *soft-cube* model (Logan et al., 1968) applied to the thermal accommodation of gas particles onto dust grain surfaces (Burke and Hollenbach, 1983). Essentially, this model assumes that a grain surface can be approximated by an array of square particles attached by a spring to an infinite mass (the lattice). The infinitesimal collisional rate onto grain surface area $\mathrm{d}A$ by a particle with mass m, number density n, and following a Maxwell-Boltzmann velocity distribution at temperature T, is given by:

$$\mathrm{d}\Gamma = n\mathrm{d}A \int_{v_z>0} \left(\frac{m}{2\pi k_\mathrm{B} T}\right)^{3/2} \exp\left(-\frac{mv^2}{2k_\mathrm{B}T}\right) v_z \mathrm{d}^3 v = n\mathrm{d}A\sqrt{\frac{k_\mathrm{B}T}{2\pi m}}, \tag{5.34}$$

where we have assumed the $x-y$ plane is parallel to the grain surface, such that only particles with $v_z > 0$ can reach the surface. Taking the integral over the full surface of the grain $4\pi a^2$ gives the total collisional rate as:

$$\Gamma = \pi n a^2 \sqrt{\frac{8k_\mathrm{B}T}{\pi m}}. \tag{5.35}$$

By a similar calculation, we can derive the average kinetic energy of the colliding particles $\langle E_\mathrm{kin}\rangle = 2k_\mathrm{B}T$. Therefore, we can express the energy transfer rate for a particle with mass m onto a dust grain of radius a and temperature T_d (Hollenbach and McKee, 1979):

$$H(a,T) = \sqrt{\frac{8k_\mathrm{B}T}{\pi m}} \pi n a^2 2k_\mathrm{B}(T-T_\mathrm{d})\mathcal{A}(T), \tag{5.36}$$

where the term in parenthesis indicates that the energy transfer goes to zero when $T = T_{\rm d}$ and allows for gas heating when $T_{\rm d} > T$. The parameter $\mathcal{A}(T)$ encapsulates the efficiency of energy transfer from the gas atom to the dust grain, termed the *accommodation* factor (Burke and Hollenbach, 1983). This is usually assumed to be of order unity, with a small dependence on the gas and dust temperatures in the range $\sim 10 - 1000$ K (see Figure 4 in Burke and Hollenbach, 1983). The *soft-cube* model is valid as long as the surface is approximately flat from the perspective of the impinging gas atom. However, more energetic gas particles are capable of interacting with a larger region of the grain surface, potentially encountering a more uneven surface topology. This limits the validity of the model to gas temperatures $T \lesssim 10^4$ K, which has not been enforced when implemented in many ISM or cloud collapse models (e.g. Wolfire et al., 2003; Grassi et al., 2014; Bialy and Sternberg, 2019; Kim et al., 2022; Katz et al., 2022b). We therefore enforce a logistic curve centred on $T = 10^4$ K, allowing for a smooth transition between the regime of applicability for Eq. 5.36, to the hard-sphere regime at high temperature (e.g. Lindhard and Nielsen, 1962; Sigmund, 2014). We note that this will have an appreciable influence on the cooling rates at solar metallicity below $n_{\rm H} < 1$ cm^{-3} (e.g. see Figure 2 in Katz et al., 2022b, for the case of the PRISM model). When the low-temperature condition is satisfied, we obtain $\mathcal{A}(T)$ for atomic H and H_2 as (Hollenbach and McKee, 1979):

$$\mathcal{A}_{\rm H,H_2} = (1 - \mathcal{A}^0_{\rm H,H_2}) \exp\left(-\sqrt{\frac{2k_{\rm B}(T + T_{\rm d})}{D_{\rm H,H_2}}}\right) + \mathcal{A}^0_{\rm H,H_2}, \tag{5.37}$$

where:

$$\mathcal{A}^0_{\rm H,H_2} = \frac{2m_{\rm H,H_2}m_{\rm d}}{(m_{\rm H,H_2} + m_{\rm d})^2}, \tag{5.38}$$

is the hard-sphere limit and $D_{\rm H,H_2} = 500k_{\rm B}$ is the depth of the potential well (i.e. the adsorption energy per particle).

As we have seen in Sec. 5.2.3, the ion-grain interaction in the high-temperature regime brings into play different physics. In this case, ions can get close enough to feel the grain potential and to travel through the grain material. This form of *transmission* is the basis behind the thermal and non-thermal sputtering of dust grains (Draine et al., 1979; Nozawa et al., 2006). Understanding ion transmission through the grain material requires accounting for the interaction of ions with nuclei and electrons,

giving rise to an effective drag force. Unfortunately, the topic of a material's stopping power (i.e. the average change in energy of an ion over an infinitesimal path length through the solid) at sub-relativistic velocities remains a question of great debate in the solid-state and nuclear physics community (see Sigmund, 2014, for a review on the different models and approximations used to account for the slowing down of ions through solids). In the high energy regime ($E \gg 1$ MeV), the Bohr and Bethe stopping equations have been of great use in predicting the transport of heavy ions. However, these theories, when extended to the low energy regime, give negative values for the stopping power below a threshold energy. Given that an ion energy gain is not considered in these theories, the origin of these negative values is an artefact caused by the approximation limits for Bessel functions used in their derivation (Sigmund, 1996). Furthermore, the first Born approximation can only be applied to the most energetic particles that we will encounter in a coronal gas, so the physical meaning of these equations also becomes questionable in these regimes[5].

We instead follow the formalism developed by Sigmund (1981) for the nuclear and electronic stopping by graphite and silicate materials. We recall (Section 5.2.3) that the stopping power is defined as the average energy loss per unit path length, l, through the solid material (Lindhard, 1964):

$$\frac{\mathrm{d}E}{\mathrm{d}l} = -N(S_\mathrm{n}(E) + S_\mathrm{e}(E)), \tag{5.39}$$

where N is the nuclear number density, S_n is the nuclear stopping cross-section defined in Eq. 5.28 and S_e is the electronic stopping cross-section given by the Lindhard and Scharff (1961) equation for an electron gas:

$$S_\mathrm{e}(E) = 8\pi\xi_\mathrm{e}\frac{Z_\mathrm{k}\langle Z_\mathrm{atom}\rangle}{\tilde{Z}}a_\mathrm{sc}e^2\frac{v(E)}{v_0}, \tag{5.40}$$

with:

$$\tilde{Z} = (Z_k^{2/3} + \langle Z_j\rangle^{2/3})^{3/2}, \tag{5.41}$$

for projectile k, and where the average grain atomic number $\langle Z_j\rangle$, and the screening length a_sc are as defined in Section 5.2.3. The factor $\xi_\mathrm{e} \simeq Z_k^{1/6}$ was included

[5]We note that one of these theories for high energy stopping power, the Bethe-Bloch approximation (Bethe et al., 1930; Bloch et al., 1933), was used in the SN dust modelling by Kirchschlager et al. (2019), resulting in numerically incorrect penetration depths in the low energy regime.

to improve agreement with experimental penetration depths, and v_0 is given by $v_0 = \sqrt{2E_0/m_\mathrm{e}}$ where:

$$E_0 = \frac{\hbar^2}{2m_\mathrm{e}}(3\pi^2\langle N_\mathrm{val}\rangle N)^{2/3}, \tag{5.42}$$

is the Fermi energy with number density provided by the material valence electrons per atom $\langle N_\mathrm{val}\rangle$. We can now numerically integrate Eq. 5.39 to determine how an ion of initial energy E slows down as it travels through the graphite and silicate materials of the dust grains modelled in Dusty-PRISM.

The heating rate of a dust grain of size a experiencing collisions with a gas atom k with mass m_k, number density n_k and following a Maxwell-Boltzmann distribution $f(E)$ of energies $E = 1/2m_k v^2$ is given by :

$$H(\vec{\mathcal{P}}_j, T, n_k) = \pi a_j^2 n_k F_\mathrm{C} \int f(E)v(E)E\zeta(\vec{\mathcal{P}}_j, E)\mathrm{d}E, \tag{5.43}$$

where $\vec{\mathcal{P}}_j$ is a vector of the material properties of the grain j

$$\vec{\mathcal{P}}_j = (a_j, s_j, \langle Z_j\rangle, \langle m_j^\mathrm{atom}\rangle, \langle N_\mathrm{val}\rangle), \tag{5.44}$$

F_C is the Coulomb enhancement factor (see Section 5.2.2, and ζ is the fraction of incident ion left in the grain, computed by integrating Eq. 5.39. Eq. 5.43 can easily be integrated resulting in:

$$H(\vec{\mathcal{P}}_j, T, n_k) = \sqrt{\frac{32}{\pi m_k}}\pi a_j^2 n_k (k_\mathrm{B}T)^{3/2} F_\mathrm{C} h(\vec{\mathcal{P}}_j, T), \tag{5.45}$$

where:

$$h(\vec{\mathcal{P}}_j, T) = \frac{1}{2}\int u^2 \zeta(\vec{\mathcal{P}}_j, E)\exp(-u)\mathrm{d}u, \tag{5.46}$$

is the distribution-averaged heating efficiency function, and $u \equiv E/(k_\mathrm{B}T)$. We compute $h(\vec{\mathcal{P}}_j, T)$ for the material properties and sizes of the dust grains in Dusty-PRISM, such that a simple linear interpolation in log-log space can be used to compute its value on-the-fly. The other quantities in Eq. 5.45 are computed on a per-cell basis during the simulation.

In gas with temperature below 10^9 K, electrons are still in the sub-relativistic regime. This implies that, outside of the most energetic electrons above ~ 10 keV, the first Born approximation breaks down and the Rutherford cross-section is no longer

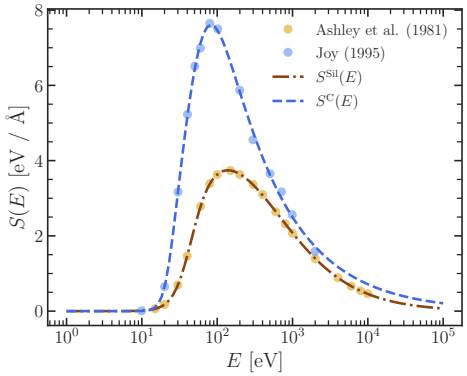


Figure 5.4: Experimental electron stopping power for solid carbon (blue markers) by Joy (1995) and silicon dioxide (yellow markers) by Ashley and Anderson (1981). The dashed lines are the fitting functions for silicate grains (brown dot-dashed line) and carbonaceous grains (dashed blue line) following Eq. 5.47.

	$\mathbf{SiO_2}$	**C**
a	7.474	-4.280×10^{-4}
b	0.892	-1.221×10^{-16}
c	7.703×10^{-6}	-1.304×10^{-7}
d	0.997	-6.502
e	-2.918	-0.985
f	0.082	-2.614×10^{-4}
g	0.223	1.544
h	0.947	1.524

Table 5.3: Analytical fitting parameters (Eq. 5.47) to the electron stopping power in solid carbon C and silicate dioxide (SiO_2) for the experimental data by Joy (1995) and Ashley and Anderson (1981).

applicable. In this regime, analytic expressions (e.g. Eq.5.40) are a poor predictor of the stopping power of electrons in different solids at low energies (Iskef et al., 1983; Luo et al., 1991; Joy et al., 1996). We therefore follow the approach in Micelotta et al. (2010a) (see also Section 5.3.2) and instead determine the energy deposition and penetration depth by obtaining fitting functions to experimental values. For carbonaceous grains we use the experiments on carbon films by Joy (1995), and in the absence of experimental data for astrophysically relevant silicates, we use the experimental data on SiO_2 stopping power by Ashley and Anderson (1981) (see blue and yellow markers in Fig. 5.4, respectively). We use the fitting equation by Micelotta et al. (2010a) for the stopping power (i.e. $\mathrm{d}E/\mathrm{d}l$) of the colliding electrons:

$$S(E) = \frac{h \log(1 + aE)}{fE^g + bE^d + cE^e}, \tag{5.47}$$

in units of eV/Å, where the electron energy E is in keV and our fitting parameters are given in Table 5.3[6]. We present the results of this fit in Fig. 5.4, indicating a larger stopping power for carbon than for SiO_2 at the peak stopping efficiency of $\sim 10^2$ eV.

5.2.5 Non-thermal sputtering in SN shocks

SNe (type II and Ia) destroy dust already present in the ISM, where the dust destruction is produced by inertial (non-thermal) sputtering and grain-grain collisions (Kirch-

[6]Note that we have re-computed the fitting values for solid carbon, which has resulted in a minor deviation from the parameters provided in Micelotta et al. (2010a). These differences are negligible.

schlager et al., 2020). As opposed to thermal sputtering, non-thermal sputtering is independent of temperature, and the energy of the collision is instead related to the kinetic energy imparted by a travelling shock in the ISM (i.e. a SN shock). The amount of SN-destroyed dust $\Delta M_{\mathrm{SN},j}$ is a fraction of the mass of gas M_{100} shocked to velocities above $100\,\mathrm{km\,s^{-1}}$ defined as

$$\Delta M_{\mathrm{SN},j} = \varepsilon_{\mathrm{SN}}(a_j)\min\left(\frac{M_{100}}{M_{\mathrm{gas}}}, 1\right) M_{\mathrm{d},j}\,, \tag{5.48}$$

with a size-dependent destruction efficiency given by Aoyama et al. (2020) (their Equation 11):

$$\varepsilon_{\mathrm{SN}}(a_j) = 1 - \exp\left(-\frac{\delta_{\mathrm{SN},j}}{a_{0.1,j}}\right)\,, \tag{5.49}$$

and M_{gas} is the gas mass in the current cell, $M_{\mathrm{d},j}$ the local dust mass in bin j, $a_{0.1,j}$ the dust grain size in units of $0.1\,\mu$m, and $\delta_{\mathrm{SN},i}$ the destruction efficiency. Small grains are more efficiently decelerated by drag forces, trapping them near the shock region where thermal sputtering can quickly destroy them (Nozawa et al., 2006). The dependence of the destruction efficiency Eq. 5.49 on grain size a reflects this. The mass of shocked gas is determined by the Sedov solution in a medium of homogeneous gas density (i.e. $M_{100} = 6800 E_{\mathrm{SN},51}\,\mathrm{M}_\odot$ McKee, 1989), where $E_{\mathrm{SN},51}$ is the energy of the SN explosion in units of 10^{51} erg. Multiple SNe occur in one time step Δt (each individual SN engulfing the gas swept up by the previous explosion), following (see Hou et al., 2017):

$$\Delta M_{\mathrm{SNe},j} = \left[1 - \left(1 - \frac{\Delta M_{\mathrm{SN},j}}{M_{\mathrm{d},j}}\right)^{N_{\mathrm{SN}}}\right] M_{\mathrm{d},j}\,, \tag{5.50}$$

with N_{SN} the number of SNe. We emphasise that in this model the SN blast wave does not destroy the dust newly formed in stellar ejecta. It only destroys pre-existing dust: the dust condensation efficiency (see Section 5.2.1) implicitly takes this into account.

We use a different value of the dust destruction efficiency for carbonaceous (0.10) and silicate (0.15) grains, following results from hydrodynamical simulations of dust sputtering in a turbulent multiphase ISM (Hu et al., 2019), where approximately 50 percent more silicate grains are destroyed than carbonaceous grains. Grain-grain collisions in shocks could also lead to efficient shattering of large grains into small grains (e.g. Jones et al., 1996; Nozawa et al., 2006; Serra Díaz-Cano et al., 2008;

Bocchio et al., 2014; Slavin et al., 2015; Kirchschlager et al., 2021). It has been argued that this shattering in SN shocks could allow for the formation of large PAH clusters (< 15 Å) from up to ~ 10 % of the carbon dust in shocks with $v_s \sim 100$ km s^{-1} (Jones et al., 1996). Nevertheless, there is still little evidence for the formation of very small grains in SN shocks (see e.g. Tielens, 2008, for a discussion of the problem), and it is not clear how much of these new small grains will survive in the hot post-shock gas. Dusty-PRISM therefore allows for different small grain production efficiencies in SN shocks, leaving them as free parameters of the model.

5.2.6 Turbulent shattering of large grains

As particles suspended in gas, dust grains experience collisions and mixing in the turbulent ISM (see e.g. McKee and Ostriker, 2007; Elmegreen and Scalo, 2004 for reviews about the presence of turbulence in the ISM). Close-range interactions can lead to elastic collisions or can compromise the physical integrity of dust grains, by deformations, coagulation or shattering. In this section we begin by detailing how large energy collisions can cause grains to shatter into smaller fragments, strongly altering their size distribution and, consequently, the extinction curve. Small grains account for the majority of the cross-sectional area of the dust distribution, and thus they are of great importance to modelling the dust-radiation coupling as well as the chemistry on the surface of grains (e.g. molecular hydrogen formation). Hence the top-down processing of the dust distribution from large grain injection by stellar processes to their transformation into small grains, ultimately including PAHs, cannot be neglected in a dust model for galaxy formation.

The statistical properties of magnetised, compressible gas turbulence are fundamental for determining the motion of dust grains. The dynamics of (charged or neutral) grains is primarily driven by hydrodynamic drag and Lorentz force acceleration. Efficient dust grain acceleration (against damping mechanisms) occurs via gyroresonance when the Doppler-shifted frequency of the wave in the frame of reference of the grain is a multiple of the gyrofrequency of the grain in the local magnetic field. In the original work of Yan et al. (2004) (see Lazarian and Yan, 2001; Yan and Lazarian, 2002, for the theoretical MHD turbulence framework), large grains ($a \geq 0.2$ μm) can decouple from the turbulent flow in the WNM (due to a higher ratio

of stopping time to flow characteristic time, i.e. Stokes' number) and be accelerated to ∼km/s, i.e. above the shattering threshold, by the Lorentz force (Jones et al., 1996). However, the computations in Yan et al. (2004) are limited to grains with $a \geq 0.01$ μm, and to specific thermodynamical conditions rather than the full multiphase conditions that arise in realistic galaxy formation simulations. Full modelling of dust dynamics in MHD turbulence remains a difficult problem (e.g. Fromang and Nelson, 2009; Zhu et al., 2015; Lee et al., 2017; Commerçon et al., 2023), and translating the results of simulations where the large grain decoupling is resolved ($\ll 0.01$ pc) to galactic scales simulations without magnetic fields is not a trivial task. We leave further developments of the dust and MHD coupling within the RAMSES code (see e.g. Moseley et al., 2022; Moseley and Teyssier, 2024, for current efforts) to future work.

Instead, we follow the purely HD formulation of turbulent-induced collision velocities for dust grains by Ormel and Cuzzi (2007). The Ormel and Cuzzi model is an updated version of the pioneering work of Völk et al. (1980). Völk et al.-like models are based on the classification of turbulent eddies according to whether their lifetime (i.e. turnover timescale $\tau_{\rm p}$) is comparable to the stopping time $t_{\rm s}$ of the particle (Class I) or not (Class III). In our case the particle is the dust grain. This classification provides a straightforward derivation of the particle-eddy relative velocity and in turn the variance of the particle-particle relative velocity.

We assume that dust particles and gas are coupled to each other via collisions and are in thermal equilibrium, meaning that the final relative velocity between grains is a combination of Brownian motion and the turbulent-induced velocities discussed above. The relative velocity due to thermal (Brownian) motion for two dust particles of masses m_i and m_j is:

$$\Delta V_{i,j}^{\rm B} = \sqrt{\frac{8 k_{\rm B} T_{\rm gas} (m_i + m_j)}{\pi m_i m_j}}. \tag{5.51}$$

In the context of collapsing molecular clouds (e.g. Guillet et al., 2020; Kawasaki et al., 2022b) the forcing timescale for the turbulent cascade is assumed to be the free-fall time of the cloud $t_{\rm ff}$ (e.g. Lebreuilly et al., 2022). In our case, and consistent with the turbulent enhancement of the gas density PDF used for dust metal accretion (see Section 5.2.2), we consider the local forcing timescale to be $\tau_{\rm L} = \Delta x_{\rm cell}/\sigma$ (σ is the local gas velocity dispersion, defined in Section 2.1.3), and hence the turbulent

Mach number is simply $\mathcal{M} = \sigma/c_\mathrm{s}$. Assuming a Kolmogorov turbulent spectrum, the eddy turnover time on the viscous dissipation scale is:

$$\tau_\eta = \frac{\tau_\mathrm{L}}{\sqrt{\mathrm{Re}}}, \tag{5.52}$$

with the Reynolds number, Re, parameterised by the local thermodynamic conditions as $\mathrm{Re} = 6.2 \times 10^7 \sqrt{\frac{\rho_\mathrm{gas}/m_\mu}{10^5 \mathrm{cm}^{-3}}} \sqrt{\frac{T_\mathrm{gas}}{10\mathrm{K}}}$ (Ormel et al., 2009). The motion of dust particles in a fluid is governed by the drag forces caused by gas. Based on Epstein's law, the stopping time is:

$$t_\mathrm{s} = \frac{sa}{\rho_\mathrm{gas} v_\mathrm{th}}, \tag{5.53}$$

with $v_\mathrm{th} = \sqrt{8/\pi} c_\mathrm{s}$ the thermal velocity of the gas and s the material density of the grain. Eq. 5.53 applies when the mean free path l_mfp of the gas is larger than the particle size (Commerçon et al., 2023). When this is no longer the case, one should use Stokes' law, with a transition particle size given by the condition $a_\mathrm{tr} \geq (9/4) l_\mathrm{mfp}$. Given that the largest particle size considered in this work is of 0.1 μm, this corresponds to $n_\mathrm{H} \geq 7.5 \times 10^{19}$ cm^{-3}, well out of reach of current galaxy formation simulations. Therefore, it is safe to assume that all dust particles modelled are well within the Epstein regime. Given these definitions of the stopping time and turbulent forcing timescale, we can define the particle Stokes' number as $\mathrm{St} = t_\mathrm{s}/\tau_\mathrm{L}$.

Consider Stokes' numbers for dust particles i and j with $\mathrm{St}_i \geq \mathrm{St}_j$ (thus $t_\mathrm{s}^i \geq t_\mathrm{s}^j$). Ormel and Cuzzi (2007) provide closed forms for the turbulent-induced relative velocities in three limiting regimes dictated by the viscous timescale τ_η and the turnover timescale τ_L:

$$\Delta V_{i,j}^\mathrm{T} = \begin{cases} \sqrt{\frac{3}{2}}\sigma \sqrt{\frac{\mathrm{St}_i - \mathrm{St}_j}{\mathrm{St}_i + \mathrm{St}_j}} \sqrt{\frac{\mathrm{St}_i^2}{\mathrm{St}_i + \mathrm{St}_\mathrm{min}} - \frac{\mathrm{St}_j^2}{\mathrm{St}_j + \mathrm{St}_\mathrm{min}}}, & \text{if } \tau_\eta > t_\mathrm{s}^i, \\ \sqrt{\frac{3}{2}}\sigma \sqrt{f\left(\frac{\mathrm{St}_j}{\mathrm{St}_i}\right) \mathrm{St}_i}, & \text{if } \tau_\eta \leq t_\mathrm{s}^i < \tau_\mathrm{L}, \\ \sqrt{\frac{3}{2}}\sigma \sqrt{\frac{1}{1+\mathrm{St}_i} + \frac{1}{1+\mathrm{St}_j}}, & \text{if } \tau_\mathrm{L} \leq t_\mathrm{s}^i, \end{cases} \tag{5.54}$$

with the function f given by

$$f(x) = 3.2 - (1+x) + \frac{2}{1+x}\left(\frac{1}{2.6} + \frac{x^3}{1.6+x}\right), \tag{5.55}$$

and $\mathrm{St}_\mathrm{min} \equiv \tau_\eta/\tau_\mathrm{L} = 1/\sqrt{\mathrm{Re}}$. The final relative velocity is obtained by combining the Brownian and turbulent contributions:

$$\Delta V_{i,j} = \sqrt{(\Delta V_{i,j}^\mathrm{B})^2 + \Delta V_{i,j}^\mathrm{T})^2}. \tag{5.56}$$

Recall that the collision velocity determines whether shattering, coagulation or simple bouncing (we do not consider effect of deformations on the dust grain geometrical properties) takes place. Furthermore, in the case of shattering, the energy of the collision determines the fragment distribution that will emerge from the two-body interaction (Jones et al., 1996; Hirashita and Yan, 2009), which depends on a number of material properties. Hirashita and Li (2013) showed that the most relevant parameter is the velocity threshold for catastrophic fragmentation (i.e. when more than half of the target grain mass is shocked above the grain internal sound speed). Therefore, following Hirashita and Li (2013) we simplify the shattering model using the prescription presented by Kobayashi and Tanaka (2010). We assume that the disrupted mass ejected from m_i is proportional to

$$\phi = \frac{E_{\rm imp}}{m_i Q^*_{\rm d}}, \tag{5.57}$$

where

$$E_{\rm imp} = \frac{1}{2}\frac{m_i m_j}{m_i + m_j}(\Delta V_{i,j})^2, \tag{5.58}$$

is the impact energy for m_i colliding with m_j and $Q^*_{\rm d}$ is the specific impact energy for catastrophic disruption (estimated to be $\simeq 8.9 \times 10^9$ dyn cm/g for carbonaceous grains and $\simeq 4.3 \times 10^{10}$ dyn cm/g for silicate grains, Jones et al., 1996). Using ϕ, the ejected mass $m_{\rm ej}$ is estimated as

$$m_{\rm ej} = \frac{\phi}{1+\phi} m_i. \tag{5.59}$$

The maximum $a_{\rm f,max}$ and minimum $a_{\rm f,min}$ sizes of the fragments are taken to be

$$m_{\rm f,max} = 0.02 m_{\rm ej}, \tag{5.60}$$

$$m_{\rm f,min} = 10^{-6} m_{\rm f,max}, \tag{5.61}$$

with the fragment mass distribution following (i.e. given the collision of grains of masses m_i and m_j with relative velocity $\Delta V_{i,j}$ it returns the probability of fragment of mass m)

$$\mu_{\rm frag}(m; \Delta V_{i,j}, m_i, m_j) = \frac{(4-\alpha_{\rm f}) m_{\rm ej} m^{(-\alpha_{\rm f}+1)/3}}{3\left[m_{\rm f,max}^{(4-\alpha_{\rm f})/3} - m_{\rm f,min}^{(4-\alpha_{\rm f})/3}\right]} \tag{5.62}$$

$$+(m_i - m_{\rm ej})\delta(m - m_i + m_{\rm ej}), \tag{5.63}$$

where we have dropped the dependence of $m_{\rm ej}(\Delta V_{i,j}, m_i, m_j)$ for clarity. This is a power law distribution with exponent $\alpha_{\rm f} = 3.3$ in agreement with the results of Jones et al. (1996), plus a remnant fragment of mass $m_i - m_{\rm ej}$ (last term on the RHS of the equation).

These results need to be applied and implemented into our discretised dust distribution framework. Equation 5.62 can be easily integrated over the limits corresponding to large grains, small grains, and in the case of carbonaceous grains, PAHs (see Section 5.3), in order to obtain the contribution of the shattered fragments to each bin. Integrating Equation 5.62 over the whole spectrum of fragments gives m_i, allows us to define the fraction of target mass fragments that fall within the dust grain bin centred on grain size a_x and limited by minimum and maximum masses $m_{x,\rm min}$ and $m_{x,\rm max}$:

$$\chi_{\rm f}(a_x; \mathcal{M}, a_i, a_j) \equiv \chi_{\rm f}(m_x; \Delta V_{i,j}, m_i, m_j) = \frac{1}{m_i} \int_{m_{x,\rm min}}^{m_{x,\rm max}} \mu_{\rm frag}(m; \Delta V_{i,j}, m_i, m_j) dm, \tag{5.64}$$

Using Equation 5.64 we define the local timescale of fragment production for a given collision model (Hirashita and Aoyama, 2019):

$$t_{\rm sha}(a_x; \mathcal{M}, a_i, a_j) = (\sigma_{i,j} \Delta V_{i,j} n_{{\rm d},j} \chi_{\rm f})^{-1}, \tag{5.65}$$

where we have dropped the arguments of $\chi_{\rm f}$ for clarity, and defined the collision cross section of grains of sizes a_i and a_j as $\sigma_{i,j} = \beta\pi(a_i + a_j)^2$, where β allows for corrections to the geometrical cross section. We choose the simple case $\beta = 1$. This definition of the shattering timescale allows us to obtain separate timescales for the production of shattered fragments within different grain size bins. Therefore, for carbonaceous grains we compute the timescales for the production of large grains (i.e. inefficient shattering), small grains, PAHs and full destruction (i.e. return to the gas phase). We do similar calculations for silicates, except that we do not follow the shattering of very small grains in this case; instead every fragment below 4.5Å is considered to return to the gas phase. This is based on the result that smaller silicate grains are photolytically unstable in the ISM (Guhathakurta et al., 1989). Fig. 5.5 shows the results of this turbulent shattering model for the CNM, WNM and WIM as defined in Table 1 of Yan et al. (2004), using a fixed gas-to-dust ratio (GDR) of 10^2 for both large and small grains. In the top row we consider the collision of large grains with

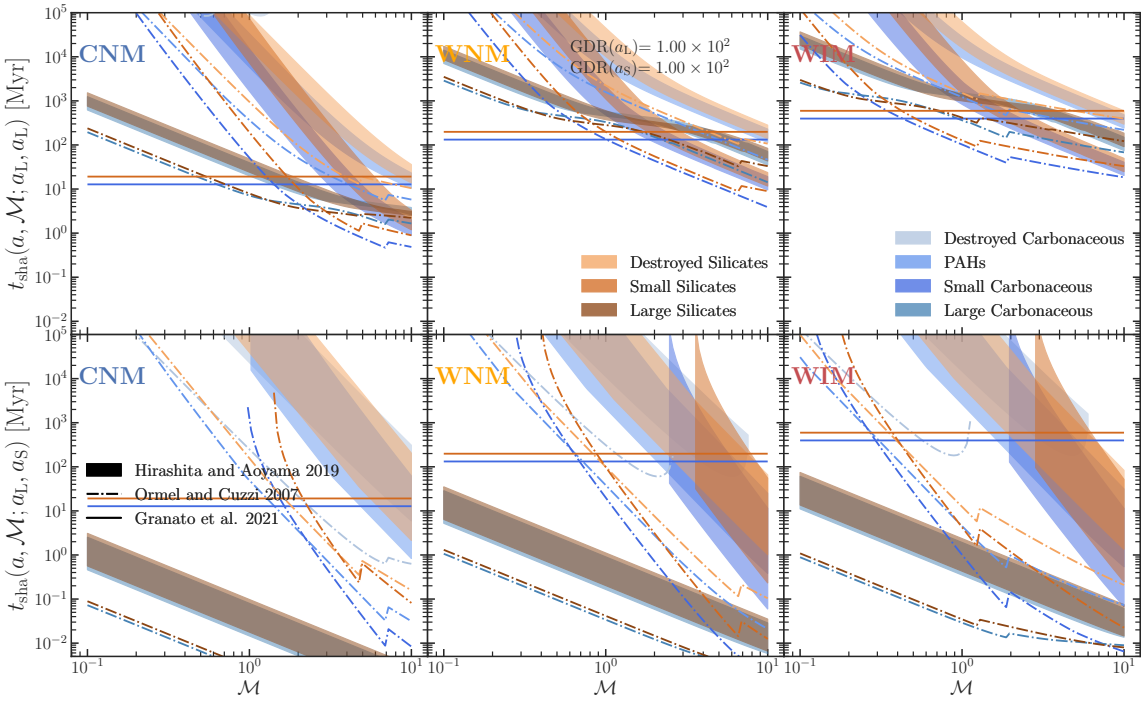


Figure 5.5: Shattering timescale vs turbulent Mach number in 3 different ISM phases (CNM at $n_H = 30$ cm^{-3} (left), WNM at $n_H = 0.3$ cm^{-3} (middle), WIM at $n_H = 0.1$ cm^{-3} (right)) for the turbulent shattering models detailed in Section 5.2.6. Each line represents the timescale for the production of fragments for different grain types and sizes. Earth-like tones are used for silicate grains, while silver-blue tones are used for carbonaceous grains (see legend in top panels). Shattering is computed using three different models for comparison: (i) our fiducial model based on the collision velocity results of Ormel and Cuzzi (2007) (dotted dashed lines), (ii) our model with the basic velocity scaling from Hirashita and Aoyama (2019) (shaded regions), and (iii) the basic shattering model (solid lines) by Granato et al. (2021) (see Dubois et al., 2024, for this implementation in RAMSES). *Top row:* Results for the models using only the collisions between large grains with $a_L = 0.1$ μm. *Bottom row:* Results for the collision between large $a_L = 0.1$ μm and small grains $a_S = 0.005$ μm. Both models assume a fixed GDR of 10^2 for small and large grains, typical of a $\sim Z_\odot$ ISM. Collisions between large grains in the WNM and the WIM allow for efficient shattering of large grains into smaller grains. In the WNM, the fragment mass is dominated by large silicate grains (i.e. ineffective shattering) for $\mathcal{M} \lesssim 2$ and at $\mathcal{M} \lesssim 1$ for large carbonaceous grains. For the WIM, shattering begins to be important at up to 2 times lower $\mathcal{M}$. Both phases show that at high $\mathcal{M}$ the efficiency of (destruction) PAH formation is an order of magnitude slower than the formation of small (silicate) carbonaceous grains. The basic modelling by Hirashita and Aoyama (2019) significantly underestimates the shattering efficiency at low $\mathcal{M}$, and the basic model of Granato et al. (2021) can be up to 1 dex slower than the prediction of Ormel and Cuzzi (2007). The bottom panels show that the timescale curves for large and small grains never cross for our fiducial model within the turbulent Mach number range explored. We argue that these types of collisions are inefficient for shattering under the conditions found in galaxy simulations.

other large grains (i.e. $m_i = m_j$), while in the bottom row we consider the collision of large and small grains (i.e. $m_i > m_j$). A way to determine whether shattering is efficiently removing dust mass from the large grain bins is if the shattering timescale of small grains and PAH destruction is shorter than the production timescale of large grain, i.e. the point at which these lines cross one other in Fig. 5.5. Earth-like tones are used for silicate grains, while blue-grey tones are for carbonaceous grains, with the colour evolving from dark to light for larger to smaller fragments. In order to put our results within the context of previous simplified treatments of the shattering timescale, we also compare the results of the Ormel and Cuzzi (2007) model to Hirashita and Aoyama (2019) (see their appendix C) which scales the velocity with $\mathcal{M}$ and grain radius. Some issues arise with this simplified form. First, since it is derived assuming an equal particle mass in the calculation of $\Delta V_{i,j}$ (Ormel et al., 2009), it cannot be directly applied to the case of particles with different sizes. Secondly, it assumes that the particle sits in the intermediate regime given in Eq. 5.54, which is a good approximation for the molecular ISM, but not for the high $\mathcal{M}$ typical of the WNM or WIM. We only consider silicate-silicate, or carbon-carbon collisions, i.e. we do not allow silicate-carbon collisions. Following Hirashita and Li (2013), we posit that approaching particles have a uniform probability of hitting each other from any direction, so we obtain maximum and minimum estimates for the relative velocity given by head-on collisions and tangential collisions, respectively. These results are represented in Fig. 5.5 by the shaded bands. Compared to our fiducial implementation using the Ormel and Cuzzi (2007) model, we find that, although the Hirashita and Aoyama (2019) model reproduces the qualitative behaviour of the shattering timescale (i.e. decreases with $\mathcal{M}$ with a shallower slope at higher $\mathcal{M}$), it strongly underestimates the collision velocity, causing the shattering efficiency to be underestimated and the final shattering timescale to be overestimated. This approximated form only becomes valid at very high $\mathcal{M}$ for the lower density phases (WNM and WIM). The results of the approximation are even less reliable for the case of non-equal mass collisions (see bottom panel). These panels also include the basic scaling relation used in the original RAMSES implementation of the two-size dust model (Dubois et al., 2024), based on Granato et al. (2021) (solid horizontal lines). This model does not consider the local Mach number, and instead provides a parametric scaling of the dust dispersion

velocity with gas density[7], varying from ~ 10 km/s to ~ 1 km/s from the WIM to the molecular cloud regime. Therefore, t_{sh} only scales with density, which explains why the curves for the Granato et al. (2021) model appear as constants in the fixed $n_{\rm H}$ ISM phases of Fig. 5.5. Our fiducial shattering model agrees with this estimate at $\mathcal{M} \sim 2-3$, but yields larger timescales for lower $\mathcal{M} \sim 2-3$ and lower ones (by up to 1 dex) for higher values of $\mathcal{M}$. This means that the Granato et al. (2021) model is a fair approximation for local Milky Way-like galaxies, but not for high redshifts systems and local starbursts, featuring larger Mach numbers (e.g. Falgarone et al., 2017).

Focusing again on the equal-size collision model (top row), the shattering timescales only become short enough for the destruction of large grains in the CNM at $\mathcal{M} \gtrsim 2$ and $\gtrsim 3$, for carbonaceous and silicate grains, respectively. These high values of turbulent Mach numbers are very rarely achieved in the CNM, or at least cannot be maintained for sufficiently long periods due to the short dissipation timescale (e.g. Equation 5.52). Therefore, consistent with previous work (e.g. Hirashita and Yan, 2009; Aoyama et al., 2017), shattering is not an efficient destruction process of 0.1 μm grains in the CNM. Furthermore, the results for the WNM and WIM suggest qualitatively similar results to the prescription for shattering used in models with the two-size approximation (Aoyama et al., 2017; Gjergo et al., 2018; Granato et al., 2021). Shattering becomes efficient significantly earlier in the WIM than in the WNM (at ~ 3 times lower $\mathcal{M}$). However, if both phases can attain the same maximum $\mathcal{M} = 10$, the slightly larger density of the WNM allows for a shorter shattering timescale than in the WIM. However, both phases and compositions converge to similar behaviours for large $\mathcal{M}$: 73% in small grains, 20% in large grains, and 7% in very small grains (returned to the gas phase in the case of silicates, converted to PAHs in the case of carbonaceous grains). We therefore expect shattering of big grains to be an interesting process for the formation of PAHs (Seok et al., 2014). Additionally, our fiducial model finds that the production of small and very small shattered fragments through the collision of large grains and small grains is a very inefficient process (see bottom row of Fig. 5.5).

[7]We note that the Granato et al. (2021) model was constructed assuming that shattering only takes place between equal-size grains, so its inclusion on the non-equal collision model plots is just for information.

5.2.7 Turbulent coagulation of small grains

When two grains collide at sufficiently low velocities, they can fuse together, coagulating into a larger grain. The process of dust grain coagulation has been invoked to explain the lack of small grains contributing to the 60 μm emission at ISM gas densities $\gtrsim 10^3$ cm^{-3} (e.g. Stepnik et al., 2003; Roy et al., 2012). Coagulation has been extensively explored in the study of proto-stellar core collapse (Ormel et al., 2009; Guillet et al., 2020; Marchand et al., 2021; Kawasaki et al., 2022a; Lebreuilly et al., 2022) with the unanimous conclusion that dust grains grow by coagulation in high density gas. Previous models including coagulation (e.g. Chokshi et al., 1993; Hirashita and Yan, 2009; Aoyama et al., 2017; Yan et al., 2004) assume that coagulation between grains i and j only takes place below a threshold velocity

$$v_{\rm coa}^{i,j} = 21.4 \left[\frac{a_i^3 + a_j^3}{(a_i + a_j)^3}\right]^{1/2} \frac{\gamma^{5/6}}{E^{1/3} R_{i,j}^{5/6} s^{1/2}}, \tag{5.66}$$

above which bouncing (i.e. elastic collision) will be the end result of the collision. Again, a_i and a_j are the radii of target and projectile grains. This expression depends on a series of material properties of the dust grains (see Table 3 of Chokshi et al., 1993, for the values of γ, the grain material surface energy per unit area, $R_{i,j} = a_i a_j/(a_i + a_j)$, the reduced radius of the grains, and E, which is related to the Poisson's ratios and Young's modulus of the grain material). Experimental studies with micron-size silica spheres (Poppe et al., 1997) have shown that indeed there is a sharp transition velocity from coagulation to grain bouncing, but the estimate from Equation 5.66 is 4 times lower than the measured velocity, argued to be a result of the formation of ice mantles on grain surfaces. Consistent with our maximum density $n_{\rm H} = 10^4$ cm^{-3} for accretion of refractory materials limited by the formation of icy mantles (see Section 5.2.2), we consider that above a $n_{\rm H} \geq 10^4$ cm^{-3} water, CO and CH_4 ices freeze on the surfaces of dust grains (Hollenbach et al., 2008; Silsbee et al., 2021). This causes the coagulation threshold velocity to be a factor of 4 larger (Guillet et al., 2020) than the one predicted by Equation 5.66.

The coagulation timescale is computed similarly to the way we compute the shattering collision timescale, using the relative velocity from the Ormel and Cuzzi (2007) turbulent model (see Section 5.2.6)

$$t_{\rm coa}(\mathcal{M}; a_i, a_j) = (\sigma_{i,j} \Delta V_{i,j} n_{{\rm d},j})^{-1}, \tag{5.67}$$

which makes use of the same variables defined for Equation 5.65, and again assuming no corrections to the geometrical cross section (i.e. $\beta = 1$) due to grain charging or radius increase by the ice mantle. In Fig. 5.6 we show the coagulation timescale as predicted by different velocity and collision models for carbonaceous and silicate grains in the molecular cloud (i.e. MC, as defined in Table 1 of Yan et al., 2004) phase. The top panel is based on a collision model that assumes that grains in the small bin coagulate, forming grains that contribute to the large grains bin. The bottom panel instead considers small grains sticking on the surface of large grains, once again forming grains that fall into the large grains bin. Both models effectively transfer mass from the small grains to the large grains, conserving the total dust mass. Similar to the shattering timescales, we compute coagulation timescales using the models for the relative collision velocities from Ormel and Cuzzi (2007) (dot-dashed lines) and the maximum and minimum relative velocity from Hirashita and Aoyama (2019) (shaded bands), distinguishing carbonaceous grains (silver-blue) and silicate grains (brown). Additionally, we compare our results to the simple prescription by Aoyama et al. (2017) (solid lines), originally used in the dust model implementation of RAMSES (Equation 19 in Dubois et al., 2024). This simple model fixes the velocity dispersion of small grains to 0.1 km/s in gas with $n_{\rm H} \geq 10^2$ cm^{-3}, only allowing coagulation above this Hydrogen density. Additionally, for all models considered here, we also apply the un-resolved turbulence enhancement of the gas density[8] as done for accretion (see Section 5.2.2).

The Aoyama et al. (2017) model results in a constant timescale of ~ 10 Myr in the MC phase with $n_{\rm H} = 300$ cm^{-3} at $\mathcal{M} \lesssim 3$. Above this Mach number, turbulent enhancement of gas density quickly develops, decreasing $t_{\rm coa}$ by 2-3 orders of magnitude. For the case of small grain collisions (top panel), turbulent enhancement of the relative velocity is inefficient at $\mathcal{M} \lesssim 1$, which means that relative velocities are dominated by thermal Brownian motion, which is constant for a given ISM phase. For $\mathcal{M} \lesssim 1$, small grains are barely affected by turbulent flows and the Ormel and Cuzzi (2007) based model gives similar results to the Hirashita and Aoyama (2019) scaling. However, both models predict a larger (up to 2 dex at low Mach number) $t_{\rm coa}$ below $\mathcal{M} \sim 1$ compared to the fixed velocity dispersion (0.1 km/s) model of Aoyama et al. (2017).

[8] In the vanilla dust model for RAMSES that we have presented in Dubois et al. (2024) we do not consider the un-resolved density PDF. Instead, we assume that half the gas mass above $n_{\rm H} > 10\,{\rm cm}^{-3}$ has an actual density of $10^3\,{\rm cm}^{-3}$.

This behaviour inverts at $\mathcal{M} \sim 2-3$, when the Aoyama et al. (2017) model sits above the other models by up to a factor of $\sim 5-6$.

In the bottom panel we can see that for equal GDR of large and small grains in the MC phase, coagulation due to collisions with large grains is ~ 2 dex less efficient compared to small grain collisions (we also include the prediction of small coagulation by the Aoyama et al. (2017) model as a guide in this panel). Instead of abruptly shutting off coagulation when $\Delta V_{i,j} > v_{\rm coa}$, we apply a sigmoidal smoothing that returns a maximum $t_{\rm coa}$ of 10^5 Myr (i.e. one order of magnitude larger than the Hubble time) in order to effectively stop coagulation. Previous works (e.g. Asano et al., 2014) have shown that the extinction curve of the Milky Way cannot be explained by a sharp cutoff in coagulation. In both panels this can be seen as the fast rise of $t_{\rm coa}$ at high $\mathcal{M}$, which happens earlier for the large-small grain collision model due to the longer stopping time of large grains. Although at an equal GDR large-small grain collisions are less efficient, we leave it as a possibility that this coagulation process may become an important last stage of coagulation in long-lived dense clouds, when the number density of large grains may increase the frequency of collisions with small grains. Therefore, we also explore in our model the effect of including this extra coagulation path.

5.2.8 Molecular hydrogen formation on dust surfaces

Molecular hydrogen is the most abundant molecule in the Universe (e.g. Fraser et al., 2002; Bolatto et al., 2013). It strongly influences the thermal state of star-forming gas as well as the formation of other molecules in the ISM. In Section 2.1.2 we mentioned the primordial formation pathway for molecular hydrogen anchored in H^- implemented in PRISM. While this process plays a dominant role in the dust-free formation of the first stars (e.g. Abel et al., 2000; Abel et al., 2002), H_2 is believed to be primarily formed via catalytic reactions on dust grain surfaces. The consistent, on-the-fly modelling of H_2 formation on dust grains is then one of the strengths of Dusty-PRISM.

When an atom encounters a grain surface, it can either be physisorbed, chemisorbed or return to the gas phase if it finds the site occupied by another H atom. Imagine that an atom has been physisorbed. From there, it may begin a random walk along the grain surface, either crossing to another physisorbed site, or falling into a deeper

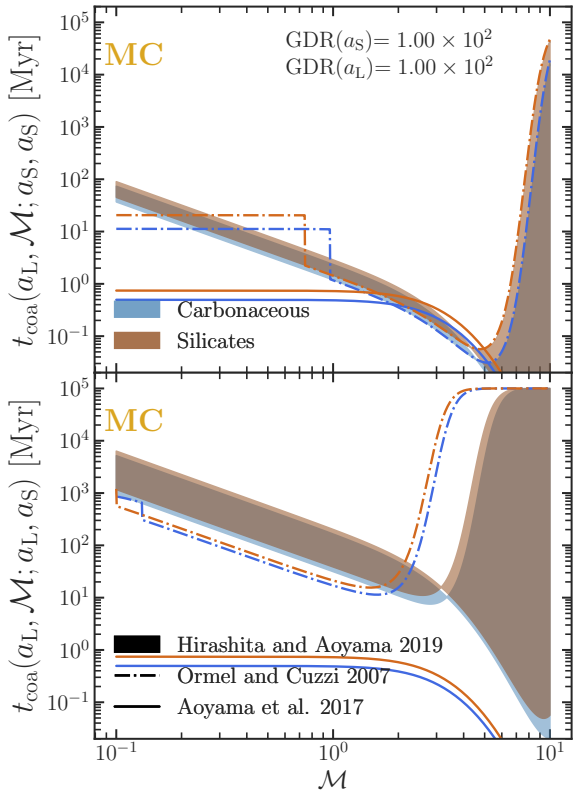


Figure 5.6: Coagulation timescale versus the local turbulent Mach number $\mathcal{M}$ for the different coagulation/velocity models explored. These have been computed for carbonaceous grains (silver-blue) and silicate grains (brown) in the molecular cloud (MC) ISM phase of Yan et al. (2004), considering the collisions of small to small grains (top panel) and the collisions of small to large grains (bottom panel). The range of timescales assuming the maximum to minimum relative velocity of Hirashita and Aoyama (2019) is given by the shaded bands, while the model using relative collision velocities from Ormel and Cuzzi (2007) is represented by the dash-dotted lines. We also include the prediction of the Aoyama et al. (2017) model with a fixed dust dispersion velocity of 0.1 km/s. For collisions of small to small grains (top panel), the simple Aoyama et al. (2017) model underpredicts by 2 dex t_{coa} for $\mathcal{M} \lesssim 1$, and for $\mathcal{M} \sim 2-3$ it is larger by a factor of $\sim 5-6$ compared to the Hirashita and Aoyama (2019) and Ormel and Cuzzi (2007) models.

chemisorbed site. Between these different sites, the atom will encounter a saddle point (i.e. activation barrier, E_S). To compute the probability of crossing from one attachment site to another, Cazaux and Tielens (2002) calculate the transmission coefficients corresponding to these transitions, considering the experimentally measured H desorption energies from a physisorbed site E_{H_P} and a chemisorbed site E_{H_C}. The mobility of atoms on the dust grain surface is governed by thermal hopping at elevated temperatures and by quantum tunnelling for very low temperatures. This means that the chances of an adsorbed H atom diffusing from one site to another increase as the dust temperature increases, but it also causes an H atom to evaporate faster from the

surface before it can recombine with another H atom. If the dust temperature allows for chemisorption evaporation, the atom leaves the site before combining, effectively quenching the production of H_2. On the contrary, if the flux of H atoms reaching a grain surface increases, the number of chemisorbed atoms increases, and H_2 formation becomes more efficient. If the diffusing atoms encounter another attached H atom in a chemisorbed or physisorbed site, the production mechanism is denominated Langmuir-Hinshelwood. If instead the incoming atom directly recombines with an already attached atom, the mechanism is termed Eley-Rideal. In this case, the H_2 molecule will leave with a significantly higher excitation energy.

The Langmuir–Hinshelwood formation rate of H_2 for dust bin j is given by:

$$R_{\mathrm{d},j} = \frac{1}{2} n_{\mathrm{H}} v_{\mathrm{H}} n_{\mathrm{d},j} \sigma_{\mathrm{d},j} \epsilon_{\mathrm{H_2},j} S_{\mathrm{H},j} \,, \tag{5.68}$$

where v_{H} is the thermal velocity of hydrogen atoms, $\sigma_{\mathrm{d},j}$ is the geometrical dust cross section, $\epsilon_{\mathrm{H_2},j}$ is the H_2 formation efficiency, and $S_{\mathrm{H},j}$ is the sticking coefficient of H atoms (not to be confused with $\alpha(T)$ in Section 5.2.2). The sticking coefficient depends on the dust and gas temperatures (Hollenbach and McKee, 1979):

$$S_{\mathrm{H,j}}(T) = \left[1 + 0.4\sqrt{\frac{T+T_{\mathrm{d},j}}{100\,\mathrm{K}}} + 0.2\frac{T}{100\,\mathrm{K}} + 0.08\left(\frac{T}{100\,\mathrm{K}}\right)^2\right]^{-1}, \tag{5.69}$$

where $T_{\mathrm{d},j}$ is the dust temperature computed with the method outlined in Section 5.2.9. A grain sustains a H flux given by:

$$F_{\mathrm{H}} = \frac{n_{\mathrm{H}} v_{\mathrm{H}}}{N_{\mathrm{S}}}, \tag{5.70}$$

where N_{S} is the number of free chemi- and physisorption sites per unit surface area of the grain. The H_2 recombination efficiency appears to be independent of the H flux over the range of temperatures expected for molecular clouds (see figure 1 in Cazaux and Tielens, 2002), so we assume a fixed value of N_{S} for our molecular hydrogen formation route of $N_{\mathrm{S}} = 2 \times 10^{15}$ sites cm^{-2} (Cazaux and Tielens, 2004). As in the original model by Cazaux and Tielens (2002), we consider three different populations: physisorbed H, chemisorbed H, and physisorbed H_2, with abundances given by H_{P}, H_{C} and H_2, respectively. Their respective evaporation rates are given

by $\beta_{\mathrm{H_P}}$, $\beta_{\mathrm{H_C}}$, and $\beta_{\mathrm{H_2}}$. The general desorption rate β_i is given by the Polanyi-Wigner equation (Tielens and Alexander, 2021):

$$\beta_i = \nu_i \exp\left\{-\frac{E_i}{k_{\mathrm{B}}T}\right\}, \tag{5.71}$$

where ν_i is the vibrational frequency of species i on the grain surface, and E_i is the adsorption energy. We can then define a general expression for the recombination efficiency that is valid at all cloud temperatures:

$$\epsilon_{\mathrm{H_2},j} = \left(1 + \frac{\chi_{\mathrm{H_2}} F_{\mathrm{H}}}{2\beta_{\mathrm{H_2}}} + \frac{\beta_{\mathrm{H_P}}}{\alpha_{\mathrm{PC}}}\right)^{-1} \xi(T), \tag{5.72}$$

where $\chi_{\mathrm{H_2}}$ is the fraction of molecular hydrogen that stays on the surface after formation, and α_{PC} is the mobility (in terms of hops per second) of a hydrogen to move from a physisorbed to a chemisorbed site (due to a combination of quantum mechanical tunnelling and thermal hopping). However, considering the temperatures at which these reactions take place (~ 20 K, see Figure 4 in Cazaux et al., 2004, but also the discussion in Katz et al., 1999), thermal hopping still dominates over quantum effects, which implies that we can safely assume that the recombination efficiency is independent of the width of the energy barriers. Then, the correction factor ξ at high temperatures reflecting the evaporation of chemisorbed H is given by[9]:

$$\xi(T) = \left[1 + \frac{\nu_{\mathrm{H_C}}}{2F_{\mathrm{H}}} \exp\left\{-\frac{1.5E_{\mathrm{H_C}}}{k_{\mathrm{B}}T}\right\} \left(1 + \sqrt{\frac{E_{\mathrm{H_C}} - E_{\mathrm{S}}}{E_{\mathrm{H_P}} - E_{\mathrm{S}}}}\right)^2\right]^{-1}, \tag{5.73}$$

where $\nu_{\mathrm{H_C}}$ is the frequency factor of the desorption rate of chemisorbed H and the energy parameters are the ones described above and included in Table 5.4. Furthermore, the ratio of physisorbed desorption rate to the mobility parameter α_{PC} in Equation 5.72 can be expressed as:

$$\frac{\beta_{\mathrm{H_P}}}{\alpha_{\mathrm{PC}}} = \frac{1}{4}\left(1 + \sqrt{\frac{E_{\mathrm{H_C}} - E_{\mathrm{S}}}{E_{\mathrm{H_P}} - E_{\mathrm{S}}}}\right)^2 \exp\left\{-\frac{E_{\mathrm{S}}}{k_{\mathrm{B}}T}\right\}. \tag{5.74}$$

In practice, we compute the contribution of each grain size bin to the total local formation rate of molecular hydrogen, considering the on-the-fly dust temperature T_{d}. We use the physical parameters for olivine silicate surfaces and amorphous graphite given by Cazaux et al. (2004), which are themselves derived from the experimental results from laboratory irradiation of grain surfaces performed in Pirronello et al. (1996), Pirronello et al. (1997), and Pirronello et al. (1999).

[9] As given in the erratum for Cazaux and Tielens (2002).

Grain surface	E_{H_2} [K]	χ_{H_2}	E_S [K]	E_{H_P} [K]	E_{H_C} [K]	ν_{H_2} [s^{-1}]	ν_{H_C} [s^{-1}]
Silicate	340	0.3	200	650	3×10^4	2×10^{12}	1×10^{13}
Graphite	540	0.4	250	800	3×10^4	3×10^{12}	2×10^{13}

Table 5.4: Reaction parameters for physisorbed and chemisorbed sites for the recombination of molecular hydrogen on silicate and graphite surfaces, as provided in Cazaux et al. (2004).

5.2.9 Dust optical properties

We use the optical properties for graphite and 'UV smoothed' astronomical silicates by Draine et al. (1984) (see also Laor and Draine, 1993; Weingartner and Draine, 2000)[10] for our carbonaceous and silicate grains. The total local dust optical depth is given by:

$$\tau(\lambda) = L \sum_i C_{\mathrm{ext,\,i}}(\lambda) n_{\mathrm{d,\,i}}, \tag{5.75}$$

where L is the path length for light propagating through a medium of dust density $n_{\mathrm{d,\,i}}$, $C_{\mathrm{ext,\,i}}$ is the wavelength dependent extinction cross-section, and the sum is over dust components (large, small, silicate, carbonaceous grains). Consider a monochromatic plane wave with frequency ν and flux F_0 hitting a dust grain. Then, the flux of light scattered to a large distance r in the direction specified by angles (θ, ϕ) with respect to the normal vector of the original plane wave at is

$$F(\theta, \phi) = \frac{F_0}{k^2 r^2} \mathcal{L}(\theta, \phi), \tag{5.76}$$

where $k = 2\pi/\lambda$ is the wavenumber of the incident radiation and $\mathcal{L}(\theta, \phi)$ is a function that does not depend on r nor on F_0. If we require that the total energy per unit time scattered in all directions is $F_0 C_{\mathrm{sca}}$ then the scattering cross section C_{sca} is

$$C_{\mathrm{sca}}(\lambda) = \int_0^{2\pi} \int_0^{\pi} \frac{\mathrm{d}\sigma(\lambda)}{\mathrm{d}\Omega} \sin\theta \mathrm{d}\theta \mathrm{d}\phi, \tag{5.77}$$

where $\mathrm{d}\sigma/\mathrm{d}\Omega = \mathcal{L}(\theta, \phi)/k^2$ is the differential cross-section. We can also define the scattering phase function asymmetry as the mean value of the scattered light $\cos\theta$

$$g \equiv \langle \cos\theta \rangle = \frac{1}{C_{\mathrm{sca}}} \int_0^{2\pi} \int_0^{\pi} \cos\theta \frac{\mathrm{d}\sigma(\lambda)}{\mathrm{d}\Omega} \sin\theta \mathrm{d}\theta \mathrm{d}\phi, \tag{5.78}$$

which can be further simplified by recognising that for spheres, by symmetry arguments, there is no dependence on the angle ϕ. The asymmetry factor g is related to how electromagnetic radiation exerts pressure on a dust grain. A photon that is absorbed

[10] We use the publicly available optical properties from Bruce T. Draine's personal website (https://www.astro.princeton.edu/~draine/dust/dust.diel.html).

deposits its full momentum $h\nu/c$. If it is scattered by an angle θ, it only deposits the fraction $1 - \cos\theta$ of its original momentum. Therefore, the cross-section for radiation pressure is

$$C_{\rm rp} = C_{\rm ext} - gC_{\rm abs} = C_{\rm abs} + (1-g)C_{\rm sca}, \tag{5.79}$$

where the extinction cross-section is $C_{\rm ext} \equiv C_{\rm abs} + C_{\rm sca}$.

Based on these optical properties, we can derive dust temperatures in the equilibrium approximation using the local radiation properties. Ignoring the small amount of energy that goes into luminescence or photo-electrons (e.g. Weingartner and Draine, 2001c), the heating rate of a grain by absorption of radiation is:

$$\frac{{\rm d}E_{\rm abs}}{{\rm d}t} = \int \frac{u_\nu {\rm d}\nu}{h\nu} ch\nu C_{\rm abs}(\nu), \tag{5.80}$$

where $\frac{u_\nu {\rm d}\nu}{h\nu}$ is the number density of photons with frequencies in the range $[\nu, \nu + {\rm d}\nu]$ for the radiation field energy density u_ν. In practice, we compute a spectrum-averaged[11] absorption cross-section for each radiation bin i in RAMSES-RTZ:

$$\overline{C}_{{\rm abs},i} = \frac{\int_{\lambda^i_{\rm min}}^{\lambda^i_{\rm max}} \lambda C_{\rm abs}(\lambda) u_\lambda {\rm d}\lambda}{\int_{\lambda^i_{\rm min}}^{\lambda^i_{\rm max}} \lambda u_\lambda {\rm d}\lambda}, \tag{5.81}$$

where the integral is over the minimum $\lambda^i_{\rm min}$ and maximum $\lambda^i_{\rm max}$ wavelengths covered by radiation bin i. The energy loss due to IR emission is given by:

$$\frac{{\rm d}E_{\rm em}}{{\rm d}t} = \int {\rm d}\nu 4\pi B_\nu(T_{\rm d}) C_{\rm abs}(\nu), \tag{5.82}$$

with B_ν being Planck's blackbody function. To simply this calculation at runtime, we can compute a Planck-averaged emission efficiency defined as:

$$\overline{C}_{{\rm abs},T_{\rm d}} \equiv= \frac{\int {\rm d}\nu B_\nu(T_{\rm d}) C_{\rm abs}(\nu)}{\int {\rm d}\nu B_\nu(T_{\rm d})}, \tag{5.83}$$

which allows us to write the IR emission rate as:

$$\frac{{\rm d}E_{\rm em}}{{\rm d}t} = 4\overline{C}_{{\rm abs},T_{\rm d}} \sigma_{\rm SB} T_{\rm d}^4, \tag{5.84}$$

[11] This is based on the stellar-polling approximation in RAMSES-RT, which recomputes the average spectrum in each radiation bin at every coarse timestep by performing a weighted average over all stellar sources in the simulation volume (e.g. Rosdahl et al., 2018). In the case of including radiation from other bright sources with very different spectrum to the dominant stellar emission (e.g. accretion disk of a SMBH) this approximation may fail in capturing the effective radiation field near the secondary source.

with $\sigma_{\rm SB}$ the Stefan-Boltzmann constant. With these simplifications, we can determine the steady state temperature for grain bin j (Draine, 2010) based on the balance of absorbed energy for all radiation bins (below the Lyman limit of 13.6 eV) and collisional heating sources (Eq. 5.36 and 5.45, see Section 5.2.4):

$$4\overline{C}_{{\rm abs},T_{{\rm d},j}}\sigma_{\rm SB}T_{{\rm d},j}^4 = \sum_i \overline{C}_{{\rm abs},i,j}u_i c + \sum_k H_{{\rm coll},k}(\vec{P}_j, T, n_k) \tag{5.85}$$

where k loops over all gas species contributing to the collisional heating and:

$$u_i = \int_{\lambda^i_{\rm min}}^{\lambda^i_{\rm max}} \lambda u_\lambda {\rm d}\lambda. \tag{5.86}$$

We set a floor for the dust temperature given by the current CMB temperature ($T_{\rm CMB}(z)$) at redshift z.

5.2.10 Radiative torque disruption of large grains

In Section 5.2.6 we have seen that shattering is fundamental to generating small grains in the diffuse ISM. However, the production of small grains by shattering in dense, star-forming regions remains a challenge for current dust evolution models, as we expect coagulation to dominate in these regions (see Section 5.2.7), resulting in a GSD biased towards large grains. A popular method to probe the GSD in these regions is by optical-NIR observations of the polarisation fraction P (see Andersson et al., 2015, for a recent review on the topic). Since starlight polarisation was discovered in 1949 (Hall et al., 1949; Hiltner, 1949), many theories have been developed to model the physical mechanisms that explain the observed P and its dependence with wavelength (e.g. Davis et al., 1951; Gold et al., 1952; Lazarian, 2003; Hoang and Lazarian, 2009). Observations towards dark clouds show a particularly large wavelength for the maximum polarisation ($\lambda_{\rm max} \sim 0.6 - 1.2\ \mu$m), increasing with the optical attenuation A_V (Andersson and Potter, 2007; Clemens et al., 2016; Wang et al., 2017). Considering that the maximum polarisation for a particular grain size a is expected at $\lambda_{\rm max} \sim a$, these results support the claim that in dense clouds the average grain size is significantly larger than in the diffuse ISM.

One of the most successful theories for grain alignment is the Radiative Alignment Theory (RAT) introduced by Dolginov et al. (1976) and further developed around the DDSCAT code (Draine et al., 1994; Draine and Weingartner, 1996) using its

capabilities to numerically test the scattering properties of irregular grains. The physical reasoning behind RAT can be understood as follows: irregular grains (not perfect spheres) have differential extinction cross-sections for the left- and right-hand polarisation components of light. This non-uniform surface radiation force is then capable of inducing an effective torque on the grain[12]. RAT predicts that the efficiency of these torques increases with the strength and anisotropy of the local radiation field. Therefore, it came as a surprise that, when high resolution observations first studied the alignment of large grains in dense molecular cores, they revealed a 'polarisation hole' in the vicinity of protostars (e.g. Hull et al., 2014; Cox et al., 2018). If alignment is dominated by the Barnett effect in paramagnetic grains, highly tangled magnetic fields could explain this observed reduced alignment. However, it remains difficult to explain the misalignment of these grains in a region of intense radiation in which the alignment with the radiation field (as opposed to the alignment with the magnetic field) is expected to be larger (Cho and Lazarian, 2005; Cho and Lazarian, 2007).

If grains remain in these intense radiation fields, can RAT indefinitely accelerate their spin? Recently, this question has led to the development of the Radiative Torque Disruption (RATD) mechanism (Hoang, 2019; Hoang et al., 2019; Hoang, 2020). The spin-up by RAT can reach such extreme regimes in these environments that centrifugal stress can exceed the grain material tensile strength, effectively breaking the original grain into smaller fragments. The overall effect of this process (moving dust mass from large to small grains) is the same as shattering, but unlike shattering RATD does not depend on the dust abundance. The RATD mechanism is therefore capable of enhancing the small grain population in the high radiation field, low DTM ISM conditions typical of high redshift galaxies, over very short timescales (Hirashita and Hoang, 2020).

We have implemented the RATD mechanism in Dusty-PRISM , a process that may affect the grain size distribution in starburst systems and near high radiation

[12]If the grain is made of a paramagnetic material (as is commonly assumed for silicate grains), a net internal magnetisation parallel to the spin axis (i.e. Barnett magnetisation) will cause the grain to Larmor precess around the local magnetic field direction. This effect has played a fundamental role in the study of magnetic fields in the ISM (e.g. Crutcher, 2012; Pattle and Fissel, 2019; Tram et al., 2021; Duc Hoang et al., 2022). We will explore the modelling of dust alignment in future Dusty-PRISM simulations with CRMHD.

sources in the ISM (young stellar clusters or AGN). Let a be the effective radius of our irregular dust grain. The radiative torque induced is (Hoang et al., 2021):

$$\Gamma_\lambda = \pi a^2 \gamma u_\lambda \left(\frac{\lambda}{2\pi}\right) Q_\Gamma, \tag{5.87}$$

with Q_Γ the RAT optical efficiency (Draine and Weingartner, 1996; Lazarian and Hoang, 2007), γ the radiation field anisotropy, and u_λ the radiation field energy density at λ. Numerical calculations with DDSCAT (Lazarian and Hoang, 2007) suggest that RAT efficiency can be approximated by a power law:

$$Q_\Gamma(\lambda) = \alpha \left(\frac{\lambda}{a}\right)^{-\eta}, \tag{5.88}$$

with the wavelength λ given in microns and where $\alpha = 0.4$ and $\eta = 0$ for $a_{\rm trans} < a \leq \lambda/0.1$, and $\alpha = 2.33$ and $\eta = 3$ for $a \leq a_{\rm trans}$. The transition size at which the RAT efficiency slope changes is given by $a_{\rm trans} = \lambda/1.8$. In practice, we compute the radiative torque averaged over a given radiation bin i:

$$\Gamma_{\rm RAT,\,i} = \pi a^2 \gamma_i u_i \left(\frac{\overline{\lambda}_i}{2\pi}\right) \overline{Q}_{\Gamma,i}, \tag{5.89}$$

where we have introduced the radiation bin averaged RAT efficiency $\overline{Q}_{\Gamma,i}$, and radiation anisotropy γ_i:

$$\overline{Q}_{\Gamma,i} = \frac{\int_{\lambda^i_{\rm min}}^{\lambda^i_{\rm max}} \lambda Q_\Gamma(\lambda) u_\lambda {\rm d}\lambda}{\int_{\lambda^i_{\rm min}}^{\lambda^i_{\rm max}} \lambda u_\lambda {\rm d}\lambda} \tag{5.90}$$

$$\gamma_i = \frac{\sqrt{F_{i,x}^2 + F_{i,y}^2 + F_{i,z}^2}}{N_{{\rm ph},i}\tilde{c}}, \tag{5.91}$$

where $\mathbf{F}_i$ is the local i-group radiation flux vector (as given in Rosdahl et al., 2013), $N_{{\rm ph},i}$ its local photon density, and $\tilde{c}$ the reduced speed of light. The equilibrium rotation rate is given by (Lazarian and Hoang, 2007; Hoang and Lazarian, 2009):

$$\omega_{\rm RAT} = \frac{\Gamma_{\rm RAT}\tau_{\rm damp}}{I_a}, \tag{5.92}$$

where $\Gamma_{\rm RAT} = \sum_i \Gamma_{\rm RAT,\,i}$ is the radiative torque summed over all radiation bins, I_a is the principal moment of inertia of a spherical grain of radius a, and $\tau_{\rm damp}$ is the rotational damping timescale given by:

$$\tau_{\rm damp}^{-1} = \tau_{\rm gas}^{-1}(1 + F_{\rm IR}), \tag{5.93}$$

encompassing contributions from IR radiation resulting from the loss of rotational energy: $F_{\rm IR}$ being the IR damping factor, and the loss of rotational energy from gas collisions followed by evaporation with $\tau_{\rm gas}$ given by (Draine and Lazarian, 1998):

$$\tau_{\rm gas} = \frac{3}{4\sqrt{\pi}} \frac{I_a}{\mu m_{\rm H} n_{\rm H} \langle v_{\rm th} \rangle a^4}, \tag{5.94}$$

where $\langle v_{\rm th} \rangle \simeq \sqrt{\frac{2k_{\rm B}T}{\mu m_{\rm H}}}$. Deriving this damping timescale $\tau_{\rm damp}$ involves accounting for the influence of collisional dragging, plasma drag, H_2 formation, surface evaporation and infrared emission (Draine and Weingartner, 1996) on the total torque. Eq. 5.94 assumes (Roberge et al., 1993) that (a) every colliding atom/molecule sticks to the dust grain surface long enough so that its kinetic energy thermalises to the grain temperature, (b) every sticking collision is followed by thermal evaporation, (c) evaporation does not occur in a preferred location of the grain surface, and (d) the gas drift velocity is negligible (perfect gas-dust coupling).

The IR damping can be understood as the negative torque caused by IR photons carrying part of the grain angular momentum. This is given by (Draine and Weingartner, 1996):

$$F_{\rm IR} = 67.26 G_0^{2/3} \left(\frac{10^{-3}\,\mu{\rm m}}{a} \right) \left(\frac{20\,{\rm cm}^{-3}}{n_{\rm H}} \right) \left(\frac{100\,{\rm K}}{T} \right)^{1/2} \left(\frac{20\,{\rm K}}{T_{\rm d}} \right), \tag{5.95}$$

where, as usual, the grain radius a is in μm and $T_{\rm d}$ is the local dust temperature computed on-the-fly with the method in Section 5.2.9, and G_0 denotes the radiation field in Habing units.

The mechanical properties of dust grains are mainly prescribed by our choice of their tensile strength $S_{\rm max}$, defined as the maximum stress that a grain can withstand before breaking apart (Hoang, 2019). Compact, crystalline grains are expected to have a large $S_{\rm max} \sim 10^9 - 10^{10}\,{\rm erg\,cm^{-3}}$ (Burke et al., 1974; Draine et al., 1979), while fluffy aggregates (like the ones expected from accretion and coagulation in the ISM) will likely have a composite structure with a significantly lower tensile strength, of the order of $10^6 - 10^8\,{\rm erg\,cm^{-3}}$, as they are dominated by van der Waals forces ($\sim 10^{-3}$ eV) joining monomers of different sizes. Given the large uncertainty in the value of $S_{\rm max}$, in future work we plan to use observations of extinction in the diffuse ISM to constrain its value.

Assuming that internal relaxation can rapidly induce a perfect alignment of the rotation axis with the major axis of inertia, and that we do not model the dust grain mantle thickness, the centrifugal surface stress for rotational frequency ω is:

$$S = \frac{sa^2\omega^2}{4}. \tag{5.96}$$

This stress exceeds the tensile strength of the grain for the disruption frequency:

$$\omega_{\rm disr} = \frac{2}{a}\left(\frac{S_{\rm max}}{s}\right)^{1/2}. \tag{5.97}$$

When the condition $\omega_{\rm RAT} \geq \omega_{\rm disr}$ is satisfied, we compute the characteristic timescale for rotational disruption (Hoang, 2019):

$$t_{\rm RATD} = \frac{I_a\omega_{\rm disr}}{{\rm d}J/{\rm d}t} = \frac{I_a\omega_{\rm disr}}{\Gamma_{\rm RAT}}. \tag{5.98}$$

There is no current theory for the fragment distribution resulting from rotational disruption, so we follow Hirashita and Hoang (2020) and assume a fragment distribution similar to the power-law used for shattering in Section 5.2.6:

$$\theta_{\rm frag}(m; m_1) = \frac{(4-\alpha_f)m_1 m^{(-\alpha_f+1)/3}}{3\left(m_{f,\rm max}^{(4-\alpha_f)/3} - m_{f,\rm min}^{(4-\alpha_f)/3}\right)}\Phi(m; m_{f,\rm max}, m_{f,\rm min}), \tag{5.99}$$

where Φ is a top-hat function defined as $\Phi(m; m_{f,\rm max}, m_{f,\rm min}) = 1$ for $m_{f,\rm min} \leq m \leq m_{f,\rm max}$ and $\Phi(m; m_{f,\rm max}, m_{f,\rm min}) = 0$ otherwise. Contrary to Equation 5.62, this distribution does not depend on the local RATD properties, so it can easily be pre-computed at the beginning of the simulation for each grain bin to determine the fraction of grain mass that is returned. Using the fiducial GSD from Table 5.5, we calculate that the large carbonaceous grains return $\sim 92.2\%$ to small carbonaceous grains, $\sim 7.3\%$ to large PAHs, $\sim 0.4\%$ to small PAHs and $\sim 0.02\%$ is returned to the gas phase; while for large silicate grains $\sim 20\%$ of the mass remains in fragments within the large grain bin, $\sim 40\%$ is converted to small silicates, and $\sim 40\%$ is fully evaporated to the gas phase. Therefore, RATD efficiently transfers mass to small grains, with a significant fraction returned to the gas phase for large silicate grains.

	s [g cm^{-3}]	$N_{\rm C}$	a_0 [μm]	$a_{\rm min}$ [μm]	$a_{\rm max}$ [μm]	σ
small PAHs	2.0	54	5×10^{-4}	3×10^{-4}	1×10^{-3}	0.3
large PAHs	2.0	418	1×10^{-3}	3×10^{-4}	9×10^{-3}	0.4
small C	2.2	-	1×10^{-2}	1×10^{-3}	1×10^{-1}	0.7
large C	2.2	-	1×10^{-1}	5×10^{-3}	1.0	0.8
small Sil	3.3	-	5×10^{-3}	5×10^{-4}	1×10^{-1}	0.75
large Sil	3.3	-	1×10^{-1}	5×10^{-3}	1.0	0.75

Table 5.5: Fiducial parameters for the full Dusty-PRISM model. All grain/molecules assume a modified log-normal GSD given by Eq. 5.9. From left to right columns: material density, number of carbon atoms in the PAH molecule, grain/molecule centroid radius, minimum and maximum size cut-offs, and width of the log-normal distribution.

5.3 Polycyclic aromatic hydrocarbons in galaxy formation

In this section we detail our extension of the two-size grain approximation to account for the properties of very small particles containing C atoms: polycyclic aromatic hydrocarbons (PAHs). By computing the ratio of flux in IR emission features (attributed to PAHs) to the far-IR flux, one can obtain the fraction of UV flux that is absorbed by PAHs and, by adopting standard dust parameters (Allamandola et al., 1989), one can then predict the fraction of C locked in different PAHs. We again follow the modified log-normal distribution in Section 5.2 for the PAH bins. The original small carbonaceous (small C) grains centroid of 5×10^{-3} μm has been displaced to 1×10^{-2} μm to account for the higher discretisation of very small grains allowed by our two PAH bins. Our choice of PAH centroids is based on the abundance constraints of the Milky Way SED (Allamandola et al., 1989; Draine and Li, 2007) in resemblance to table 2 in Tielens (2008). We separate traditional PAHs ($\sim$ 54 C atoms) that are photolytically stable in the ISM (Guhathakurta et al., 1989) from large PAH clusters of $\sim$ 400 C ($\sim$ 10Å, the maximum size of PAHs considered in the NASA Ames PAH IR Spectroscopic Database Ricca et al., 2012; Bauschlicher et al., 2018; Mattioda et al., 2020) atoms contributing to the emission plateau underlying the IR emission features Tielens (2008). The effective radius a (in Å) of a PAH molecule is given by Equation 8 in Draine et al. (2021):

$$a = 10 \left(\frac{N_{\rm C}}{418} \right)^{1/3} . \tag{5.100}$$

Fig. 5.7 shows the decomposition of the underlying GSD for the full Dusty-PRISM model, separating carbonaceous grains in the left panel, from silicate grains in the right panel.

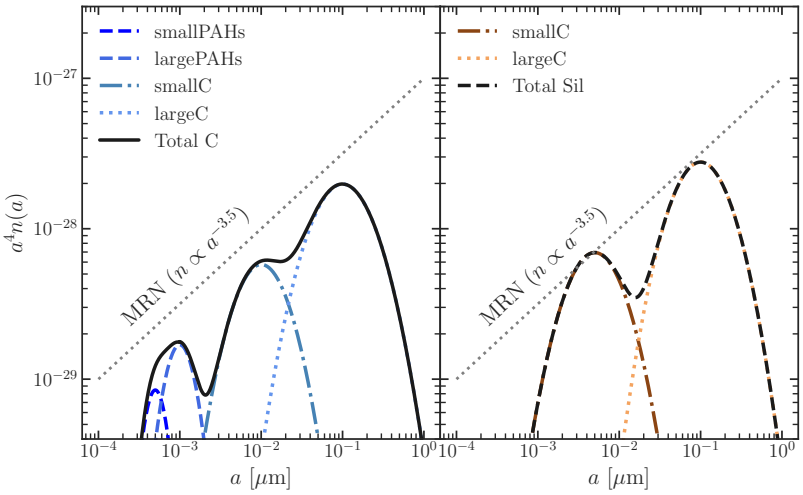


Figure 5.7: Underlying grain size distribution assumed in the Dusty-PRISM model for PAHs, carbonaceous grains and silicate grains. This has been computed for a gas density of 1 H cm^{-3} and using the DTG of the BARE-GR-S model in Zubko et al. (2004). See Section 5.3 for further details on the GSD parameter choice.

Abundance for each grain type is inferred using the BARE-GR-S model in Zubko et al. (2004). The modified log-normal parameters (width and limits, see Table 5.5) are based on fitting results to diffuse gas in the Milky Way by Hensley and Draine (2023). We compare our results to the slope of the MRN distribution: our choice of underlying GSD and Milky Way abundances assumption agrees with a MRN extending from large grains to the smallest PAHs.

5.3.1 PAH optical properties

As for the regular dust grains (Section 5.2.9), we use self-consistent optical properties for small and large PAHs. A main goal for the Dusty-PRISM model is to be able to predict the source of the ubiquitous mid-IR emission features at 3.3, 6.2, 7.7, 8.6, 11.3, 12.7, and 17 μm attributed to PAHs (see the extensive review by Tielens, 2008). In Chapter 1 we introduced the interesting possibility of using spectral variations in these features to further probe the conditions of the environment from which they emanate (e.g. Rigopoulou et al., 1999; Peeters et al., 2004; Li, 2020; Rigopoulou et al., 2021). These variations occur from one source to another (e.g. Sloan et al., 2007), and even sometimes around the same source (e.g. Rapacioli et al., 2005; Berne et al., 2008). The variation of these spectral features arises from a combination of different environments as well as different PAH properties/species. Therefore, a

fundamental aim of Dusty-PRISM is to be capable of accounting for the variability due to both components self-consistently.

For flexibility, we use the optical properties for PAHs derived by Li and Draine (2001) and publicly available[13], allowing us to obtain GSD-averaged cross-sections for any choice of PAH centroid a_0 (see Eq. 5.9). The intrinsic spectral properties of PAHs vary primarily because of their ionisation state (the 3.3 μm is reduced in ionised PAHs, and the features at the 11-15 μm are considerably boosted Bauschlicher et al., 2009), and the size of the molecule (contribution to the mid-IR plateau increases with increasing size, and the peak position of the major bands becomes more stable Hudgins et al., 1999; Bauschlicher et al., 2009). The optical properties in Li and Draine (2001) allow us to capture these changes in the strength of the different features and the scale of the mid-IR continuum with different charge states and sizes.

5.3.2 PAH sputtering

In the same manner as for classical dust grains, PAHs immersed in a hot gas experience frequent collisions with energetic ions. These collisions may impart sufficiently large energies to cause PAH molecular dissociation. The survival of PAHs in hot supernova gas remains a debated topic, with some observations presenting tentative evidence of PAH emission co-spatial with known SNRs (Reach et al., 2005; Tappe et al., 2006). Extra-galactic observations find that PAH emission follows ionised gas in starburst winds (McCormick et al., 2013; Bolatto et al., 2024). Therefore, understanding the processing of PAHs in hot gas is a fundamental step in modelling the PAH life-cycle within a realistic galactic environment. We follow the modelling of thermal sputtering of PAHs presented in Micelotta et al. (2010a), with a series of modifications and adaptations to our PAH model.

Ion-PAH collisions can be described by the simultaneous processes of nuclear stopping (elastic energy loss), and electronic stopping (inelastic energy loss). Nuclear stopping involves a binary collision of an ion with a single atom of a PAH molecule. If the collision energy exceeds the threshold for atom removal, the atom is ejected. For electronic stopping, the interaction is instead between the electrons of the PAH and the projectile ion. The transferred energy is then shared between the

[13]Again, from B. Draine's personal website (https://www.astro.princeton.edu/~draine/dust/dust.diel.html).

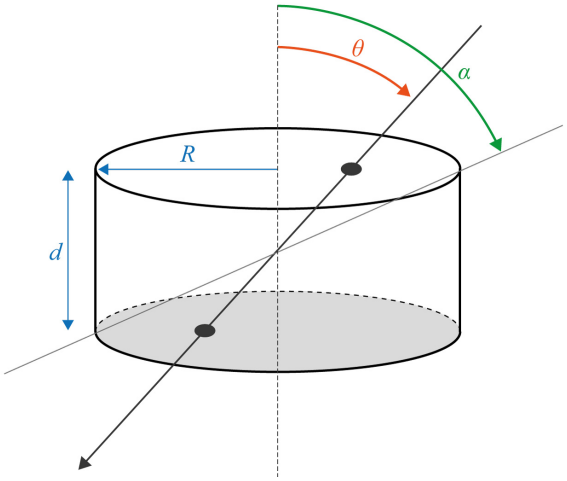


Figure 5.8: Geometrical representation of the path travelled by a colliding ion through a PAH molecule approximated as a disc. The volume of the molecule is defined by its radius R, thickness d, angle of the diagonal axis α, while the collision is parameterised by the incidence angle θ.

vibrational modes of the molecule, resulting in either IR emission (photo-relaxation) or in fragmentation via hydrogen or C_2H_n loss where $n = 0, 1, 2$. The transfer of energy in an electronic interaction for a PAH is a topic that remains, by-and-large, theoretically unexplored. We use the theoretical modelling developed for fullerenes in Schlathölter et al. (1999) and Hadjar et al. (2001). We consider that a PAH delocalised valence electrons behave like an electron gas, giving rise to an effective stopping power of the ion S (Sigmund, 1981):

$$S = \frac{\mathrm{d}T}{\mathrm{d}l} = \gamma(r_s)v, \tag{5.101}$$

where $\mathrm{d}T$ is the energy loss over the path length $\mathrm{d}l$ through the PAH electron gas, γ is the friction coefficient (Puska et al., 1983), and v is the incident ion velocity. The friction coefficient depends on the density parameter $r_s = (\frac{4}{3}\pi n_0)^{-1/3}$ which is itself a function of the valence electron density n_0. In the fullerene jellium model of Puska et al. (1983) n_0 assumes a spherical geometry, which requires some tweaking for our PAH disc geometry. In Fig. 5.8 we show the geometry of a PAH molecule. The effective PAH radius R is computed using Equation 5.100, and the π-electron cloud thickness is fixed to $d \sim 4.31$Å. Applying the jellium model to n_0 for PAHs Hadjar et al. (2001), n_0 is given in terms of the coordinates l and θ:

$$n_0(l, \theta) = 0.15 \exp\Big\{-(s\cos\theta)^2/2.7\Big\} \tag{5.102}$$

Element	Γ_0/a_0^2	R_2	T_0	E_{0n}(H)	E_{0n}(He)	E_{0n}(C)
			4.5	15.8	6.0	4.5
H	0.33	2.28	7.5	26.4	10.0	7.5
He	0.75	0.88	10.0	35.2	13.0	10.0
C	1.68	0.90	12.0	42.3	16.0	12.0
			15.0	52.8	20.0	15.0

Table 5.6: Fitting parameters for the electron friction (Equation 5.103) taken from the experimental data of Puska et al. (1983). The scaling parameter Γ_0 is given in units of the the Bohr radius $a_0 \simeq 5.291 \times 10^{-11}$ m.

where θ is the angle between the minor axis of the PAH and the direction of the incoming ion. The friction parameter has been computed by Puska et al. (1983) for different projectile ions with the following functional form:

$$\gamma(r_s) = \Gamma_0 \exp\left(-\frac{r_s(s,\theta) - 1.5}{R_2}\right), \tag{5.103}$$

where Γ_0 and R_2 are fitting parameters to their experimental results and given in Table 5.6 for the main ion projectiles that contribute to thermal sputtering (i.e. H, He and C). The total energy transferred can then be computed by integrating Equation 5.101 for a given incidence angle θ:

$$T_e(\theta) = \int_{-L(\theta)/2)}^{L(\theta)/2} \gamma(r_s(l,\theta))v\mathrm{d}s, \tag{5.104}$$

where L is the total path length through the PAH. By looking at Fig. 5.8, we can see that if $|\tan(\theta)| < \tan(\alpha)$, then $L(\theta) = d/\cos(\theta)$, and otherwise $L(\theta) = 2R/|\sin(\theta)|$. This means that if the angle of incidence is $\theta = \pi/2$ the path length will be maximal, and hence so will the energy transferred.

Ions colliding with a PAH may also remove a C atom from the PAH skeleton, for which we need to consider the theory of nuclear collisions by Micelotta et al. (2010b). In this case, we only consider collisions with energies above the threshold energy, T_0, of C removal. The destruction rate $R_{\rm N}^k(T, N_{\rm C})$ (the subscript N stands for 'Nuclear') is given by a collisional rate weighted by the Maxwellian velocity distribution $f(v,T)$ for ion k in the gas, and adding the correction due to Coulomb focusing with the $F_{\rm C}$ factor (see Section 5.2.2) to the original derivation in Micelotta et al. (2010a):

$$R_N^k(T, N_{\rm C}) = \frac{1}{2} N_{\rm C} n_k \int_{v_0}^{\infty} F_{\rm C} v \sigma_{N,k}(v, T_0) f(v,T)\mathrm{d}v, \tag{5.105}$$

where n_k is the local number density of ion k, $N_{\rm C}$ is the number of Carbon atoms, v_0 is the velocity corresponding to the threshold energy T_0, and $\sigma_{N,k}(v, T_0)$ is the nuclear

interaction cross-section per C atom, taken from interpolating the results in Figure 2 of Micelotta et al. (2010b). The threshold energy T_0 is the minimum energy that a collision must transfer to a C atom to eject it from the PAH skeleton. However, as detailed in Micelotta et al. (2010b) the choice of T_0 is very uncertain, as there are no experimental nor theoretical determinations of its value for astrophysically relevant PAHs. The physical meaning of T_0 is also different from the threshold energy for atomic displacement used in solid state physics, which for graphite has been measured to vary from 12 eV (Nakai et al., 1991) up to 30 eV (Montet et al., 1967), while for amorphous carbon the value is suggested to be lower and close to 5 eV (Cosslett, 1978). We hence choose a value of 7.5 eV as in Micelotta et al. (2010b) to be consistent with the experimental data observed for pseudo-PAH materials. We found that varying the value of T_0 from 4.5 to 15 eV mainly introduces a shift in the gas temperature at which sputtering starts to be relevant, from $\sim 5 \times 10^3$ K to $\sim 10^4$ K.

In the coronal hot gas (up to $\sim 10^8$ K), electrons can reach very high thermal velocities, with kinetic energies capable of significantly altering the internal energy of a PAH molecule. In these sub-relativistic regimes ($\sim$ 10 keV), elastic collisions between electrons and target nuclei are not effective, and instead inelastic interactions with target electrons dominate. Similar to the case of electronic excitations by hot ions, these inelastic interactions excite molecules, followed by either dissociation or IR photo-relaxation. However, at these low kinetic energies, the Born approximation is no longer valid (no impulsive interaction, see also Section 5.2.3), which obliges us to instead use experimentally motivated stopping powers. We use the fit to the electron stopping power S of solid carbon given by Eq. 5.47 with the parameters in Table 5.3. Since $S = -\frac{\mathrm{d}E}{\mathrm{d}l}$, we can find the maximum pathlength $L(\theta)$ through the PAH by numerically integrating Equation 5.47:

$$\int \mathrm{d}l = -\int_{E_0}^{E_1} \frac{\mathrm{d}E}{S(E)} = l_1 - l_0 = L(\theta), \tag{5.106}$$

where we integrate from the initial energy of the electron E_0 to its final energy E_1 upon exit from the PAH. Given that we know for a given θ the value of L, we can numerically solve Equation 5.106 to determine the value of E_1, such that the energy transferred by the electron to the π-valence electron cloud is simply $T_{\mathrm{elec}}(\theta) = E_0 - E_1$.

In the microcanonical description of a PAH (e.g. Tielens, 2005), and under the ergodic approximation[14], the microcanonical temperature $T_{\rm m}$ can be approximated by:

$$T_{\rm m} \simeq 2000 \left(\frac{E_{\rm in}}{N_{\rm C}}\right)^{0.4} \text{ K}, \tag{5.107}$$

with the energy in eV, which is valid over the range $35 - 1000$ K. This can then be related to the effective temperature of the PAH for a particular internal energy $E_{\rm in}$:

$$T_{\rm eff} = T_{\rm m} \left(1 - 0.2\frac{E_{\rm bind}}{E_{\rm in}}\right), \tag{5.108}$$

with $E_{\rm bind}$ the binding energy of the dissociated fragment (e.g. C_2H_n). The second term in Equation 5.108 is a correction factor due to the finite heat bath obtained when Taylor expanding the system energy E around the average energy $\langle E(T_{\rm m})\rangle$. Therefore, the effective PAH temperature for a given excitation energy $T_{\rm e}$ (in eV) is approximately (Draine and Li, 2001; Tielens, 2005):

$$T_{\rm eff} \simeq 2000 \left(\frac{T_{\rm e}}{N_{\rm C}}\right)^{0.4} \left(1 - 0.2\frac{E_{\rm bind}}{T_{\rm e}}\right) \text{ K}. \tag{5.109}$$

In the Gibbs microcanonical distribution, the bond dissociation rate $k_{\rm diss}$ is estimated via the Arrhenius law (Tielens, 2005):

$$k_{\rm diss} = k_0(T_{\rm eff}) \exp\left(-\frac{E_{\rm bind}}{k_{\rm B}T_{\rm eff}}\right), \tag{5.110}$$

where k_0 is a coefficient estimated by:

$$k_0(T_{\rm eff}) = \frac{k_{\rm B}T_{\rm eff}}{h} \exp\left(1 + \frac{\Delta S}{\mathcal{R}}\right), \tag{5.111}$$

where h is Planck's constant, ΔS is the change in entropy due to dissociation, and $\mathcal{R}$ is the ideal gas constant. We use the dissociation parameters for the acetylene fragment (C_2H_2) given in Micelotta et al. (2010a) and Ling and Lifshitz (1998). We now need to consider the competition between this dissociation pathway and IR photo-relaxation.

[14]The ergodic approximation establishes that in a thermodynamic system, the mixing of the different modes is so fast that the system quickly forgets about its initial conditions. Equivalently, the time average of a specific property (e.g. dissociation) is equal to the average over the full phase space. While this is a fair approximation for the high excitation energies that we consider in this derivation, if the internal energy of the molecule becomes very low, states will decouple and the energy will be well localised in specific modes. Because of energy localisation, the flow of energy will be reduced, hence affecting in our case the final dissociation rate. This may particularly affect the extrapolation of laboratory rates to the low interaction rates of astrophysical conditions (see section 8.5.3 in Tielens and Alexander, 2021, for a discussion on the breakdown of this statistical approach).

Computing the probability for dissociation requires evaluating the photon emission and photo-dissociation rates over the energy cascade resulting from each IR photon emission. This quickly becomes a difficult numerical task, but because of the steep dependence of the dissociation rate k_{diss} on the internal energy (Eq. 5.110), one can simplify this computation by evaluating the internal energy before IR cooling sets in (Tielens and Alexander, 2021). We follow an approach to this method presented in Micelotta et al. (2010a), in which we assume all photons have the same energy $\Delta\epsilon = 0.16$ eV, corresponding to a typical C-C vibrational mode. In this case, the normalised dissociation probability[15] is given by:

$$P(n_{\max}) = \frac{k_0 \exp[-E_{\rm bind}/(k_{\rm B}T_{\rm av})]}{k_{\rm IR}/(n_{\max}+1) + k_0 \exp[-E_{\rm bind}/(k_{\rm B}T_{\rm av})]}, \tag{5.112}$$

where $T_{\rm av}$ is the geometric mean of the PAH effective temperature between the initial excitation energy and the final equilibrium internal energy after $n_{\max}$ IR photon emissions. Naively, $n_{\max}$ could be estimated as $n_{\max} = (T_{\rm eff} - E_{\rm bind})/\Delta\epsilon$, assuming that the probability for dissociation after each IR photon emission is the same. However, an accurate computation of the probability indicates that these probabilities decrease. In Micelotta et al. (2010a) they instead determine the value of $n_{\max}$ as the step at which the probability has decreased by a factor of 10 with respect to the previous step. We have obtained a simple scaling from their $n_{\max}$ for different $N_{\rm C}$ given by $n_{\max} = \lceil N_{\rm C}/5 \rceil$. Once the dissociation probability $P(v, \theta, N_{\rm C})$ is computed, we can obtain the mean dissociation rate per ion velocity:

$$R^k_{\rm e}(v, N_{\rm C}) = v_k n_k F_{\rm C} \int_0^{\pi/2} \sigma_{\rm PAH,geo}(N_{\rm C}, \theta) P(v, \theta, N_{\rm C}) \sin\theta {\rm d}\theta, \tag{5.113}$$

where the PAH geometrical cross-section seen by a particle colliding with a PAH depends on the angle θ as follows:

$$\sigma_{\rm PAH,geo}(N_{\rm C}, \theta) = \pi R(N_{\rm C})^2 \cos\theta + 2R(N_{\rm C}) d \sin\theta. \tag{5.114}$$

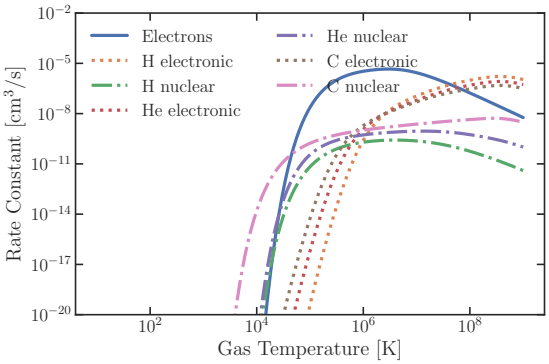
This can be integrated over the full Maxwellian distribution to give the total collision rate constant at a given T:

$$R^k_{\rm e}(T, N_{\rm C}) = \int_{v_0}^{\infty} R^k_{\rm e}(v, N_{\rm C}) f(v, T) {\rm d}v, \tag{5.115}$$

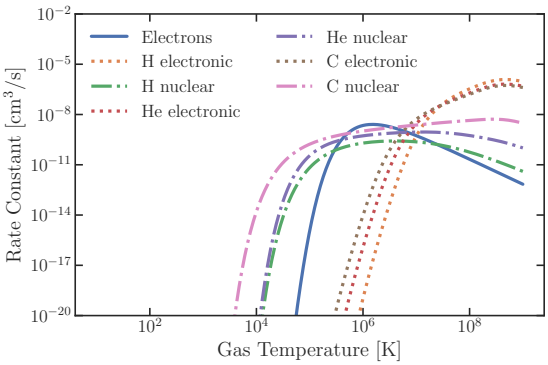
where v_0 is the electron/ion velocity corresponding to the binding energy of the acetylene group $E_{\rm bind}$.

Fragment	E_0 [eV]	ΔS [cal K^{-1} mol^{-1}]
H	4.3	11.8
H_2	3.52	-12.69
C_2H_2	4.6	10.0

Table 5.7: Dissociation parameters used for our PAHs with normal hydrogen coverage.



(a) Results for small PAHs ($N_C = 54$). Nuclear collisions are only important at the onset of sputtering at $\sim 10^4$ K, quickly overcome by the free electron destruction rate, peaking at $\sim 10^6$ K. Ion electronic excitations play an important role at very high gas temperatures.



(b) Results for large PAHs ($N_C = 418$). In this case, nuclear collisions dominate at low temperatures, and ion electronic excitations at very high temperatures, with an overall destruction rate lower by ~ 3 dex compared to small PAHs.

Figure 5.9: Sputtering rate constants for different PAH sizes due to free electron collisions (solid blue line), ion electronic excitations (dashed lines), and nuclear collisions (dot-dashed lines), separated by the dominant sputtering agents: H, He and C.

In Figure 5.9a we present the results of our PAH sputtering model for small PAHs ($N_C = 54$). We drop the dependence on n_k and the Coulomb focusing factor F_C as these two quantities are computed on a per-cell basis during a Dusty-PRISM simulation. Also, for the case of the nuclear collision, we drop the factor of N_C in Equation 5.105, hence removing the only dependence on N_C for this rate. Therefore, these rate constants are in units of cm^3 s^{-1}, for electronic ion collisions (Equation 5.115 with the probability obtained for the excitation energy given by Equation 5.104), nuclear ion collisions (Equation 5.105), and free electron collisions (Equation 5.115 with the deposited energy given by 5.106). For the ions, we separate the contributions into electronic and nuclear rates coming from the dominant sputtering agents: hydrogen, helium and carbon. Thermal sputtering becomes a relevant process for PAHs at $\sim 10^4$ K, i.e. approximately 1 dex lower in temperature than thermal sputtering for regular dust grains (see Section 5.2.3). At this temperature, the nuclear collisions dominate

[15]Note that in Micelotta et al. (2010a) $P(n_{max})$ is defined as the un-normalised probability, i.e. is missing the second term in the denominator.

the destruction rate, with a small dependence on ion mass, resulting in C collisions providing a higher destruction rate than H and He. Above $\sim 10^4$ K the destruction rate by free electrons grows sharply becoming the dominant sputtering agent in warm ionised gas (blue solid line). The electron sputtering peaks at $\sim 10^6$ K, decreasing at higher temperatures due to decreasing stopping power (Equation 5.101) at these thermal energies. Ion electronic collisions start to dominate the PAH sputtering rate only when gas temperatures reach $\sim 10^8$ K.

We have also computed these rates for our large PAHs ($N_{\rm C} = 418$) in Fig. 5.9b. As expected, the ion nuclear sputtering rates have not changed from their values in Fig. 5.9a as we have dropped the linear dependence with $N_{\rm C}$ in these plots. However, the $N_{\rm C}$-dependence is implicit in the electron excitations, which means that electron and ion electronic collisions differ significantly from their smaller PAH counterparts. We find that for large PAHs, free electron collisions are subdominant at all temperatures except around the peak at $\sim 10^6$ K, when their rate is similar in magnitude to the nuclear sputtering rate. Electronic interactions become relevant at larger gas temperatures compared to small PAHs, dominating the destruction rate for $T \gtrsim 10^6$ K.

We compute the sputtering timescale as:

$$\tau_{\rm spu}(N_{\rm C}) = \frac{N_{\rm C}}{2R_{\rm elec} + \sum_k (2R_{\rm e}^k + R_{\rm n}^k)}, \tag{5.116}$$

where electron excitations (either by electron collision $R_{\rm elec}$ or by nuclear collision $R_{\rm e}^k$) are multiplied by 2 as each dissociation event leads to the ejection of two carbon atoms. The sum is over the k ions. This expression implies that the nuclear destruction rate is independent of $N_{\rm C}$.

We also include non-thermal sputtering in SN shock for PAHs, as we did for regular grains (Section 5.2.5). Again, we do not track the properties of individual shocks in Dusty-PRISM, but instead determine the amount of PAHs destroyed based on the amount of gas mass shocked above 100 km/s (McKee, 1989). We use the results of Micelotta et al. (2010b) and assume that small PAHs are fully destroyed in all gas above 100 km/s, but only 50% of the large PAHs are destroyed. This lost mass is returned to the local carbon gas-phase density.

5.3.3 Photo-electric heating by PAHs

Photo-electric heating (PEH) is the dominant source of heating in the diffuse ISM as the gas metallicity approaches solar values (e.g. Wolfire et al., 2008; Bialy and Sternberg, 2019; Kim et al., 2022; Katz et al., 2022b). PEH is the dominant process that couples the sub-ionising ($E < 13.6$ eV) far-UV radiation field to the diffuse gas, therefore controlling the ionisation state of PDRs and the phase structure of the ISM. Originally proposed by Spitzer et al. (1948), it has been the subject of extensive theoretical modelling (e.g. Bakes et al. (1994) and Weingartner and Draine (2001b)). Essentially, absorption of a far-UV photon results in the release of an electron, which loses energy as it travels through the dust material. If it reaches the dust surface with sufficient energy to overcome the work function W of the material, it may escape the grain and become a free electron that contributes to the thermal state of the gas. Since the absorption depth of far-UV radiation (~ 100Å) can be significantly smaller than the mean free path of emitted electrons, the free electron yield quickly decreases for large grains. Additionally, large grains easily acquire a positive charge (see Section 5.2.2), making it even harder for an electron to escape the electric potential of the grain. This means that in practice $\gtrsim 50\%$ of the PEH in a full GSD modelling originates in grains with < 1500 C (Bakes et al., 1994), and grains larger than 100Å have a negligible contribution. Therefore, for a long time, PAHs have been recognised as fundamental contributors to the very small dust grain PEH (Verstraete et al., 1990). Recently, Berné et al. (2022a) developed an updated model of the PAH contribution to the PEH using new molecular parameters from laboratory experiments and quantum mechanical calculations. They show that with only the contribution of small PAHs (i.e. circumcoronene, ~ 54 C) one can reconcile the observed ratio of gas emission in the IR (by cooling lines like [CII] and [OI]) and the total IR emission also including the dust emission (Okada et al., 2013). We follow a similar derivation to Berné et al. (2022a) for the contribution to PEH by small and large PAHs.

To be consistent with the rest of the photo-physical processes considered for PAHs, we use the distribution-averaged cross-sections in Section 5.3.1 which have been computed for the small and large PAH bins based on the theoretical curves by Li and Draine (2001). In this model we assume that with both grain sizes we can explore the charge parameter space $Z \in -1, 0, 1, 2$. Larger grains are capable

of reaching higher ionisation states than smaller grains (Ibanez-Mejia et al., 2019). While this could be the case for the larger PAHs (~ 10Å), we have opted to maintain the di-cation as the maximum ionisation state for all PAHs (see also Andrews et al., 2016; Ibanez-Mejia et al., 2019). Experimental data for the ionisation potential (IP) of the di-cation is limited (Zhen et al., 2016), but it seems that it is higher than 13.6 eV for small PAHs, and theoretical modelling argue for a negligible variation at least up to circumcircumcoronene ($N_{\rm C} = 96$ Andrews et al., 2016). For the rest of the charge states, we use the IP fitting function from Jochims et al. (1996) and Verstraete et al. (1990) and updated by Wenzel et al. (2020):

$$IP^{(Z+1)+} = 3.9\text{eV} + \frac{1}{4\pi\epsilon_0}\frac{e^2}{a}\left[\left(Z+\frac{1}{2}\right) + (Z+2)\frac{0.03\text{nm}}{a}\right]\frac{1\text{C}}{e}\text{eV}, \tag{5.117}$$

where ϵ_0 is the vacuum permittivity in F nm^{-1}, a is the effective PAH radius in nm and $Z \geq 0$ is the grain charge. We assume that $IP = 0$ for $Z = -1$. Based on the experimental studies of neutral (Jochims et al., 1996; Verstraete et al., 1990) and cationic (Zhen et al., 2016) PAHs (Wenzel et al., 2020), empirical functions can be derived for the electron yield of different PAHs. For the neutral species, we use the yields from Jochims et al. (1996):

$$Y(E,Z) = \begin{cases} \frac{E-IP^+}{9.2} & ,E \leq IP^+ + 9.2 \\ 1 & E > IP^+ + 9.2 \end{cases}, \tag{5.118}$$

with IP^+ referring to the ionisation potential from $Z = 0$ to $Z = 1$. In the case of the first cation, we use the yields from Wenzel et al. (2020):

$$Y(E,Z) = \begin{cases} 0 & ,E < IP^{2+} \\ \frac{\alpha}{11.3-IP^{2+}}(E-IP^{2+}) & ,IP^{2+} \leq E < 11.3 \\ \alpha & ,11.3 \leq E < 12.9 \\ \frac{\beta(N_{\rm C})-\alpha}{2.1}(E-12.9) & ,12.9 \leq E < 15.0 \\ \beta(N_{\rm C}) & ,E \geq 15.0 \end{cases}, \tag{5.119}$$

where $\alpha = 0.3$ and the correction factor β is given by:

$$\beta(N_{\rm C}) = \begin{cases} 0.59 + 8.1\times10^{-3}N_{\rm C} & ,32 \leq N_{\rm C} < 50 \\ 1 & ,N_{\rm C} \geq 50 \end{cases}. \tag{5.120}$$

We set the ionisation yield of the anion equal to 1. This is an approximation, as recent experimental data (Iida et al., 2021) has shown that electron detachment does not occur for the energy expected from electron affinity for the pentacene anion

($C_{22}H_{14}$), but instead experiments show efficient detachment for photon energies E beyond 2.8 eV. It remains unclear how this extrapolates to the larger PAH molecules and PAH clusters that we consider in Dusty-PRISM, but given the little effect on the PEH efficiency of having $IP^0 > 0$ (Berné et al., 2022a), we have maintained this approximation across our PEH model.

The ionisation cross-section is defined as:

$$\sigma_{\rm ion}(N_{\rm C}, E, Z) = Y(E, Z)\langle C_{\rm abs}(N_{\rm C}, E, Z)\rangle, \tag{5.121}$$

which we assume to be in units of m^2 in this section and $C_{\rm abs}$ is the absorption cross-section in Section 5.3.1. From this definition we can compute the ionisation rate for a PAH molecule of charge Z and number of carbons $N_{\rm C}$:

$$k_{\rm pe}(N_{\rm C}, Z) = \int_{IP^{Z+1}}^{13.6} \frac{\sigma_{\rm ion}(N_{\rm C}, E, Z)F(E)}{E}{\rm d}E, \tag{5.122}$$

where $F(E)$ is the flux density of the radiation field. Photo-ionisation is only allowed for photons with energy E above the ionisation potential and below the Lyman limit. The recombination rate is calculated using Spitzer's method adapted by Verstraete et al. (1990) for cations:

$$k_{\rm rec} = 1.28 \times 10^{-10} N_{\rm C}\sqrt{T}(1 + \Phi), \tag{5.123}$$

in units of $\mathrm{cm}^3\ \mathrm{s}^{-1}$ and we have defined the dimensionless quantity:

$$\Phi = \frac{eU}{k_{\rm B}T} = \frac{1.85 \times 10^5 \mathrm{K}}{T\sqrt{N_{\rm C}}}, \tag{5.124}$$

where U is the mean electrostatic potential evaluated at the radius of the PAH. This equation can be extended to allow all cations ($Z > 0$):

$$k_{\rm rec} = 1.28 \times 10^{-10} N_{\rm C}\sqrt{T}(1 + \Phi(1 + Z)). \tag{5.125}$$

The electron attachment rate comes from empirical rates fitted to the quantum mechanical computations of Carelli et al. (2013):

$$k_{\rm att} = a\left(\frac{T}{300\,\mathrm{K}}\right)^b \exp\left(-\frac{c}{T}\right), \tag{5.126}$$

in $\mathrm{cm}^3\ \mathrm{s}^{-1}$. For the fitting parameters a, b and c we use the results for coronene, the largest molecule in their study. Both electron recombination and attachment rates are

very uncertain aspects of our PEH modelling. Following geometrical arguments for a conducting disc (Spitzer, 1978), Tielens (2005) derives a recombination rate given by:

$$k_{\rm rec} \simeq 1.3 \times 10^{-6} \sqrt{N_{\rm C} \frac{300\,{\rm K}}{T}}. \tag{5.127}$$

Experimentally measured rates for ionised small PAHs (Abouelaziz et al., 1993; Rebrion-Rowe et al., 2003; Novotný et al., 2005; Bienner et al., 2005), fall well below the rate given by Eq. 5.125. One explanation for this unexpected low sticking efficiency in small PAHs could be that dissociative recombination becomes important. When PAH cations recombine with electrons their internal energy is increased by the value of IP. This excited state needs to reach a new stable state, which could trigger molecular dissociation. However, for the IP of circumcoronene cations (5.9 and 8.8 eV for the first and second ionisation states) the IR relaxation rate is about 2 orders of magnitude larger than the dissociation rate (e.g. Montillaud et al., 2013; Andrews et al., 2016), and for larger PAHs IP is even smaller. This means that, for the PAHs of interest in this model, recombination is expected to be non-dissociative. Therefore, we assume that this extrapolated stability to larger PAHs results in a roughly constant k_{rec} value of 10^{-5} cm^3 s^{-1}, close to the prediction of Eq. 5.125. Similarly, for electron attachment to neutral PAHs, the electron affinity increases with PAH size and for $N_{\rm c} > 30$ it exceeds 1 eV and auto-ionisation is very unlikely. Therefore the Langevin rate coefficient can be obtained from the PAH polarisability (Tielens and Alexander, 2021):

$$k_{\rm att} \simeq 1.3 \times 10^{-7} N_{\rm C}. \tag{5.128}$$

Again, this rate falls well above the experimental results of Tobita et al. (1992) and Canosa et al. (1994), which reported a rate close to 10^{-9} cm^3 s^{-1}. Given the lack of experimental studies on astrophysically relevant PAHs, we have opted to maintain the results for coronene determined by the more recent work of Carelli et al. (2013). In the future, these rates will need to be revised once further progress has been made on the experimental measurements of large PAHs.

By assuming equilibrium between the different processes driving the evolution of

the different population charges, we obtain (Berné et al., 2022b):

$$f^{-} = \left(1 + \frac{k_{\rm det}}{k_{\rm att} n_e} + \frac{k_{\rm det} k^0_{\rm pe}}{k_{\rm att} k^+_{\rm rec} n_e^2} + \frac{k_{\rm det} k^0_{\rm pe} k^+_{\rm pe}}{k_{\rm att} k^+_{\rm rec} k^{2+}_{\rm rec} n_e^3}\right)^{-1}, \tag{5.129}$$

$$f^{0} = \left(1 + \frac{k_{\rm att} n_e}{k_{\rm det}} + \frac{k^0_{\rm pe}}{k^+_{\rm rec} n_e} + \frac{k^0_{\rm pe} k^+_{\rm pe}}{k^+_{\rm rec} k^{2+}_{\rm rec} n_e^2}\right)^{-1}, \tag{5.130}$$

$$f^{+} = \left(1 + \frac{k^+_{\rm rec} n_e}{k^0_{\rm pe}} + \frac{k^+_{\rm pe}}{k^{2+}_{\rm rec}} + \frac{k_{\rm att} k^+_{\rm rec} n_e^2}{k_{\rm det} k^0_{\rm pe}}\right)^{-1}, \tag{5.131}$$

$$f^{2+} = \left(1 + \frac{k^{2+}_{\rm rec} n_e}{k_{\rm pe}}\right)^{-1}, \tag{5.132}$$

where f^-, f^0, f^+ and f^{2+} are the fractions of PAH molecules in the anion, neutral, cation and di-cation states, respectively. Based on this, we can compute the power injected by the photo-electrons from the first three charge states above:

$$P_e^{\rm tot} = f^- P_e^- + f^0 P_e^0 + f^+ P_e^+, \tag{5.133}$$

where the power injected in the gas by the charge state Z is defined as:

$$P_e^Z = \int_{IP^{Z+1}}^{13.6} \gamma_e(E)(E - IP^{Z+1}) \sigma_{\rm ion}(Nc, E, Z) \frac{F(E)}{E} {\rm d}E, \tag{5.134}$$

with $\gamma_e(E)$ encapsulating the fraction of the energy which goes into the kinetic energy $E_{\rm K}$ of the photo-electron. Energy conservation requires $E - IP = \Delta E^*(E) + E_{\rm K}(E) + E_{\rm K}^{\rm PAH}(E)$, where ΔE^* is the change in internal energy of the PAH upon excitation by ionisation and $E_{\rm K}^{\rm PAH}$ is its kinetic energy. PAH molecule has much larger mass than the electron's and due to conservation of momentum, the kinetic energy of the PAH molecule is negligible compared to that of the electron. Therefore, assuming that the photon energy is primarily used for the ionisation reaction, the internal energy of the PAH is barely modified, allowing to define the energy averaged partition coefficient (D'Hendecourt et al., 1987):

$$\langle \gamma_e(E) \rangle = \left\langle \frac{E_{\rm K}(E)}{E - IP} \right\rangle. \tag{5.135}$$

We use the estimated value of $\langle \gamma_e(E) \rangle = 0.46 \pm 0.06$ obtained by Berné et al. (2022b) from the spectroscopic measurements performed for the coronene molecule by Bréchignac et al. (2014). The final outcome of any PEH model is the total heating

efficiency, $\epsilon_{\rm PAH}$, defined as the ratio of the power injected by the photo-electrons and the power absorbed by the PAHs:

$$\epsilon_{\rm PAH}(N_{\rm C}) = \frac{P_e^{\rm tot}}{P_{\rm abs}^{\rm tot}} = \frac{P_e^{\rm tot}}{f^- P_{\rm abs}^- + f^0 P_{\rm abs}^0 + f^+ P_{\rm abs}^+ + f^{2+} P_{\rm abs}^{2+}}, \tag{5.136}$$

where the power absorbed by each PAH charge state is:

$$P_{\rm abs}^Z = \int_0^{13.6\,{\rm eV}} \langle \sigma_{\rm abs}(N_{\rm C}, E, Z) \rangle F(E) {\rm d}E. \tag{5.137}$$

This definition of the PEH efficiency is similar to that used by Weingartner and Draine (2001c) but differs from Bakes et al. (1994) as they only consider photons in the range $6 - 13.6$ eV. From this, the local PEH rate for each PAH size bin writes:

$$\Gamma_{\rm PAH}(N_{\rm C}) = \epsilon_{\rm PAH} P_{\rm abs}^{\rm tot} n_{\rm PAH}(N_{\rm C}), \tag{5.138}$$

with $n_{\rm PAH}(N_{\rm C})$ being the local number density of PAH molecules with carbon number $N_{\rm C}$.

In Fig. 5.10 we show the results of our modelling of the PAH charge distribution and PEH for the small (solid lines) and large (dashed lines) PAHs. As our modelling depends on G_0, T and n_e, the visualisation of the charge population and $\epsilon_{\rm PAH}$ can quickly become complex. We simplify this by fixing the gas temperature to 10^3 K, varying the value of G_0 on the x-axis and using different colour/line widths for the different values of n_e, such that we explore the same range of ionisation parameter γ for each combination of (G_0, T, n_e). Compared to the traditional models of Bakes et al. (1994) and Wolfire et al. (2003), our results are on average $20 - 40\%$ larger than their predictions. Given our explicit dependence on electron density, we can predict the variability of $\epsilon_{\rm PAH}$ with n_e, which becomes more important at high γ. In the bottom panels we show the charge population fractions for different n_e, as indicated by the line width (thicker lines meaning higher n_e), effectively showing that for a higher n_e and the same γ and T, G_0 needs to increase accordingly, which results in lower PEH efficiency as the PAHs are fully ionised (i.e. $Z = 2$). The most effective PAH charges for photo-electron ejection are the anion and the neutral, which dominate for $\gamma \lesssim 10^4$ K$^{1/2}$ cm^{-3}, explaining the plateau in $\epsilon_{\rm PAH}$ observed below this ionisation parameter value. We note that our results differ from the Berné et al. (2022b) model for $N_{\rm C} = 54$ due to slightly different optical properties (they make use

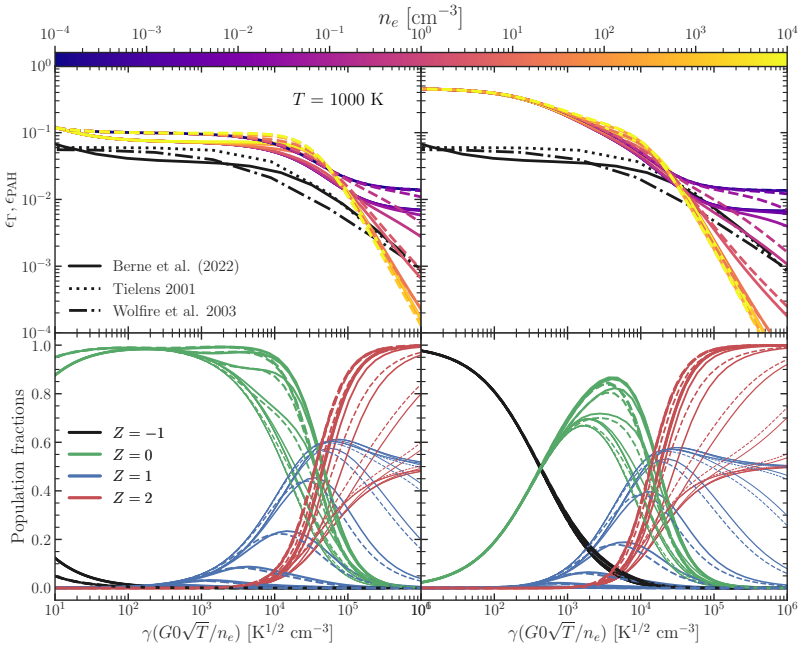


Figure 5.10: *Top row*: PE Heating efficiency $\epsilon_{\rm PAH}$ for our small (solid lines) and large (dashed lines) PAHs and their charge distribution ϵ_Γ for a range of values of the ionisation parameter γ. *Bottom row*: Population fractions for the different charge states Z for small and large PAHs. We fix the gas temperature to 1000 K varying for a given n_e the value of G_0. We show results for 10 different values of n_e between 10^{-4} cm^{-3} and 10^4 cm^{-3}, identified in the top panels by colors given by the colorbar, and by the thickness of the line (thicker lines for higher n_e) in the bottom panels. The two PAH sizes are compared for the two recombination models: Verstraete et al. (1990) (left column), and Tielens and Alexander (2021) (right column). As a guide, we also include the GSD-averaged PE heating efficiency by Berné et al. (2022a) (solid black line in all the panels), Bakes et al. (1994) (dotted black line in all the panels), and Wolfire et al. (2003) (dot-dashed black line in all the panels).

of the Theoretical spectral database of PAHs[16] by Malloci et al. 2004). We also show our results for the recombination rate given by Tielens and Alexander (2021) instead of the fiducial Verstraete et al. (1990). This has a critical effect on the distribution of PAH charges, allowing for the dominance of anions ($Z = -1$) at low γ, and therefore an efficiency 4 times larger. The choice of recombination law is an important source of uncertainty in the Dusty-PRISM model, and we will come back to it in Section 5.3.7.

5.3.4 PAH clustering

The high polarisability of PAH molecules results in large van der Waals forces, providing a strong bonding force between aromatic planes of PAHs (Zacharia et al., 2004) and the formation of PAH clusters. We follow the dimerisation (or clustering) of small PAHs to form large PAH clusters in light of kinetic theory and the binding energy of monomers

[16] https://www.dsf.unica.it/~gmalloci/pahs/

forming large carbon clusters (e.g. Rapacioli et al., 2005; Rapacioli et al., 2006; Tielens and Alexander, 2021; Khabazipur and Eaves, 2023). We consider the binding energy per C-atom from Zacharia et al. (2004) to estimate a binding energy $\simeq 2.8$ eV for circumcoronene monomers (see also e.g. Herdman and Miller, 2008; Montillaud and Joblin, 2014), approaching covalent binding values. From this, one can obtain a simple expression for the collisional rate of neutral PAHs (Tielens and Alexander, 2021):

$$k_{\rm coal,neu} \simeq 4 \times 10^{-11} \sqrt{\frac{T}{10\,{\rm K}}} \sqrt{\frac{N_{\rm C}}{50}}, \tag{5.139}$$

in units of cm^3 s^{-1}. In the case of ionised PAHs, we need to consider the faster effective rate caused by the polarisation-induced interaction potential. In this case, the collision reaction rate is given by the Langevin rate (see Equation 5.128):

$$k_{\rm coal,ion} \simeq 2\pi e \sqrt{\frac{\alpha}{\beta_{i,j}}} \simeq 8.48 \times 10^{-10}, \tag{5.140}$$

in cm^3 s^{-1}, and where $\beta_{i,j} = (m_i m_j)/(m_i + m_j)$ is the collision reduced mass for target mass m_i and projectile mass m_j. We have also used the standard polarisability of small, compact PAHs $\alpha \simeq 1.5 \times 10^{-24} N_{\rm C}$ cm^{-3}. In practice, we compute the total coalescence rate by using the local fraction of ionised small PAHs, $f_{\rm PAH,ion}$:

$$\tau_{\rm coal} = \left(\frac{1}{k_{\rm coal,neu}(1 - f_{\rm PAH,ion})} + \frac{1}{k_{\rm coal,ion} f_{\rm PAH,ion}} \right)^{-1}. \tag{5.141}$$

At low temperatures (~ 10 K), the collision energy is significantly smaller than the interaction energy, which implies that long-lived compounds can form in the interaction, allowing for the PAH monomers to re-arrange into the most energetically favoured orientations (in the case of circumcoronene monomers stacking generally yields the most stable cluster; Rapacioli et al., 2005). However, if the collision imparts too much energy to the system, monomer evaporation may occur before this re-orientation can take place. We extend the above rates by considering a variable sticking efficiency $C_{\rm eff}$ fitted to numerical experiments by Totton et al. (2012):

$$C_{\rm eff}(T) = \frac{1}{1 + A[\log_{10}(T)]^B}, \tag{5.142}$$

where the fitting parameters are $A = 9.928 \times 10^{-7}$ and $B = 1.38$. In this case, the timescale for coalescence is given by:

$$\tau_{\rm coal} = (\sigma_{\rm smallPAH,col} \Delta V C_{\rm eff} n_{\rm smallPAH})^{-1}, \tag{5.143}$$

where $\sigma_{\mathrm{smallPAH,col}} = 4\pi a^2_{\mathrm{smallPAH}}$ is the cross-section for collision between two small PAHs, ΔV is the collision velocity given by Brownian motion (Equation 5.51), and n_{smallPAH} is the local number density of small PAHs.

We also consider the opposite process, known as PAH cluster evaporation (Rapacioli et al., 2006). Similar to the photo-dissociation of small PAH molecules due to excitation by UV photons, large PAH clusters may lose their monomers (in our case, circumcoronene molecules) if their internal energy exceeds the monomer binding energy. Therefore, determining the dissociation rate requires the calculation of the full energy probability distribution for a PAH cluster exposed to a given photon energy E. This is achieved by using the Arrhenius expression derived from the Rice-Ramsperger-Kassel-Marcus (RRKM) theory (Tielens, 2005). While solving these equations for thermal collisions (see Section 5.3.2) can be simplified by assuming that the probability of dissociation changes very little after each IR photon emission, for the case of the absorption of UV photons by large PAH clusters one needs to fully compute the energy probability distribution in an iterative fashion. Indeed, the larger heat capacity of these systems (Bakes et al., 2001; Tielens, 2005) allows them to maintain a significant fraction of their internal energy between UV excitations (or equivalently, the cooling rate is slower than the absorption rate). This means that for these large molecular clusters the dissociation rates deviate from the linear scaling with the radiation intensity in the Habing band G_0, instead needing more photons to dissociate (e.g. $3-4$ photons for the dissociation of $C_{96}H_{24}$; Montillaud et al., 2013). This multi-photon tracking of the heating/cooling of large PAHs, either via Monte-Carlo methods (e.g. Lange et al., 2021; Lange et al., 2023) or statistical iterative methods (Purcell et al., 1976; Bakes et al., 2001; Andrews et al., 2016; Montillaud and Joblin, 2014), is beyond the scope of our current modelling. We instead refer to the work of Rapacioli et al. (2006) and Montillaud and Joblin (2014) on the effective dissociation rate of large PAH clusters. Considering that the large PAHs used in Dusty-PRISM ($N_{\mathrm{C}} \sim 400$) are formed from the clustering of our small PAHs (circumcoronene, $C_{54}H_{18}$), we use the results by Montillaud and Joblin (2014) for the evaporation timescales of circumcoronene clusters with a number of monomers ranging from 4 to 12. They find that for these large monomer clusters the evaporation time scales more steeply than $1/G_0$, until the radiation field becomes very intense

($G_0 \sim 10^6$), at which point the time between two UV photon absorptions becomes shorter than the cooling timescale. We thus use a scaling of the evaporation time given by the maximum of two functions fitted to their results:

$$\tau_{\rm evap} = \max\left[\frac{0.19306}{G_0}, 10^{-3.169x+13.564}\right], \tag{5.144}$$

where $x \equiv \log_{10}(G_0)$.

5.3.5 PAH freezing

Similar to PAH coalescence (Sections 5.3.4 and 5.2.7), we also consider the adsorption of small and large PAHs on dust grains (also called freeze-out or sequestration of PAHs). For this, we follow exactly the same procedure as in Section 5.2.7 for the coagulation of small grains, but computing the relative velocity (ΔV, Eq. 5.54) between the small and large PAHs and the small and large carbonaceous grains[17]. With a similar argument as for the threshold velocity for coagulation (Section 5.2.7), we impose the requirement that the collision energy does not exceed the van der Waals bond energy (see also Lange et al., 2023) attaching the PAH molecule/cluster to the grain surface ($\sim$ 1 eV; Rapacioli et al., 2006):

$$\tau_{\rm free} = (\sigma_{\alpha,\beta}\Delta V_{\alpha,\beta}\psi_{\rm vdW}(E)n_{{\rm d},\beta})^{-1}, \tag{5.145}$$

where the indices α and β go over the combination of PAH sizes and carbonaceous sizes, respectively, $\sigma_{a,b} = \pi(a_\alpha + a_\beta)^2$ is the collision geometrical cross-section, and E is the kinetic energy of the collision in eV, used to compute the efficiency for the adsorption via van der Waals forces:

$$\psi_{\rm vdW}(E) = \frac{1}{1+\exp[(E-1)/0.1]}. \tag{5.146}$$

5.3.6 PAH photo-dissociation

Due to the temperature spikes experienced by a small PAH, there is a non vanishing probability that it can eject H, H_2 or even C_2H_2 when it experiences an intense UV radiation field in the diffuse ISM and in PDRs (Jochims et al., 1994; Allain et al., 1996; Le Page et al., 2001). There is observational evidence of this destruction effect around

[17]We do not consider freezing of PAHs on silicate grains, as this would alter their chemical composition.

young stellar clusters and in HII regions (Galametz et al., 2016; Relanõ et al., 2016), which suggests that PAH fractions (or VSG fractions) can be used to trace the UV radiation field intensity (Pilleri et al., 2012; Boutéraon et al., 2019). When a molecule is photo-excited, it divides its energy among vibrational degrees of freedom via intra-molecular vibrational redistribution (IVR). An assumption of the uni-molecular dissociation reaction (e.g. Le Page et al., 2001; Tielens, 2005) is that there exists a transition state (TS) that, if reached, will lead to bond dissociation (e.g. H-loss):

$$C_{54}H_n + h\nu \rightarrow (C_{54}H_n)^* \rightarrow C_{54}H_{n-1} + H, \tag{5.147}$$

where $(C_{54}H_n)^*$ represents the circumcoronene molecule in its TS. In the reverse process, H atoms can be re-attached to the molecule (Rauls et al., 2008; Goumans et al., 2011; Jones et al., 2014). The balance of these two reactions determines the hydrogen covering fraction of the molecule, termed the hydrogenation state of the PAH. Similar to Section 5.3.2 and 5.3.4, the acetylene (C_2H_2) dissociation rate can be treated using a statistical approach based on RRKM theory (e.g. Tielens, 2005; Montillaud et al., 2013; Andrews et al., 2016). However, at the photon energies common of PDRs and the diffuse ISM, photo-dissociation by loss of H and H_2 is faster by $\sim$ 2 dex compared to the loss of acetylene (Allain et al., 1996; Le Page et al., 2001; Montillaud et al., 2013; Andrews et al., 2016; Castellanos et al., 2018b). Experiments have shown that for small PAHs, H-loss dominates over C-loss (Jochims et al., 1994), and for larger PAHs stripping of hydrogen atoms takes place before the C-loss starts (Zhen et al., 2014; Zhen et al., 2015; Castellanos et al., 2018a). Therefore, a prior requirement for the fragmentation of aromatic rings in a small PAH is its full de-hydrogenation. This requires tracking the hydrogen coverage of our PAH bins, adding further computational cost to our model. We present here an alternative approach. One can define the dissociation parameter:

$$\psi = \frac{p_{\rm d} k_{\rm UV}}{k_{\rm a} n_{\rm H}}, \tag{5.148}$$

where $p_{\rm d}$ is the probability for H dissociation, $k_{\rm UV}$ is the photon absorption rate, $k_{\rm a}$ is the H attachment rate and $n_{\rm H}$ the hydrogen number density. This parameter effectively captures the hydrogenation balance of a PAH. Considering an attachment rate of $k_{\rm a} = 2 \times 10{-}8\sqrt{N_{\rm C}/50}$ cm^3 s^{-1} and an average UV absorption rate $k_{\rm UV} \simeq 2.3 \times G_0$ s^{-1},

one arrives at the relation $\psi \propto p_{\rm d} G_0 / n_{\rm H}$ (Tielens, 2005; Berné and Tielens, 2011). Numerical computation of the hydrogenation of small and intermediate size PAHs has shown that the transition from fully de-hydrogenated to normally hydrogenated is very sharp in the $G_0 - n_{\rm H}$ plane (Montillaud et al., 2013; Andrews et al., 2016). Since the relevant quantity for C-loss is the fraction of small PAHs that are de-hydrogenated ($\chi_{\rm dH}$), we use fitting functions for the limiting region between de-hydrogenated and normally hydrogenated circumcoronene provided in Figure 10 of Montillaud et al. (2013), allowing for a 1 dex dispersion, where PAHs transition from being 10% to 90% totally de-hydrogenated. We then assume that upon photon absorption, the energy is either spent on IR emission or on C-loss. Therefore, the probability for dissociation of a PAH upon absorption of a photon with energy E is given by (see also Section 5.3.2):

$$P_{\rm diss}^{\rm C_2H_2}(E) = \frac{k_{\rm diss}^{\rm C_2H_2}(E)}{k_{\rm diss}^{\rm C_2H_2}(E) + k_{\rm IR}/(n_{\rm max} - 1)}, \tag{5.149}$$

where we compute the dissociation rate as in the thermal sputtering calculation of Section 5.3.2 (see also Murga et al., 2020). From this, one can calculate the dissociation rate for a Draine et al. (1979) radiation field as:

$$R_{\rm diss}^{\rm C_2H_2}(G_0) = \int_{6\,{\rm eV}}^{13.6,{\rm eV}} \chi_{\rm dH} \sigma_{\rm PAH}(E) P_{\rm diss}^{\rm C_2H_2}(E) \frac{F(E)}{E} {\rm d}E. \tag{5.150}$$

The numerical value of this rate for diffuse ISM conditions ($n_{\rm H} = 0.1$ cm^{-3} and $G_0 = 1$) is 4.68×10^{-17} s^{-1}, which is significantly larger than the estimated rate of 3.56×10^{-18} s^{-1} for a ~ 50 C PAH given by Allain et al. (1996).

5.3.7 Molecular hydrogen formation mediated by PAHs

In Section 5.2.8 we based our modelling of molecular hydrogen formation on the assumption that the attachment surface for hydrogen on dust grains can be separated into physisorbed and chemisorbed sites. The former are characterised by weak van-der-Waals forces of a few tens of meV, which implies that when the dust temperature increases beyond ~ 20 K H atoms quickly evaporate from the grain surface. This causes a drop in the H_2 formation efficiency, since beyond this point the total formation rate relies solely on the recombination via the Eley-Rideal mechanism on chemisorbed sites. This appears to be in disagreement with observations of PDRs (Habart et al., 2003b; Allers et al., 2005), where estimated formation rates close to $\sim 3 \times 10^{-17}$ cm^3

s^{-1} are well above the predictions for dust at high temperature. This points to additional physical mechanisms that can efficiently form H_2 in these regimes in which traditional dust grain formation mechanisms appear to fail.

Recently, more accurate modelling of PAH photo-physics (e.g. Montillaud et al., 2013; Boschman et al., 2015; Andrews et al., 2016; Barrera et al., 2023) and accelerated progress in experimental studies of PAH-hydrogen reactivity (e.g. Thrower et al., 2012; Boschman et al., 2012; Mennella et al., 2012; Castellanos et al., 2018b), is enabling the ISM community to re-evaluate the pathways to H_2 formation in the ISM (see the review by Wakelam et al., 2017). Observed correlations between H_2 and PAH emission (Habart et al., 2003a; Habart et al., 2003b) appear to support the scenario where PAHs can efficiently form H_2 in a highly excited state within PDRs. We therefore include molecular hydrogen formation catalysed by PAHs in Dusty-PRISM.

H_2 formation on PAHs is usually considered to take place via two possible routes:

- A hydrogen atom forms a covalent bond with a PAH molecule, and then it is abstracted by a second colliding hydrogen atom.
- UV photon absorption by a super-hydrogenated PAH molecule leads to relaxation by the loss of H_2.

Molecular hydrogen abstraction has been observed in desorption experiments on coronene deuterium bombardment (Thrower et al., 2012), as well as predicted by theoretical modelling (Rauls et al., 2008). The abstraction (as well as the hydrogenation) is subject to energy barriers in neutral coronene (Boschman et al., 2012) of 10 meV, while Bauschlicher et al. (2001) predicts no barriers for H_2 abstraction from coronene and circumcoronene anions. Given the experimentally determined abstraction cross-section of 0.06 $Å^2$ per coronene C atom, we assume for all abstraction of super-hydrogenated anion and neutral PAHs (both small and large) the Eley-Rideal rate:

$$k_{\rm ER} \simeq 8.7 \times 10^{-13} \sqrt{\frac{T}{100}} n_{\rm H}. \tag{5.151}$$

We now need to determine what fraction of the PAH population is in a super-hydrogenated state. Similar to the approximations made in Section 5.3.6, it is safe to assume that the transition from normally hydrogenated to super-hydrogenated is very sharp in $G_0 - n_{\rm H}$ space (see Figure 9 in Andrews et al., 2016), and that

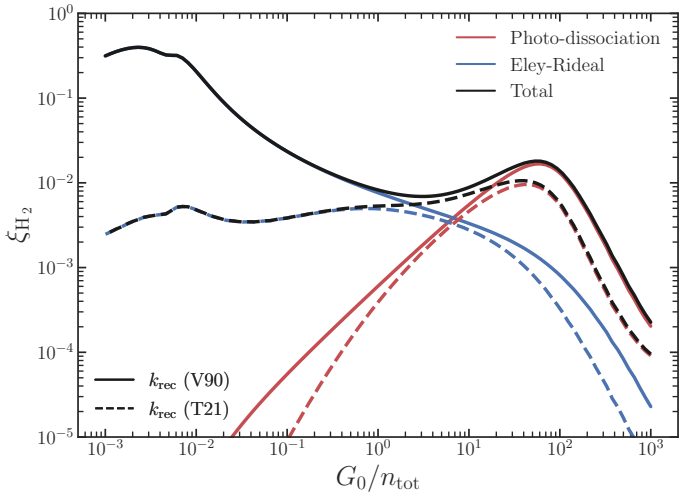


Figure 5.11: Molecular hydrogen formation efficiency by small PAHs (circumcoronene). We fix the radiation field intensity to the Habing parameter $G_0 = 100$, the free electron fraction to $X_e = 0.1$, and assume half of the H abundance is already in H_2. Molecular hydrogen is formed via two mechanisms: Eley-Rideal desorption (blue lines) of H_2 for neutral super-hydrogenated PAHs, and photo-desorption (red lines) of H_2 from normal and partially de-hydrogenated PAHs. The former dominates at high gas density in low radiation field, while the latter is important in a narrow regime at low density before radiation strips circumcoronene of all its H atoms. We compare the resulting efficiencies following two different models for electron recombination on PAHs by Verstraete et al. (1990) and Tielens and Alexander (2021).

this transition is approximately independent of size for PAHs with $N_{\rm C} \geq 54$. We obtain a transition curve given by:

$$\log_{10} G_0 = 0.995 \log_{10} n_{\rm H} - 1.945, \tag{5.152}$$

with the width of the transition being $\Delta \simeq 0.05$ in log-log space as extracted from Figure 9 in Andrews et al. (2016). H_2 abstraction is only allowed for anion and neutral PAHs.

For normally hydrogenated and partially de-hydrogenated PAHs, the absorption of a UV photon may give rise to the loss of a H atom or a H_2 molecule (Allain et al., 1996). Following the microcanonical description of bond dissociation used in Sections 5.3.2 and 5.3.6, we compute the H_2 photo-desorption rate as:

$$k_{\rm H_2} = \int_{E_{\rm min}}^{13.6\,{\rm eV}} \frac{k_{\rm diss}({\rm H_2})}{k_{\rm diss}({\rm H_2}) + k_{\rm diss}({\rm H}) + k_{\rm IR}/(n_{\rm max}+1)} \chi_{\rm pdH} \sigma_{\rm PAH}(E) \frac{F(E)}{E} {\rm d}E, \tag{5.153}$$

where $F(E)$ is the flux density of the radiation field at energy E, $E_{\rm min} = n_{\rm max}\Delta\epsilon$ (see Section 5.3.2), $\chi_{\rm pdH}$ is the fraction of partially de-hydrogenated PAHs, and the dissociation rates $k_{\rm diss}$ are given by Eq. 5.110. We note that in this case we cannot use directly the fraction of de-hydrogenated PAHs $\chi_{\rm dH}$ to compute the rate of dissociation

from normally to partially de-hydrogenated PAHs. As the PAH molecules becomes completely de-hydrogenated, relaxation upon UV photon absorption is no longer available through H or H_2 loss, but rather C-loss becomes important (see Section 5.3.6). Hence, to maintain consistency across our model and prevent unrealistic H_2 production from fully de-hydrogenated PAHs, we suppress the fraction of de-hydrogenated PAHs $\chi_{\rm dH}$ when it exceeds 99% of the total PAH population, assuming at this point that all de-hydrogenated PAHs are bare carbon skeletons. This is done by applying a logistic equation correction to the fraction of de-hydrogenated PAHs:

$$\chi_{\rm pdH} \equiv \frac{\chi_{\rm dH}}{1+\exp[(\chi_{\rm dH}-0.99)/8\times10^{-4}]}, \tag{5.154}$$

which reproduces the width of the transition to fully de-hydrogenated PAHs in Montillaud et al. (2013) and Andrews et al. (2016). We note that this is only applied for small PAHs, as H_2 photo-desorption is not an efficient process for our large PAH clusters because UV absorption is instead followed by evaporation of the circumcoronene monomers (Eq. 5.144). Large PAHs only contribute to H_2 formation via the Eley-Rideal mechanisms.

In Fig. 5.11 we present the H_2 formation efficiency for small PAHs in an environment with $G_0 = 100$, with a fixed free electron fraction $X_e = 0.1$, and half of the H abundance already in the form of H_2. The H_2 formation efficiency is defined as (Andrews et al., 2016; Castellanos et al., 2018b):

$$\xi_{\rm H_2}(Z) = \sum_i \frac{2k_{\rm H_2}(Z,i)f(Z,i)}{k^i_{\rm col}(Z)}, \tag{5.155}$$

where $f(Z,i)$ is the fraction of PAHs with charge Z, and the sum is over all hydrogenation states for a PAH with charge Z and $k_{\rm col}$ its hydrogen collisional rate. For neutral species we use a collisional rate with the average H addition energy barrier (Rauls et al., 2008; Boschman et al., 2015) of $E_{\rm add} = 60$ meV:

$$k^0_{\rm col} = n_{\rm H}\sigma_{\rm geo}\sqrt{\frac{8k_{\rm B}T}{\pi m_{\rm H}}}\exp\left(-\frac{E_{\rm add}}{k_{\rm B}T}\right), \tag{5.156}$$

where $\sigma_{\rm geo}$ is the PAH geometrical cross section. For anions and (di-)cations, we follow Andrews et al. (2016) and consider fiducial rates of $k^-_{\rm col} = 7.8\times10^{-10}n_{\rm H}$ s^{-1} and $k^{+/2+}_{\rm col} = 1.4\times10^{-10}n_{\rm H}$ s^{-1}. The charge population of PAHs is obtained from the method described in Section 5.3.1. We have computed separately the contribution

from Eley-Rideal (blue lines) and photo-dissociation (red lines) to the total molecular hydrogen formation efficiency (black lines). While keeping G_0 fixed, we vary the value of the total gas density ($n_{\rm tot} = n_{\rm H} + 2n_{\rm H_2}$), exploring a slice in $G_0 - n_{\rm H}$ space. We find that at high $G_0/n_{\rm tot}$ photo-dissociation dominates H_2 formation for a narrow range of values, quickly dropping as the PAH population becomes dominated by totally bare carbon skeletons. H_2 abstraction via the Eley-Rideal mechanism is the dominant route of molecular hydrogen formation at low $G_0/n_{\rm tot}$. Eley-Rideal at high densities is highly reliant on the abundance of neutral and anionic PAH species. As discussed in Section 5.3.3, the charge state in those regimes depends on the assumptions regarding electron recombination and attachment. Tielens and Alexander (2021) predict a dominant anion population at very high gas/electron number densities, for which the collision rate is larger, resulting in a lower efficiency. This effect can be appreciated by comparing the solid curves using the Spitzer recombination rate modified by Verstraete et al. (1990), and the dashed curves using the Tielens and Alexander (2021) recombination rate. Overall, we find that maximum efficiencies are on the order of $\xi_{\rm H_2} \sim 1\%$, in agreement with previous models of H_2 formation on PAHs (e.g. Le Page et al., 2009; Boschman et al., 2015; Andrews et al., 2016; Castellanos et al., 2018b).

5.4 Conclusions

In this Chapter, we have detailed extensively the theoretical development of a novel dust model for radiation-hydrodynamics simulations of galaxy formation implemented in the RAMSES code (Teyssier, 2002). This model is based on the two-size approximation (small and large grains) for dust evolution (Hirashita, 2015), allowing us to calculate the main properties of the grain-size distribution for the two main types of grains in the ISM: carbonaceous and silicate grains. We have further extended this model to include the molecular regime of polycyclic aromatic hydrocarbons (PAHs). Dusty-PRISM thus tracks a grain population divided into 6 different type of grains, for which we have introduced an extensive network of physical and chemical processes, resulting in a self-consistent coupling of the thermo-chemistry of the ISM and the evolution of dust and PAH properties. The model can be summarised as follows:

1. Dust grains are seeded (with a large size) by stellar evolution processes, mainly by Type II SN and AGB winds. After they are injected into the ISM, grains are allowed to evolve, either by growing or being destroyed. Therefore, grains are a *live* component during the cosmic evolution of a galaxy.

2. Dust grows in mass by adsorbing metal ions from the gas phase, taking into consideration both their kinetic and electrostatic energies. This model includes a sub-resolution description of the gas turbulence, to facilitate convergence across a large range of simulation resolutions.

3. Dust grains are affected by energetic collisions with ions in hot gas, which either raise their internal energy or peel off atoms from them. We have developed a new model for the nuclear and electronic interactions of grains with ions and electrons, resulting in a larger fraction of dust grain surviving in hot gas than previously considered, as well as a consistent collisional cooling for dust-enriched ISM gas.

4. Coupled with self-consistent dust optical properties, our dust implementation in RAMSES-RTZ allows us to compute on-the-fly grain equilibrium temperatures, predicting the catalytic formation of molecular hydrogen on their surface.

5. For the first time, we have introduced the destructive effect of radiative torques on large grains in high radiation environments, critical for the prediction of the grain size distribution within starbursts and around AGN.

6. In keeping with our sub-resolution modelling of turbulence for accretion and star formation, we have developed a novel treatment of turbulent shattering and coagulation of grains, predicting the transfer of mass between different grain sizes, including the formation of very small grains and PAHs.

7. PAHs are modelled as molecules of carbon and hydrogen forming aromatic rings, with a population of small molecules (54 carbon atoms, i.e. circumcoronene) and large clusters formed by the clustering of these small molecules ($\sim$ 418 carbon atoms).

8. PAHs interact with high energy ions and electrons leading to dissociating excitations. We directly couple this modelling of thermal sputtering with the local ion abundances and ionisation states predicted by the non-equilibrium chemistry in RAMSES-RTZ.

9. We follow a careful treatment of the photo-physics of PAHs, for which we have implemented the modelling of PAH charge states and their influence in photo-electric heating, photo-dissociation and evaporation.

10. PAHs are also allowed to grow by coalescence of small molecules to form large clusters, or to be sequestrated at the surface of carbonaceous grains in cold, dark clouds.

6

The imprint of dust processes in simulated extinction and attenuation curves

Contents

6.1 Motivation 188
6.2 The suite of G8, G9 and G10 galaxies 190
6.3 The critical metallicity for dust growth 196
6.4 Bump or no bump: the dust extinction laws in the Local Group 200
6.5 From extinction to attenuation with SKIRT 204
6.6 Conclusions 220

6.1 Motivation

In extragalactic astronomy, our grasp of dust properties is fundamentally determined by the information encoded in the decrease of expected to observed flux at a particular wavelength due to the interaction of light with dust particles. Before dwelling on the nitty-gritty difficulties related to extracting this information, it is useful to recall the basic concepts related to extinction.

The total extinction or extinction magnitude is defined as:

$$A_\nu = 2.5 \log_{10} \left(\frac{F_\lambda^{\rm int}}{F_\lambda^{\rm obs}} \right), \tag{6.1}$$

with $F_\lambda^{\rm int}$ and $F_\lambda^{\rm obs}$ being the intrinsic and observed spectrum of the source, respectively. The optical depth is defined as (assuming homogeneous properties along the line of sight):

$$\tau_\lambda = \kappa_\lambda \, \rho_{\rm d} L, \tag{6.2}$$

where κ_λ is the mass opacity (in units of cm^2 g^{-1}), $\rho_{\rm d}$ is the dust density, and L is the path-length along the line of sight. By assuming no contribution of dust emission to

the observed flux as well as no scattering of light into the line of sight, the observed flux can be expressed as function of the optical depth:

$$F_\lambda^{\rm obs} = F_\lambda^{\rm int} \exp(-\tau_\lambda), \tag{6.3}$$

which leads to the conclusion:

$$A_\lambda = 1.086\tau_\lambda. \tag{6.4}$$

We refer to the wavelength dependence of this flux decrement as the extinction 'curve' or 'law'. Therefore, if we observe point sources (e.g stars) for which we know the intrinsic spectrum (or can compare to the same source type at another location in the sky free of intervening dust), we can obtain information about the opacity and density of the dust material along the line of sight. The prediction of these quantities is one of the main goals of dust models (e.g. Weingartner and Draine, 2001a; Zubko et al., 2004; Draine and Li, 2007; Compiègne et al., 2008; Jones et al., 2017; Hensley and Draine, 2021), as we have extensively remarked in the motivation and development of our own dust model implementation for RAMSES (see Chapter 5). However, it is impractical to describe the extinction of an entire galaxy as resulting from the extinction along the line of sight to each of its individual stars. This limitation forces us to study galaxy attenuation curves, which are significantly affected by radiation transfer effects (like e.g. scattering) and geometric factors (the spatial distribution of dust with respect to sources). These complexities hinder our understanding of intrinsic dust properties, as the observed attenuation curves are a composite result of these intricate interactions.

Fortunately, the Local Group provides us with a unique opportunity to delve deeper into these phenomena. By examining galaxies such as our own Milky Way (MW), the Large Magellanic Cloud (LMC), and the Small Magellanic Cloud (SMC), we can investigate the imprint of intrinsic dust properties on the attenuation curve and disentangle it from the effects of dust-star geometry. These 'local' studies are pivotal in refining Dusty-PRISM and improving our understanding of dust evolution in galactic environments. However, despite their proximity, understanding the origin of the differences between average extinction curves in these three galaxies is still an area of active debate (see the review by Galliano et al., 2018). Early investigations of the LMC (Nandy et al., 1981; Koornneef et al., 1981; Clayton et al., 1985; Fitzpatrick,

Table 6.1: Galaxy initial conditions identifier with halo mass $M_{\rm h}$, gas mass $M_{\rm gas}$, disc stellar mass $M_{\star,\rm d}$, bulge stellar mass $M_{\star,\rm b}$, gas fraction in the galaxy $f_{\rm gas}$, baryon fraction in the halo $f_{\rm bar}$, and disc scaling radius $R_{\rm d}$.

Galaxy identifier	$M_{\rm h}$ ($10^{10}\,{\rm M}_\odot$)	$M_{\rm gas}$ ($10^{10}\,{\rm M}_\odot$)	$M_{\star,\rm d}$ ($10^{10}\,{\rm M}_\odot$)	$M_{\star,\rm b}$ ($10^{10}\,{\rm M}_\odot$)	$f_{\rm gas}$ %	$f_{\rm bar}$ %	$R_{\rm d}$ (kpc)
G10LG	100	0.35	1.7	0.35	15	2.4	3.2
G9LG	10	0.05	0.3	0.035	13	3.8	1.5
G9HG	10	0.17	0.17	0.035	45	3.8	1.5
G8HG	1	0.017	0.017	0.0035	45	3.8	0.7

1985) revealed that its average UV extinction curve is notably steeper than that of the MW. Similar studies of the SMC (Prevot et al., 1984; Gordon and Clayton, 1998) identified even steeper UV curves. These findings highlight the inadequacy of characterising extinction curves solely through a differential extinction parameter $R_{\rm V} = A_{\rm V}/(A_{\rm B} - A_{\rm V})$, and underscore the need for more comprehensive models that better account for the observed variations across a large wavelength range.

The goal of this chapter is to use our novel RAMSES dust model to provide a theoretical understanding of the physical origin of the dust properties and, hence, of the different shapes of the extinction curves observed in the Milky Way and the Magellanic Clouds. Furthermore, we extend this study to account for the dust-star geometry using Monte-Carlo Radiative Transfer simulations (SKIRT), and show examples of the broader implications for extragalactic observations. This work not only provides insights into the Local Group but also seeks to underpin our interpretation of observations of more distant and extreme galactic systems across cosmic time.

6.2 The suite of G8, G9 and G10 galaxies

6.2.1 Initial conditions

Isolated galaxy simulations are an ideal test bed for new galactic scale sub-grid models, as they allow to probe the large majority of numerical and physical modules that are present in a full cosmological context (e.g. see Chapters 3 and 4). Thus they constitute a fundamental step in the testing and bench-marking of our novel dust model. Our isolated galaxy simulations consist of the G8, G9 and G10 galaxies from Rosdahl and Teyssier (2015) which were constructed with the MAKEDISK tool by Springel et al. (2005). These simulations are performed with RAMSES in its hydrodynamics version (Teyssier, 2002), solving the hydrodynamics on a cartesian grid with AMR

Table 6.2: Simulation names with their corresponding initial gas-phase metallicity, spatial resolution, and dust physics. See Section 6.2.2 for further details.

Simulation name	$Z_{g,0}$ ($Z_\odot$)	Coagulation model	Shattering model
G10LG	1	Fid.	Fid.
G10LG_HZ	2	Fid.	Fid.
G10LG_LZ	0.3	Fid.	Fid.
G10LG_VLZ	0.1	Fid.	Fid.
G10LG_cF	1	3× Fast	Fid.
G10LG_cS	1	3× Slow	Fid.
G10LG_sF	1	Fid.	3× Fast
G10LG_sS	1	Fid.	3× Slow
G10LG_csF	1	3× Fast	3× Fast
G9HG_LZ	0.3	Fid.	Fid.
G9HG_VLZ	0.1	Fid.	Fid.
G9HG_VVLZ	0.03	Fid.	Fid.
G9HG_VVVLZ	0.01	Fid.	Fid.
G9LG_LZ	0.3	Fid.	Fid.
G9LG_VLZ	0.1	Fid.	Fid.
G9LG_VVLZ	0.03	Fid.	Fid.
G9LG_VVVLZ	0.01	Fid.	Fid.
G8HG_LZ	0.3	Fid.	Fid.
G8HG_VLZ	0.1	Fid.	Fid.
G8HG_VVLZ	0.03	Fid.	Fid.
G8HG_VVVLZ	0.01	Fid.	Fid.

using the unsplit MUSCL-Hancock scheme with a MinMod slope limiter, and the HLL approximate Riemann solver to obtain fluxes at cell interfaces (see Chapter 2). We use a spatial resolution of 18 pc. The halo mass is either $M_\mathrm{h} = 9 \times 10^9$, 9×10^{10}, or $9 \times 10^{11}\,\mathrm{M}_\odot$ with a total baryonic mass (gas and stars) that represents 4.4% of the halo virial mass, meaning $M_\mathrm{gal} = 3.8 \times 10^8$, 3.8×10^9, and $3.8 \times 10^{10}\,\mathrm{M}_\odot$ for G8, G9 and G10, respectively. The halo, stellar disc and bulge are initialised with respectively 10^6, 10^6 and 10^5 particles, or equivalently a particle mass resolution of $173\,\mathrm{M}_\odot$, $1.73 \times 10^3\,\mathrm{M}_\odot$ and $1.73 \times 10^4\,\mathrm{M}_\odot$ for G8, G9 and G10. We allow refinement in cells where the total mass exceeds $8 \times 10^3\,\mathrm{M}_\odot$ from an initial root grid of 64^3 cells. The box sizes are respectively 150, 300 and 600 kpc for G8, G9 and G10, using outflowing boundary conditions. In addition to this pseudo-Lagrangian mass refinement, we also enforce a refinement criterion on the thermal Jeans length so that it is refined with at least 4 cells down to the maximum level of refinement.

The DM mass distribution follows a Navarro et al. (1997) profile with concentration $c = 10$ and a spin parameter of $\lambda_\mathrm{DM} = 0.04$ (Macciò et al., 2008). The disc is

decomposed into a stellar and a gaseous component, with density profiles of $\rho \propto e^{-R/R_{\rm d}}{\rm sech}^2(z/(2H))$, where R is the cylindrical radius, $R_{\rm d}$ is the disc scale length, z is the position along the disk axis, and H is the disc scale height, chosen to be $H = 0.1R_{\rm d}$. The bulge follows a Hernquist density profile with bulge scale length equals to H. The gas disc density profile, with a uniform temperature of $10^4\,{\rm K}$, extends to a maximum radius of of $5R_{\rm d}$ and a height of $5H$. Beyond these points we impose a uniform density of $10^{-6}\,{\rm cm}^{-3}$ and a uniform temperature of $10^7\,{\rm K}$. For the G8, G9, and G10 galaxies, we use respectively a disc scale radius of 0.7, 1.5 and 3.2 kpc. See Table 6.1 for the details.

The gas metallicity is initialised with a decreasing radial profile, following

$$\begin{aligned} Z(R) &= Z_0 \times 10^{0.5-R/R_c}, \text{ if } R < R_c \text{ and } z < H_c, \\ &= 0, \text{ elsewhere,} \end{aligned}$$

where $R_c = 7.42\,{\rm kpc}$, and Z_0 is the scaling metallicity of the profile, which takes values of $Z_0 = 0.045, 0.15, 0.45, 0.90\,{\rm Z}_\odot$, with $Z_\odot = 0.01345$. These values yield a mean gas metallicity of $0.1, 0.3, 1, 3\,{\rm Z}_\odot$ respectively. In this implementation of dust and chemical evolution, the various elements tracked (H, He, C, N, O, Mg, Fe, Si, and S) are initialised in the gas phase with solar mass fractions (Asplund et al., 2009). Furthermore, we initialise the dust mass such that 10% of the refractory mass (Mg, Fe, Si, O and C) is already depleted for the G10 galaxy. For the lower mass galaxies G8 and G9 we use a 0.1% depletion instead. This dust mass is then distributed equally between the different bins of dust grain sizes (i.e. grain sizes do not follow a MRN distribution initially). We note that for the large gas fraction simulations we need to actively alter their early dynamical evolution to allow a smooth relaxation of the initial conditions. This is done by introducing a perturbation in the initial vertical velocity field and imposing a linear ramp up of the star formation over a timescale of 100 Myr. We refer the interested reader to Dubois et al. (2024) for further details.

Star formation follows the gravo-turbulent implementation detailed in Section 2.1.3 and used in the HD simulations of Chapters 3 and 4. Star formation can only occur in regions with gas number density above n_0 which varies with resolution ($n_0 = 0.6, 2.5, 10, 40\,{\rm H\,cm}^{-3}$ for a minimum spatial resolution of respectively $\Delta x = 72$,

36, 18, 9 pc). This corresponds to a stellar mass resolution for newly formed stars of respectively $= 7.4 \times 10^3, 3.7 \times 10^3, 1.9 \times 10^3, 0.9 \times 10^3\,\mathrm{M}_\odot$.

We limit our simulations to individually track the amount of C, N, O, Mg, Si, Fe, S (which represents $\sim 85\%$ of the mass of heavy elements at solar abundance), of total metallicity Z, and H. We assume a Chabrier (2005) initial mass function for the distribution of zero age star (ZAS) masses. Stellar gas plus dust yields for intermediate stars are those of Karakas (2010) for ZAS masses $M_{\rm ZAS} < 8\,\mathrm{M}_\odot$ (asymptotic giant branch, AGB, stars), while yields from Limongi and Chieffi (2018) for massive stars $M_{\rm ZAS} \geq 8\,\mathrm{M}_\odot$ are employed. The yields for massive stars are parameterised by the rotation velocity of the star (either 0, 150 or $300\,\mathrm{km\,s^{-1}}$). We adopt the initial distribution of rotational velocities as a function of the initial metallicity of the star from Prantzos et al. (2018) (obtained from multiple Milky Way chemical constraints), with the corresponding grid[1] of velocity-to-metallicity of ZAS: $V_{\rm ZAS} = 150, 100, 50, 50, 50, 50, 50\,\mathrm{km\,s^{-1}}$ for $Z_{\rm ZAS} = 10^{-3}, 10^{-2}, 10^{-1}, 10^{-0.6}, 10^{-0.3}, 1, 10^{0.3}\,Z_\odot$. Since the Limongi and Chieffi (2018) stellar yields largely underproduce the amount of Mg, with respect to Si and solar abundances (Prantzos et al., 2018), we artificially boost the amount of Mg released by massive stars by a factor 2. The IMF of stars is assumed to span the $[0.1, 100]\,\mathrm{M}_\odot$ mass range, with massive stars only exploding as SNII and releasing metals for $M_{\rm ZAS} \leq 30\,\mathrm{M}_\odot$. By contrast, mass is released by stellar winds over the entire mass range ($[8, 100]\,\mathrm{M}_\odot$). The evolution of each individual intermediate mass star follows the Padova stellar tracks (Girardi et al., 2000) including the thermally pulsating AGB phase (Vassiliadis et al., 1993). We further assume that the mass release of individual AGB stars happens instantaneously at the end of their evolution (pulsating evolution is not individually time-resolved).

For type Ia SN (SNIa), we adopt the delay time distribution of Maoz and Mannucci (2012) with a time-integrated number of SNIa of $N_{\rm Ia}(< t) = 2.35 \times 10^{-4}(\log(t/\mathrm{Gyr}) + 3)\,\mathrm{M}_\odot^{-1}$ (limiting the range of SNIa between 50 Myr and 13.7 Gyr), together with the stellar yields of Iwamoto et al. (1999) (using their W70 carbon-deflagration model).

[1]The range of available stellar yields for a given value of metallicity and rotational velocity is more limited so we simply bi-linearly interpolate the individual stellar yields from their data, which provides a finer sampled grid of IMF-weighted SSP yields as a function of metallicity. In addition, it should be noted that the yields of Limongi and Chieffi (2018) are given as a function of the Fe content of ZAS. We prefer using Z instead of Fe, as it is more flexible. We have therefore converted their Fe into Z by simply assuming solar ratios.

We include SNII feedback following the mechanical feedback model (see Kimm and Cen, 2014, but also Section 2.1.4) in RAMSES. We further simplify SNII feedback by assuming that all the mass and energy are released in one single explosive event 5 Myr after the birth of the star. Stars with initial mass in the range of $M_{\rm ZAS} = [8, 30]{\rm M}_\odot$ explode as SNII, releasing a canonical individual energy of 10^{51} erg, corresponding to a SNII specific energy of $10^{49}\,{\rm erg\,M}_\odot^{-1}$. We also include a minimal model for UV radiation from young OB stars, by imparting an extra amount of momentum to the gas provided by the UV-radiation pre-heating (Geen et al., 2015).

6.2.2 The simplified 4-bins model

For this study we have focused on the major processes affecting the bulk of the dust mass. Therefore, some of the processes described in Chapter 5 are absent and we leave the analysis of their influence on our conclusions to future work. The simplified 4-bins model (2 carbonaceous bins and 2 silicate bins) we use in this chapter is presented in detail in Dubois et al. (2024), but this is the same modelling in essence as what has been outlined in Chapter 5. In what follows, we only highlight the main differences with the full Dusty-PRISM model.

We do not use the PRISM model for RAMSES-RTZ to calculate the non-equilibrium thermo-chemistry of the gas. Instead, we use the standard cooling prescription of RAMSES and the hydrodynamics solver (i.e. we do not perform radiative transfer on-the-fly). Gas is allowed to cool down to 10 K through H and He collisions with a contribution from metals in the gas phase using rates tabulated by Sutherland and Dopita (1993) above 10^4 K and those from Dalgarno et al. (1972) below 10^4 K. Dust affects the cooling efficiency of the gas as it reduces the amount of metals available for cooling[2]. We also include dust collisional cooling (see Section 5.2.4), albeit only by high energy electrons and for uncharged grains (Dwek and Werner, 1981):

$$\Lambda_{\rm d}(a,T) = \mathcal{D}\frac{3m_{\rm H}}{X_{\rm H}4\pi s a^3} n_{\rm H} n_{\rm e} \mathcal{H}(a,T)\,, \tag{6.5}$$

where a is the grain radius, s the grain material density, DTG the dust-to-gas ratio, $n_{\rm H}$ the hydrogen number density, $n_{\rm e}$ the (free) electron number density (we assume a

[2]Note that this approach is not consistent with the RAMSES tabulated cooling rates, as these assume that metal relative abundances remain at solar composition, while different elements will experience different depletions in our model. This caveat is addressed in the full Dusty-PRISM model.

fully ionised gas at these temperatures), $X_{\rm H} = 0.76$ the hydrogen mass fraction, $m_{\rm H}$ the hydrogen mass, and $\mathcal{H}(a, T)$ is given by Equation A13 in Dwek and Werner (1981).

Accretion of refractory elements from the gas phase is done as described in Section 5.2.2, although the Coulomb correction is not self-consistently computed from the local dust charge, but instead based on the Weingartner and Draine (2000) values of $F_{\rm C}$ for a range of sizes of carbonaceous and silicate grains for three typical phases of the ISM. To mimic their complex dependencies, we adopt a value of $F_{\rm C} = 1$ for all kind of grains everywhere, except for large carbonaceous and small silicate grains in the cold neutral medium with $T < 2 \times 10^4\,{\rm K}$ and $n > 10\,{\rm cm^{-3}}$, for which we adopt $F_{\rm C}(0.1\,\mu{\rm m}) = 0$, and $F_{\rm C}(5\,{\rm nm}) = 10$, respectively. Additionally, we include a cut in accretion for carbonaceous grains for $n_{\rm H} > 10^3\,{\rm cm^{-3}}$ since we do not explicitly model CO formation in these simulations.

Coagulation and shattering are modelled by collisions with grains of the same size, hence coagulation only transfers dust mass from the small grain bin to the large grain bin, and vice-versa for shattering. The shattering timescale is obtained by considering the timescale for grain collisions $\tau_{\rm col} = (\sigma_{\rm d}\tilde{\sigma}n_{\rm d})^{-1}$, where $\tilde{\sigma}$ is the grain cross section, $\sigma_{\rm d}$ the dust grain velocity dispersion and $n_{\rm d}$ the dust number density, which results in the following expression (Aoyama et al., 2017):

$$\tau_{\rm sha,\,i} = 54\,a_{0.1,{\rm L}}\,s_{3,\,i}\left(\frac{\mathcal{D}_{\rm L,\,i}}{0.01}\right)^{-1}\left(\frac{n}{1\,{\rm H\,cm^{-3}}}\right)^{-1}\left(\frac{\sigma_{\rm D,L}}{10\,{\rm km\,s^{-1}}}\right)^{-1}{\rm Myr}\,, \tag{6.6}$$

where $\mathcal{D}_{\rm L}$ and $\sigma_{\rm D,L}$ are, respectively, the dust-to-gas ratio and velocity dispersion of the large grain population, $a_{0.1,{\rm L}} = a_{\rm L}/0.1\ \mu{\rm m}$, and the index i runs over the dust species (carbonaceous and silicates). Typical velocities required to shatter grains are above a few ${\rm km\,s^{-1}}$ (Jones et al., 1996), which limit the effect of shattering to the diffuse phase of the ISM. Yan et al. (2004) provide grain-gas relative velocities for various phases of the ISM and show that large grains ($a_{\rm L} = 0.1\,\mu{\rm m}$) reach the turbulent velocity of the forcing scale, i.e. $\sigma_{\rm D,L} \simeq 10\,{\rm km\,s^{-1}}$ in the warm ionised medium, $\simeq 1\,{\rm km\,s^{-1}}$ for the warm or cold neutral medium, and $\simeq 0.1 - 1\,{\rm km\,s^{-1}}$ for molecular clouds. We simplify our turbulent model described in Section 5.2.6 and follow Granato et al. (2021) in adopting the following functional form instead:

$$\tau_{\rm sha,\,i} = 54\,a_{0.1,{\rm L}}s_{3,\,i}\left(\frac{\mathcal{D}_{\rm L,\,i}}{0.01}\right)^{-1}\left(\frac{n}{1\,{\rm cm^{-3}}}\right)^{-p_{\rm sh}}{\rm Myr}\,, \tag{6.7}$$

with $p_{\rm sh} = 1$ for $n < 1\,{\rm cm}^{-3}$, and $p_{\rm sh} = 1/3$ for $1 < n < 10^3\,{\rm cm}^{-3}$, which enforces a dispersion velocity variation from $10\,{\rm km\,s}^{-1}$ in the warm ionised phase ($1\,{\rm cm}^{-3}$) to $1\,{\rm km\,s}^{-1}$ at molecular cloud densities. In Section 5.2.6 we discuss the different predictions for shattering from our turbulence model when compared to this simplified implementation.

Similarly, coagulation is greatly simplified with respect to our full model presented in Section 5.2.7. Densities required to achieve grain velocity dispersions that are low enough to pass below the coagulation threshold velocity of $\lesssim 0.1 - 1\,{\rm km\,s}^{-1}$ for grains of size $a = 0.005\,\mu{\rm m}$ (Chokshi et al., 1993; Poppe et al., 1997) are on the order of $n_{\rm H} \sim 10^2 - 10^3\,{\rm cm}^{-3}$, which we barely reach with our fiducial resolution of $\Delta x \simeq 20\,{\rm pc}$. Following Aoyama et al. (2017), in the case where the local Jeans length is unresolved, the gas density exceeds $0.1\,{\rm cm}^{-3}$ and the temperature lies below $10^4\,{\rm K}$, we assume that half of the gas mass actually has a larger gas density of $10^3\,{\rm cm}^{-3}$ and a small grain turbulent velocity dispersion of $0.1\,{\rm km\,s}^{-1}$ (Yan et al., 2004).

As in the full Dusty-PRISM model, we also include dust injection by stellar processes (Section 5.2.1)[3], dust destruction by SN shocks (Section 5.2.5) albeit without accounting for its shattering into small grains, and thermal sputtering of dust grains in hot gas (Section 5.2.3). For the latter we opt to use fitting functions to the results of Nozawa et al. (2006) for the erosion rate of carbonaceous and silicate grains given by Hu et al. (2019) (i.e. ignoring our updated penetration depth calculation and grain finite size corrections).

6.3 The critical metallicity for dust growth

From a semi-analytical perspective, one can construct simplified models which, to some extent, can explore dust growth within a global galactic gas enrichment framework (see e.g. the original work by Dwek, 1998). Many models are now capable of making such predictions (e.g. Dwek et al., 2007; Zhukovska et al., 2008; Galliano et al., 2008; Hirashita and Kuo, 2011; Asano et al., 2013; Rowlands et al., 2014; Galliano et al., 2021). They principally rely on three parameters: the efficiency of dust

[3]Contrary to the fiducial Dusty-PRISM model, we also include in these simulations SNIa injection with $\delta_{\rm Sil}^{\rm SNIa} = 1$ following Dwek (1998). Although this value of condensation efficiency for SNIa is extreme, SNIa ejecta are completely irrelevant in these simulations because galaxies are only evolved for a few 100 Myr.

production by SNII, the timescale of dust growth by accretion, and the dust destruction efficiency of SNII shocks. A fundamental result which emerged from these models is what has been dubbed the 'critical metallicity' (Inoue et al., 2011; Asano et al., 2013). At low metallicities, the dust mass growth is dominated by injection from stars, as the deposited dust mass per SNII explosion greatly exceeds the dust mass destroyed in the gas swept by the blast wave. When the dust accretion timescale decreases below the timescale for dust destruction from SNII, gas-phase metal accretion becomes a suitable process for fast dust mass growth. Asano et al. (2013) have shown that the 'critical metallicity' for which this happens decreases with decreasing star-formation timescale. This agrees with the inferred star-formation histories of local galaxies and their DTG (Rémy-Ruyer et al., 2014), and explains the observed scatter for a given galaxy metallicity.

In Fig. 6.1, we show both the DTG and the dust-to-metal ratio (DTM) as a function of the gas-phase metallicity of the galaxy measured in a cylinder of radius 2 kpc for G8 and G9, and 4 kpc for G10, and semi-height 0.2 kpc (above and below the disc plane). This is shown for the different simulated galaxy masses, metallicities, and gas fractions (see Table 6.2), at 4 different times (t = 100, 200, 300, and 400 Myr). It is compared with the observational relation obtained by Rémy-Ruyer et al. (2014) where they fit the data with a broken power law (note that the data from De Vis et al., 2017, and also De Vis et al., 2019, shows a similar break in the DTM although with a larger scatter at low metallicities). The values of DTG increase with the gas phase metallicity across all mass ranges with a significant departure from the linear relation corresponding to constant DTM, in agreement with predictions from cosmological simulations (e.g. Popping et al., 2017; Hou et al., 2019; Li et al., 2019; Graziani et al., 2020; Parente et al., 2022; Lewis et al., 2023). The simulation data are reasonably well described by a nearly linear relation (i.e. constant DTM) at high ($>\sim 0.1 Z_{\odot}$) metallicities and a steeper, super-linear behaviour below $\sim 0.1 Z_{\odot}$. Galaxies with different initial gas fractions also show different behaviour in their DTM-metallicity relation. For G9HG galaxies (purple squares in Fig. 6.1), their DTM is nearly constant after 100 Myr, except for the lowest metallicity case, and their gas is continuously enriched as a result of important levels of SFR ($\simeq 0.5\,\mathrm{M}_{\odot}\,\mathrm{yr}^{-1}$). Gas-poor (purple discs) intermediate mass galaxies G9LG have little evolution in

metallicity (low SFR $\simeq 0.03 - 0.04\,\mathrm{M_\odot\,yr^{-1}}$), but they undergo a significant increase in DTM. This different behaviour can be understood by the fact that such simulations sit around the 'critical metallicity' transition region. At low metallicity, for runs (dark purple) with a low gas fraction, the low SFR results in a low metal enrichment, but at the same a low rate of dust destruction by SN shocks. This means that, over the 400 Myr of evolution explored in this plot, dust is slowly, but continuously, growing in mass by accreting gas-phase metals. By contrast, in the high-gas fraction simulations (dark purple squares), the enhanced initial gas density (and turbulence) allows for a much faster accretion of the initial gas-phase metallicity, and the DTM rapidly jumps from an initial value of 0.01 to 0.1 in less than 100 Myr. After this point, the slow growth in DTM is a signature of dust accretion having reached saturation. For the lowest mass galaxies G8HG (gas-rich), the two lowest initial metallicity cases ($0.01\,\mathrm{Z_\odot}$ and $0.03\,\mathrm{Z_\odot}$) both show a strong evolution in metallicity and DTM, and the higher metallicity cases (0.1 and $0.3\,\mathrm{Z_\odot}$) only have an important evolution in DTM. Therefore we conclude that the various evolution histories arising from varying initial metallicities, galaxy mass, or gas fractions all contribute to the break in the DTM/DTG-metallicity relation at $0.1\,\mathrm{Z_\odot}$ and to its large dispersion around this value.

The difference in evolution between the low and high gas fraction G9 simulations can also be understood from the perspective of individual element enrichment. We assume MW chemical compositions for the initial conditions, but during the significant release of fresh metals over the first 100 Myr in the high gas fraction simulations, there is an increase of α elements (Mg, Si, O) over Fe. This means that Fe quickly becomes the limiting element for silicate grains gas-phase accretion (recall the concept of limiting element in Section 5.2.2). This results in a larger reservoir of α elements that are not accreted due to Fe being highly depleted from the gas phase. We explore this by computing the mass of elements locked into dust $1 - f_{\rm dep}(X)$ (where $f_{\rm dep}(X) = 1 - M_{\rm d}(X)/M_Z(X)$ and $M_{\rm d}(X)$ and $M_Z(X)$ are the respectively the dust mass and the total (dust+gas) mass of element X) in Fig. 6.2. We find that this quantity increases with the gas-phase metallicity as a result of an increased accretion rate of refractory elements. The top and middle panels for O and Fe support our claim of Fe being the limiting element, as above the transition around $\sim 0.1 Z_\odot$ the Fe mass locked in dust exceeds 50%, while at the same metallicity O is closer to

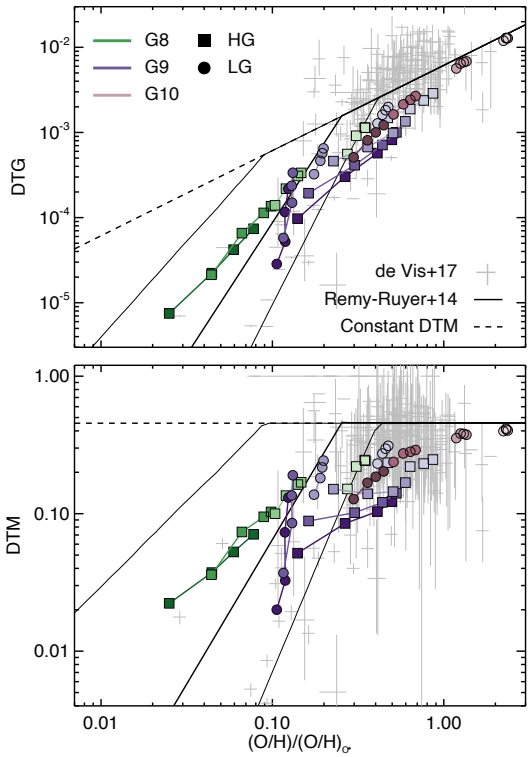


Figure 6.1: DTG (top panel) and DTM (bottom panel) as a function of gas phase metallicity for different simulated galaxies (with different initial masses and gas metallicities) using the model for dust evolution described in the text. Symbols of different colours connected by lines each represent a different simulation sampled at different times (100, 200, 300 and 400 Myr as metallicity increases). Squares are for galaxies with high gas (HG) fractions, and circles for galaxies with low gas (LG) fractions. The dashed black line represents a linear relation $\mathcal{D} \propto [\mathrm{O/H}]$, and the solid black lines are the broken power-laws inferred from the observations of Rémy-Ruyer et al. (2014) for the mean (black thick solid) and the first and third quartiles (thin solid lines). The grey crosses are the observational data from De Vis et al. (2017) with error bars.

15%. Another key insight is that the break in the depletion of Fe as a function of metallicity happens at a different value than for the depletion of C (see also Choban et al., 2022), i.e. $f_{\mathrm{dep}} = 0.5$ is reached at $Z \simeq 0.1\,\mathrm{Z}_{\odot}$ and $Z \simeq \mathrm{Z}_{\odot}$ for Fe and C, respectively. We will return to this result when we explore the variation in attenuation curves in Section 6.5.3, but it implies that the first grains to experience efficient accretion-driven growth are silicate grains, while a significantly more enriched ISM is needed for carbonaceous grain growth.

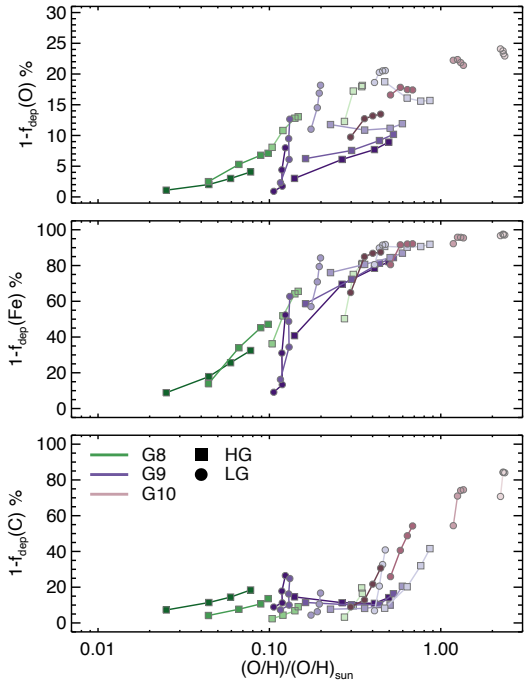


Figure 6.2: Depletion factors for O (top panel), Fe (middle panel) and C (bottom panel) for the different simulations at different times. Symbols and colour coding are identical to Fig. 6.1.

6.4 Bump or no bump: the dust extinction laws in the Local Group

Individually comparing a large number of extinction/attenuation curves may quickly turn into a difficult task. We can greatly simplify this comparison by characterising these curves using their prominent features. Following Salim and Narayanan (2020), we define:

- The overall UV-optical slope $S \equiv A_{1500}/A_{\rm V}$ as the ratio of extinctions at 1500 Å and in the V-band ($\lambda_V = 5500$ Å).
- The UV bump strength $B \equiv A_{\rm bump}/\tilde{A}_{2175}$ as the ratio of extra extinction due to the bump at 2175 Å to the baseline extinction at 2175 Å. We compute the baseline extinction (i.e. without the contribution from the bump) by interpolating the extinction on both sides of the bump $\tilde{A}_{2175} = A_{1500}/3 + 2A_{3000}/3$ and defining $A_{\rm bump} = A_{2175} - \tilde{A}_{2175}$.
- The UV slope as the ratio of extinctions at 1500 Å and 3000 Å, $S_{\rm UV} \equiv A_{1500}/A_{3000}$.

- The optical slope, which is related to the selective extinction $R_{\rm V} = A_{\rm V}/(A_{\rm B} - A_{\rm V})$ (B-band; $\lambda_B = 4400$ Å) as $A_{\rm B}/A_{\rm V} \equiv 1/R_{\rm V} + 1$.

Once again, we emphasise that extinction and attenuation curves, although both traditionally identified with A_λ, provide information about dust from different perspectives. For nearby galaxies (and the MW), one can study the properties of dust absorption by looking at individual sight lines, allowing to probe the grain size distribution and the grain chemical composition (e.g. Mathis et al., 1977; Draine et al., 1984; Weingartner and Draine, 2001a). This information is encoded in the extinction curve. In the case of extra-galactic observations where one is incapable of resolving individual sight-lines to sources, the ratio of observed to intrinsic spectrum (Eq. 6.1) is the end product of blending multiple source spectra, affected by different dust populations as well as radiative transfer effects (e.g. scattering into and out of the line of sight) and the complex geometry which characterises the spatial distribution of dust grains relative to sources. This results in the observed attenuation curve.

In this Section, we focus on the former, and move to the latter using post-processing with Monte-Carlo RT simulations in Section 6.5. The total extinction curve A_λ is obtained from the contributions $A_{\lambda,i}$ of each of the 4 grain bins i, given by:

$$\frac{A_{\lambda,i}}{N_{\rm H}} = 2.5 \log {\rm e} \int_0^\infty \pi a^2 n_i(a) Q_{{\rm ext},i}(a,\lambda) {\rm d}a \,, \tag{6.8}$$

where $N_{\rm H}$ is the hydrogen column number density, and $Q_{{\rm ext},i}(a,\lambda)$ is the extinction efficiency which is a function of grain size a, wavelength λ and grain composition. The GSD ($n_i(a)$) is defined in Eq. 5.9. We compute $Q_{{\rm ext},i}(a,\lambda)$ using the Mie theory (Bohren and Huffman, 1983) with optical constants for carbonaceous and silicate grains taken from Weingartner and Draine (2001a).

The bump versus UV slope relation is shown in Fig. 6.3 with the mean values for the global extinction curves of the MW, LMC and SMC inferred from the Pei et al. (1992) extinction curves. Individual line-of-sight values for the MW from Fitzpatrick and Massa (2007), and for the LMC and SMC from Gordon et al. (2003) are also plotted. G10 simulations are, by-and-large, in good agreement with MW observations at all times, except for the lower initial metallicity runs (i.e. for $Z_{\rm g,0} = 0.1$ and $0.3\,{\rm Z}_\odot$), which require $\sim 400\,$Myr to land into the region spanned by the individual

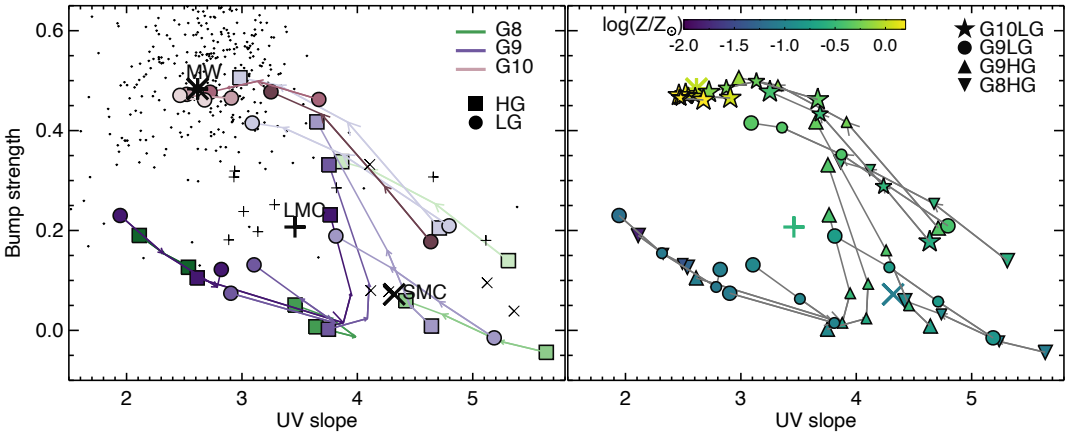


Figure 6.3: Bump strength versus UV slope for the different simulations. Arrows indicate the direction of time, sampled at 100, 200, 300 and 400 Myr. The large black crosses mark the average values observed in the MW, LMC and SMC by Pei et al. (1992) and the small grey dots are values from individual sight-lines for the MW (Fitzpatrick and Massa, 2007) and the SMC and LMC (Gordon et al., 2003). The left panel is colour-coded by simulated galaxy mass (as indicated in the panel), gas fraction (different symbols indicated in the panel), and initial metallicity (by their colour shade, from dark to light for increasing initial metallicity $Z_{g,0}$). The right panel is colour-coded by gas metallicity at the given time (colour bar indicated in the panel). MW-like galaxies (G10LG) are naturally attracted to extinction curve features that closely resemble that of the MW, and the closer they get to the observed metallicity of the MW the closer their extinction properties match those of the MW. Lower mass galaxies (G8 and G9) explore a much larger volume of the extinction curve features' space, due to their lower metallicity.

MW sight lines. This serves as a reminder of the importance of initial metallicities for the growth of DTG (see Section 6.3).

The LMC and SMC show a clear departure from the MW extinction curve with i) a lower bump strength, and ii) a steeper UV slope. For G9HG, simulated extinction curve features display values in the broad range of those observed for the SMC and LMC, in particular for low initial metallicity runs. Nonetheless, they strongly evolve in time mostly due to their strong evolution in metallicity (see right panel of Fig. 6.3). The impact of metallicity evolution in the different runs on the bump strength - UV slope plane appears to follow a clear trend: 1) simulations with metallicities well below the 'critical metallicity' begin at intermediate bump strength and low UV slope (a result of our same-mass initial GSD), 2) they progress towards higher UV slope while the bump strength decreases (the grain cross section is dominated by large grain injection from stellar ejecta), 3) they finally return to a low UV slope but with a high bump strength this time around, as accretion begins to dominate dust mass growth, and converge towards a MW-like extinction curve.

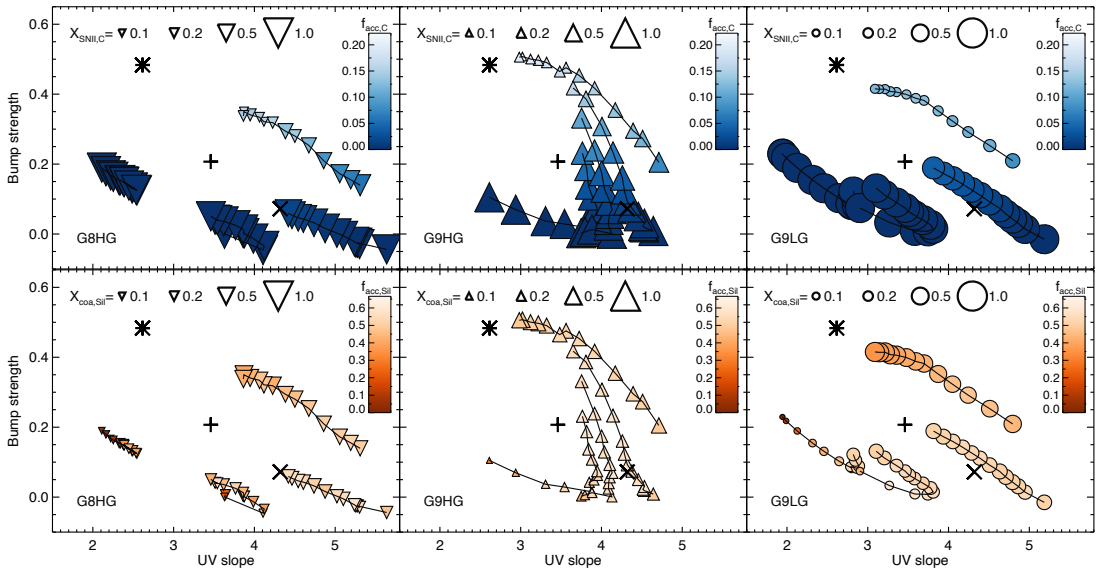


Figure 6.4: Similar to Fig. 6.3 where values of the extinction curve features are size-coded either by the SN ejecta $X_{\rm SNII,C}$ growth strength for the case of carbonaceous grains, or by the coagulation growth strength $X_{\rm coa,Sil}$ for the case of silicate grains, and are color-coded by the accretion fractions $f_{\rm acc,C}$ in blue or $f_{\rm acc,Sil}$ in red (see text for details). Values are shown every 25 Myr from 100 Myr to 400 Myr. Extinction curves features for different galaxy type (G8HG, G9HG, G9LG) are shown in different panels (left, middle and right panel respectively), and each panel contains simulations with different initial metallicities $Z_{\rm g,0}$, from low to high initial metallicity moving from the bottom left of each panel to the top/top-right of the panel in anti-clock wise manner.

We quantify this effect in Fig. 6.4: the slope and bump for the low mass galaxies are color-coded by $f_{{\rm acc},i} = \dot{M}_{{\rm acc},i}/(\dot{M}_{{\rm acc},i} + \dot{M}_{\rm ej} + \dot{M}_{{\rm coa},i})$ (i = C or Sil, for carbonaceous and silicate grains) and are size-coded either by $X_{\rm SNII,C} = \dot{M}_{\rm SNII,C}/(\dot{M}_{\rm SNII,C} + \dot{M}_{\rm acc,C})$ or by $X_{\rm coa,Sil} = \dot{M}_{\rm coa,Sil}/(\dot{M}_{\rm coa,Sil} + \dot{M}_{\rm acc,Sil})$. The corresponding growth rates are computed by taking the average value from the previous 30 Myr of evolution before the given time to smooth out the high-frequency variations (in particular for the ejection rates). The reason we employ $M_{{\rm coa},i^*}$ and not $M_{{\rm acc},i^*}$ in the calculation $f_{{\rm acc},i}$ is because the damping of the bump (produced by small carbonaceous grains) or the UV-to-optical slope (produced by small silicate grains) is mostly due to large grains.

Simulated galaxies exhibit a low bump strength when both $X_{\rm SNII,C}$ values are high and $f_{\rm acc,C}$ values are low (dark colors), as a natural consequence of the larger fraction of large carbonaceous grains released in stellar ejecta compared to the fraction of small grains formed by accretion in the ISM. When the accretion of C atoms onto carbonaceous dust grains is large with respect to their release by ejecta, the bump strength becomes more pronounced and the UV-to-optical slope becomes shallower.

This increase in bump strength with $X_{\rm SNII,C}$ also corresponds to an increase in $f_{\rm acc,C}$, i.e. in the fraction contributed by accretion to the total growth of dust (carbonaceous and silicate grains). The increase in the UV-to-optical slope also follows an increase in accretion ($f_{\rm acc,Sil}$), which corresponds to an increase in metallicity (compare with Fig. 6.3) until it saturates at the highest metallicities. Importantly one can see that, for some of the runs, these extinction curve feature trajectories bifurcate, coinciding with a significant increase in $X_{\rm coa,S}$. For the largest initial metallicity runs, $f_{\rm acc,Sil}$ is lower compared to the lower initial metallicity counterparts, i.e. the relative growth of carbonaceous grains increases (see top panels of Fig. 6.4), and they also present a large relative contribution from coagulation $X_{\rm coa,Sil}$, both conspiring to reduce the steepness of the UV-to-optical slope.

In summary for low metallicity galaxies, ejecta dominate the growth of dust until they reach a sufficiently high metallicity when silicate accretion takes over and the UV-to-optical slope increases. The behaviour is similar for carbonaceous grains but it happens at higher metallicities (and this can be traced back to the depletion of Fe and C in the gas phase, see Fig. 6.2), yielding an increase in bump strength. Finally, the UV-to-optical slope gets shallower at the largest metallicities when both the amount of small carbonaceous grains (grown by accretion) and the coagulation of silicate grains increase.

6.5 From extinction to attenuation with SKIRT

6.5.1 Preparing RAMSES data for SKIRT

We obtain mock attenuation curves from a selected sample of G10 simulations using the Monte-Carlo radiative-transfer code SKIRT (Baes et al., 2011; Camps and Baes, 2015) in its version 9[4]. We do not modify SKIRT in this work, and an extensive introduction to the field of 3D dust radiative transfer simulations is beyond the scope of this manuscript. We recommend that the interested reader turn to the review of radiative transfer methods by Steinacker et al. (2013) and simply summarise the Monte-Carlo (MC) solution method and our parameter choices for the dust radiative transfer (RT) modelling with SKIRT.

[4]The open-source SKIRT code is registered at the ASCL with the code entry ascl:1109.003. Documentation and other information can be found at The SKIRT Project.

In the MC RT method the radiation field is treated as a probabilistic flow of a large number of photon packages. In other words, instead of solving the RT equations, the MC method predicts the propagation of photons in a probabilistic way, by generating random number from an appropriate probability distribution function (PDF). For each source in the simulation domain (e.g. a stellar particle), its intrinsic SED provides a PDF from which to extract a photon initial energy. Once a photon is launched into the dusty medium, the next step consists in determining whether it will interact with the medium traversed, or if it will continue to the next location in the grid (i.e. a cell) given by the domain decomposition performed (i.e. in our case, an octree like in RAMSES, see Chapter 2). The amount that the photon is displaced between RT steps is determined from an exponential distribution of the optical depth τ in the current intervening cell. This is converted into a physical path length s by integrating the extinction coefficient over the path of the photon across the cell until it converges to τ. When the photon reaches this location, it can either be absorbed or scattered, as determined from the dust albedo $\omega = C_{\rm sca}/C_{\rm ext}$ (recall the optical definitions in Section 5.2.9). The new propagation direction after scattering is sampled from the phase function Φ, which is approximated by (Henyey et al., 1941):

$$\Phi(\cos\theta) = \frac{1-g^2}{(1+g^2-2g\cos\theta)^{3/2}}, \tag{6.9}$$

where g is the scattering phase function asymmetry given by Eq. 5.78, and θ is the angle between the incident photon direction and the scattered photon direction. With its new propagation direction thus established, the previous steps are repeated until the photon either leaves the spatial domain or is absorbed. In practice, simple MC RT methods like the one outlined here are rarely used, and symmetries and biases are exploited to increase the MC efficiency. Given the requirement of our mock observations, we have opted to use a series of biases and techniques within SKIRT to improve the speed at which convergence is reached in the setting of dust scattering and absorption in spiral galaxies. SKIRT is a multi-purpose radiative transfer Monte-Carlo framework that allows the modelling of absorption, scattering and emission of a transfer medium using a large number of pre-set geometries, radiation sources, grid decompositions and detectors relevant for many astrophysical phenomena. It is written in C++ allowing for a user-friendly, object-oriented design with hybrid parallel processing.

Before detailing our specific choice of parameters and biases, we describe how the information provided by our RAMSES dust simulations are imported into the SKIRT code. For each G10 simulation, we extract a cubic region spanning 30 kpc on each side and centred on the galaxy. Star particles formed during the 400 Myr of evolution of these simulations are directly saved as plain text files. We also include the 'fake' initial stellar particles by assigning them stellar ages based on their cylindrical radius:

$$t_{\rm form}(R) = t_0 - \alpha_{\rm form} R + \delta_{\rm rand} + t_{\rm sim}, \tag{6.10}$$

where we choose $t_0 = 13.7$ Gyr and an age slope of $\alpha_{\rm form} = 0.5$, $\delta_{\rm rand}$ is a random number sampled from a Gaussian distribution with standard deviation of 3 Gyr, and $t_{\rm sim} = 400$ Myr is the current time of the simulation. This results in a final stellar age distribution with the initial conditions 'fake' particles having a median age of ~ 9 Gyr combined with the young stellar particles formed during the 400 Myr of the simulation. Stellar particles in a simulation of this scale are interpreted as stellar clusters (i.e. SSP, see Section 2.1.3), so treating them as individual point sources in the MC RT would be inconsistent with our modelling. Instead, photons are randomly sampled from a 3D Gaussian kernel centred on the particle position and with full width at half maximum given by the cell size of the AMR level at which the particle sits. In other words, we equate the gravitational softening scale corresponding to the stellar particle in the Poisson multi-grid solver (Chapter 2) with its physical extent in the simulated galaxy. Stellar clusters SEDs are based on their metallicities and ages. To calculate these, we use the FSPS stellar population synthesis code (Conroy and Wechsler, 2009; Conroy and Gunn, 2010; Conroy et al., 2010), which is then normalised using the initial mass of the stellar particle and a Chabrier (2005) IMF is assumed. For the 'fake' stars, their initial mass is based on the integrated mass return predicted from our choice of stellar yields (see Section 6.2.1 for further details). In simulations by Trayford et al. (2017), Rodriguez-Gomez et al. (2017), Nanni et al. (2022), or Hsu et al. (2023) young stellar particles (< 10 Myr) are treated differently than the rest of the stellar particles. Their SEDs are instead sampled from the MAPPINGS III model (Groves et al., 2007), which takes into account the influence of the birth cloud of young stars (intrinsic dust obscuration and emission, HII and PDRs, etc.) on the final SED of the stellar cluster. Such an approach is used in these simulations as a way to overcome

the limited spatial resolution and the lack of a multi-phase ISM necessary to predict the clumping of gas/dust in the high density regions where star formation is taking place. However, the MAPPINGS III model requires information which is lacking in our simulations (as is the case in the simulations previously mentioned), like the ionisation fraction, the covering fraction of PDRs, or the dust grain distribution within dense clouds (e.g. Camps and Baes, 2015; Lahén et al., 2018). Therefore, we do not maintain this approach for our attenuation modelling, but instead take the dust GSD and stellar obscuration as directly predicted by the simulations. We will explore the influence of gas ionisation state and nebular emission in future high-resolution Dusty-PRISM simulations. Stellar photons are emitted from 0.091 μm to 3 μm. In order to accelerate the convergence of the MC RT simulation in this wavelength range extending from the UV to the NIR, we add a photon emission biasing factor of 0.5, meaning that half of the total number of photon emitted are equally shared between all stellar particles (independent of their luminosity), while the other half is distributed across all sources depending on their bolometric luminosity.

We do not consider dust emission in the NIR and FIR (we limit the spectrum to 3 μm), neither stimulated emission from the gas phase, so we run SKIRT without explicit absorption, which means that extinction (sum of scattering and absorption) is considered for computing the photon's next interaction point along its path. Given that we consider systems that may include regions of low dust extinction, we reduce the MC noise by activating the forced scattering method of SKIRT, such that photons continue moving across the grid until their weight, reduced at every step by the dust albedo ω, falls below 4 dex of its original value. All simulations use 4×10^8 photon packets.

6.5.2 The impact of inclination on attenuation curves

In Fig. 6.5 we compare the attenuation curve for the G10LG simulation (i.e. the low gas fraction G10 simulation in Section 6.2.1) at different inclination angles i to the intrinsic extinction curve (black solid line). As a reference, we include empirical fits to the MW (dashed green line, Gordon et al., 2008), and the LMC and SMC (red and blue dashed lines, respectively, Gordon et al., 2003). These curves are all normalised to the attenuation/extinction in the V-band A_V. The most fundamental characteristic of these mock attenuation curves is their consistent deviation from

the intrinsic extinction curve, presenting an overall steeper slope. This is a result of the rather complex[5] dust distribution present in our simulated MW, compared to a uniform dust 'screen' that would be a proxy for the intrinsic extinction. Young stars are formed in the dense, thin disk of the isolated simulations, where they are easily enshrouded in dust. The old stellar population from our initial conditions (i.e. the 'fake' stellar particles) instead follow a disk morphology with a significantly larger scale height and radius (see Section 6.2.1). This implies that the old stellar population (with median age of ~ 9 Gyr) is largely decoupled from the thin dusty disk. The young stars, which would be expected to dominate the emission in the UV, only correspond to 0.7% of the total stellar mass in G10LG[6]. Thus the final observed SED is dominated by the old stars, which are themselves unobscured by dust, resulting in the observed flux at optical and NIR bands to being weakly obscured overall. Therefore, if dust is primarily distributed around young stars and old stars are free from it, the observed attenuation curve reaches maximal steepness. This result is in agreement with the idealised experiments performed by Narayanan et al. (2018).

Different inclination angles i can be used to estimate the amount of scatter present in attenuation curves at fixed dust and stellar population properties, with $\sin(i) = 0$ representing fully face-on galaxies and $\sin(i) = 1$ their perfectly edge-on counterparts. In line with the seminal work by Witt et al. (1996), higher inclination angles position a higher fraction of the line-of-sight dust column density in front of the whole stellar population of the galaxy, effectively reducing the effects of the 'complex' geometry described above. This results in the attenuation curve becoming shallower (or 'grey') as the galaxy approaches a fully edge-on perspective. This effect was also tested in the cosmological zoom simulations of Narayanan et al. (2018), where the authors observed a maximum variation of $\sim 2-3$ in the FUV attenuation (although the average dispersion in their figure 9 is closer to a factor of unity or less). In the case of G10LG, we find that we can easily obtain a dispersion of a factor 3 in the normalised UV extinction. We note that, although not clarified in Narayanan et al. (2018), by

[5]We follow the convention of defining a 'complex' dust distribution as the one that cannot be approximated as uniform dust screen obscuring equally or radiation sources (i.e. non-trivial distribution).

[6]In the Milky Way, for an average SFR of 1-2 solar masses per year, we expect that over the past 10 Myr the total mass of young stars is in the range of $10-20$ million solar masses. That contributes to less than 0.1 % of the total Milky Way's stellar mass (e.g. Cautun et al., 2020)

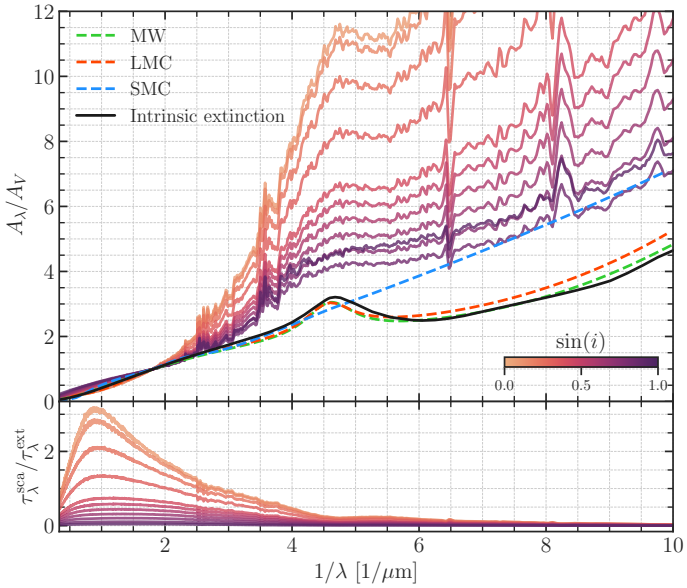


Figure 6.5: Top: Mock attenuation curves for G10LG obtained with SKIRT for a range of inclination angles i. We compare to the intrinsic extinction curve (black solid line) and include fitting functions to the extinction of the MW (dashed green line, Gordon et al., 2008), and the LMC and SMC (red and blue dashed lines, respectively, Gordon et al., 2003) for reference. **Bottom**: Ratio between the scattering and extinction optical depths for different inclination angles. The dominance of the old stellar population in our idealised MW model results in an overall steeper attenuation curve when compared to the intrinsic extinction. The transition to a scattering-dominated geometry with increasing inclination angle i results in a shallower attenuation curve with a lower 2175Å bump strength.

normalising our attenuation curves to A_V what we really measure is the change in the UV-to-optical slope (i.e. the steepness of the attenuation curve), primarily driven by the change in A_V with inclination (see also Fig. 6.6). This dispersion in attenuation curve is also in agreement with the observational constraints for experimentally determined attenuation curves (e.g. Wild et al., 2011; Kriek and Conroy, 2013; Battisti et al., 2017; Salim et al., 2018). We further note that the steepness of the attenuation curve is not maximal when a perfect edge-on inclination is achieved (i.e. $\sin(i) = 1$), but rather when the inclination angle is closer to $i \sim 80\,\mathrm{deg}$. This is due to the fact that when the galaxy is exactly edge-on, the old stellar disk below the galactic plane becomes visible to the observer along a line of sight which does not pass through the dusty disk anymore, effectively decreasing the integrated A_V.

We also draw attention to the variation of the 2175Å bump with i. The UV bump is an absorption feature, so a decrease in its strength (i.e. its contribution to the extinction compared to the underlying attenuation curve) can be caused either by light being scattered into the line of sight instead of being absorbed, or by a rise in

the fraction of unobscured UV sources (Witt and Gordon, 2000; Seon and Draine, 2016). The latter effect can easily be argued to have little influence in our case, as a higher inclination does not mean that the young population is less obscured but rather than the old population becomes more obscured. In order to test the former, we compute a proxy of the dust albedo $\omega = C_{\rm sca}/C_{\rm ext}$ given by the ratio of scattering and extinction optical depths:

$$\frac{\tau_\lambda^{\rm sca}}{\tau_\lambda^{\rm ext}} \equiv \frac{\log_{10}(1 - F_\lambda^{\rm sca}/F_\lambda^{\rm int})}{\log_{10}(F_\lambda^{\rm obs}/F_\lambda^{\rm int})}, \tag{6.11}$$

where the observed flux $F_\lambda^{\rm obs}$ includes the effects of both absorption and scattering, while $F_\lambda^{\rm sca}$ is the flux of scattered light. The result of this computation is shown in the bottom panel of Fig. 6.5 for different inclination angles. This ratio presents a peak around 1 $\mu{\rm m}^{-1}$ which decreases with inclination. It also shows, independent of inclination, low values in the UV part of the spectrum, highlighting the dominant absorption of UV and FUV photon from young stars embedded in the high density dust disk. At increasingly higher inclination, the extinction of the old stellar population increases, effectively promoting the contribution from scattered light. As the 2175Å feature is significantly reduced in the scattering cross-section (see Section 5.2.9, the augmented contribution of observed scattered light increasingly saps the strength of the bump: the galaxy transitions to a scattering-dominant geometry (Seon and Draine, 2016).

We further quantify this effect of inclination by extracting the attenuation curve features described in Section 6.4 in Fig. 6.6, progressing from low inclination (light coloured markers) to high inclination (dark coloured markers). Our fiducial simulation G10LG is represented as blue circles with a yellow edge, and the dark blue stars indicate the values extracted from the intrinsic extinction curve in Fig. 6.5. In the top left panel, we can quantitatively observe the evolution of the bump strength as a function of V-band attenuation. The bump strength starts with a face-on value similar to its intrinsic extinction value of 0.46 (dark blue star with yellow outline), but for a very modest value of $A_{\rm V}$, as expected for a dominant unobscured old population. As the inclination increases, the old stellar population becomes more obscured, and the larger contribution of scattered light (with reduced UV bump) effectively decreases the bump strength. We further remark on the radiative transfer

effects for the mock A_V values, which reaches a maximum of 0.6, compared to the average value of 1.2 in the diffuse ISM of the MW (green square) and the intrinsic extinction curve. While in the case of an extragalactic observation of the attenuation curve (like in our mock SKIRT observations) the increase in attenuation curve is effectively probing a scattering-dominated regime, in the line-of-sight determination of A_V within the MW, one captures an increase in the overall optical depth due to a larger dust column density. This is a clear difference of the physical processes captured by extinction curves as opposed to attenuation curves. We also find the variation of bump strength to be correlated with the overall slope of the attenuation curve S, in agreement with the traditional single-parameter family of curves (e.g. Calzetti et al., 2000) and observations (e.g. Kriek and Conroy, 2013; Salim et al., 2018). However, by contrast to the argument developed in analytic models and simulations (e.g. Witt and Gordon, 2000; Seon and Draine, 2016; Trayford et al., 2017) which relate the decrease in bump strength to a decrease in the UV obscuration of young stars, in our old stellar population dominated model the steepness of the attenuation curve reflects the increase in inclination angle (see also Narayanan et al., 2018). It is thus no surprise that the overall slope S strongly evolves with A_V towards a maximal grey attenuation curve (lower left panel), in agreement with Inoue (2005). We also compare the change in UV slope S_{UV} as a function of the optical slope S_{opt} with inclination angle i (top right panel of Fig. 6.6). The relation between these two slopes appears to be significantly shallower than that derived in the RT models by Narayanan et al. (2018) and Salim and Narayanan (2020). This discrepancy likely reflects our inclusion of a varying grain size distribution across the galaxy, with an enhanced presence of small grains in the diffuse ISM, by comparison to a fixed uniform grain size distribution which gives rise to a steeper UV slope for the same optical slope.

6.5.3 Can we recover the grain size distribution?

In Fig. 6.6 we have included a set of G10LG simulations with varying efficiencies for the coagulation and shattering of dust grains (see Table 2 in Dubois et al. 2024). Artificially increasing and reducing the coagulation and shattering timescales introduces modifications in the overall galactic GSD, as coagulation drives the transfer of dust mass from the small to the large grains and shattering has the opposite effect.

In Dubois et al. (2024) we saw that, while maintaining a similar DTM (similar A_V values for all simulations in the left panels of Fig. 6.6), these modifications can alter the dust mass fraction locked in small grains by up to 50%. The mock attenuations obtained with SKIRT in Fig. 6.6 show that the influence of the abundance of small grains can be appreciated by looking at the maximum bump strength measured face-on. If coagulation is slower (dark cyan markers with yellow outline) or shattering is faster (green markers with purple outline) the bump strength increases from the fiducial value of ~ 0.45 to ~ 0.61, while if coagulation is faster (magenta markers with green outline) it can decrease the bump strength to ~ 0.31. This means that the variation of the GSD observed in the intrinsic extinction curve (star markers) can be recovered from face-on attenuation curves. The exception is the simulation with lower shattering efficiency (G10LG_sS), which does not show a strong departure from the fiducial G10LG track. Slower shattering will affect the abundance of small grains in the diffuse ISM, which, in itself, is the phase with the lower mass contribution to the total dust mass. This means that in the face-on view, the effect of a slower shattering can be seen as an increase in attenuation of the old population (as the diffuse phase is more volume-filling), but it quickly becomes sub-dominant at higher inclination angles, as most of the attenuation is coming from the large integrated dust masses of denser ISM phases. This means that variations solely in the shattering efficiency are hard to distinguish unless the attenuation is obtained exactly face-on.

Consistent with our arguments in the previous section, galaxies with a lower abundance of small grains (G10LG_cF, G10LG_sF and G10LG_csF) exhibit a steeper slope in the $S_{UV} - S_{opt}$ relation due to the lack of strong UV absorption compared to the optical absorption that small grains provide. On the other hand, simulations with faster small grain production, show a shallower slope than the fiducial G10LG. It is interesting to note that these differences in the UV and optical slopes are not present in the intrinsic extinction curve. Therefore, looking at star-dust geometry and RT effects which affect attenuation curves can help with discerning different small grain abundances where integrated extinction curves cannot.

The strength of the trends in UV bump and optical slope in discerning between different dust models are combined in the bottom right panel of Fig. 6.6, where we compare B to S. Models with a large abundance of big grains show a small

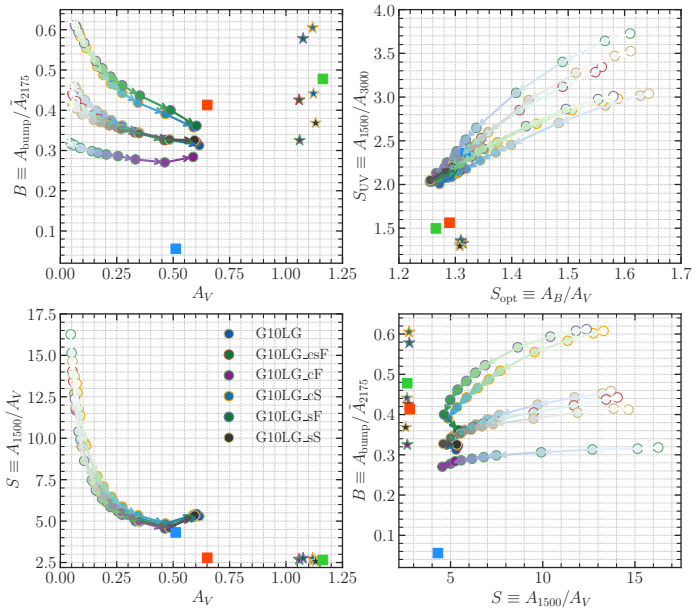


Figure 6.6: Attenuation curve features for simulated G10LG models with different coagulation and shattering efficiencies. Filled circle markers are the results for SKIRT mock observations at different inclination angles (with white hue indicating close to face-on and darker hue indicating close to edge-on inclination). The intrinsic extinction curve values for each simulation are given by markers with the same colour and outline as the circles, but with a star symbol. We also include the MW (green square, Gordon et al., 2008), and the LMC and SMC (red and blue squares, respectively, Gordon et al., 2003) extinction curve values as a reference. Bump strength, optical and UV slopes capture variations in the small grain fraction caused by different coagulation or shattering models.

bump strength and little variation with the attenuation curve slope, whereas models with fast shattering or slow coagulation that give rise to an over-abundance of small grains over large grains show large B at face-on inclinations and a steep variation with attenuation slope/inclination angle. It is important to mention that, while individually modifying the efficiency of these processes gives rise to a large variety of attenuation curve shapes, combining both fast shattering and fast coagulation does not. This implies that although these processes can create a greater contrast in B and S for specific sight lines (see Figure 14 in Dubois et al. 2024), this effect will be diminished in global attenuation curves. As a result, the combined effects of enhanced shattering and coagulation, possibly due to higher average dust velocities or lower material strength, may be difficult to discern in observed attenuation curves. Finally, we note that these differences between models are lost when studying the relation between the full attenuation slope and $A_{\rm V}$, as this is dominated by the effects of the star-dust geometry (see previous section).

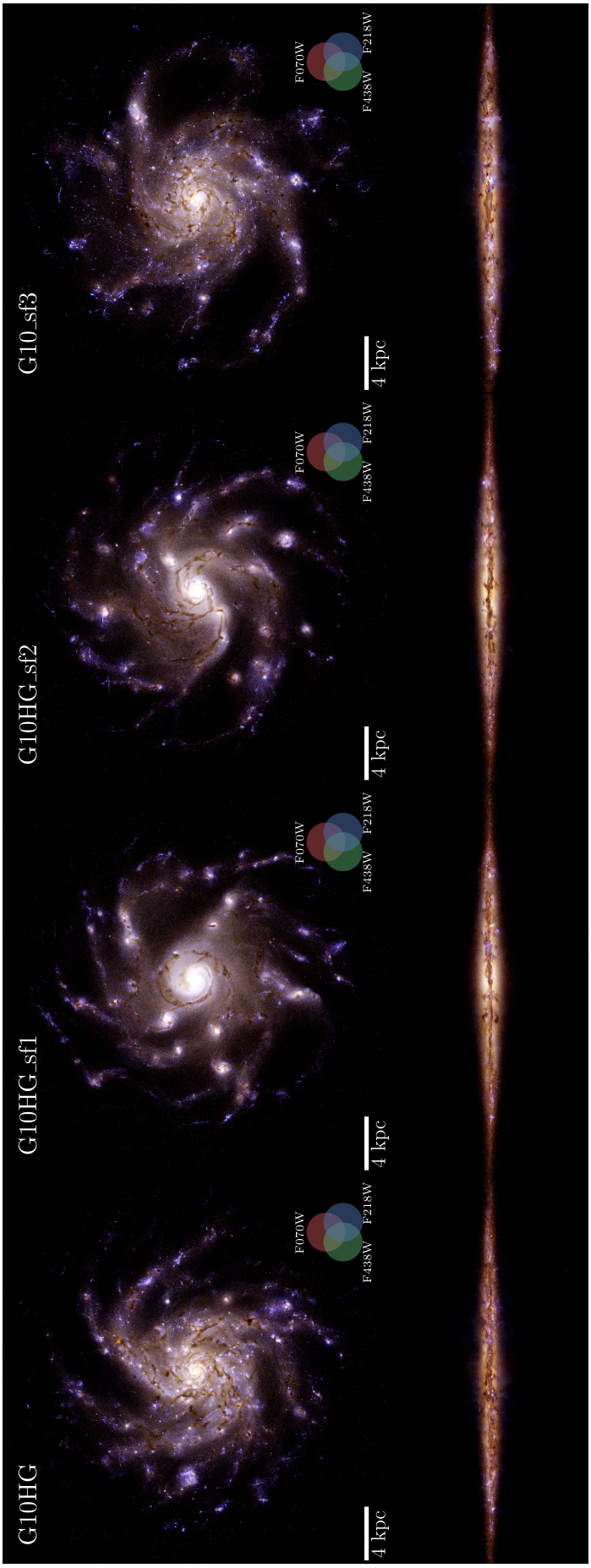


Figure 6.7: Mock face-on and edge-on RGB observations based on the results of the SKIRT post-processing of the different G10HG simulations described in the text. The colours are obtained for the combination of the JWST F070W (red), HST F438W (green), and HST F218W (blue) filters. There is a clear distinction between models that predict large $\varepsilon_{\mathrm{ff}}$ when star-formation is allowed (G10HG and G10HG_sf3), presenting spiral arms with enhanced recent star formation, to models that predict low $\varepsilon_{\mathrm{ff}} \sim 0.01$ (G10HG_sf1, G10HG_sf2), which instead show massive stellar clumps and a large bulge. Images are 30 kpc on a side, with the edge-on view having half the height (15 kpc).

6.5.4 Dust growth in massive star-forming clumps

We further assess the capabilities of our dust modelling by exploring the properties of dust growth in massive, gas-rich spiral galaxies. Early observations with HST revealed that galaxy morphologies were increasingly dominated by an irregular, clumpy structure at higher redshifts (Abraham et al., 1996; Brinchmann et al., 1998). Many of these systems appear to experience large SFRs of ~ 100 $M_{\odot}$ yr^{-1} (Hopkins and Beacom, 2006; Magnelli et al., 2009), for which much of their star formation is taking place in a few giant clumps (Cowie et al., 1995; van den Bergh et al., 1996; Elmegreen et al., 2004b; Elmegreen and Elmegreen, 2005; Elmegreen et al., 2007), contributing to about 10-40% of the total galaxy UV luminosity (Elmegreen et al., 2004a; Forster Schreiber et al., 2006; Genzel et al., 2008). Given their properties, a long-standing effort of the galaxy formation community has been to understand their formation (Noguchi, 1999; Bournaud et al., 2007; Agertz et al., 2009; Ceverino et al., 2010), and whether they can survive long enough to different feedback processes (e.g. radiation pressure, SNII) to allow the build up of proto-bulges (Murray et al., 2010; Krumholz and Dekel, 2010; Oklopčić et al., 2017; Dekel et al., 2022). Observationally, clump ages are fundamental in order to determine clump survival, but this remains a difficult task due to the lack of homogeneous coverage of the UV-optical rest-frame emission of galaxies at $z \gtrsim 2$ (Elmegreen et al., 2009; Förster Schreiber et al., 2009; Adamo et al., 2013; Johnson et al., 2017). In the JWST era, this problem is again gaining relevance, thanks to enhanced angular resolution and MIR coverage (e.g. Álvarez-Márquez et al., 2023; Claeyssens et al., 2023). The issue of age-extinction degeneracy of SED fitting codes still remains key in determining ages and stellar masses for these clumps, with many state-of-the-art observations returning to simplified attenuation curves (e.g. the Calzetti et al. 2000 curve) in order to recover un-obscured SFRs and stellar masses. Furthermore, radiation pressure, argued to be the main feedback mechanisms that can disrupt the growth of stellar mass in these massive clumps (e.g. Murray et al., 2010; Krumholz and Dekel, 2010) relies on assumptions about the IR trapping of stellar radiation from young stars, which is highly dependent on the abundance of dust and its optical properties in these systems . Therefore, understanding how dust evolution takes place in massive star-forming clumps and how different star formation prescriptions (and hence star formation efficiencies)

are imprinted in rest-frame UV-optical observables is a fundamental step for the understanding of current and future observations with JWST.

Different observations of high-redshift star forming galaxies based on CO measurements suggest an average gas fraction of 40-60% (Daddi et al., 2008a; Daddi et al., 2008b; Tacconi et al., 2008; Dessauges-Zavadsky et al., 2020; Williams et al., 2021). As argued by Dekel et al. (2009b), these massive galaxies are probably fed by a few cold filaments, sustaining the formation of massive gas clumps of $\sim 10^9$ $M_\odot$ due to violent gravitational instabilities triggered by the high gas surface densities maintained by this rapid and substantial accretion. We thus setup an idealised experiment by performing some modifications to our G10 initial conditions described in Section 6.2.1. The galaxy is made of a stellar disc, a stellar bulge component, and a gaseous disc component, with respective masses of $M_{\star,\rm d} = 1.7 \times 10^{10}\, M_\odot$, $M_{\star,\rm b} = 3.5 \times 10^9\, M_\odot$, and $M_{\rm g} = 1.7 \times 10^{10}\, M_\odot$, i.e. with an initial 45 % gas fraction, hence mimicking a massive star-forming high-redshift galaxy. All simulations use the same metallicity distribution as the G10LG simulations in Section 6.2.1 with average solar metallicity $Z_\odot$.

The star formation follows a Schmidt law, where the local star formation rate density is $\dot{\rho}_\star = \varepsilon_\star \rho / t_{\rm ff,g}$, where $\varepsilon_\star$ is the star formation efficiency per free fall time, ρ is the gas mass density, and $t_{\rm ff}$ is the gas free-fall time. Several efficiencies (SF laws) were used, all requiring that the gas be denser than $n > 10\,{\rm H\,cm^{-3}}$:

- G10HG: the variable gravo-turbulent SF efficiency that follows the multi-free fall model (Hennebelle and Chabrier, 2011) of Padoan and Nordlund (2011), with a proto-stellar feedback efficiency of 50 %. This model depends on the turbulent Mach number ($\mathcal{M}$) and on the virial parameter ($\alpha_{\rm vir}$) and is the same as the one used in the HD simulations of our NUT suite (Section 2.2). It is our default model, and the same as the one used for the G8, G9 and G10 runs with low gas fraction presented in Section 6.2.1.
- G10HG_sf1: a constant low SF efficiency of $\varepsilon_\star = 0.02$.
- G10HG_sf2: a simple gravo-turbulent model that only depends on $\alpha_{\rm vir}$ as $\varepsilon_\star = 0.5 \exp(-1.6 t_{\rm ff}/t_{\rm dyn})$ (Padoan et al., 2012), where $t_{\rm dyn} = \Delta x/(2\sigma_{\rm t})$ and $\sigma_{\rm t}$ is the gas turbulent velocity. This is the same SF law as adopted in Vintergatan (Agertz

et al., 2021), although they used a higher density threshold ($n > 100\,\mathrm{H\,cm^{-3}}$ in their case) for SF.

- G10HG_sf3: a constant high SF efficiency $\varepsilon_\star = 1$ that requires that the gas is gravitationnally bound $\alpha_{\rm vir} < 1$. This is similar to the SF law adopted in the FIRE simulations (Hopkins et al., 2013a).

As a qualitative overview of the differences between these models, in Fig. 6.7 we present mock RGB images of the four simulated G10HG galaxies seen face-on (top row) and edge-on (bottom row). The colours are made from the combination of the observed spectrum convolved with the response function of the JWST F070W (red), HST F438W (green), and HST F218W (blue) filters. In all simulations, realistic properties of massive star-forming disks (e.g. Genzel et al., 2010; Johnson et al., 2017; Puschnig et al., 2023) are clearly visible in these mock UV-NIR mock images: spiral structures populated by bright and young stellar clusters, and dense dust filaments closely tracking high gas density regions. These are seen as a thick dust lane in the edge-on view, with some of them extending beyond the thin disk in the vertical direction. Despite these similarities, their differences are clear to see upon closer examination. Models that are based on more stringent conditions for star formation but allow for larger star formation efficiencies $\varepsilon_{\rm ff}$ (G10HG and G10HG_sf3) present similar morphologies which are very different to the more permissive models which enforce a lower $\varepsilon_{\rm ff}$ (G10HG_sf1 and G10HG_sf2). The former yield spiral systems with star forming regions of a large variety of sizes, effectively populating the whole extent of their spiral arms, while the latter are instead dominated by a bulge-like structure with a limited number of very massive stellar clumps and very thin and dim spiral arms. Furthermore, these models feature a complex network of dust filaments, which both surround star-forming regions but also appear to cross from one spiral arm to another (e.g. see the dark filament on the centre, top left limit of the bulge in the G10HG face-on image). The G10HG_sf1 and G10HG_sf2 instead exhibit a more uniform dust distribution in which thick, individual filaments closely map the stellar distribution. Therefore, upon preliminary examination, these SF models appear to support low $\varepsilon_{\rm ff} \sim 0.01$ to allow for the growth of massive stellar clumps (e.g. Krumholz and Dekel, 2010). However, we have to be extremely cautious about these conclusions, as in our idealised isolated simulations we neglect the environmental

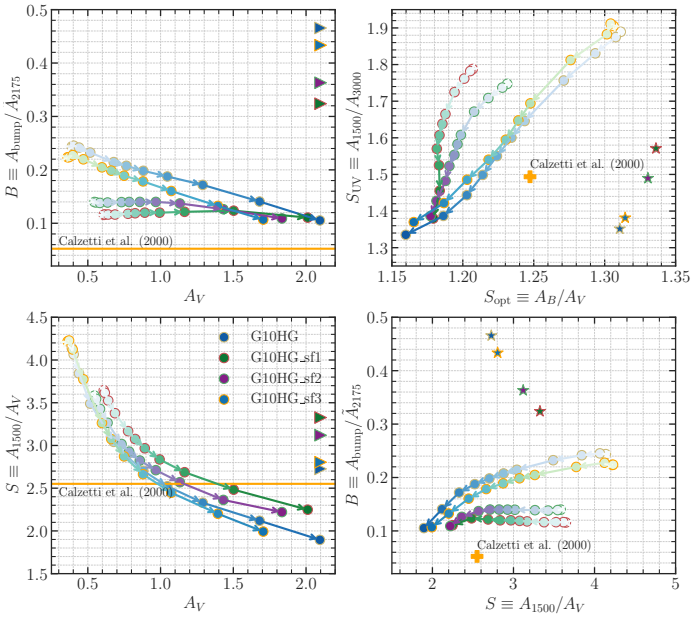


Figure 6.8: Attenuation curve features for simulated G10HG models with different SF models. Filled circle markers are the results for SKIRT mock observations at different inclination angles (with white hue indicating close to face-on and darker hue indicating close to edge-on). The intrinsic extinction curve values for each simulation are given by markers with the same color and outline as the circles, but with a star symbol. Triangles are used to indicate intrinsic $A_{\rm V}$ values extending beyond the limits of the figure. We also include the equivalent attenuation curve parameters extracted from the Calzetti et al. (2000) law, widely used by SED fitting codes to predict stellar ages of massive star-forming clumps.

effects of a realistic CGM and the high density streaming flows predicted for these high mass systems at high redshift (e.g. Dekel and Birnboim, 2006). These analysis needs to be revisited in the framework of cosmological simulations.

We further quantify the signatures of different SF prescriptions on the dust properties by exploring the main attenuation curve features of the UV-optical range in Fig. 6.8. We follow similar conventions as in Fig. 6.6, although we further include triangles to indicate the value of the intrinsic extinction $A_{\rm V}$. Given the large gas density in these simulations and the fast injection of metals due to high SFR (10, 20, 15 and 10 $\rm M_\odot\ yr^{-1}$ for G10HG, G10HG_sf1, G10HG_sf2 and G10HG_sf3, respectively), dust growth is boosted, giving rise to $A_{\rm V} \sim 5-6$. As was the case for the G10LG galaxies, the integrated attenuation $A_{\rm V}$ is lower than the value obtained from the intrinsic extinction. Therefore, in order to facilitate the reading of the observed attenuation curve properties, we use triangle markers to indicate that the extinction $A_{\rm V}$ is much larger than the diagram limits.

As expected from our qualitative analysis of the mock images presented in Fig. 6.7,

the low efficiency models (G10HG_sf1 and G10HG_sf2) and the high efficiency models (G10HG and G10HG_sf3) span different regions of the attenuation curve parameter space. The latter present higher bump strengths both in the extinction curve and in the face-on attenuation curve (see top left panel). The low efficiency models instead show a very flat relation between the bump strength and the A_V/inclination angle, suggesting that the dominant galactic emission goes (at all inclinations) through gas which is highly depleted of small carbonaceous grains. Therefore, although these simulations have (albeit smaller) a contribution from small carbonaceous grains, the attenuation curve does not enable one to recover their UV absorption signatures. This lack of contribution from small grains to the UV extinction can also be apprehended by comparing optical and UV slopes in the top right panel of Fig. 6.8, in agreement with the arguments developed in Section 6.5.3. While the G10LG models in Dubois et al. (2024) were dominated in emission (and mass) by the underlying old stellar population from the initial conditions, in the case of these high-redshift galaxy simulations the intense star formation experience results in the quick growth of stellar mass, with the new stars contributing to $\sim 20\%$ of the total stellar mass after 400 Myr. This means that the UV-optical bands are no longer driven by an unobscured old stellar population dominating over obscured young stars. Instead, we are seeing the signatures of young stars which become increasingly decoupled from the dust distribution, resulting in their 2175Åunobscured emission washing out the UV bump (e.g. Narayanan et al., 2018). Indeed we can see that these massive stellar clumps in the mock images of G10HG_sf1 and G10HG_sf2 are strongly devoid of dust obscuration, and also appear to be sufficiently long lived for their colours to not be dominated by the young stellar, blue emission. We also find that despite this, when seen face-on, the galaxies in these models have consistently larger A_V compared to those of the high efficiency models. Although these large clumps are depleted from dust (DTM$\sim$ 0.2 in these simulations as opposed to 0.3 in G10HG), the integrated DTM in these simulations is larger than their high star formation efficiency counterparts. Despite the lower DTM, these clumps are much more gas-rich, which can still result in a larger dust column density.

Finally, we compare our results for the main attenuation curve features to a reference attenuation curve used in past and current observations of star forming clumps (e.g. Elmegreen and Elmegreen, 2005; Förster Schreiber et al., 2009; Claeyssens

et al., 2023; Álvarez-Márquez et al., 2023): the Calzetti et al. (2000) attenuation law. This widespread attenuation law used in many SED fitting codes is a bumpless attenuation with a slope similar to the MW, and easily parameterised by A_V. Using complementary methods, different observational works have shown evidence for the consistency of the Calzetti et al. attenuation law (e.g. Reddy and Steidel, 2004; Scoville et al., 2015; Cullen et al., 2017; Cullen et al., 2018), with the bump-less extinction derived from observations of distant gamma-ray bursts[7] (Zafar et al., 2011; Schady et al., 2011; Zafar et al., 2018). In contrast with these observations, there also exists observational evidence of composite attenuation curves with steeper slope than Calzetti et al. (Reddy et al., 2015; Shivaei et al., 2015), and evidence of a UV bump (Conroy et al., 2010; Wild et al., 2011; Elíasdóttir et al., 2008; Kriek and Conroy, 2013; Scoville et al., 2015; Tress et al., 2018). In Fig. 6.8 we show how assuming a Calzetti et al. attenuation deviates from predicted attenuation curve properties for our massive, gas-rich spiral system. For example, the assumed fixed attenuation slope for any A_V fails to capture the effects of inclination and the intrinsic influence of different dust abundances and star-dust geometry. We thus advocate for a revision of estimated properties of star-forming clumps from SED fitting, which would better account for dust growth and destruction and complex star-dust geometries.

6.6 Conclusions

In this Chapter, we have introduced a suite of isolated galaxy simulations using our novel dust model in RAMSES. This model decomposes dust into carbonaceous and silicate grains with two grain sizes of 5 nm and 0.1 μm. This testbed of our dust model, with a multiphase ISM structure captured at a resolution of 20 pc, has allowed us to explore various galaxy masses, metallicities, gas fractions, and their effect on the galactic dust properties and extinction curves:

- The DTM/DTG-Z relation is naturally reproduced in our model with a rapid decrease in DTM below 0.1 $Z_\odot$ as suggested by observations. This transition is

[7] We remind the reader that these methods, although potentially relevant, are limited to sampling the extinction curve in the immediate vicinity of gamma-ray bursts (GRB). Additionally, the strong radiation field near a GRB can quickly alter the GSD due to RATD (e.g. Hoang, 2019), hence these GRB based methods very likely constitute a biased way of sampling the average dust properties of the host galaxy.

due to a dominant growth mode by ejecta, at low metallicities, to growth by accretion, at high metallicities.

- A crucial insight is that the break in the depletion of silicate-bearing elements as a function of metallicity happens at a different value than that of C. This offset, driven by the different accretion efficiencies of silicate and carbonaceous grains, is key to explain variations in extinction curves for low mass and low metallicity galaxies.
- By exploring different galaxy masses, gas fractions and metallicities, we obtain diversity in the bump strength and UV-to-optical slope of extinction curves. In particular, these features are strongly correlated with the metallicity of the gas, as it controls the relative amount of growth by accretion (small grains) relative to ejecta (large grains) and to coagulation.
- Due to their lower metallicity, we can interpret the steeper slopes and the weaker bumps of the extinction curves of the Magellanic Clouds with respect to that of the Milky Way as the result of a lower accretion of metals onto dust relative to ejecta (especially for C), of a more efficient accretion of silicate elements with respect to C, as well as of a less efficient coagulation of grains.
- We have obtained mock attenuation curves for our Milky Way-like simulations using SKIRT. These are consistently steeper than the intrinsic attenuation curve, with face-on views being steeper than edge-on views. This is caused by the flux from the unobscured old stellar population dominating over the highly-obscured young stars formed withing the thin, dusty disk.
- The radiative transfer effects imprinted in mock attenuation curves aids in discerning different small grain abundances compared to intrinsic extinction curves. We attribute this to the fact that the volume-filling phase, dominating the obscuration of old stars, is the diffuse ISM in which the abundance of small grains is more dramatically altered.
- To showcase the capabilities of our dust model, we present preliminary results of the evolution of dust in massive gas rich galaxies. We find that low-efficiency star formation models can easily be distinguished in their attenuation curve properties from more stringent star formation models but with higher efficiency.

7 Conclusions

Contents

7.1 Summary 222
7.2 Outlook 225

Despite the immense success of our current theoretical models in predicting the properties of the galaxy population in the local Universe, they have failed to forecast many of the properties of individual galaxies in the local Universe, as well as the growth of the most extreme galaxies in the early Universe. The theoretical challenges posed by current observations with facilities, like the Atacama Large Millimetre/submillimeter Array (ALMA) and the James Webb Space Telescope (JWST), have fuelled a new era of theoretical and numerical research in galaxy formation in a cosmological context. In this thesis, we have advocated for a holistic approach to galaxy formation and evolution, which carefully explores the complex interplay of a large variety of physical processes and how they interact to give rise to the emergent properties of galaxies. We outline here the main results of this effort, and introduce current and future work towards the understanding of the microphysical components of galaxy formation across cosmic time.

7.1 Summary

7.1.1 Cosmic rays and magnetic fields in the cosmological evolution of Milky Way-analogues

Many implementations of calibrated SN feedback in models and simulations (e.g. Pillepich et al., 2018; Rosdahl et al., 2018; Davé et al., 2019) claim to capture the enhanced momentum deposition caused by CRs due to their long cooling times and their relativistic nature (see e.g. Rodríguez Montero et al., 2022). In this thesis, we have explored the direct dynamical influence of CR protons injected by SN remnants

in a suite of cosmological zoom galaxy simulations. The results in Chapter 3 have shown that when CRs contribute just 10% of the energy deposited by a single Type II SN, they can dramatically decelerate the mass growth of a Milky Way-analogue at high redshift. This results in better agreement with observational models without the need for enhanced supernova (SN) energy or calibrated winds. CRs also support cold, low-density gas against collapse, leading to a more dominant warm phase in the interstellar medium (ISM) and a smoother gas distribution within the galaxy's disk. CRs alter the environment at the sites of SN explosions, rendering feedback more efficient. Outflow mass-loadings are dramatically increased compared to the simulations without CRs, resulting in 'momentum' driven winds in agreement with observations of local dwarf galaxies. We find that the origin of enhanced outflows is a combination of a shallower gravitational potential due to bulge growth suppression at high redshift, and the acceleration of outflows by CR pressure gradients in the CGM.

In Chapter 4, we explore the properties of the CGM and inflowing gas in the presence of CRs. We find that CRs significantly disturb the CGM, making it denser, colder, and more metal-enriched compared to the CGM in the HD and MHD simulations. In the HD and MHD simulations, cold inflows can penetrate the super-bubble around the galaxy, but in CRMHD, strong feedback disrupts these inflows well beyond the virial region, resulting in lower-density material approaching the inner halo. This deceleration of streaming inflows creates a reservoir of low-velocity gas at a distance between 0.3 and 0.5 times the virial radius. While cold inflows persist until $z \sim 2.5$ in models without CRs, in CRMHD they are largely disrupted in the inner regions of the halo already at $z \sim 6$. We have determined that this reservoir of low velocity gas is predominantly warm ionised gas supported by CR pressure gradients, continuously heated by the UV-background. We term this newly characterised region of the CGM the *meta-stable CR corona*. Based on our physical understanding of the influence of CRs in the CGM and inflowing gas, we have updated the classical virial shock stability criteria (Birnboim and Dekel, 2003; Dekel and Birnboim, 2006) to take into account the influence of CR heating and a CR+thermal gas mixture. The presence of CRs strongly disturbs the virial shock, resulting in slower inflows and a softer equation of state, preventing the formation of a strong virial shock throughout the cosmic time explored in the simulations.

7.1.2 Modelling radiation, dust and chemistry for the future of galaxy formation simulations

Dust particles, PAHs, and molecules like H_2 significantly impact the thermal and chemical evolution of galaxies, particularly through interactions with radiation and gas. However, modelling these processes is fraught with challenges, especially due to the assumptions about dust properties and the limitations of large-scale cosmological simulations. It is through many of these atomic and molecular line diagnostics that we are able to probe galactic properties. In Chapter 5, we have introduced Dusty-PRISM, a state-of-the-art chemical model designed to simulate the formation, growth, and destruction of dust and PAHs within galaxies and their ISM across their cosmological evolution. By coupling dust evolution with non-equilibrium thermo-chemistry and on-the-fly radiation hydrodynamics, Dusty-PRISM aims to provide a self-consistent framework for predicting the influence of dust on observable galaxy properties. This model is unique, being particularly innovative in its ability to account for various dust processes, from accretion to radiative torque destruction, offering a more realistic and comprehensive understanding of dust evolution.

We showcase the potential of our novel dust model by addressing the complexities of interpreting dust extinction curves in Chapter 6. The simulations naturally reproduce the observed relationship between DTM and DTG ratios as a function of metallicity, highlighting a transition from ejecta-dominated growth of dust grains at low metallicities to accretion-dominated growth at higher metallicities. A key finding is the offset in depletion breaks between silicate and carbonaceous grains, driven by their differing accretion efficiencies, which helps explain the diversity in extinction curves. Using mock attenuation curves, we observed that the attenuation curves for face-on views are consistently steeper than those for edge-on views, driven by the dominance of flux from older, less obscured stars. Our study further demonstrates that radiative transfer effects can distinguish small grain abundances more effectively than intrinsic extinction curves. Finally, preliminary results on dust evolution in massive, gas-rich galaxies suggest that attenuation curve properties can effectively differentiate between star formation models with varying efficiencies.

7.2 Outlook

What is the role of CRs in high-redshift starbursts and how do they influence dusty outflows? How reliable are dust emission and cold gas diagnostics in sampling the conditions of the ISM? What are the signatures of obscured SMBH accretion in SMGs? To address these questions, future galaxy formation simulations need to couple the microphysical components that have been the subject of this thesis (magnetic fields, cosmic rays, radiation and dust) and then simulate the growth of extreme galaxies and their SMBH across cosmic time. We are currently developing (in collaboration with Joakim Rosdahl and Yohan Dubois) a version of RAMSES-RTZ that couples radiation, thermo-chemistry, and the dust evolution from Dusty-PRISM, to CRMHD using a new solution to the CR transport using the M1 method as in the original implementation of radiation-transfer in RAMSES-RT. CRs are one of the main heating mechanisms in dense UV-shielded clouds (Papadopoulos, 2010). By updating the sub-grid model of magneto-turbulent star formation to include a dependence on local CR and dust properties, we will reduce the gap between ISM properties in galaxy formation simulations and the ultimate formation of stars.

There remain many open questions in the field of CR transport. In a soon-to-be-submitted study, we explore the influence of CR streaming transport and heating on the conclusions presented in this thesis, finding a very important role of CR streaming heating on the growth of stellar mass at early times. An important caveat of our current modelling of CR transport is the assumption of constant diffusion coefficient. By coupling the M1 method of CR transport with the local ionisation fractions, sub-resolution turbulence (including the new developments on sub-grid magnetic dynamo; Liu et al., 2022), and dust abundances, we plan to study the self-consistent transport of CRs in realistic multi-phase simulations of galaxy formation.

As [CII] is the dominant cooling line for the cool ISM gas, its brightness has made it the work-horse for explorations of the distant cold ISM (see review of Carilli and Walter, 2013). However, [CII] can trace both the neutral and the ionised medium, and be depleted in high-density gas and in systems harbouring a SMBH (Decarli et al., 2018), resulting in lower [CII] emission for the observed far-IR emission. One proposed explanation for this [CII]/FIR deficit is that the interstellar medium in high redshift galaxies is highly disturbed and undergoing intense star formation and

feedback processes. These processes can lead to a depletion of gas-phase carbon, which is responsible for the [CII] emission, and a heating of the dust that emits in the FIR. Additionally, a harder and more intense UV radiation field from the quasar can ionise carbon away from CII, while further heating the dust to higher temperatures (and, hence, larger luminosities). By coupling the full CRMHD+Dusty-PRISM version of RAMSES with an on-the-fly radiation model of SMBH accretion, we will study the influence of intense, obscured SMBH growth, obtaining mock observations of [CII], dust continuum and PAH emission lines, to deliver profound insights on the obscured phases of SMBH growth.

There is no way around the fact that we are entering an increasingly challenging era for galaxy formation. However, this period is likely to, as we have shown in this thesis, fuel a fascinating paradigm shift in our understanding of galaxy formation. By adopting a holistic approach, as demonstrated in our work, we can more accurately capture the complex physical processes that shape galaxies and simultaneously predict direct observables. This new methodology not only enhances our comprehension of early galaxy evolution but also offers unprecedented predictive power, bridging the gap between theoretical models and observations, and heralding a bright future for the field.

References

Abel, T., Bryan, G. L., and Norman, M. L. (2000). *ApJ* 540.1, pp. 39–44.
Abel, T., Bryan, G. L., and Norman, M. L. (2002). *Science (New York, N.Y.)* 295.5552, pp. 93–98.
Abouelaziz, H. et al. (1993). *JChPh* 99.1, pp. 237–243.
Abraham, R. G. et al. (1996). *MNRAS* 279.3, pp. L47–L52.
Adamo, A. et al. (2013). *ApJ* 766.2, p. 105.
Agertz, O., Teyssier, R., and Moore, B. (2009). *MNRAS: Letters* 397.1, pp. L64–L68.
Agertz, O., Teyssier, R., and Moore, B. (2011). *MNRAS* 410.2, pp. 1391–1408.
Agertz, O. et al. (2021). *MNRAS* 503.4, pp. 5826–5845.
Aghanim, N. et al. (2020). *A&A* 641, A6.
Alfvén, H. (1943). *Arkiv f. Mat., Astron. o. Fys.* 29B, p. 1.
Algera, H. S. B. et al. (2020). *ApJ* 903.2, p. 138.
Allain, T., Leach, S., and Sedlmayr, E. (1996). *A&A* 305.2, pp. 602–615.
Allamandola, L. J. et al. (1989). *ApJS* 71, p. 733.
Allers, K. N. et al. (2005). *ApJ* 630.1, pp. 368–380.
Álvarez-Márquez, J. et al. (2023). *A&A* 671, A105.
Andersen, H. H. and Bay, H. L. (1981). "Sputtering yield measurements". In: *Sputtering by Particle Bombardment I: Physical Sputtering of Single-Element Solids*. Ed. by R. Behrisch. Vol. 47. Springer-Verlag, p. 145.
Andersen, P. W. (1972). *Science* 177.4047, pp. 393–396.
Andersson, B.-G., Lazarian, A., and Vaillancourt, J. E. (2015). *ARA&A* 53.1, pp. 501–539.
Andersson, B.-G. and Potter, S. B. (2007). *ApJ* 665.1, pp. 369–389.
Andrews, H., Candian, A., and Tielens, A. G. G. M. (2016). *Astronomy & Astrophysics* 595, A23.
Anninos, P. et al. (1997). *New Astron.* 2.3, pp. 209–224.
Aoyama, S., Hirashita, H., and Nagamine, K. (2020). *MNRAS Letters* 491.3, pp. 3844–3859.
Aoyama, S. et al. (2017). *MNRAS* 466.1, pp. 105–121.
Arellano-Córdova, K. Z. et al. (2022). *ApJL* 940.1, p. L23.
Armillotta, L., Ostriker, E. C., and Jiang, Y.-F. (2022). *ApJ* 929.2, p. 170.
Armillotta, L. et al. (2024). *ApJ* 964.1, p. 99.
Asano, R. S. et al. (2013). *MNRAS* 432.1, pp. 637–652.
Asano, R. S. et al. (2014). *MNRAS* 440.1, pp. 134–142.
Ashley, J. C. and Anderson, V. E. (1981). *IEEE Trans. Nucl. Sci.* 28.6, p. 4131.
Asplund, M. et al. (2009). *ARA&A* 47.1, pp. 481–522.
Aung, H., Nagai, D., and Lau, E. T. (2021). *MNRAS* 508.2, pp. 2071–2078.
Babyk, I. V. et al. (2018). *ApJ* 862.1, p. 39.
Baczynski, C., Glover, S. C., and Klessen, R. S. (2015). *MNRAS* 454.1, pp. 380–411.
Baes, M. et al. (2011). *ApJS* 196.2, p. 22.
Bakes, E. L. O., Tielens, A. G. G. M., and Bauschlicher Charles W., J. (2001). *ApJ* 556.1, p. 501.
Bakes, E. L. O. et al. (1994). *ApJ* 427, p. 822.
Baldry, I. K. et al. (2020). *MNRAS* 500.2, pp. 1557–1574.
Bardeen, J. M. et al. (1986). *ApJ* 304, p. 15.
Bardeen, J. M. et al. (1983). *PhRvD* 28.4, pp. 679–693.
Barlow, M. J., Barlow, and J., M. (1978). *MNRAS* 183.3, pp. 367–395.
Barrera, N. F. et al. (2023). *MNRAS* 524.3, pp. 3741–3748.
Barro, G. et al. (2013). *ApJ* 765.11pp, p. 104.
Battisti, A. J., Calzetti, D., and Chary, R.-R. (2017). *ApJ* 851.2, p. 90.
Bauschlicher, C. W. et al. (2001). *CP* 274.1, pp. 11–14.
Bauschlicher, C. W. et al. (2018). *ApJS* 234.2, p. 32.

Bauschlicher C. W., J., Peeters, E., and Allamandola, L. J. (2009). In: *The Evolving ISM in the Milky Way and Nearby Galaxies*. Ed. by K. Sheth et al., 6, p. 6.
Beck, R. (2016). *A&ARv* 24.1, p. 4.
Behroozi, P. S., Wechsler, R. H., and Conroy, C. (2013). *ApJ* 770.1, p. 57.
Bell, A. R. (1978a). *MNRAS* 182.3, pp. 443–455.
Bell, E. F. (1978b). *MNRAS* 182.2, pp. 147–156.
Bell, E. F. et al. (2003). *ApJS* 149.2, pp. 289–312.
Berne, O. et al. (2008). *A&A* 479.3, pp. L41–L44.
Berné, O. et al. (2022a).
Berné, O. et al. (2022b). *A&A* 667, A159.
Berné, O. and Tielens, A. G. G. M. (2011). *PNAS* 109.2, pp. 401–406.
Bertone, G., Hooper, D., and Silk, J. (2005). *Phys. Rep.* 405.5-6, pp. 279–390.
Bethe, H., Bethe, and H. (1930). *AnP* 397.3, pp. 325–400.
Bialy, S. and Sternberg, A. (2019).
Bienner, L. et al. (2005). *IAUS* 231, p. 217.
Biermann, L. (1950). *Z. Naturforsch* 5, p. 65.
Binney, J., Binney, and J. (1977). *ApJ* 215, pp. 483–491.
Binney, J. and Tremaine, S. (2008). *Galactic Dynamics*. 2nd. Princeton University Press, p. 888.
Birnboim, Y. and Dekel, A. (2003). *MNRAS* 345.1, pp. 349–364.
Birnboim, Y., Dekel, A., and Neistein, E. (2007). *MNRAS* 380.1, pp. 339–352.
Bleuler, A. and Teyssier, R. (2014). *MNRAS* 445.4, pp. 4015–4036.
Bloch, F., Bloch, and F. (1933). *AnP* 408.3, pp. 285–320.
Blondin, J. M. et al. (1998). *ApJ* 500.1, pp. 342–354.
Bocchio, M. et al. (2012). *A&A* 545, A124.
Bocchio, M., Jones, A. P., and Slavin, J. D. (2014). 570, A32.
Boettcher, E. et al. (2016). *ApJ* 832.2, p. 118.
Bohdansky, J. (1984). *Nucl. Instrum. Methods Phys. Res. B.* 2.1-3, pp. 587–591.
Bohdansky, J. et al. (1980). *JAP* 51.5, pp. 2861–2865.
Bohren, C. F. and Huffman, D. R. (1983). *asls*.
Bolatto, A. D., Wolfire, M., and Leroy, A. K. (2013). *ARA&A* 51.1, pp. 207–268.
Bolatto, A. D. et al. (2024). *ApJ* 967.1, p. 63.
Booth, C. M. et al. (2013). *ApJ* 777.1, p. L16.
Boschman, L. et al. (2012). *ApJL* 761.2, p. L33.
Boschman, L. et al. (2015). *A&A* 579, A72.
Bothwell, M. S. et al. (2017). *MNRAS* 466.3, pp. 2825–2841.
Bouché, N. et al. (2015). *ApJ* 150.3, p. 92.
Bournaud, F., Elmegreen, B. G., and Elmegreen, D. M. (2007). *ApJ* 670.1, pp. 237–248.
Bournaud, F. et al. (2013). *ApJ* 780.1, p. 57.
Boutéraon, T. et al. (2019). *A&A* 623, A135.
Boyett, K. et al. (2024). *arXiv* 000, arXiv:2401.16934.
Bréchignac, P. et al. (2014). *JChPh* 141.16, p. 164325.
Breitschwerdt, D., McKenzie, J. F., and Völk, H. J. (1991). *A&A* 245, p. 79.
Brinchmann, J. et al. (1998). *ApJ* 499.1, pp. 112–133.
Bringa, E. M. et al. (2007). *ApJ* 662.1, pp. 372–378.
Bron, E., Le Bourlot, J., and Le Petit, F. (2014). *A&A* 569, A100.
Bryan, G. L. and Norman, M. L. (1998). *ApJ* 495.1, pp. 80–99.
Buck, T. et al. (2020). *MNRAS* 497.2, pp. 1712–1737.
Bunker, A. J. et al. (2023). *A&A* 677, A88, A88.
Burke, J. R. and Hollenbach, D. J. (1983). *ApJ* 265, p. 223.

Burke, J. R. et al. (1974). *ApJ* 190, pp. 1–10.
Burton, M. G. et al. (1990). *ApJ* 365, p. 620.
Cadiou, C., Dubois, Y., and Pichon, C. (2022). *MNRAS* 514.4, pp. 5429–5442.
Calzetti, D. et al. (2000). *ApJ* 533.2, pp. 682–695.
Cameron, A. J. et al. (2023). *A&A* 677, A115.
Camps, P. and Baes, M. (2015). *Astron. Comput.* 9, pp. 20–33.
Cañas, R. et al. (2019). *MNRAS* 482.2, pp. 2039–2064.
Canosa, A. et al. (1994). *CPL* 228.1, pp. 26–31.
Capak, P. L. et al. (2011). *Nature* 470.7333, pp. 233–235.
Caprioli, D. and Spitkovsky, A. (2014). *ApJ* 794.1, p. 47.
Carelli, F., Grassi, T., and Gianturco, F. A. (2013). *A&A* 549, A103.
Carilli, C. and Walter, F. (2013). *ARA&A* 51.1, pp. 105–161.
Casey, C. M. et al. (2019). *ApJ* 887.1, p. 55.
Castellanos, P. et al. (2018a). *A&A* 616, A167.
Castellanos, P. et al. (2018b). *A&A* 616, A166.
Cau, P. (2002). *A&A* 392.1, p. 203.
Cautun, M. et al. (2020). *MNRAS* 494.3, pp. 4291–4313.
Cazaux, S. and Tielens, A. G. G. M. (2002). *ApJ* 575.1, pp. L29–L32.
Cazaux, S. and Tielens, A. G. G. M. (2004). *ApJ* 604.1, pp. 222–237.
Cazaux, S. et al. (2004). *ApJ* 604.1, pp. 222–237.
Ceverino, D., Dekel, A., and Bournaud, F. (2010). *MNRAS* 404.4, pp. 2151–2169.
Chaabouni, H. et al. (2012). *A&A* 538, A128.
Chabrier, G. (2005). In: *The Initial Mass Function 50 Years Later*. Ed. by E. Corbelli, F. Palla, and H. Zinnecker. Vol. 327. Astrophysics and Space Science Library, p. 41.
Chan, T. K. et al. (2019). *MNRAS* 488.3, pp. 3716–3744.
Chan, T. K. et al. (2022). *MNRAS* 517.1, pp. 597–615.
Chapman, S. C. et al. (2005). *ApJ* 622.2, pp. 772–796.
Chastenet, J. et al. (2022).
Chen, C.-C. et al. (2017). *ApJ* 846.2, p. 108.
Cherchneff, I. et al. (1992). *ApJ* 401, p. 269.
Chiar, J. E. and Tielens, A. G. G. M. (2005). *ApJ* 637.2, pp. 774–785.
Chisholm, J. et al. (2017). *MNRAS* 469.4, pp. 4831–4849.
Cho, J. and Lazarian, A. (2005). *ApJ* 631.1, pp. 361–370.
Cho, J. and Lazarian, A. (2007). *ApJ* 669.2, pp. 1085–1097.
Choban, C. R. et al. (2022).
Chokshi, A. et al. (1993). *ApJ* 407, p. 806.
Christensen, C. R. et al. (2016). *ApJ* 824.1, p. 57.
Claeyssens, A. et al. (2023). *MNRAS* 520.2, pp. 2180–2203.
Clayton, G. C. et al. (1985). *ApJ* 288, pp. 558–568.
Clemens, D. P., Tassis, K., and Goldsmith, P. F. (2016). *ApJ* 833.2, p. 176.
Cochrane, R. K. et al. (2019). *MNRAS* 488.2, pp. 1779–1789.
Commerçon, B., Marcowith, A., and Dubois, Y. (2019). *A&A* 622, A143.
Commerçon, B. et al. (2023).
Compiègne, M. et al. (2008). *A&A* 491.3, pp. 797–807.
Compiègne, M. et al. (2010). *A&A* 525.5, A103.
Concas, A. et al. (2022). *MNRAS* 513.2, pp. 2535–2562.
Condon, J. J. (1992). *ARA&A* 30.1, pp. 575–611.
Conroy, C. and Gunn, J. E. (2010). *ApJ* 712.2, pp. 833–857.
Conroy, C. and Wechsler, R. H. (2009). *ApJ* 696.1, pp. 620–635.
Conroy, C., White, M., and Gunn, J. E. (2010). *ApJ* 708.1, pp. 58–70.

Cosslett, V. E. (1978). *J. Microsc.* 113.2, pp. 113–129.
Cowie, L. L., Hu, E. M., and Songaila, A. (1995). *ApJ* 110.4, p. 1576.
Cox, E. G. et al. (2018). *ApJ* 855.2, p. 92.
Crutcher, R. M. (2012). *ARA&A* 50, pp. 29–63.
Cullen, C. (1996). *Astronomy and Mathematics in Ancient China*.
Cullen, F. et al. (2017). *MNRAS* 470.3, pp. 3006–3026.
Cullen, F. et al. (2018). *MNRAS* 476.3, pp. 3218–3232.
Cuppen, H. M. and Herbst, E. (2007). *ApJ* 668.1, pp. 294–309.
D'Eugenio, F. et al. (2023). *arXiv*, arXiv:2311.09908.
D'Hendecourt, L. B. et al. (1987). *A&A* 180.1-2, pp. L9–L12.
Da Cunha, E. et al. (2015). *ApJ* 806.1, p. 110.
Daddi, E. et al. (2008a). *ApJ* 694.2, pp. 1517–1538.
Daddi, E. et al. (2008b). *ApJL* 673.1, p. L21.
Dahlem, M., Lisenfeld, U., and Golla, G. (1995). *ApJ* 444, p. 119.
Dalcanton, J. J., Spergel, D. N., and Summers, F. J. (1996). *ApJ* 482.2, pp. 659–676.
Dalgarno, A. et al. (1972). *ARA&A* 10.1, p. 375.
Dalla Vecchia, C. and Schaye, J. (2012). *MNRAS* 426.1, pp. 140–158.
Danielson, A. L. R. et al. (2017). *ApJ* 840.2, p. 78.
Danovich, M. et al. (2012). *MNRAS* 422.2, pp. 1732–1749.
Danovich, M. et al. (2015). *MNRAS* 449.2, pp. 2087–2111.
Dashyan, G. and Dubois, Y. (2020). *A&A* 638, p. 123.
Davé, R. et al. (2010). *MNRAS* 404.3, pp. 1355–1368.
Davé, R. et al. (2013). *MNRAS* 434.3, pp. 2645–2663.
Davé, R. et al. (2019). *MNRAS* 486.2, pp. 2827–2849.
Davies, R. et al. (2011). *ApJ* 741.2, p. 69.
Davis Leverett, J. et al. (1951). *ApJ* 114.6, p. 206.
Davis, M. et al. (1985). *ApJ* 292, pp. 371–394.
De Jong, T. et al. (1985). *A&A* 147, pp. L6–L9.
De Bernardis, P. et al. (2000). *Nature* 404.6781, pp. 955–959.
De Vis, P. et al. (2017). *MNRAS* 471.2, pp. 1743–1765.
De Vis, P. et al. (2019). *A&A* 623, A5.
Decarli, R. et al. (2018). *ApJ* 854.2, p. 97.
Dekel, A. and Birnboim, Y. (2006). *MNRAS* 368.1, pp. 2–20.
Dekel, A. et al. (2009a). *Nature* 457.7228, pp. 451–454.
Dekel, A. et al. (2009b). *Nature* 457.7228, pp. 451–454.
Dekel, A. et al. (2022). *MNRAS* 511.1, pp. 316–340.
Delhaize, J. et al. (2017). *A&A* 602, A4.
Dessauges-Zavadsky, M. et al. (2020). *A&A* 643, A5.
Devriendt, J. E. G. and Guiderdoni, B. (2000). *A&A* 363.3, pp. 851–862.
Di Teodoro, E. M. and Fraternali, F. (2015). *MNRAS* 451.3, pp. 3021–3033.
Dolginov, A. Z. et al. (1976). *Ap&SS* 43.2, p. 257.
Dopcke, G. et al. (2011). *ApJL* 729.1, p. L3.
Dorfi, E. A. and Breitschwerdt, D. (2012). *A&A* 540, A77.
Dorschner, J., Dorschner, and J. (1982). *Ap&SS* 81.1-2, pp. 323–328.
Draine, B. T. and Salpeter, E. E. (1979). *ApJ* 231, pp. 77–94.
Draine, B. T. (2011). *ApJ* 732.2, p. 100.
Draine, B. T. and Bertoldi, F. (1996). *ApJ* 468, p. 269.
Draine, B. T. and Lazarian, A. (1998). *ApJ* 508.1, pp. 157–179.
Draine, B. T. and Li, A. (2001). *ApJ* 551.2, pp. 807–824.
Draine, B. T. and Li, A. (2007). *ApJ* 657.2, pp. 810–837.

Draine, B. T. and Sutin, B. (1987). *ApJ* 320, p. 803.
Draine, B. T. and Weingartner, J. C. (1996). *ApJ* 470, p. 551.
Draine, B. T. et al. (1979). *ApJ* 231, pp. 438–455.
Draine, B. T. et al. (1984). *ApJ* 285, p. 89.
Draine, B. T. et al. (2021). *ApJ* 917.1, p. 3.
Draine, B. T. (2010). *Physics of the Interstellar and Intergalactic Medium*. Princeton University Press.
Draine, B. T. et al. (1994). *JOSAA* 11.4, pp. 1491–1499.
Dressler, A. et al. (2024). *ApJ* 964.2, p. 150.
Dubois, Y. and Commerçon, B. (2016). *A&A* 585, pp. 1–10.
Dubois, Y. et al. (2016). *MNRAS* 463.4, pp. 3948–3964.
Dubois, Y. et al. (2019). *A&A* 631, A121.
Dubois, Y. et al. (2024). *A&A* 687, A240, A240.
Duc Hoang, T. et al. (2022). *ApJ* 929.1, p. 27.
Duncan, K. J. et al. (2020). *MNRAS* 498.3, pp. 3648–3657.
Dunkley, J. et al. (2009). *ApJS* 180.2, pp. 306–329.
Durrer, R. and Neronov, A. (2013). *A&ARv* 21.1, p. 62.
Dwek, E. (1998). *ApJ* 501.2, pp. 643–665.
Dwek, E., Galliano, F., and Jones, A. P. (2007). *ApJ* 662.2, pp. 927–939.
Dwek, E. and Werner, M. W. (1981). 248, p. 138.
Dye, S. et al. (2015). *MNRAS* 452.3, pp. 2258–2268.
Efstathiou, G. et al. (1983). *FCPh* 9, pp. 1–138.
Efstathiou, G. et al. (1990). *Nature* 348.6303, pp. 705–707.
Eggen, O. J. et al. (1962). *ApJ* 136, p. 748.
Egorov, O. V. et al. (2022).
Einasto, J. et al. (1974). *Nature* 252.5479, pp. 111–113.
Elahi, P. J. et al. (2019). *PASA* 36, p. 26.
Elias, L. M. et al. (2020). *MNRAS* 494.4, pp. 5439–5448.
Elíasdóttir, Á. et al. (2008). *ApJ* 697.2, pp. 1725–1740.
Elliott, E. J., Baugh, C. M., and Lacey, C. G. (2021). *MNRAS* 506.3, pp. 4011–4030.
Elmegreen, B. G. and Elmegreen, D. M. (2005). *ApJ* 627.2, pp. 632–646.
Elmegreen, B. G. and Scalo, J. (2004). *ARA&A* 42.1, pp. 211–273.
Elmegreen, D. M., Elmegreen, B. G., and Hirst, A. C. (2004a). *ApJL* 604.1, pp. L21–L23.
Elmegreen, D. M., Elmegreen, B. G., and Sheets, C. M. (2004b). *ApJ* 603.1, pp. 74–81.
Elmegreen, D. M. et al. (2007). *ApJ* 658.2, pp. 763–777.
Elmegreen, D. M. et al. (2009). *ApJ* 701.1, pp. 306–329.
Elyajouri, M. et al. (2024). *A&A* 685, A76.
Ensslin, T. (2004). *J. Korean Astron. Soc.* 37.5, pp. 439–446.
Esmerian, C. J. et al. (2021). *MNRAS* 505.2, pp. 1841–1862.
Falgarone, E. et al. (2017). *Nature 2017 548:7668* 548.7668, pp. 430–433.
Farber, R. et al. (2018). *ApJ* 856.2, p. 112.
Farcy, M. et al. (2022). *MNRAS* 513.4, pp. 5000–5019.
Farmer, A. J. and Goldreich, P. (2003). *ApJ* 604.2, pp. 671–674.
Faucher, C.-A., Ere, G., and Peng Oh, S. (2023).
Federrath, C. and Banerjee, S. (2015). *MNRAS* 448.4, pp. 3297–3313.
Federrath, C. and Klessen, R. S. (2012). *ApJ* 763.1, p. 51.
Ferland, G. J. et al. (1998). *Publ. Astron. Soc. Pac.* 110.749, pp. 761–778.
Ferland, G. J. et al. (2017). *RMxAA* 53, pp. 385–438.
Field, G. B. et al. (1969). *ApJL* 155, p. L149.
Fielding, D. et al. (2017). *MNRAS* 466.4, pp. 3810–3826.

Finkelstein, S. L. et al. (2023). *ApJL* 946.1, p. L13.
Fitzpatrick, E. L. (1985). *ApJ* 299, pp. 219–235.
Fitzpatrick, E. L. and Massa, D. (2007). *ApJ* 663.1, pp. 320–341.
Fontanot, F. et al. (2007). *MNRAS* 382.2, pp. 903–914.
Forbes, J. C., Krumholz, M. R., and Speagle, J. S. (2019). *MNRAS* 487.3, pp. 3581–3606.
Forster Schreiber, N. M. et al. (2006). *ApJ* 645.2, pp. 1062–1075.
Förster Schreiber, N. M. et al. (2009). *ApJ* 706.2, pp. 1364–1428.
Fraser, H. J., McCoustra, M. R., and Williams, D. A. (2002). *A&G* 43.2, pp. 10–2.
Frenklach, M. (n.d.) ().
Friedmann, A., Friedmann, and A. (1922). *ZPhy* 10.1, pp. 377–386.
Fromang, S., Hennebelle, P., and Teyssier, R. (2006). *A&A* 457.2, pp. 371–384.
Fromang, S. and Nelson, R. P. (2009). *A&A* 496.3, pp. 597–608.
Fry, J. N., Fry, and N., J. (1996). *ApJL* 461.2, p. L65.
Gaches, B. A. et al. (2022). *A&A* 664, A150.
Galametz, M. et al. (2016). *MNRAS* 456.2, pp. 1767–1790.
Galilei, G. (1610). *Sidereus nuncius*.
Galliano, F., Dwek, E., and Chanial, P. (2008). *ApJ* 672.1, pp. 214–243.
Galliano, F., Galametz, M., and Jones, A. P. (2018). *ARA&A* 56.1, pp. 673–713.
Galliano, F. et al. (2021). *A&A* 649, A18.
Gamow, G. and Teller, E. (1939). *PhRv* 55.7, pp. 654–657.
Gao, Y. and Solomon, P. M. (2004). *ApJ* 606.1, pp. 271–290.
Geen, S., Slyz, A., and Devriendt, J. (2013). *MNRAS* 429.1, pp. 633–651.
Geen, S. et al. (2015). *MNRAS* 448.4, pp. 3248–3264.
Geen, S. et al. (2017). *MNRAS* 471.4, pp. 4844–4855.
Gell-Mann, M. (1995). *J. Complex.* 1.1, pp. 16–19.
Gent, F. A. (2012). *Space Sci. Rev.* 166.1-4, pp. 281–291.
Genzel, R. et al. (2008). *ApJ* 687.1, pp. 59–77.
Genzel, R. et al. (2010). *ApJ* 733.2, p. 101.
Girardi, L. et al. (2000). *A&AS* 141.3, pp. 371–383.
Girichidis, P. et al. (2016). *ApJ* 816.2, p. L19.
Girichidis, P. et al. (2018). *MNRAS* 479.3, pp. 3042–3067.
Gjergo, E. et al. (2018). *MNRAS* 479.2, pp. 2588–2606.
Glover, S. C. O. and Clark, P. C. (2011). *MNRAS* 421.1, pp. 116–131.
Glover, S. C. O. and Jappsen, A.-K. (2007). *ApJ* 666.1, pp. 1–19.
Gnat, O. and Sternberg, A. (2007). *ApJS* 168.2, pp. 213–230.
Gold, T., Gold, and T. (1952). *MNRAS* 112.2, p. 215.
Goldsmith, P. F. and Langer, W. D. (1978). *ApJ* 222, p. 881.
Gomez, H. L. et al. (2012). *MNRAS* 420.4, pp. 3557–3573.
Gordon, K. D. and Clayton, G. C. (1998). *ApJ* 500.2, pp. 816–824.
Gordon, K. D. et al. (2003). *ApJ* 594.1, pp. 279–293.
Gordon, K. D. et al. (2008). *ApJ* 682.1, pp. 336–354.
Gorski, K. M. et al. (2005). *ApJ* 622.2, pp. 759–771.
Gott J. R., I. et al. (1976). *ApJ* 204, pp. 649–667.
Goumans, T. P. M., Goumans, and M., T. P. (2011). *MNRAS* 415.4, pp. 3129–3134.
Graham, J. R. et al. (1987). *ApJ* 319, p. 126.
Granato, G. L. et al. (2000). *ApJ* 542.2, pp. 710–730.
Granato, G. L. et al. (2021). *MNRAS* 503.1, pp. 511–532.
Grassi, T. et al. (2014). *MNRAS* 439.3, pp. 2386–2419.
Graziani, L. et al. (2020). *MNRAS* 494.1, pp. 1071–1088.
Groves, B. et al. (2007). *ApJS* 176.2, pp. 438–456.

Gu, M. et al. (2009). *Phys. D: Non. Phen.* 238.9, pp. 835–839.
Guhathakurta, P. et al. (1989). *ApJ* 345, p. 230.
Guillet, V. et al. (2020). *A&A* 643, p. 17.
Guo, F. and Oh, S. P. (2008). *MNRAS* 384.1, pp. 251–266.
Gutcke, T. A. et al. (2022). *ApJ* 941.2, p. 120.
Guth, A. H. et al. (1982). *PhRvL* 49.15, pp. 1110–1113.
Haardt, F. and Madau, P. (1996). *ApJ* 461, p. 20.
Haarsma, D. B. et al. (1999). *ApJ* 544.2, pp. 641–658.
Habart, E. et al. (2003a). *A&A* 397.2, pp. 623–634.
Habart, E. et al. (2003b). *A&A* 414.2, pp. 531–544.
Hadjar, O. et al. (2001). *PhRvA* 63.3, p. 033201.
Hall, J. S., Hall, and S., J. (1949). *Sci* 109.2825, pp. 166–167.
Harrison, C. M. et al. (2012). *MNRAS* 426.2, pp. 1073–1096.
Hauser, M. G. et al. (1998). *ApJ* 508.1, pp. 25–43.
Hawking, S. W., Hawking, and W., S. (1982). *PhLB* 115.4, pp. 295–297.
Hayward, C. C. et al. (2021). *MNRAS* 502.2, pp. 2922–2933.
Heckman, T. M. et al. (2015). *ApJ* 809.2, p. 147.
Heger, A. et al. (2003). *ApJ* 591.1, pp. 288–300.
Heintz, E. and Zweibel, E. G. (2018). *ApJ* 860.2, p. 97.
Hellyer, B. (1970). *MNRAS* 148, p. 383.
Helou, G., Soifer, B. T., and Rowan-Robinson, M. (1985). *ApJ* 298, p. L7.
Hennebelle, P. and Chabrier, G. (2011). *ApJL* 743.2.
Hennebelle, P. and Falgarone, E. (2012). *ARA&A* 20.1, p. 55.
Hennebelle, P. and Iffrig, O. (2014). *A&A* 570, A81.
Hennebelle, P. et al. (2022). *A&A* 668, A147.
Hennebelle, P. et al. (2024). *arXiv*, arXiv:2404.17368.
Hensley, B. S. and Draine, B. T. (2021). *ApJ* 906.2, p. 73.
Hensley, B. S. and Draine, B. T. (2023). *ApJ* 948.1, p. 55.
Henyey, L. G. et al. (1941). *ApJ* 93.3733, pp. 70–83.
Herdman, J. D. and Miller, J. H. (2008). *J. Phys. Chem. A* 112.28, pp. 6249–6256.
Hickox, R. C. et al. (2012). *MNRAS* 421.1, pp. 284–295.
Hiltner, W. A. (1949). *Sci* 109.2825, p. 165.
Hirashita, H. (2015). *MNRAS* 447.3, pp. 2937–2950.
Hirashita, H. and Aoyama, S. (2019). *MNRAS* 482.2, pp. 2555–2572.
Hirashita, H. and Hoang, T. (2020). *MNRAS* 494.1, pp. 1058–1070.
Hirashita, H. and Kuo, T. M. (2011). *MNRAS* 416.2, pp. 1340–1353.
Hirashita, H. and Li, Z. Y. (2013). *MNRAS: Letters* 434.1, pp. L70–L74.
Hirashita, H. and Yan, H. (2009). *MNRAS* 394.2, pp. 1061–1074.
Hirschmann, M. et al. (2014). *MNRAS* 442.3, pp. 2304–2324.
Hoang, T. (2019). *ApJ* 876.1, p. 13.
Hoang, T. (2020). *Galaxies* 8.8, p. 52.
Hoang, T. and Lazarian, A. (2009). *ApJ* 695.2, p. 1457.
Hoang, T. et al. (2019). *Nat. Astron.* 3.8, pp. 766–775.
Hoang, T. et al. (2021). *ApJ* 908.2, p. 218.
Hockney, R. and Eastwood, J. (2021). *Computer Simulation Using Particles*. CRC Press.
Hodge, J. A. et al. (2012). *ApJ* 760.1, p. 11.
Hodge, J. A. et al. (2015). *ApJL* 798.1, p. L18.
Holland, W. S. et al. (1999). *MNRAS* 303.4, pp. 659–672.
Hollenbach, D. and McKee, C. F. (1979). *ApJS* 41, pp. 555–592.
Hollenbach, D. and McKee, C. F. (1989). *ApJ* 342, p. 306.

Hollenbach, D. et al. (2008). *ApJ* 690.2, pp. 1497–1521.
Hopkins, A. M. and Beacom, J. F. (2006). *ApJ* 651.1, pp. 142–154.
Hopkins, P. F. et al. (2021a). *MNRAS* 501.3, pp. 3640–3662.
Hopkins, P. F. (2013). *MNRAS* 430.3, pp. 1880–1891.
Hopkins, P. F. (2017). *MNRAS* 466.3, pp. 3387–3405.
Hopkins, P. F., Narayanan, D., and Murray, N. (2013a). *MNRAS* 432.4, pp. 2647–2653.
Hopkins, P. F., Quataert, E., and Murray, N. (2012). *MNRAS* 421.4, pp. 3522–3537.
Hopkins, P. F. et al. (2013b). *MNRAS* 430.3, pp. 1901–1927.
Hopkins, P. F. et al. (2020). *MNRAS* 492.3, pp. 3465–3498.
Hopkins, P. F. et al. (2021b). *MNRAS* 501.3, pp. 4184–4213.
Hou, K. C. et al. (2017). *MNRAS* 469.1, pp. 870–885.
Hou, K. C. et al. (2019). *MNRAS* 485.2, pp. 1727–1744.
Hsu, Y. M. et al. (2023). *MNRAS* 519.2, pp. 2475–2485.
Hu, C.-Y., Sternberg, A., and van Dishoeck, E. F. (2023).
Hu, C.-Y. et al. (2019). *MNRAS* 487.3, pp. 3252–3269.
Hubble, E., Hubble, and Edwin (1929). *PNAS* 15.3, pp. 168–173.
Hudgins, D. M. et al. (1999). *ApJL* 513.1, pp. L69–L73.
Hughes, D. H., Dunlop, J. S., and Rawlings, S. (1997). *MNRAS* 289.4, pp. 766–782.
Hull, C. L. et al. (2014). *ApJS* 213.1, p. 13.
Ibanez-Mejia, J. C. et al. (2019). *MNRAS* 485.1, pp. 1220–1247.
Iida, S. et al. (2021). *PhRvA* 104.4, p. 043114.
Indriolo, N. et al. (2018). *ApJ* 865.2, p. 127.
Inoue, A. K., Inoue, and K., A. (2011). *EP&S* 63.10, pp. 1027–1039.
Inoue, A. K. (2005). *MNRAS* 359.1, pp. 171–182.
Inoue, S. et al. (2016). *MNRAS* 456.2, pp. 2052–2069.
Iserles, A. (2008). *A First Course in the Numerical Analysis of Differential Equations*, pp. 33–52.
Iskef, H. et al. (1983). *PMB* 28.5, pp. 535–545.
Ivison, R. J. et al. (2010a). *MNRAS* 402.1, pp. 245–258.
Ivison, R. J. et al. (2010b). *A&A* 518.4, p. 12.
Ivison, R. J. et al. (2013). *ApJ* 772.2, p. 137.
Iwamoto, K. et al. (1999). *ApJS* 125.2, pp. 439–462.
Jäger, C. et al. (2003). *A&A* 401.1, pp. 57–65.
Jeans, J. H., Jeans, and H., J. (1902). *RSPTA* 199.312-320, pp. 1–53.
Jenkins, E. B. (2009). *ApJ* 700.2, pp. 1299–1348.
Ji, S. et al. (2020). *MNRAS* 496.4, pp. 4221–4238.
Ji, S. et al. (2021). *MNRAS* 505.1, pp. 259–273.
Jochims, H. W. et al. (1994). *ApJ* 420, p. 307.
Jochims, H. W. et al. (1996). *A&A* 314, pp. 1003–1009.
Jóhannesson, G., Porter, T. A., and Moskalenko, I. V. (2019). *ApJ* 879.2, p. 91.
Johnson, T. L. et al. (2017). *ApJL* 843.2, p. L21.
Jones, A. P. et al. (1996). *ApJ* 469, p. 740.
Jones, A. P. et al. (2017). *A&A* 602, A46.
Jones, A. P. et al. (2014). *Farad. Disc.* 168.0, pp. 313–326.
Jones, O. C. et al. (2012). *MNRAS* 427.4, pp. 3209–3229.
Jones, T. et al. (2023). *ApJL* 951.1, p. L17.
Joy, D. C. (1995). *J. Scanning Microsc.* 17.5, pp. 270–275.
Joy, D. C. et al. (1996). *Scanning Microscopy* 10.3.
Jubelgas, M. et al. (2008). *A&A* 481.1, pp. 33–63.
Juodžbalis, I. et al. (2023). *MNRAS* 525.1, pp. 1353–1364.

Juodžbalis, I. et al. (2024). *arXiv e-prints*, arXiv:2403.03872.
Jurac, S., Johnson, R. E., and Donn, B. (1998). *ApJ* 503.1, pp. 247–252.
Kaiser, N., Kaiser, and N. (1984). *ApJL* 284, pp. L9–L12.
Karakas, A. I. (2010). *MNRAS* 403.3, pp. 1413–1425.
Karim, A. et al. (2011). *ApJ* 730.2, p. 61.
Katz, H. (2022). *MNRAS* 512.1, pp. 348–365.
Katz, H. et al. (2017). *MNRAS* 468.4, pp. 4831–4861.
Katz, H. et al. (2020). *MNRAS* 494.2, pp. 2200–2220.
Katz, H. et al. (2021). *MNRAS* 507.1, pp. 1254–1282.
Katz, H. et al. (2022a). *MNRAS* 000, pp. 1–10.
Katz, H. et al. (2022b). *arXiv e-prints*, arXiv:2211.04626.
Katz, N. et al. (1999). *ApJ* 522.1, pp. 305–312.
Katz, N. (1992). *ApJ* 391, p. 502.
Katz, N. et al. (1991). *ApJ* 377, p. 365.
Kauffmann, G. et al. (1993). *MNRAS* 264.1, pp. 201–218.
Kawasaki, Y., Kawasaki, Y., and Machida, M. N. (2022a). *MNRAS* 515.4, pp. 6073–6092.
Kawasaki, Y., Koga, S., and MacHida, M. N. (2022b). *MNRAS* 515.2, pp. 2072–2087.
Kemper, F., Vriend, W. J., and Tielens, A. G. G. M. (2004). *ApJ* 609.2, pp. 826–837.
Kemper, F., Vriend, W. J., and Tielens, A. G. G. M. (2005). *ApJ* 633.1, p. 534.
Kemper, F. et al. (2001). *A&A* 369.1, pp. 132–141.
Kennedy, E. S. (1956). *Trans. Am. Philos. Soc.* 46.2, p. 123.
Kereš, D. et al. (2005a). *MNRAS* 363.1, pp. 2–28.
Kereš, D. et al. (2005b). *MNRAS* 363.1, pp. 2–28.
Kereš, D. et al. (2009). *MNRAS* 395.1, pp. 160–179.
Khabazipur, A. and Eaves, N. (2023). *Proc. Combust. Inst.* 39.1, pp. 919–927.
Kim, C. G. and Ostriker, E. C. (2015). *ApJ* 802.2, p. 99.
Kim, J.-G. et al. (2022).
Kimm, T. and Cen, R. (2014). *ApJ* 788.2, p. 121.
Kimm, T. et al. (2015). *MNRAS* 451.3, pp. 2900–2921.
Kimm, T. et al. (2017). *MNRAS* 466.4, stx052.
Kimura, H. et al. (1998). *ApJ* 499.1, pp. 454–462.
Kirchschlager, F., Barlow, M. J., and Schmidt, F. D. (2020). *ApJ* 893.1, p. 70.
Kirchschlager, F., Mattsson, L., and Gent, F. A. (2021). *MNRAS* 509.3, pp. 3218–3234.
Kirchschlager, F. et al. (2019). *MNRAS* 489.4, pp. 4465–4496.
Kobayashi, H. and Tanaka, H. (2010). *Icarus* 206.2, pp. 735–746.
Koornneef, J. et al. (1981). *ApJ* 247, pp. 860–868.
Koyama, H. and Inutsuka, S.-I. (2000). *ApJ* 532.2, pp. 980–993.
Kriek, M. and Conroy, C. (2013). *ApJL* 775.1, p. L16.
Kroupa, P. (2001). *MNRAS* 322.2, pp. 231–246.
Krügel and Endrik (2008). *IPID* 918058779.
Krumholz, M. R. (2014). *The big problems in star formation*.
Krumholz, M. R. and Dekel, A. (2010). *MNRAS* 406.1, pp. 112–120.
Krumholz, M. R. and McKee, C. F. (2005). *ApJ* 630.1, pp. 250–268.
Kulsrud, R. and Pearce, W. P. (1969). *ApJ* 156, p. 445.
Kuwabara, T. and Ko, C.-M. (2020). *ApJ* 899.1, p. 72.
Kuwabara, T. and Ko, C.-M. (2006). *ApJ* 636.1, pp. 290–302.
Lacki, B. C. and Thompson, T. A. (2010). *ApJ* 717.1, pp. 196–208.
Lacki, B. C., Thompson, T. A., and Quataert, E. (2010). *ApJ* 717.1, pp. 1–28.
Lahén, N. et al. (2018). *MNRAS* 475.3, pp. 3934–3958.
Lamberts, T., De Vries, X., and Cuppen, H. M. (2014).

Lange, K., Dominik, C., and Tielens, A. G. (2021). *A&A* 653, A21.
Lange, K., Dominik, C., and Tielens, A. G. (2023). *A&A* 674, A200.
Laor, A. and Draine, B. T. (1993). *ApJ* 402, p. 441.
Larson, R. B., Larson, and B., R. (1975). *MNRAS* 173.3, pp. 671–699.
Larson, R. B., Larson, and B., R. (1976). *MNRAS* 176.1, pp. 31–52.
Larson, R. B., Larson, and B., R. (1974a). *MNRAS* 166.3, pp. 585–616.
Larson, R. B., Larson, and B., R. (1974b). *MNRAS* 169.2, pp. 229–246.
Lazarian, A. (2003). *JQSRT* 79-80, pp. 881–902.
Lazarian, A. and Yan, H. (2001). *ApJL* 566.2, pp. L105–L108.
Lazarian, A. and Beresnyak, A. (2006). *MNRAS* 373.3, pp. 1195–1202.
Lazarian, A. and Hoang, T. (2007). *MNRAS* 378.3, pp. 910–946.
Le Bourlot, J. et al. (2012). *A&A* 541, A76.
Le Page, V., Snow, T. P., and Bierbaum, V. M. (2009). *ApJ* 704.1, pp. 274–280.
Le Page, V. et al. (2001). *ApJS* 132.2, pp. 233–251.
Lebreuilly, U. et al. (2022). *MNRAS* 518.3, pp. 3326–3343.
Lee, H., Hopkins, P. F., and Squire, J. (2017). *MNRAS* 469.3, pp. 3532–3540.
Leitherer, C. et al. (1999). *ApJS* 123.1, pp. 3–40.
Lemaître, G. (1927). *Annales de la Société Scientifique de Bruxelles* 47, p. 49.
Lenok, V. (2021).
Levermore, C. D., Levermore, and D., C. (1984). *JQSRT* 31.2, pp. 149–160.
Lewis, J. S. W. et al. (2023). *MNRAS* 519.4, pp. 5987–6007.
Li, A. (2020). *Nat. Astron.* 4, pp. 339–351.
Li, A. and Draine, B. T. (2001). *ApJ* 554.2, pp. 778–802.
Li, Q., Narayanan, D., and Davé, R. (2019). *MNRAS* 490.1, pp. 1425–1436.
Lifshitz, E. M., Lifshitz, and M., E. (1946). *ZhETF* 16, pp. 587–602.
Limongi, M. and Chieffi, A. (2018). *ApJS* 237.1, p. 13.
Lindhard, J. (1964). *Phys. Lett.* 12.2, pp. 126–128.
Lindhard, J. and Nielsen, V. (1962). *Phys. Lett.* 2.5, p. 209.
Lindhard, J. and Scharff, M. (1961). *Phys. Rev.* 124.1, p. 128.
Ling, Y. and Lifshitz, C. (1998). *JMSp* 33.1, pp. 25–34.
Lisenfeld, U., Völk, H. J., and Xu, C. (1996). *A&A* 314, pp. 745–753.
Litke, K. C. et al. (2019). *ApJ* 870.2, p. 80.
Liu, Y., Kretschmer, M., and Teyssier, R. (2022). *MNRAS* 513.4, pp. 6028–6041.
Logan, R. M. et al. (1968). *JChPh* 49.2, pp. 860–876.
Lovell, C. C. et al. (2021). *MNRAS* 502.1, pp. 772–793.
Low, M. M. M. and Klessen, R. S. (2004). *RMP* 76.1, pp. 125–194.
Lu, Y. S. et al. (2024). *MNRAS* 527.4, pp. 11256–11287.
Luo, S., Zhang, X., and Joy, D. C. (1991). *Radiat. Eff. Defect. S.* 117.1-3, pp. 235–242.
Lynden-Bell, D., Lynden-Bell, and D. (1967). *MNRAS* 136.1, p. 101.
Macciò, A. V., Dutton, A. A., and Van Den Bosch, F. C. (2008). *MNRAS* 391.4, pp. 1940–1954.
Maddox, S. J. et al. (1990). *MNRAS* 243, pp. 692–712.
Magnelli, B. et al. (2009). *A&A* 496.1, pp. 57–75.
Magnelli, B. et al. (2015). *A&A* 573, p. 45.
Maiolino, R. et al. (2024a). *A&A* 687, A67.
Maiolino, R. et al. (2024b). *Nature* 627.8002, pp. 59–63.
Malloci, G. et al. (2004). *A&A* 426.1, pp. 105–117.
Mancini, M. et al. (2015). *MNRAS: Letters* 451.1, pp. L70–L74.
Mandelker, N. et al. (2016). *MNRAS* 463.4, pp. 3921–3947.
Mandelker, N. et al. (2019a). *MNRAS* 484.1, pp. 1100–1132.

Mandelker, N. et al. (2019b). *ApJL* 881.1, p. L20.
Mao, S. A. and Ostriker, E. C. (2018). *ApJ* 854.2, p. 89.
Maoz, D. and Mannucci, F. (2012). *PASA* 29.4, pp. 447–465.
Marasco, A. et al. (2023). *A&A* 670, A92.
Marchand, P. et al. (2021). *A&A* 649, A50.
Marini, E. et al. (2023). *A&A* 670, A97.
Marri, S. and White, S. D. M. (2002). *MNRAS* 345.2, pp. 561–574.
Marrone, D. P. et al. (2018). *Nature* 553.7686, pp. 51–54.
Martin-Alvarez, S. et al. (2018). *MNRAS* 479.3, pp. 3343–3365.
Martin-Alvarez, S. et al. (2020). *MNRAS* 495.4, pp. 4475–4495.
Martin-Alvarez, S. et al. (2021). *MNRAS* 504.2, pp. 2517–2534.
Martin-Alvarez, S. et al. (2022). *MNRAS* 000, pp. 1–23.
Masson, J. et al. (2012). *ApJS* 201.2, p. 24.
Mathis, J. S. et al. (1977). *ApJ* 217, pp. 425–433.
Matsunami, N. et al. (1984). *At. Data Nucl. Data Tables* 31.1, pp. 1–80.
Mattioda, A. L. et al. (2020). *ApJS* 251.2, 22, p. 22.
Mattsson, L., Mattsson, and Lars (2020). *MNRAS* 491.3, pp. 4334–4344.
McAlpine, S. et al. (2019). *MNRAS* 488.2, pp. 2440–2454.
McCormick, A. et al. (2013). *ApJ* 774.2, p. 126.
McKee, C. (1989). *IAUS* 135, p. 431.
McKee, C. F. and Ostriker, E. C. (2007). *ARA&A* 45.1, pp. 565–687.
McKenzie, J. F. et al. (1982). *A&A* 116.2, pp. 191–200.
McKinnon, R., Torrey, P., and Vogelsberger, M. (2016). *MNRAS* 457.4, pp. 3775–3800.
McQuinn, K. B. W., van Zee, L., and Skillman, E. D. (2019). *ApJ* 886.1, p. 74.
McQuinn, M. (2016). *ARA&A* 54.1, pp. 313–362.
Mennella, V. et al. (2012). *ApJL* 745.1, p. L2.
Micelotta, E. R., Jones, A. P., and Tielens, A. G. G. M. (2010a). *A&A* 510, A37.
Micelotta, E. R., Jones, A. P., and Tielens, A. G. (2010b). *A&A* 510.1, A36.
Michałowski, M., Hjorth, J., and Watson, D. (2010). *A&A* 514.14, A67.
Miettinen, O. et al. (2015). *A&A* 577, A29.
Miettinen, O. et al. (2017). *A&A* 602.
Mihalas, D. and Mihalas, B. W. (1984). *OUP*.
Min, M. et al. (2007). *A&A* 462.2, pp. 667–676.
Mitchell, P. D. et al. (2020). *MNRAS* 494.3, pp. 3971–3997.
Miyoshi, T. and Kusano, K. (2005). *J. Comput. Phys.* 208.1, pp. 315–344.
Mo, H. J., Mao, S., and White, S. D. M. (1998). *MNRAS* 295.2, pp. 319–336.
Mo, H. J. and White, S. D. (1996). *MNRAS* 282.2, pp. 347–361.
Mocz, P. et al. (2016). *MNRAS* 463.1, pp. 477–488.
Montet, G. L., Montet, and L., G. (1967). *ApPhL* 11.7, pp. 223–224.
Montillaud, J., Joblin, C., and Toublanc, D. (2013). *A&A* 552, A15.
Montillaud, J. and Joblin, C. (2014). *A&A* 567, A45.
Morlino, G. and Caprioli, D. (2012). In: *AIP Conference Proceedings*. Vol. 1505, pp. 241–244.
Moseley, E. R., Teyssier, R., and Draine, B. T. (2022). *MNRAS* 518.2, pp. 2825–2844.
Moseley, E. R. and Teyssier, R. (2024). *arXiv e-prints*, arXiv:2405.18463, arXiv:2405.18463.
Moster, B. P. et al. (2013). *MNRAS* 428.4, pp. 3121–3138.
Mulcahy, D. D. et al. (2014). *A&A* 568, A74.
Munshi, F. et al. (2013). *ApJ* 766.1, p. 56.
Muratov, A. L. et al. (2015). *MNRAS* 454.3, pp. 2691–2713.
Murga, M. S. et al. (2020). *MNRAS* 497.2, pp. 2327–2339.

Murphy, E. J. (2009). *ApJ* 706.1, pp. 482–496.
Murray, N., Quataert, E., and Thompson, T. A. (2005). *ApJ* 618.2, pp. 569–585.
Murray, N., Quataert, E., and Thompson, T. A. (2010). *ApJ* 709.1, pp. 191–209.
Naab, T. and Ostriker, J. P. (2017). *ARA&A* 55.1, pp. 59–109.
Nakai, Y. et al. (1991). *NIMPB* 58.3-4, pp. 452–462.
Nandy, K. et al. (1981). *MNRAS* 196.4, pp. 955–966.
Nanni, L. et al. (2022). *MNRAS* 515.1, pp. 320–338.
Narayanan, D. et al. (2018). *ApJ* 869.1, 70, p. 70.
Navarro, J. F., Frenk, C. S., and White, S. D. M. (1997). *ApJ* 490.2, pp. 493–508.
Nelson, D. et al. (2019). *MNRAS* 490.3, pp. 3234–3261.
Nelson, R. P. et al. (1997). *ApJ* 482.2, pp. 796–826.
Noguchi, M. (1999). *ApJ* 514.1, pp. 77–95.
Novak, M. et al. (2017). *A&A* 602, p. 5.
Novotný, O. et al. (2005). *JChPh* 123.10, pp. 104303–104303.
Nozawa, T., Kozasa, T., and Habe, A. (2006). *ApJ* 648.1, pp. 435–451.
Nozawa, T. et al. (2011). *ApJ* 736.1, p. 45.
Nuñez-Castiñeyra, A. et al. (2022). *arXiv e-prints*, arXiv:2205.08163.
Ocran, E. F. et al. (2020). *MNRAS* 491.4, pp. 5911–5924.
Ocvirk, P., Pichon, C., and Teyssier, R. (2008). *MNRAS* 390.4, pp. 1326–1338.
Okada, Y. et al. (2013). *A&A* 553, A2.
Oklopčić, A. et al. (2017). *MNRAS* 465.1, pp. 952–969.
Olesen, P. (1993). *arXiv e-prints*, hep–ph/9310275.
Omont, A. et al. (2001). *A&A* 374, pp. 371–381.
Omont, A. et al. (2011). *A&A* 530, p. L3.
Omont, A. et al. (2013). *A&A* 551, A115.
Omukai, K. et al. (2005). *ApJ* 626.2, pp. 627–643.
Oñorbe, J. et al. (2015). *MNRAS* 454.2, pp. 2092–2106.
Oppenheimer, B. D. et al. (2009). *MNRAS* 406.4, pp. 2325–2338.
Ormel, C. W. and Cuzzi, J. N. (2007). *A&A* 466, pp. 413–420.
Ormel, C. W. et al. (2009). *A&A* 502.3, pp. 845–869.
Ostriker, J. (1964). *ApJ* 140, p. 1056.
Ostriker, J. P. et al. (1974). *ApJL* 193, p. L1.
Oteo, I. et al. (2017). *ApJ* 850.2, p. 170.
Padoan, P., Haugboelle, T., and Nordlund, A. (2012). *ApJL* 759.2, p. L27.
Padoan, P. and Nordlund, Å. (2011). *ApJ* 730.1, p. 40.
Pakmor, R. and Springel, V. (2013). *MNRAS* 432.1, pp. 176–193.
Palla, M. et al. (2024). *MNRAS* 528.2, pp. 2407–2427.
Pallottini, A. et al. (2022). *MNRAS*.
Pandya, V. et al. (2021). *MNRAS* 508.2, pp. 2979–3008.
Papadopoulos, P. P. (2010). *ApJ* 720.1, pp. 226–232.
Parente, M. et al. (2022). *MNRAS* 515.2, pp. 2053–2071.
Parker, E. N. (1962). In: *Physics of the Solar System*. Vol. 149, p. 23.
Parker, E. N. (1969). *Space Sci. Rev.* 9.5, pp. 651–712.
Pattle, K. and Fissel, L. (2019). *FrASS* 6, p. 15.
Peeters, E., Spoon, H. W. W., and Tielens, A. G. G. M. (2004). *ApJ* 613.2, pp. 986–1003.
Pei, Y. C., Pei, and C., Y. (1992). *ApJ* 395, p. 130.
Perlmutter, S. et al. (1999). *ApJ* 517.2, pp. 565–586.
Pfrommer, C. et al. (2017). *MNRAS* 465.4, pp. 4500–4529.
Pillepich, A. et al. (2018). *MNRAS* 473.3, pp. 4077–4106.
Pilleri, P. et al. (2012). *A&A* 542, A69.

Pirronello, V. et al. (1996). *ApJL* 475.1, pp. L69–L72.
Pirronello, V. et al. (1997). *ApJ* 483.2, pp. L131–L134.
Pirronello, V. et al. (1999). *A&A* 344, pp. 681–686.
Planck Collaboration et al. (2016). *A&A* 594, A13.
Poppe, T. et al. (1997). *AdSpR* 20.8, pp. 1595–1604.
Popping, G., Somerville, R. S., and Galametz, M. (2017). *MNRAS* 471.3, pp. 3152–3185.
Powell, L. C., Slyz, A., and Devriendt, J. (2011). *MNRAS* 414.4, pp. 3671–3689.
Power, C. et al. (2003). *MNRAS* 338.1, pp. 14–34.
Prantzos, N. et al. (2018). *MNRAS* 476.3, pp. 3432–3459.
Prevot, M. L. et al. (1984). *A&A* 132, pp. 389–392.
Pudritz, R. E. et al. (1989). *ApJ* 342, p. 650.
Purcell, E. M., Purcell, and M., E. (1976). *ApJ* 206, pp. 685–690.
Puschnig, J. et al. (2023). *MNRAS* 524.3, pp. 3913–3929.
Puska, M. J. et al. (1983). *PhRvB* 27.10, pp. 6121–6128.
Qin, Y., Balu, S., and Wyithe, J. S. B. (2023). *MNRAS* 526.1, pp. 1324–1342.
Quataert, E., Thompson, T. A., and Jiang, Y.-F. (2021). *MNRAS* 510.1, pp. 1184–1203.
Ramsøy, M. et al. (2021). *MNRAS* 502.1, p. 351.
Rapacioli, M. et al. (2005). *J. Phys. Chem.* 109.11, pp. 2487–2497.
Rapacioli, M. et al. (2006). *A&A* 460.2, pp. 519–531.
Rasera, Y. and Teyssier, R. (2006). *A&A* 445.1, pp. 1–27.
Rauls, E. et al. (2008). *ApJ* 679.1, pp. 531–536.
Reach, W. T. et al. (2005). *AJ* 131.3, pp. 1479–1500.
Rebrion-Rowe, C. et al. (2003). *IJMSp* 223-224.224, pp. 237–251.
Recchia, S., Blasi, P., and Morlino, G. (2017). *MNRAS* 470.1, p. 865.
Reddy, N. A. and Steidel, C. C. (2004). *ApJL* 603.1, pp. L13–L16.
Reddy, N. A. et al. (2015). *ApJ* 806.2, p. 259.
Rees, M. J. and Ostriker, J. P. (1977). *MNRAS* 179, pp. 541–559.
Relanõ, M. et al. (2016). *A&A* 595, A43.
Rémy-Ruyer, A. et al. (2014). *A&A* 563, A31.
Rey, M. P. et al. (2023). *MNRAS* 000, pp. 1–13.
Reyes, R. et al. (2011). *MNRAS* 417.3, pp. 2347–2386.
Rhee, J., Elahi, P., and Yi, S. K. (2022). *ApJ* 927.1, p. 129.
Ricca, A. et al. (2012). *ApJ* 754.1, p. 75.
Richings, A. J., Schaye, J., and Oppenheimer, B. D. (2014). *MNRAS* 440.4, pp. 3349–3369.
Richings, A. J. et al. (2022). *MNRAS* 517.2, pp. 1557–1583.
Rieder, M. and Teyssier, R. (2017). *MNRAS* 471.3, pp. 2674–2686.
Riess, A. G. et al. (1998). *ApJ* 116.3, pp. 1009–1038.
Rigopoulou, D. et al. (1999). *ApJ* 118.6, pp. 2625–2645.
Rigopoulou, D. et al. (2021). *MNRAS* 504.4, pp. 5287–5300.
Rivera, G. C. et al. (2018). *ApJ* 863.1, p. 56.
Roberge, W. G. et al. (1993). *ApJ* 418, p. 287.
Roberts, M. S. et al. (1973). *A&A* 26, pp. 483–485.
Rodrigues, L. F. S. et al. (2016). *ApJ* 816.1, p. 2.
Rodríguez Montero, F. et al. (2022). *MNRAS* 511.1, pp. 1247–1264.
Rodríguez Montero, F. et al. (2024). *MNRAS* 530.4, pp. 3617–3640.
Rodriguez-Gomez, V. et al. (2017). *MNRAS* 467.3, pp. 3083–3098.
Romano, D. et al. (2019). *MNRAS* 490.2, pp. 2838–2854.
Rosdahl, J. and Blaizot, J. (2011). *MNRAS* 423.1, p. 344.
Rosdahl, J. and Teyssier, R. (2015). *MNRAS* 449.4, pp. 4380–4403.
Rosdahl, J. et al. (2013). *MNRAS* 436.3, pp. 2188–2231.

Rosdahl, J. et al. (2018). *MNRAS* 479.1, pp. 994–1016.
Rosen, A. and Bregman, J. N. (1995). *ApJ* 440, p. 634.
Roth, M. A. et al. (2024). *MNRAS* 530.2, pp. 1849–1865.
Rowlands, K. et al. (2014). *MNRAS* 441.2, pp. 1040–1058.
Roy, A. et al. (2012). *ApJ* 763.1, p. 55.
Rubin, V. C., Ford W. K., J., and Thonnard, N. (1978). *ApJL* 225, pp. L107–L111.
Rubin, V. C. et al. (1980). *ApJ* 238, pp. 471–487.
Ruszkowski, M., Yang, H.-Y. K., and Zweibel, E. (2017). *ApJ* 834.2, p. 208.
Rybak, M. et al. (2015a). *MNRAS: Letters* 451.1, pp. L40–L44.
Rybak, M. et al. (2015b). *MNRAS: Letters* 453.1, pp. L26–L30.
Ryu, D. et al. (2003). *ApJ* 589.1, pp. 338–346.
Salem, M., Bryan, G. L., and Hummels, C. (2014). *ApJ* 797.2, p. L18.
Salim, S., Boquien, M., and Lee, J. C. (2018). *ApJ* 859.1, p. 11.
Salim, S. and Narayanan, D. (2020). *ARA&A* 58, pp. 529–575.
Sanders, D. B. et al. (1988). *ApJ* 325, p. 74.
Sargent, M. T. et al. (2010). *ApJS* 186.2, pp. 341–377.
Schady, P. et al. (2011). *A&A* 537, A15.
Schaye, J. et al. (2015). *MNRAS* 446.1, pp. 521–554.
Schaye, J. et al. (2023). *MNRAS* 526.4, pp. 4978–5020.
Schlathölter, T. et al. (1999). *PhRvL* 82.1, pp. 73–76.
Schmidt, M. (1959). *ApJ* 129, p. 243.
Schneider, R. and Maiolino, R. (2024). *A&AR* 32.1, p. 2.
Schneider, R. et al. (2023). *MNRAS* 526.3, pp. 3250–3261.
Scholtz, J. et al. (2023). *arXiv e-prints*, arXiv:2311.18731, arXiv:2311.18731.
Scoville, N. et al. (2015). *ApJ* 800.2, p. 108.
Seok, J. Y., Hirashita, H., and Asano, R. S. (2014). *MNRAS* 439.2, pp. 2186–2196.
Seok, J. Y., Koo, B.-C., and Hirashita, H. (2015). *ApJ* 807.1, p. 100.
Seon, K.-I. and Draine, B. T. (2016). *ApJ* 833.2, p. 201.
Serra Díaz-Cano, L. et al. (2008). *A&A* 492.1, pp. 127–133.
Sharma, P., Parrish, I. J., and Quataert, E. (2010). *ApJ* 720.1, pp. 652–665.
Sharma, P. et al. (2009). *ApJ* 699.1, pp. 348–361.
Shimizu, I., Yoshida, N., and Okamoto, T. (2012). *MNRAS* 427.4, pp. 2866–2875.
Shivaei, I. et al. (2015). *ApJ* 804.2, p. 149.
Sigmund, P. (1969). *PhRv* 184.2, pp. 383–416.
Sigmund, P. (1981). *SPB1* 47, p. 9.
Sigmund, P. (1996). *Phys. Rev. A* 54.4, p. 3113.
Sigmund, P. (2014). *Springer Ser. Solid-State Sci.* 179, pp. 343–415.
Sijacki, D. et al. (2007). *MNRAS* 380.3, pp. 877–900.
Sijacki, D. et al. (2015). *MNRAS* 452.1, pp. 575–596.
Silk, J. (1977). *ApJ* 211, pp. 638–648.
Silk, J. (1968). *ApJ* 151, p. 459.
Silsbee, K., Caselli, P., and Ivlev, A. V. (2021). *MNRAS* 507.4, pp. 6205–6214.
Simpson, C. M. et al. (2016). *ApJ* 827.2, p. L29.
Simpson, J. M. et al. (2012). *MNRAS* 426.4, pp. 3201–3210.
Simpson, J. M. et al. (2014). *ApJ* 788.2, p. 125.
Simpson, J. M. et al. (2015). *ApJ* 807.2, p. 128.
Skilling, J. (1975). *MNRAS* 172.3, pp. 557–566.
Skilling, J. (1971). *ApJ* 170, p. 265.
Slavin, J. D., Dwek, E., and Jones, A. P. (2015). *ApJ* 803.1, p. 7.
Sloan, G. C. et al. (2007). *ApJ* 664.2, pp. 1144–1153.

Smail, I., Ivison, R. J., and Blain, A. W. (1997). *ApJ* 490.1, pp. L5–L8.
Smail, I. et al. (1999). *ApJ* 528.2, pp. 612–616.
Smith, M. C., Sijacki, D., and Shen, S. (2018). *MNRAS* 478.1, pp. 302–331.
Smolcic, V. (2009). *ApJ* 699.1 PART 2, pp. 43–47.
Somerville, R. S. and Davé, R. (2015). *ARA&A* 53.1, pp. 51–113.
Somerville, R. S. and Primack, J. R. (1998). *MNRAS* 310.4, pp. 1087–1110.
Somerville, R. S. et al. (2012). *MNRAS* 423.3, pp. 1992–2015.
Sousbie, T. (2011). *MNRAS* 414.1, pp. 350–383.
Sparke, L. S. (1982). *ApJ* 260, pp. 104–110.
Spilker, J. S. et al. (2014). *ApJ* 785.2, p. 149.
Spitzer Lyman, J. et al. (1948). *ApJ* 107.6, p. 6.
Spitzer, L. (1978). *PPIM*.
Springel, V., Di Matteo, T., and Hernquist, L. (2005). *MNRAS* 361.3, pp. 776–794.
Springel, V. and Hernquist, L. (2003). *MNRAS* 339.2, pp. 312–334.
Starobinsky, A. A., Starobinsky, and A., A. (1982). *PhLB* 117.3-4, pp. 175–178.
Steinacker, J., Baes, M., and Gordon, K. D. (2013). *ARA&A* 51.1, pp. 63–104.
Stepnik, B. et al. (2003). *A&A* 398.2, pp. 551–563.
Stern, J. et al. (2018). *ApJ* 865.2, p. 91.
Stern, J. et al. (2020). *MNRAS* 492.4, pp. 6042–6058.
Stern, J. et al. (2021). *ApJ* 911.2, p. 88.
Stewart, K. R. et al. (2017). *ApJ* 843.1, p. 47.
Stinson, G. et al. (2006). *MNRAS* 373.3, pp. 1074–1090.
Stone, E. C. et al. (2019). *NatAs* 3.11, pp. 1013–1018.
Strandet, M. L. et al. (2016). *ApJ* 822.2, p. 80.
Strong, A. W., Moskalenko, I. V., and Ptuskin, V. S. (2007). *Annu. Rev. Nucl. Part. Sci.* 57.1, pp. 285–327.
Su, K. Y. et al. (2017). *MNRAS* 471.1, pp. 144–166.
Suh, K. W. (2002). *MNRAS* 332.3, pp. 513–528.
Sun, F. et al. (2024). *ApJ* 961.1, p. 69.
Sutherland, R. S. and Dopita, M. A. (1993). *ApJS* 88, p. 253.
Swinbank, A. M. et al. (2006). *MNRAS* 371.1, pp. 465–476.
Swinbank, A. M. et al. (2015). *ApJL* 806.1, p. L17.
Sylvester, R. J. et al. (1999). *A&A* 352, pp. 587–599.
Tacchella, S. et al. (2023). *ApJ* 952.1, p. 74.
Tacconi, L. J. et al. (2008). *ApJ* 680.1, pp. 246–262.
Tadaki, K.-i. et al. (2017). *ApJL* 841.2, p. L25.
Tappe, A. et al. (2006). *ApJ* 653.1, pp. 267–279.
Tegmark, M. and Peebles, P. J. E. (1998). *ApJL* 500.2, pp. L79–L82.
Teyssier, R. (2002). *A&A* 385.1, pp. 337–364.
Teyssier, R., Fromang, S., and Dormy, E. (2006). *J. Comput. Phys.* 218.1, pp. 44–67.
Teyssier, R. et al. (2013). *MNRAS* 429.4, pp. 3068–3078.
Thomas, T. and Pfrommer, C. (2019). *MNRAS* 485.3, pp. 2977–3008.
Thomas, T., Pfrommer, C., and Pakmor, R. (2023). *MNRAS* 521.2, p. 3023.
Thompson, T. A. et al. (2006). *ApJ* 645.1, pp. 186–198.
Thomson, A. P. et al. (2014). *MNRAS* 442.1, pp. 577–588.
Thornton, K. et al. (1998). *ApJ* 500.1, pp. 95–119.
Thrower, J. D. et al. (2012). *ApJ* 752.1, p. 3.
Tielens, A. G. G. M. (2005). *PCIM*.
Tielens, A. G. G. M. et al. (1991). *ApJ* 381, p. 181.
Tielens, A. G. G. M. et al. (1994). *ApJ* 431, p. 321.

Tielens, A. (2008). *ARA&A* 46.1, pp. 289–337.
Tielens and Alexander (2021). *MOAS*.
Tillson, H. et al. (2015). *MNRAS* 449.4, pp. 4363–4379.
Tobita, S. et al. (1992). *CP* 161.3, pp. 501–508.
Toft, S. et al. (2014). *ApJ* 782.2, p. 68.
Tollet, É. et al. (2019). *MNRAS* 485.2, pp. 2511–2531.
Tóth, G., Tóth, and Gábor (2000). *JCoPh* 161.2, pp. 605–652.
Totton, T. S., Misquitta, A. J., and Kraft, M. (2012). *PCCP* 14.12, pp. 4081–4094.
Tram, L. N. et al. (2021). *ApJ* 923.1, p. 130.
Trayford, J. W. et al. (2017). *MNRAS* 470.1, pp. 771–799.
Trebitsch, M. et al. (2018). *MNRAS* 478.4, pp. 5607–5625.
Tress, M. et al. (2018). *MNRAS* 475.2, pp. 2363–2374.
Trotta, R. et al. (2011). *ApJ* 729.2, p. 106.
Tumlinson, J., Peeples, M. S., and Werk, J. K. (2017). *ARA&A* 55.1, pp. 389–432.
Tweed, D. et al. (2009). *A&A* 506.2, pp. 647–660.
Uhlig, M. et al. (2012). *MNRAS* 423.3, pp. 2374–2396.
Vachaspati, T. (1991). *Phys. Lett. B* 265.3-4, pp. 258–261.
Vachaspati, T. (2021). *Rep. Prog. Phys.* 84.7, p. 074901.
Van den Bergh, S. et al. (1996). *ApJ* 112.2, p. 359.
Van Der Werf, P. P. et al. (2011). *ApJL* 741.2, p. L38.
Van der Kruit, P. C. (1971). *A&A* 15, pp. 110–122.
Van der Kruit, P. C. (1973). *A&A* 29, p. 263.
Vassiliadis, E. et al. (1993). *ApJ* 413, p. 641.
Vazza, F. et al. (2017). *MNRAS* 464.1, pp. 210–230.
Veilleux, S., Cecil, G., and Bland-Hawthorn, J. (2005). *ARA&A* 43.1, pp. 769–826.
Verstraete, L. et al. (1990). *A&A* 237.2, pp. 436–444.
Vlahakis, C. et al. (2015). *ApJL* 808.1, p. L4.
Vogelsberger, M. et al. (2013). *MNRAS* 436.4, pp. 3031–3067.
Vogelsberger, M. et al. (2019). *MNRAS* 487.4, pp. 4870–4883.
Vogelsberger, M. et al. (2020a). *Nat. Rev. Phys.* 2.1, pp. 42–66.
Vogelsberger, M. et al. (2020b). *MNRAS* 492.4, pp. 5167–5201.
Völk, H., Klein, U., and Wielebinski, R. (1989). *A&A* 213, pp. L12–L14.
Völk, H. J. et al. (1980). *A&A* 85.3, p. 316.
Wakelam, V. et al. (2017). *Mol. Astrophys.* 9, pp. 1–36.
Walter, F. et al. (2012). *Nature* 486.7402, pp. 233–236.
Wang, J.-W. et al. (2017). *ApJ* 849.2, p. 157.
Wechsler, R. H. and Tinker, J. L. (2018). *ARA&A* 56.1, pp. 435–487.
Weingartner, J. C. and Draine, B. T. (1999). *ApJ* 517.1, pp. 292–298.
Weingartner, J. C. and Draine, B. T. (2000). *ApJ* 548.1, pp. 296–309.
Weingartner, J. C. and Draine, B. T. (2001a). *ApJ* 548.1, pp. 296–309.
Weingartner, J. C. and Draine, B. T. (2001b). *ApJ* 563.2, pp. 842–852.
Weingartner, J. C. and Draine, B. T. (2001c). *ApJS* 134.2, pp. 263–281.
Wenzel, G. et al. (2020). *A&A* 641, A98.
Werhahn, M., Pfrommer, C., and Girichidis, P. (2021). *MNRAS* 508.3, pp. 4072–4095.
Whalen, D. et al. (2008). *ApJ* 682.1, pp. 49–67.
Wheeler, C. et al. (2018). *MNRAS* 490.3, pp. 4447–4463.
White, S. D. M. et al. (1978). *MNRAS* 183.3, pp. 341–358.
White, S. D. M. et al. (1991). *ApJ* 379, p. 52.
Wiener, J., Pfrommer, C., and Oh, S. P. (2017). *MNRAS* 467.1, pp. 906–921.
Wiener, J., Oh, S. P., and Guo, F. (2013). *MNRAS* 434.3, pp. 2209–2228.

Wild, V. et al. (2011). *MNRAS* 417.3, pp. 1760–1786.
Williams, C. C. et al. (2021). *ApJ* 908.1, p. 54.
Wise, J. H. et al. (2012). *ApJ* 745.1, p. 50.
Witstok, J. et al. (2023). *Nature* 621.7978, pp. 267–270.
Witt, A. N. and Gordon, K. D. (2000). *ApJ* 528.2, pp. 799–816.
Witt, A. N. et al. (1996). *ApJ* 463, p. 681.
Wolfire, M. G. et al. (1995). *ApJ* 443, p. 152.
Wolfire, M. G. et al. (2002). *ApJ* 587.1, pp. 278–311.
Wolfire, M. G. et al. (2003). *ApJ* 587.1, pp. 278–311.
Wolfire, M. G. et al. (2008). *ApJ* 680.1, pp. 384–397.
Woods, R. et al. (2014). *MNRAS* 442.1, pp. 732–740.
Wright, R. J. et al. (2019). *MNRAS* 487.3, pp. 3740–3758.
Wu, J. et al. (2005). *ApJL* 635.2, pp. L173–L176.
Xu, S. and Lazarian, A. (2022). *ApJ* 927.1, p. 94.
Yan, H. et al. (2022). *ApJL* 942.1, p. L9.
Yan, H. and Lazarian, A. (2002). *ApJL* 592.1, pp. L33–L36.
Yan, H., Lazarian, A., and Draine, B. T. (2004). *ApJ* 616.2, pp. 895–911.
Yang, C. et al. (2016). *A&A* 595, A80.
Yang, C. et al. (2019). *A&A* 624, A138.
Yang, G. et al. (2023). *ApJL* 950.1, p. L5.
Yokoyama, S. L. and Ohira, Y. (2023). *MNRAS* 523.3, pp. 3671–3677.
Yun, M. S., Reddy, N. A., and Condon, J. J. (2001). *ApJ* 554.2, pp. 803–822.
Zacharia, R., Ulbricht, H., and Hertel, T. (2004). *Phys. Rev. B* 69.15, p. 155406.
Zafar, T. et al. (2018). *MNRAS* 479.2, pp. 1542–1554.
Zafar, T. et al. (2011). *A&A* 532, A143.
Zhang, Z. Y. et al. (2014). *ApJL* 784.2, p. L31.
Zhang, Z. Y. et al. (2018). *Nature* 558.7709, pp. 260–263.
Zhen, J. et al. (2014). *ApJL* 797.2.
Zhen, J. et al. (2015). *ApJL* 804.1, p. L7.
Zhen, J. et al. (2016). *ApJ* 822.2, p. 113.
Zhu, Z., Stone, J. M., and Bai, X. N. (2015). *ApJ* 801.2, p. 81.
Zhukovska, S., Gail, H. P., and Trieloff, M. (2008). *A&A* 479.2, pp. 453–480.
Zhukovska, S. et al. (2016). *ApJ* 831.2, p. 147.
Ziegler, J. F. and Biersack, J. P. (1985). "The Stopping and Range of Ions in Matter". In: *Treatise on Heavy-Ion Science: Volume 6: Astrophysics, Chemistry, and Condensed Matter*. Ed. by D. A. Bromley. Boston, MA: Springer US, pp. 93–129.
Zier, O., Springel, V., and Mayer, A. C. (2023). *MNRAS* 527.1, pp. 1563–1579.
Zubko, V., Dwek, E., and Arendt, R. G. (2004). *ApJS* 152.2, pp. 211–249.
Zweibel, E. G. et al. (1975). *ApJ* 201, pp. 63–73.
Zwicky, F., Zwicky, and F. (1933). *AcHPh* 6, pp. 110–127.